Observing Charge Transfer Dynamics in Molecules: First Principles Simulation of Valence and Core Spectroscopies of DMABN and its derivatives

Jibrael Rolston

A thesis submitted in partial fulfillment of the requirements for the degree of

Master of Science in Chemistry

Department of Chemistry and Biomolecular Sciences

Faculty of Science

University of Ottawa

This thesis for the Master of Science degree by

Jibrael Rolston

to be approved for the

Chemistry Program

by

John Pezacki, Chair

Michael Schuurman, Supervisor

Albert Stolow, Co-Supervisor

Paul Mayer

Jacob Krich

Abstract

In order to understand the myriad of processes underlying photochemistry or photosynthesis, many of which are essential to the design of semiconductors or other technologies, it has always been important to directly observe the processes at play in the ultrafast excited state dynamics of molecules. The evolving nuclear and electronic character of excited states prepared by photo-excitation can be measured using a host of spectroscopic probe techniques, based on the valence or core excitation of molecules. Ultrafast photo-excitation generally leads to both electronic and geometrical (nuclear) rearrangements of a molecule's structure. One paradigmatic example is the twisted intramolecular charge transfer dynamics evinced by dimethylamino benzonitrile (DMABN). Here, the large amplitude motion, involving a twist and bend of the dimethylamino group, gives rise to a charge transfer state, characterized by a separation of charge between the benzene ring and the amino group, and giving rise to a large dipole moment. These nuclear and electronic rearrangements have interested physical chemists over the last 60 years, serving as a great benchmark for those testing the efficacy of their methods in detecting charge transfer states, and for those exploring the ability to achieve long lived charge separation in molecules in general. Naturally, the wealth of studies on DMABN has also led to many conflicting interpretations of the nuclear structures and electronic configurations important to the excited state dynamics of the molecule. By probing the electronic structure of DMABN with simulated valence absorption and photoelectron spectroscopies, along with new core absorption and photoelectron studies, a series of specific novel time-resolved experiments were proposed to more conclusively image the evolving charge transfer character in this system. Specifically, a dual X-ray Absorption and X-ray Photoelectron study on DMABN and its analogues is proven to be an efficient way to resolve signals attributed to charge transfer excited state minimums from other excited state minimums in this thesis. Furthermore, this thesis addresses some of these long standing controversies in the excited state dynamics of DMABN, by proposing a conclusive dynamical model that takes into account all previously performed experimental spectroscopies on the molecule. To de-

velop the validity of this model, and encourage further time resolved studies to prove said model, this thesis also presents studies of a series of DMABN-like molecules. Using these analogues, this thesis proposes a host of unique time resolved spectroscopies on charge transfer systems, allowing for the earlier proposed dynamical model to be proven with several potential time-resolved experimental studies. Charge transfer states have proven uniquely difficult to analyze for most electronic structure methods even for static calculations, independent of dynamics. This work also demonstrates the effectiveness of a new *ab initio* quantum chemistry method in replicating experimental spectroscopies, DFT/MRCI(2). Furthermore, it was proven that said method is suitable for computationally inexpensive, core and valence absorption/photoelectron spectroscopies, while also retaining the ability to treat charge transfer states appropriately.

This thesis is approved for recommendation to the Graduate committee.

Thesis Supervisor:

_____

Michael Schuurman *,†

Thesis Co-Supervisor:

_____

Albert Stolow *

* Department of Chemistry and Biomolecular Sciences, University of Ottawa, Ottawa, Canada

† National Research Council Canada, 100 Sussex Dr., Ottawa, Canada, K1A 0R6

Acknowledgement

My thanks to Michael Schuurman for his patience, kindness, and steady hand. Working under him has been a dream. My thanks to Albert Stolow for introducing me to the world of quantum chemistry, changing my life forever, and keeping an eye on me all these years. Thank you to my family, friends, and partner for their infinite support and love.

Contents

List of Figures

1 Background Information

1.1 Charge Transfer in Organic Chromophores

The continued development and application of optical techniques to measure and induce the flow of charge within a molecule has been driven by a desire to both understand natural and biological processes for harvesting light and thereby develop rational design principles for new materials.[11–13] The study of intramolecular charge transfer in particular has been key to interpreting photochemical processes such as photosynthesis and solar energy conversion.[12–16] In applied sciences, understanding charge transfer is important for the design of solar cells used in light harvesting, or in the design of chemical probes, optical light diodes, and photocatalysis.[13,16–20] A molecular electronic state that exhibits a high degree of separation of charge, as evidenced by a large permanent dipole moment, is termed a charge transfer (CT) state.[3,13,16] Due to the significant change in electronic and nuclear character that occurs after absorption, and during subsequent relaxation into the CT state, these CT processes are sometimes amenable to observation via optical spectroscopies.[11–13] One intramolecular motif that has been observed to evolve CT character involves the presence of both an electron donating and electron accepting group, coupled via a conjugated π-electron system.[13] The intramolecular CT (ICT) dynamics that result from initial photoexcitation will depend strongly on the nature of the donor and acceptor groups, as well as the coupling motif between the two. For example, in the case of zwitterionic Betaine-30 (Fig 1), upon excitation, it soon after fluoresces from an ICT state whose nuclear structure has been

proposed to have a higher twisting angle between the donor and acceptor groups than the ground state nuclear structure.[1,2,21] For larger zwitterionic molecules of this form, often classified as donor-bridge-acceptor molecules owing to the long distance between the donor and acceptor groups, changes in the electronic character of the charge transfer state can be easily monitored by experimental/theoretical spectroscopies, owing to localization at one end of the molecule or the other, which is induced by changes in the molecule's nuclear character at key points, i.e. the bridge between the acceptor and donor groups.[3,22–24] This motif while simple, often suffers from what is named Charge Recombination (CR), a process referring to the reversal of the charge transfer process, which limits the longevity of the charge transfer states involved.[3,22–25]

However, there exists a distinct set of ICT processes which have garnered the most interest from quantum chemists, owing to their complexity but also due to their non transient nature.[3,13] In these specific ICT processes, the ground state is not zwitterionic, thus, the charge is more delocalized compared to earlier examples.[3,13] Instead, at the ground state, the electrons to be excited to the charge transfer state are already delocalized over the entire nuclear framework. However, at the charge transfer state, there may exist localized regions of excess or depleted charge at specific atoms in the molecule, indicating significant changes that are tractable between the electronic character of the ground and charge transfer states.[3,13] For these ICT processes, a change in the molecule's nuclear character can induce differences in the electronic character of the excited state relative to the ground state, stabilizing it and increasing the lifetime of the excited charge transfer state. Depending on the molecule, the ensuing dynamics may involve multiple coupled nuclear coordinates and many electronic states, leaving a high degree of uncertainty as to the electronic and nuclear character of the ICT state of interest. In this thesis, molecules that possess ICT processes of this type will be examined, such that the full characterization of the nuclear and electronic structure of the ICT state can be performed. The model of ICT formation in molecules of this class will be defined such that existing experimental and theoretical spectroscopies can be interpreted

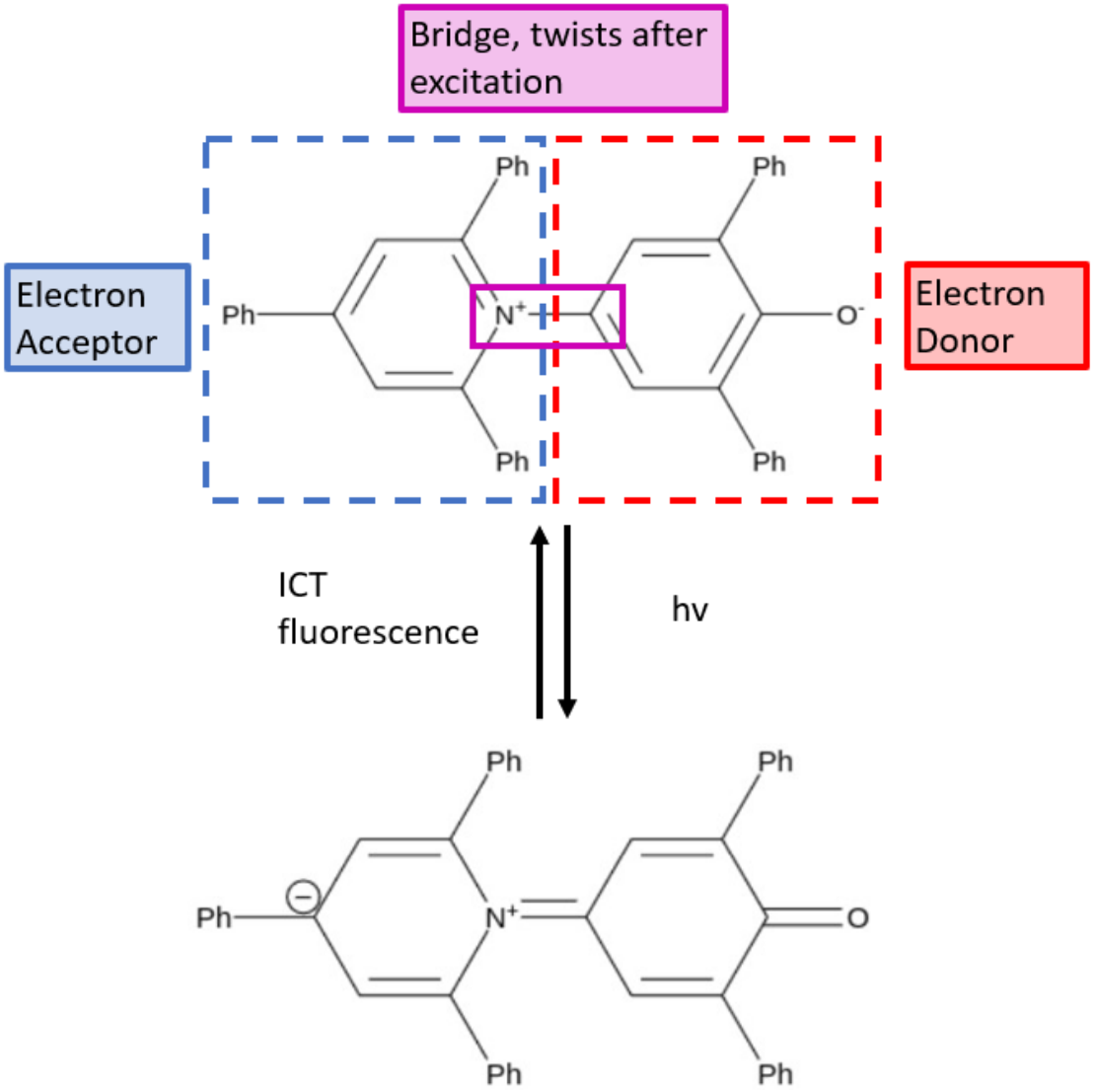

Figure 1: Betaine-30: An example of intramolecular charge transfer. After initial ground state absorption (top), charge is moved from the electron donor group to the electron acceptor group, and the bridge between the two experiences a change in nuclear character (twist, bottom structure). See ref.[1–3] for details.

and new spectroscopies can be performed to identify the extent of charge transfer for a given instance.

1.2 Models for Charge Transfer Dynamics in DMABN

One prominent molecule that exhibits ICT dynamics is para-dimethylamino benzonitrile (p-DMABN, or simply DMABN), constituting a benchmark system for detecting intramolecu-

lar charge transfer in the gas phase .[13,26,27] DMABN possesses the previously noted motifs common to molecules exhibiting ultrafast charge transfer; a π-donor group (dimethylamino group) coupled to a π-acceptor group (cyano group) via a conjugated benzene ring.[13,26,28] DMABN was first observed to possess dual fluorescence by Lippert et al.,[29] referring to the molecule's ability to fluoresce at two separate wavelengths depending on the solvent in which the experiment was conducted. This was interpreted to mean that at least two separate excited state minimum structures were the source of these individual signals. The first signal was initially attributed to a locally excited (LE) structure, characterized by the benzene ring widening, and a slight twist of the dimethylamino group ($\sim$15 to 30 degrees), minor but distinct changes compared to the nuclear ground state structure.[13,30–33] The second band was attributed to a structure possessing a large dipole moment; since this band only appeared in polar solvents, it was suggested to be due to the population of a charge transfer state with a distinct nuclear structure.[13,26,27] Depending on the experimental parameters, both bands may be visible, such as in a minorly polar solvent (and as discussed further in the text, in time resolved studies, the decay time of the first band was found to be closely correlated with the rise time of the second band).[9,10,13,34] Competing theories emerged to explain the observed dual fluorescence, specifically concerning the nuclear structure of the second band. The most prominent of these theories is the twisted intramolecular charge transfer (TICT) model proposed by Grabowski et al.[35] In this model, after initial absorption the dimethylamino group twists causing subsequent depyramidalization at the dimethylamino nitrogen.[13,35,36] This causes decoupling of the dimethylamino and benzonitrile groups, accommodating charge transfer in an apparently irreversible process (at least to the original excited state conformation before this decoupling, fluorescence to the ground state will eventually lead to the molecule populating the ground state structure).[13,35,36] The main basis for this theory was due to initial absorbance and fluorescence spectrum which did not yield dual fluorescence when the dimethylamino group was structurally inhibited, like in 6-cyanobenzquinuclidine (CBQ).[37–40]

A counter proposal that emerged after was the planar intramolecular charge transfer (PICT) model, proposed by Zachariasse et al.,[41–47] which argued that the benzonitrile and dimethylamine moieties were not entirely decoupled at the charge transfer state, and therefore the nuclear structure was not very distinct from the ground state structure. It suggested instead that the large dipole moment was due to the change in the bond lengths between the benzene group and its functional groups, retaining the planar configuration.[41,44] This theory pointed to molecules like 1-methyl-7-cyano-2,3,4,5-tetrahydro-1H-1-benz-azepine (NMC7)[43] or 4-aminobenzonitrile 1-tert-butyl-6-cyano-1,2,3,4-tetrahydroquinoline (NTC6)[47] which could not twist to form the TICT structure and yet continued to produce dual fluorescence, or molecules like m-DMABN which has a dimethylamino group that can twist without structural inhibition, yet did not produce dual fluorescence in gas phase or in solvent.[45] This reinforced the PICT model that asserted: 1) ICT was driven by the vibronic coupling between the singlet states S_1 and S_2, and that, for these molecules, the gap between the states was too large for the TICT structure (were it to exist as an excited state minimum) to be accessed via interstate decay from S_2 to S_1, and 2) the more favourable ICT state (the PICT state), was accessed by the inversion of the dimethylamino group instead of the twist.[41–43,45] However, subsequent studies argued that large-amplitude motion is essential to modulate the electronic coupling necessary to induce a large dipole moment distinct from the LE state responsible for the primary fluorescence of DMABN.[48] Furthermore, molecules such as NTC6 have appeared to have TICT states (partial twist; 69 degrees),[49] and other works have determined that the N-phenyl bond does not change in length/character at the ICT state.[50,51]

A different theory proposed by Sobolewski and Domcke, largely on the basis of *ab initio* electronic structure computations, is the Rehybridized ICT (RICT) model.[52,53] This model describes the ICT state of DMABN as a state where an electron moves from a π orbital to a σ^* orbital localized in the nitrile group, resulting in a bending of the nitrile group in plane with the rest of the molecule.[52,53] While this theory is not comprehensive enough

to explain the large amount of structures that can evolve to populate ICT states, namely the pre-twisted derivatives,[13,36] or DMABN itself,[54] the essence of the RICT model has been absorbed into the description of a separate excited state model, the $\pi\sigma^*$ state; an intermediate electronic state separate from the ICT and LE states. The $\pi\sigma^*$ excited state minimum structure has been theorized to play an important role in the dynamics of DMABN and other molecules according to several theoretical studies,[8,10,55–58] with recent work proposing it as an intermediate to the TICT structure.[10,57,58]

These interpretations, and other studies, have led to numerous theoretical models and simulations of DMABN, aimed at deciphering the electronic and nuclear structure of the excited states involved in its dynamics. For example, the electronic structure of DMABN has been determined and studied in the gas phase and with various solvent models, using several *ab initio* and semi-empirical methods, including AM1,[59] STEOM-CCSD,[60] DFT/MRCI,[61] CASSCF/CASPT2,[4,5,8,31,32,62–64] TDDFT,[33,57,65–68] CC2,[49,69] MRCI,[4] and others.[54,70,71] The majority of these studies contend that the CT state that fluoresces is consistent with the TICT model,[4,5,8,32,33,60,62,65,66,69–71] however there remains some disagreement.[10,57,58] A particularly cohesive model is the one put forward by Gomez et al.[4,5,8] This model (summarized in Fig 2) states that after the molecule is initially excited, assuming a broadband pulse, there is only significant absorption from the ground state to an electronic state designated as S_2 (for this reason, experiments are commonly tuned to the gap between the S_0 and S_2 states at t = 0 when selecting an initial pulse). Furthermore, the nuclear geometry associated with an excited state minimum on S_2 was found to resemble a charge transfer state associated with the PICT model and the first excited state minimum on S_1 was associated with the LE structure. After initial excitation to the bright S_2 state, DMABN relaxes briefly, and then quickly decays from S_2 to S_1 to the LE structure through a large crossing seam (less than 100 fs),[7,8,72] which encompasses several structures of DMABN with low to medium twisting angles of the dimethylamino group.[4,8] Some studies have suggested that there exists a small excited state population that populates the $S_1(\mathbf{R}_{TICT})$ structure directly from S_2

instead[34] if the aforementioned seam is accessed at higher twisting angles. However the nature of this mechanism is not well defined, and the majority of the excited state population from S_2 goes directly to populate the $S_1(\mathbf{R}_{LE})$ structure regardless under the initial crossing seam hypothesis.[4,8,34,73] Regardless, after the $S_1(\mathbf{R}_{LE})$ structure is populated, the primary mechanism for CT formation would be through the S_1 adiabatic pathway that connects the $S_1(\mathbf{R}_{LE})$ and $S_1(\mathbf{R}_{TICT})$ structures, i.e. through a transition state.[4,8,73] Since the $S_1(\mathbf{R}_{TICT})$ structure is lower in absolute energy than the $S_1(\mathbf{R}_{LE})$ structure, as the molecule twists, the $S_1(\mathbf{R}_{TICT})$ structure is more likely to remain populated once the barrier that separates the two is overcome. The specific nature of this barrier is often described in a way inconsistent with the large seam description discussed earlier, but were it to exist as an avoided crossing or a conical intersection, it may explain the early population of the $S_1(\mathbf{R}_{TICT})$ structure at femtosecond timescales.[8,9,34,73,74] Finally, this model is cohesive enough to describe solvent effects on the excited state dynamics, which raise or decrease the energy of the $S_1(\mathbf{R}_{TICT})$ structure, allowing for easier population at early and later timescales using polar solvents.[5,7] Overall, the specific character of the transition barrier, as well as the mechanism behind the $S_2(\mathbf{R}_{PICT}) \rightarrow S_1(\mathbf{R}_{LE})$ population is unclear. As other experimental and simulated studies have established, the interstate decay from S_2 to S_1 occurs very quickly ($<$100 femtoseconds), yet non transient signals attributed to the $S_1(\mathbf{R}_{TICT})$ structure take at least 1-3 picoseconds to appear in acetonitrile, indicating a complicated set of dynamics on the S_1 electronic excited state that occur after/during said interstate decay.[10,34,72,75] Therefore, the model put forward initially by Gomez et al has many advantages and many unanswered questions that allow it to act as a starting point for the design of a dynamical model for DMABN, in the following sections of this thesis.

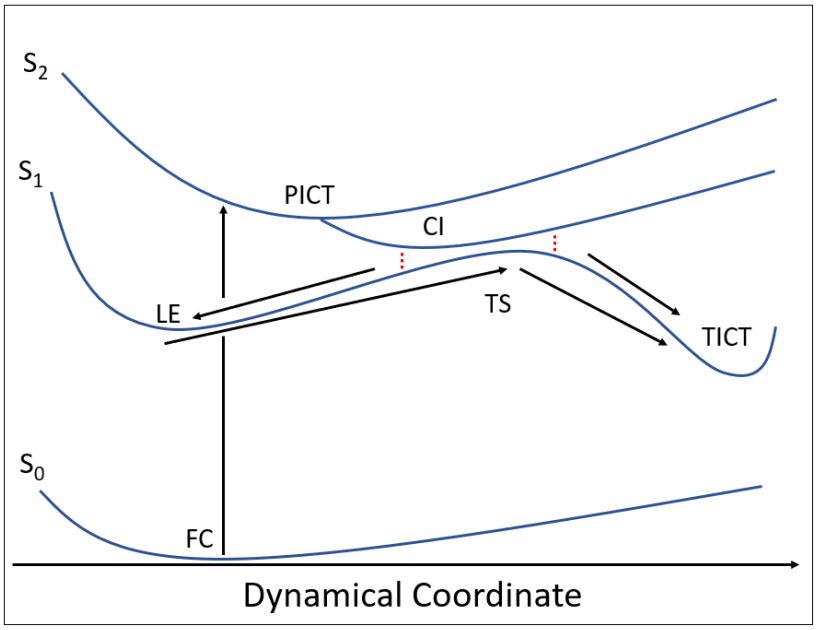

Figure 2: Proposed model for the excited state dynamics of DMABN, by Gomez et al.[4,5] From t = 0, there is ground state absorption to S_2, then relaxation into $S_2(\mathbf{R}_{PICT})$ (PICT). Due to the $S_2(\mathbf{R}_{PICT})$ minimum being shallow, the conical intersection seam between S_2 and S_1 is readily accessed at a range of geometries. Therefore, $S_1(\mathbf{R}_{TICT})$ formation is encouraged by S_2 to S_1 decay through this seam (CI), or by movement through a transition state on S_1, which is accessed after the $S_1(\mathbf{R}_{LE})$ state is populated (TS). In this case, the term Dynamical Coordinate refers to the mixed twisting and bending motions that separate the nuclear structures of the $S_0(\mathbf{R}_{FC})$ structure and the proposed $S_1(\mathbf{R}_{TICT})$ structure. Along this coordinate the $S_1(\mathbf{R}_{LE})$ and $S_2(\mathbf{R}_{PICT})$ structures are much closer to the ground state structure than the $S_1(\mathbf{R}_{TICT})$ structure, but still distinct.

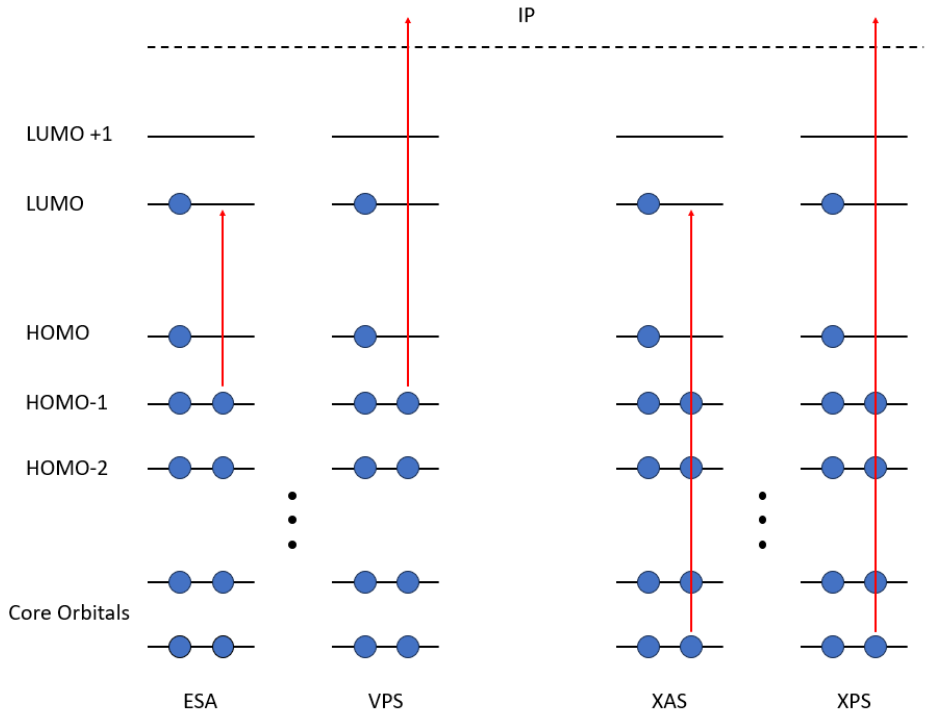

Figure 3: A summary of the excited state spectroscopies discussed in this chapter. ESA, excited state absorption, a key process and source of excited state signals in transient absorption spectroscopy. Existing time resolved experimental data, and new static simulations in Chapter 3. VPS, valence photoelectron spectroscopy. New time resolved experimental data, and static simulations in Chapter 4. XAS, X-ray absorption spectroscopy, and XPS, X-ray photoelectron spectroscopy. New static simulations in Chapter 5.

1.3 Time Resolved Spectroscopic Techniques

In order to characterize the charge transfer state of DMABN, a number of excited state spectroscopies at sub-picosecond timescales have been performed, and proposed to track the excited state dynamics of the molecule, a summary of which can be found in Fig 3. After the initial discovery of dual fluorescence by Lippert et al. and after thorough investigation with theoretical electronic structure methods, time resolved absorbance/fluorescence spectrum were recorded for the DMABN molecule, where it was found that the rise time of the second band was directly correlated to the fall time of the first band.[9] The model initially proposed by Druzhinin et al. to interpret these time resolved spectra closely resembled the model that would come later proposed by Gomez et al (Fig 2.[5,9,34] In the interim between these two works, and for some time afterwards, the majority of the time-resolved studies on DMABN have been transient absorption experiments in various solvents (as previously mentioned, the formation of a CT state in the excited state dynamics of DMABN has only been observed in polar solvent). While the results are at times evocative, as will be discussed subsequently, these studies are unable to confirm with absolute certainty any of the proposed dynamical models given that many of the absorption bands originating from the different electronic states at different nuclear configurations overlap. Furthermore, depending on the solvents employed, the nature of the pump pulse energy and bandwidth, and the method of data analysis, the reported transient absorption (TA) spectra display significant differences from one study to another. One such study interprets that the TA spectrum implies that ICT emission is due to a partially twisted (pTICT) structure, as opposed to the weakly fluorescent TICT structure studied in most electronic structure calculations.[10,58,76] This assertion is based on initial studies by Zgierski and Lim, which calculated transient absorption spectra using TDDFT,[55,56] and found that after excitation, DMABN absorbs strongly at 700 nm, which Zgierski et al. attributed to excitation from the $\pi\sigma^*$ structure.[55,56] Furthermore, the excited state signals attributed to the $\pi\sigma^*$ structure had a decay time that was discovered to

be closely related to the rise time of the excited state signals attributed to the ICT state, for DMABN and for some of its derivatives.[57,67] However, this assignment of the 700 nm band has received some scrutiny, as other derivatives lacking the nitrile functional group have been found to absorb at similar bands,[9,77] and other studies maintain that the 700 nm band could easily be attributed to the $S_1(\mathbf{R}_{LE})$ structure instead.[7,9,73,78,79] Coto et al. added to this discussion after comparing time resolved fluorescence and transient absorption spectra, and apparent detection of a second ICT state, represented by the $S_1(R_{pTICT})$ structure.[10,58] Specifically, the difference between the apparent rise times in these two spectra (transient absorption, and time resolved absorbance/fluorescence spectroscopy) led Coto et al. to propose that two separate ICT states exist.[10,58] A dual pathway model was proposed, where the $S_1(\mathbf{R}_{\pi\sigma*})$ structure acts as an intermediate in $S_1(\mathbf{R}_{TICT})$ formation, and the $S_1(\mathbf{R}_{LE})$ structure acts as an intermediate in $S_1(R_{pTICT})$ formation.[10,58] A response to this dual pathway model is provided by a separate time resolved fluorescence spectra taken by Park et al.[34] which state that the discrepancy between the $S_1(\mathbf{R}_{LE})$ and $S_1(\mathbf{R}_{TICT})$ decay and rise times is explained by a heavily twisted $S_1(R_{pTICT})$ intermediate that forms within 160 fs, which later decays to the familiar $S_1(\mathbf{R}_{TICT})$ structure after about 4.8 ps, in addition to the familiar $S_1(\mathbf{R}_{LE})$ to $S_1(\mathbf{R}_{TICT})$ channel which has a time scale of 3.3 ps. This is consistent with other experimental time resolved Raman spectra,[75] which also indicate an initial excitation to a "hot" CT structure (implied to be a partially twisted CT structure), which then vibrationally relaxes into a more stable configuration within 6 picoseconds. The study is not sensitive to the specific CT structure, but the two step process from the $S_1(\mathbf{R}_{LE})$ to the S1-CT structure is consistent with the $S_1(\mathbf{R}_{LE}) \rightarrow S_1(R_{pTICT}) \rightarrow S_1(\mathbf{R}_{TICT})$ process advocated by Park et al. and others.[5,8,34,73] In comparison to the earlier model in Fig 2 ($S_0(\mathbf{R}_{Min}) \rightarrow S_2(\mathbf{R}_{PICT}) \rightarrow S_1(\mathbf{R}_{LE}) \rightarrow S_1(\mathbf{R}_{TICT})$), the dual pathway model is focused primarily on the nuclear structures involved and the experimental observables produced thus far. Therefore its difficult to compare the two models side by side, since the latter model has yet to establish specific details, such as the vibrational motions required to go from

the $S_1(\mathbf{R}_{\pi\sigma*})$ structure to the $S_1(\mathbf{R}_{TICT})$ structure.[57,80] In order to evaluate its validity, the excited state pathways present in works by advocates of this theory must be directly evaluated using theoretical methods similar to other work on the subject.[8]

The continued existence of conflicting experimental results and dynamical models strongly suggest that additional experimental and computational work is required to establish a consensus on the ultrafast dynamics of this benchmark system. In recent years, a host of similar time resolved studies have been performed, but none have been conclusive enough to definitively assign a spectral signature to the TICT structure.[7,9,10,34,55–58,72–75,77,81–83] Experimental studies have been limited to transient absorption spectroscopies, or rarely, time resolved fluorescence spectroscopies, but these spectroscopies are often conflicting, and have not been sufficient to establish a definitive model of TICT formation on their own.[10,34,75,84] This is in part due to the high degree of uncertainty that has persisted for analogous theoretical dynamics studies conducted so far. Due to most computational studies being limited to time scales shorter than 1 picosecond due to computational expense, it has proven difficult to correlate experimental signals with theoretical signatures for each of the excited state structures of DMABN.[7,72–74,81–83] Dynamics simulations of DMABN are able to occasionally detect the ICT state, but not consistently, as it takes at least a picosecond for the molecule to fully relax into a stable ICT configuration,[9,10,34,85] which is a longer timescale than at which most time-resolved simulations on DMABN have been performed.[72,73] The limited time resolved theoretical simulations that have produced the population of the TICT structure do not do so on timescales consistent with experimental data, indicating a fundamental inconsistency between the theoretical and the experimental descriptions of the molecule's excited state dynamics.[9,73] This is in part due to the various approximations inherent to most modern quantum chemistry methods that are required to trade off of potentially sacrificing qualitatively correct results to reduce computational expense.[9,73] Finally, the potential role of other states such as the $\pi\sigma^*$ state and the pTICT state are not well understood, as dynamics studies are typically focused on changes in specific coordinates, like the twisting of

the dimethylamino group,[7,73] which is a metric that is not appropriate when measuring the population of certain excited states such as the $\pi\sigma^*$ structure.[72,73] In order to determine the specifics of the excited state dynamics of DMABN, it is necessary to apply new spectroscopic techniques which may better elucidate details regarding the nuclear character of the charge transfer state.

For example, a time resolved technique that has been previously applied to analyze the excited state dynamics of molecules, particularly those that experience significant changes in nuclear and electronic structure, has been time-resolved photoelectron spectroscopy (TRPES),.[86–90] *Ab Initio* simulations of TRPES have proven to be key in interpreting a series of experimental TRPES results for the photochemical processes of molecules of similar sizes,[91–93] but have not been used to study the charge transfer process of DMABN or analogues of the molecule. However, TRPES is well suited to study these analogues, as they experience 1) charge transfer states that can form quickly between 100 femtoseconds (fs) and 1 picosecond (ps),[34,73] and 2) potential persistent charge transfer states that may exist for several picoseconds onward.[9,85] Furthermore, the density of cation electronic states accessed through photoelectron spectroscopy is often less than the density of excited states accessed in other techniques such as transient absorption, which can make correlating rise/decay times of various signals easier. There is also an absence of dark cation electronic states when probing a single molecule with TRPES, making resolution of distinct signals per excited state structure easier.[86,92] Ideally, analogues of DMABN would be suitable for a joint experimental and simulated TRPES study. However, as time resolved simulations for DMABN have proven previously,[7,72,73] it is presently challenging to simulate the excited state dynamics of DMABN with existing *ab initio* electronic structure methods at time scales larger than 1 picosecond. Therefore, in order to definitively describe the excited state dynamics of DMABN in a cohesive model, and in order to incentivize a TRPES experiment, static valence photoelectron spectrum must be computed using an electronic structure method which is aptly suited for describing excited states, and then extended to predict simulated TRPES with an

appropriate kinetic model. By identifying signals in both data sets, it may be possible to discern the presence of excited state structures (LE, $\pi\sigma^*$, TICT) playing a role.

Alternatively, owing to the developments in modern synchrotrons, X-ray free electron lasers (XFELs),[94–97] and lab-based High Harmonic X-Ray Sources,[98–101] which allow for the production of ultrafast femtosecond X-ray pulses, time resolved X-ray absorption spectroscopy (TRXAS)[94,95,102–104] has become a viable tool to probe the electronic and nuclear structure of molecules such as DMABN. X-ray spectroscopic techniques are useful for larger, conjugated molecules due to being element specific, with an intrinsic sensitivity to a molecule's electronic and nuclear structure.[105,106] For a given molecule, each element has an entirely separate absorption or binding energy of its core electrons, which in turn are sensitive to local electron density, allowing for XAS and X-ray photoelectron spectroscopy (XPS) to probe the bonding environment around specific elements, and the overall electronic and nuclear character of the studied molecule.[105,106] X-ray spectroscopies are quite sensitive to changes in the local electron density of a molecule over time, and have proven apt in studying isomerization in molecules,[107] photo dissociation and re-association,[100,108] charge transfer dynamics in transition metal complexes,[109–111] and dynamics mediated by conical intersections.[112] Encouraged by the recent advances in experimental X-Ray spectroscopies, many theoretical techniques have also been used to calculate static X-ray absorption spectra,[113–129] X-ray photoelectron/photoemission spectra,[130–133] and time-resolved XAS simulations.[112,131,134–136] However the complexity and computational cost of most of these techniques (such as CVS-ADC(2) or CVS-ADC(2)x[118–120] or CVS-EOM-CCSD[114,126,132]) limits the ability of XAS to simulations to organic chromophores smaller than DMABN.

1.4 Background Electronic Structure Theory

1.4.1 Quantum Chemistry for Ground Electronic States

Quantum chemical methods are computational approaches to solving the electronic Schrödinger equation,[137,138]

$$\hat{\mathcal{H}}_e(r,R)|\Psi_i^e(r,R)\rangle = E^e|\Psi_i^e(r,R)\rangle \tag{1}$$

for molecular systems, where the electronic Hamiltonian is comprised of the following terms.[137,138]

$$\hat{\mathcal{H}}_e = \hat{T}_e(r) + \hat{V}_{ee}(r) + \hat{V}_{eN}(r,R) \tag{2}$$

The terms e and N refer to operators that describe either electron or nuclei based interactions respectively.[137,138] T refers to kinetic energy terms, V refers to potential energy terms, and (r/R) indicate a dependence on either electronic or nuclear coordinates.[137,138]

The simplest formalism, that yields physically meaningful solutions to solve the electronic Schrödinger equation is known as the Hartree Fock (HF) method, which approximates the electronic wavefunction as an antisymmetrized product of one-electron orbitals (the electronic wavefunction, Ψ_e, will be subsequently be denoted Ψ to simplify notation),

$$\Psi^{HF}(x_1,x_2,...,x_n) = (1/\sqrt{N!})\begin{vmatrix} \psi_1(x_1) & \cdots & \psi_N(x_1) \\ \vdots & \ddots & \vdots \\ \psi_1(x_N) & \cdots & \psi_N(x_N) \end{vmatrix} \tag{3}$$

where ψ designates a single one-electron orbital, and x designates electronic coordinates.[137] If two orbitals are occupied by the same electron (with the same spin), or if one orbital is occupied by two same spin electrons, then the wavefunction vanishes in accordance with the Pauli Exclusion Principle.[137] Slater determinants are thus physically motivated; their mathematical properties allow for basic chemical principles such as the Pauli Exclusion Principle to be automatically satisfied.[137] One-electron orbitals are also referred to as molecular orbitals, which are constructed based on linear sums of atomic orbitals, which are individual

approximations to the locations of electrons around each atom in the system.[137]

The Hartree Fock method of determining the electronic energy of the system from the electronic wavefunction is achieved through the use of the variational principle (a detailed proof can be found in Ostland et al. pg 31-33).[137] The Hartree Fock method for a multi body system proceeds by determining the solution to the following set of eigenvalue equations (these equations are coupled, one for each electron N),

$$h(i) + \sum_{b \neq a}^{N} (J_b(i) - K_b(i))\psi_a(i) = \epsilon_i \psi_i(i) \tag{4}$$

where h includes the electronic kinetic energy and electron-nuclei coloumb interaction terms, J represents the electron-electron coloumbic interaction terms, and K represents the electron-electron exchange interaction terms.[137] ϵ_i represents the orbital energy associated with the molecular orbital ψ_a.[137] These terms for a given multi body system of electrons are compressed into the Fock operator, such that the equation above becomes the following.[137]

$$f(i)\psi_a(i) = \epsilon_i \psi_i(i) \tag{5}$$

The Hartree Fock method proceeds as follows. Based on an initial guess of atomic orbitals and molecular orbitals, the fock operator is constructed and used to estimate the orbital energies for each molecular orbital, as well as a set of eigenfunctions ψ_i which correspond to new molecular orbitals.[137] These molecular orbitals are inserted back into the fock operator and the cycle repeats until the orbital energies converge to minimal energy values.[137] It is then trivial to use these orbital energies and the final molecular orbitals to solve for values or quantities such as the overall ground state energy of the system, E_{HF}.[137]

The Hartree-Fock method is a useful technique for obtaining a zeroth order description of the ground electronic state.[137] The difference between the Hartree Fock energy of a system and the true ground state energy of a system is dubbed the correlation energy, and there are two common sources of correlation energy that the HF method misses.[137] Firstly, the

use of a single Slater determinant to describe the electronic wavefunction is inadequate at properly describing instantaneous electron-electron repulsion (between electrons of the same spin or even different spin).[137,139,140] This is because under the HF formalism, each electron perceives a mean probability distribution of where all other electrons could be, instead of avoiding collisions with other electrons classically when they are too close in proximity (correlation energy neglected by the HF formalism due to this phenomenon is dubbed dynamic correlation).[137,139,140] Second, the use of a single Slater determinant can be a poor guess when describing the ground state for several molecular systems.[137,139,140] For example, molecules in the middle of bond breaking, or other phenomenon that involve transition state barriers, where the description of the ground state must be described using multiple Slater determinants as there are multiple nearly degenerate configurations of electrons all contributing to the wave function.[137,139–141] For excited electronic states in particular, an apt description of the correlation energy using multiple Slater determinants (dubbed static correlation) is absolutely necessary.[137,141] Modern quantum chemistry methods are set apart by their approach in solving for missing correlation energy, and their emphasis on certain forms of correlation energy over others.

There exist several electronic structure methods that improve on the formalism set by the HF method, broadly falling into two main classes. The first class refers to wavefunction based methods. The term wavefunction in this case implies that the method being discussed approaches the description of molecular orbitals in a similar method to Hartree Fock, using the variational principle to estimate orbitals with the lowest energy.[137] Most wavefunction approaches use the Configuration Interaction (CI) approach, which can be represented as follows,

$$\Psi^{CI} = c_0|\Psi_0\rangle + \sum_{ar} c_a^r|\Psi_a^r\rangle + \sum_{a<b,r<s} c_{ab}^{rs}|\Psi_{ab}^{rs}\rangle + \dots \tag{6}$$

The CI approach defines the electronic wavefunction as a linear sum of multiple determinants, which are singly excited (Ψ_a^r), doubly excited (Ψ_{ab}^{rs}), etc. relative to the ground state determinant (Ψ_0).[137] The c values refer to the configuration interaction coefficients associated

with each determinant.[137] Considering every possible excited state determinant is typically infeasible for larger molecules (this approach is named full configuration interaction), so configuration interaction in practice is typically limited to only considering singly and doubly excited state determinants in addition to the ground state determinant.[137] To solve for the CI wavefunction the simple eigenvalue equation is solved,

$$\hat{H}_{CI}|\Psi^{CI}\rangle = E|\Psi^{CI}\rangle \tag{7}$$

which leads to the diagonalization of what is known as the CI matrix.[137] This matrix is expressed as follows,

$$\mathbf{H} = \begin{pmatrix} \langle\Psi_0|\hat{H}_{CI}|\Psi_0\rangle & 0 & \langle\Psi_0|\hat{H}_{CI}|D\rangle & \cdots \\ 0 & \langle S|\hat{H}_{CI}|S\rangle & \langle S|\hat{H}_{CI}|D\rangle & \cdots \\ \langle D|\hat{H}_{CI}|\Psi_0\rangle & \langle D|\hat{H}_{CI}|S\rangle & \langle D|\hat{H}_{CI}|D\rangle & \cdots \\ \vdots & \vdots & \vdots & \ddots \end{pmatrix} \tag{8}$$

where the terms S and D refer to singly and doubly excited determinants.[137] Diagonalizing this matrix yields the aforementioned CI coefficients and the lowest eigenvalue yields the ground state energy with any missing correlation energy neglected by HF included.[137] It can be observed that some matrix elements of the CI matrix are automatically set to 0, due to Slater Condon rules (matrix elements which differ by three or more orbitals will automatically be 0), and Brillouin's Theorem (matrix elements which are concerned with the mixing of singly excited determinants with the ground state determinant are set to 0 due to the form of the ground state Hartree Fock determinant).[137]

1.4.2 Quantum Chemistry for Excited Electronic States

There are several quantum chemistry methods concerned specifically with the determination and analysis of electronic excited states, and are set apart by their multireference character.[137] That is to say, instead of considering excitations out of a single reference configuration, multireference methods consider several different excited state determinants simultaneously

from multiple configurations.[137] The most basic of these is known as multi configuration SCF, or MCSCF.[137,142,143] MCSCF typically uses a slightly different formalism compared to CI to describe excitations.[137,142,143] Instead of including only single and double excitations, MCSCF considers a subspace of orbitals (often user defined) from which excitations are allowed, allowing for a more compact form of the overall wave function.[137,142,143] This can be shown as,

$$\Psi^{MCSCF} = \sum_{I} c_I \Psi_I \tag{9}$$

where Ψ_I refers to either a single Slater determinant, or more commonly a configuration state function (a symmetry adapted linear combination of Slater determinants, CSF), and c_I represents the CI coefficients associated with each CSF.[137,142,143] CSFs include all the Slater determinants arising from the same electron configuration that can contribute to the description of an electronic state, and are a useful way to group excited Slater determinants together.[137,142,143] MCSCF is a dual optimization procedure in which the orbitals and CI expansion coefficients are optimized simultaneously.[137,142,143] The variational condition will often be the minimization of the average energy of the states of interest.[137,142,143] Typically, the orbitals and CI coefficients are optimized separately, and thus iteratively, until convergence is reached.[137,142,143] One particular type of MCSCF prescribes which reference CSFs to include in the expansion by defining an orbital subspace, comprised of frontier occupied and unoccupied orbitals.[137,143] Then, all possible orbital occupations within this space are generated and employed to construct a set of CSFs to included in the MCSCF expansion.[137,143] This approach is termed complete active space self-consistent field, CASSCF.[137,143] It's has the attractive feature of being a black-box approach for generating MCSCF reference spaces, but number of CSFs produced by this procedure means that only relatively small orbital active spaces can be employed.[137,143] While the CASSCF provides a black-box route to generate references spaces that can provide a qualitative description of a set states that are close in energy, it does not account for dynamic correlation energy.[137,143]

There are several methods which attempt to expand upon CASSCF to account for said

missing correlation energy, for example, second order complete active space perturbation theory (CASPT2).[144–146] CASPT2 treats the interaction of the reference space defined by CASSCF, with the space of functions excited by singles and doubles via perturbation theory.[137,144–146] Overall, CASPT2 is broadly considered a dynamic correlation correction to the CASSCF wave function.[137,144–146] Another method which attempts to recapture missing dynamic correlation from CASSCF is multiconfiguration configuration interaction (MRCI).[147] MRCI refers to any further CI expansions of a multireference space; it's often well suited to be used with a method such as CASSCF where CASSCF is used to generate an initial wavefunction (of several CSFs, named a reference space), and MRCI is used to generate additional CSFs by considering all single and double excitations out of the reference space.[141,147,148] The choice of a multireference active space to generate excitations tends to result in compact CI expansions with a lack of trailing lowly contributing CSFs/excited state determinants, which has been interpreted to demonstrate a balanced treatment of dynamic and static correlation.[141,147,148] Similarly to CASPT2 however, MRCI requires a good initial guess in the form of CASSCF and cannot be used to correct for errors intrinsic to the choice of active space in the original multireference wavefunction.[141,147,148]

Recently, an electronic structure method called DFT/MRCI has seen success in the description of electronic excited states, possessing comparable accuracy to high level wavefunction based methods such as CASPT2, at a significantly reduced computational cost.[124,141,149–151] DFT/MRCI uses density functional theory (DFT) to generate a set of Kohn-Sham (KS) orbitals which are considered to treat primarily dynamic correlation, and uses them as the orbital basis for an MRCI expansion for the description of electronic excited states.[124,151] Similar to previously implementations of MRCI, a semi empirical parameter is used to discard lowly contributing CSFs after an MRCI calculation, and then the MRCI calculation repeats, until convergence.[124,141,149,151] This process is "black-box", and in contrast to a method such as CASSCF, does not require initial user input to set an active space of electrons from which excitations are generated.[124,141,149,151] Between the generation of KS orbitals and the

iterative MRCI expansions, there is an intermediate CIS (configuration interaction, single excitations) calculation that is performed to generate a reference space, and this is enough for the MRCI expansions to proceed.[124,151] For a DFT/MRCI calculation, the user defines a set of N roots corresponding to the number of electronic states included.[124,151–153] After a given MRCI expansion finishes, the wavefunction at each of these roots is examined, where only configurations that contribute greater than some empirical threshold are retained in the reference space, and the rest are discarded.[124,151–153] Then, another MRCI expansion calculation is run with the new reference space until the reference space ceases to change, typically converging after 2-3 iterations.[124,151–153] The use of KS orbitals in general improves the relative accuracy of the method, due to a better agreement with experimental excitation energies as compared to those obtained with a Hartree Fock orbital basis.[124,141,149] These functions differ from implementation to implementation, for the purposes of this work there is a particular focus on the implementation of these parameters to the DFT/MRCI version in the GRaCI quantum chemistry package.[154]

The MRCI wavefunction ($|\Psi_I\rangle$) is generally expressed as a sum of two components, the reference space, and the first order interacting space (FOIS), referring to all CSFs that are generated via single and double excitations out of the reference space.[124,151]

$$|\Psi_I\rangle = \sum_{\Omega \in Ref} C_\Omega^{(I)} |\Omega\rangle + \sum_{\Omega \in FOIS} C_\Omega^{(I)} |\Omega\rangle \tag{10}$$

The on diagonal elements of the effective DFT/MRCI Hamiltonian are represented as follows.[124,151]

$$\langle \mathrm{w}\omega | \hat{H}^{DFT} - E_{DFT} | \mathrm{w}\omega \rangle = \langle \mathrm{w}\omega | \hat{H} - E_{SCF} | \mathrm{w}\omega \rangle + \sum_i (\epsilon_{ii}^{KS} - F_{ii}) \Delta \mathrm{w}_i + \Delta E_x + \Delta E_c \tag{11}$$

A number of the terms in this equation come from the native DFT/MRCI formalism advocated by Grimme et al and their incorporation are discussed in detail elsewhere.[124,151,155] For brevity, each element of the effective Hamiltonian corresponds to a specific spin (w)and spa-

tial (ω) configuration.[124,151] The term $\sum_i \Delta \mathrm{w}_i$ refers to the differences between the ground state configuration and the configuration being evaluated in the on diagonal element of interest, with respect to all the differences in the molecular orbital occupations of the two configurations.[124,151] Grimme et al. importantly noted that excitation energies between the ground state and electronic states are well approximated via the corresponding Kohn Sham orbital energy differences of the ground state and the excited state configurations ($\sum_i \epsilon_{ii}^{KS} \Delta \mathrm{w}_i$) instead of their fock matrix elements as in the CI formalism ($\sum_i F_{ii} \Delta \mathrm{w}_i$).[124,141,151,155] However, this decision introduces a number of coulomb and exchange interactions due to Kohn Sham molecular orbitals being closer together in energy than Hartree Fock orbitals.[124,141,151,155] Therefore the potential energy terms referring to these two electron interactions are scaled using semi empirical parameters (coulomb, ΔE_c, exchange, ΔE_x).[124,151] The off diagonal elements of the DFT/MRCI Hamiltonian are expressed as,

$$\langle \mathrm{w}\omega | \hat{H}^{DFT} - E_{DFT} | \mathrm{w}'\omega' \rangle = \langle \Omega | \hat{\mathcal{H}} - E_{SCF} | \Omega' \rangle D(\Delta E_{\Omega\Omega'}) \tag{12}$$

where the damping functions ($D(\Delta E_{\Omega\Omega'})$ are introduced to account for any extra double counting of dynamic correlation (induced by the use of DFT and MRCI simultaneously, methods which both individual account for dynamic correlation).[124,141,151] The damping function is scaled with the energy difference between the two CSFs (Ω, Ω') being considered in the Hamiltonian matrix element, resembling an exponential function.[124,151] The farther apart in energy the two CSFs are, the more significantly dynamic correlation effects are damped, which has the effect of decoupling the reference and FOIS spaces such that non contributing CSFs are less likely to appear to contribute, and are easily removed using a separate set of semi empirical parameters, shown below.[124,151]

$$d_{\mathrm{w}} = \sum_p \Delta \mathrm{w}_p \epsilon_p^{KS} - \delta E_{sel} \tag{13}$$

Here, for a given FOIS configuration separate from the ground state configuration $\sum_i \Delta \mathrm{w}_i$,

the value d_{w} is computed based on the Kohn Sham orbital energy Differences ϵ_p^{KS}, and a semi empirical parameter set most often to 0.8 or 1.0 δE_{sel}.[124,151] If d_{w} is smaller than the d_{w} value for the highest eigenvalue in the reference space, than all CSFs associated with that configuration are discarded.[124,151] This results in a compact FOIS space that is easily reduced at each optimization cycle in DFT/MRCI in 3 to 4 cycles.[124,151]

DFT/MRCI(2) represents an approximation to DFT/MRCI where rather than consider explicitly single and double excitations out of the reference space, the interaction of the reference and FOIS space is treated using second-order degenerate perturbation theory.[124,151] For the purposes of this thesis, DFT/MRCI(2) did not deviate from the results of DFT/MRCI for any simulated spectrum, consistent with previous works devoted exclusively to DFT/MRCI(2) which have benchmarked the computational cost of the method and numerical stability when comparing excitation energies computed with DFT/MRCI and DFT/MRCI(2).[151] Other approximations to the DFT/MRCI method include the use of the core valence separation (CVS) approximation, commonly used in the derivation of core excited states when simulating X-ray spectroscopies.[95,112,120,124] Core excited states lie at high energies in the 100s of eVs, and so typically require the calculation of all the valence excited states when diagonalizing the DFT/MRCI Hamiltonian (or ADC(2) and ADC(3) matrices).[120] Even in small systems where this is computationally favorable, the portion of the Hamiltonian corresponding to core excitations is infected with higher lying valence excited states, that are poorly described.[120,124,126] A necessary estimation is to block diagonalize the Hamiltonian, explicitly separating the core and valence CSFs, and neglecting coupling between the two.[120,124,126] This process is known as the CVS approximation, and has been essential for several core excited state studies in the past.[120,124,126] DFT/MRCI(2) is well suited for the CVS approximation; CSFs that describe core excitation are already decoupled from valence excitation though the application of the equation described by d_{w}. The method as implemented in GRaCI has already taken advantage of the CVS approximation in previous studies.[112,124] Since these states are informally decoupled, CVS-DFT/MRCI(2) simply

refers to the working of DFT/MRCI(2) within the CVS space, i.e., only including excitations from core orbitals to unoccupied orbitals and neglecting any valence contributions.[124,151]

1.4.3 Adiabatic and Diabatic States

Intrinsic to the solution of the electronic Schrödinger equation is an adiabatic approximation, which describes a separation of the electronic and nuclear degrees of freedom; this separation is justified due to the large difference in mass between atomic nuclei and electrons.[137,138] According to the Born-Oppenhemier approximation, we can treat the nuclei as evolving on a potential energy surface that is defined by the electronic energy at each nuclear configuration (R).[137,138] At a given configuration (R), the eigenfunctions of the electronic Hamiltonian represent adiabatic states, which are surfaces, ordered by energy, and comprised of these solutions at each point in coordinate space.[137,138]

However, at points of degeneracy between PESs (i.e. conical intersections), this approximation breaks down as the coupling between adiabatic states becomes significant, while also introducing large off diagonal elements (corresponding to nuclear kinetic energy terms) into the Hamiltonian and incurring computational cost. At conical intersections, the electronic character is rapidly changing from one nuclear configuration to another, meaning that the earlier physical approximation that electrons instantaneously adjust to nuclear motion is no longer valid.[137,138] Therefore, conical intersections represent a particular challenge for quantum chemistry methods that adopt the formalism described so far, but for most cases the Born-Oppenheimer approximation is sufficient when solving for the energy at a given set of electronic and nuclear coordinates.[137,138]

Diabatic states represent a rotation of the adiabatic electronic state basis to minimize non adiabatic couplings between electronic states.[138,156] There is only one adiabatic representation of a polyatomic multi electron system, but there exist infinite diabatic representations of the same system.[137,138,156] Compared to their adiabatic equivalents, diabatic states are more useful to analyze changes in physical or electronic character that occur with respect to the

nuclear coordinates of the system, since of their properties is to conserve electronic character upon nuclear displacements.[138,156,157] In GRaCI, adiabatic states can be converted to quasi diabatic states using what is known as the Propagative Block Diagonalization Diabatization (p-BDD) scheme.[156] p-BDD is a technique for determining adiabatic to diabatic transformations which has been implemented using DFT/MRCI wave functions in the software package GRaCI.[156] In p-BDD, the ADT matrix ($U_{JI}(R)$) relates adiabatic ($\Psi_J(r,R)$) and diabatic ($\Phi_I(r,R)$) states by the following.[156]

$$\Phi_I(r,R) = \sum_J U_{JI}(R)\Psi_J(r,R) \tag{14}$$

In order to reduce non adiabatic couplings, the desired form of the ADT matrix is one which block diagonalizes the electronic Hamiltonian, such that a P and Q space are defined.[156]

$$U(R) = \begin{pmatrix} U_P(R) & 0 \\ 0 & 1 \end{pmatrix} \tag{15}$$

The P space refers to the subset of electronic states of interest, and Q is the orthogonal component.[156] In practice, the P space is comprised of the lowest N states, so chosen so as to ensure a sizable energy gap with the remaining states in the Q space over the nuclear configurations of interest.[156] The form of this specific ADT matrix block diagonalizes the electronic Hamiltonian, but is unknown, so the derivation becomes a question of how to block diagonalize the electronic Hamiltonian first, and work back to determine the form of $U_P(R)$.[156] To begin, assume the electronic Hamiltonian operator $\hat{\mathcal{H}}_e$ can be expressed in a basis of initial, arbitrary states $\phi_I(r,R)$.[156]

$$H_{IJ}(R) = \langle \phi_I(r,R)|\hat{\mathcal{H}}_e|\phi_J(r,R)\rangle \tag{16}$$

To make the electronic Hamiltonian matrix block diagonal, the following transformation

is applied,

$$\mathrm{H}(R) = B^{\dagger}(R)H(R)B(R) = \begin{pmatrix} \mathrm{H}_P & 0 \\ 0 & \mathrm{H}_Q \end{pmatrix} \tag{17}$$

where $B(R)$ may take infinite forms, but in the case of BDD, takes the unique form below.[156]

$$B(R) = S(R)U(R) \tag{18}$$

The term $S(R)$ refers to the overlaps between the arbitrary states and the adiabatic states (eigenfunctions of the electronic Hamiltonian).[156]

$$S_{IJ}(R) = \langle \phi_I(r,R) | \Psi_J(r,R) \rangle \tag{19}$$

$U(R)$ from the definition of $B(R)$ necessarily is defined as the following,

$$U(R) = S_{BD}^{-1}(R)[S_{BD}(R)S_{BD}^{\dagger}(R)]^{\frac{1}{2}} \tag{20}$$

where $S_{BD}(R)$ refers to the block diagonal portion of $S(R)$, and the equation for $U(R)$ working in solely the P space is defined as the following.[156]

$$U(R) = S_{P}^{-1}(R)[S_{P}(R)S_{P}^{\dagger}(R)]^{\frac{1}{2}} \tag{21}$$

Therefore, the only quantities required to compute the ADT matrix are a good choice of initial states, and the adiabatic states.[156] In practice, one begins at the geometry R_1, where the adiabatic and diabatic states are equivalent. Then, at a new displaced geometry, R_2, the initial states are the adiabatic/diabatic states at R_1 and the adiabatic states at R_2 are rotated to obtain quasi-diabatic states that are in maximum coincidence with the states at R_1. This process is that repeated for all subsequent geometries, R_N.

1.5 Additional Theoretical Methods

1.5.1 Natural Transition Orbitals

The electronic character of adiabatic electronic states at a given nuclear geometry can be visualized by a number of electronic structure tools. For a given excited state minimum structure, the molecular orbitals themselves can be visualized directly using quantum chemistry packages such as jmol,[6] and the configuration state functions returned by a method such as DFT/MRCI can be used to estimate the changes in electronic character that occur in transitions from these molecular orbitals (such as in a HOMO to LUMO transition). These molecular orbitals are converted to what are known as natural orbitals (NOs), by diagonalization of the final MO basis, yielding occupation numbers to determine whether a given orbital is singly or doubly occupied.[158] For excited state minimum structures, it is often more convenient to take advantage of what are known as natural transition orbitals (NTOs). NTOs assume an hole-particle picture, wherein the hole orbitals (originally occupied at the ground adiabatic state, S_0) and the particle orbitals (orbitals occupied at the adiabatic excited state) are extracted from a singular value decomposition of the transition density matrix (computed using the ground state and excited state wavefunctions) and converted into densities to be visualized using quantum chemistry packages such as jmol.[6,158] NTOs provide an in-depth understanding of why different excited state structures yield different excited state signals in various forms of spectroscopy.[158] For example, the NTOs of an excited state structure may imply that at S_1, there is more electron density in the middle of the molecule than at S_0, indicating a one electron transition.[158] This would imply that at S_1 there exist two half filled molecular orbitals, and may explain why a small amount of energy is required to fill that higher lying orbital using a technique such as excited state absorption.[158] There exist other formalisms which compute similar visualizations of electronic transitions such as natural density orbitals (NDOs), but for the purposes of the excited state structures studied in this thesis, the NTOs were sufficient to visualize their differences (and

easier to compare with NTOs computed by other electronic structure techniques in literature).[158] Overall, these tools have become essential in any electronic structure study, as they provide an intuitive, visual descriptor of the electronic character of the excited state structure under study.[95,122,129,156]

1.5.2 Rice-Ramsperger-Kassel-Marcus (RRKM) Theory

Finally, in this thesis it became necessary to estimate the rate at which transition state barriers were overcome in order to correlate a hypothetical dynamical model with existing experimental spectroscopies. When evaluating these rates, the Rice-Ramsperger-Kassel-Marcus (RRKM) theory was used.[159–166] Under this theory, the energy dependent rate constant is expressed as:

$$k(E) = W(E^{\dagger})/h\rho(E) \tag{22}$$

In this equation, $W(E)$ represents the sum of vibrational states at a given state, h represents Planck's constant, and $\rho(E)$ represents the density of vibrational states at a given electronic state. Specifically, E represents the internal energy available to the reactant, E_0 represents the size of the energy barrier separating the zero point energies of the reactant and the transition state, and $E^{\dagger}$ is equivalent to $E - E_0$. Therefore, $W(E^{\dagger})$ can be interpreted as the sum of vibrational states at the transition state available with $E - E_0$ of internal energy, and $\rho(E)$ represents the density of vibrational states available at the reactant with E of internal energy. In order to determine the sum of states and the density of states the Beyer and Swinehart direct counting method was used,[167] based on the vibrational modes returned from the excited state hessians computed at the given reactant and transition state being studied per case.

In this work, there is a particular focus on using DFT/MRCI(2) to simulated excited state spectroscopies, and on validating DFT/MRCI(2) as an appropriate electronic structure technique to study the DMABN system using comparisons to other high level electronic

structure techniques such as CASSCF and CASPT2. DFT/MRCI as implemented in GRaCI has already been used to determine the electronic structure of smaller molecules, and specifically simulate core spectroscopies of molecules, a technique which is typically unfeasible for *ab initio* methods.[112,124,151] In these sorts of studies, the NTO formalism and p-BDD have often also been used to gain an introductory understanding of the excited state dynamics of a molecule in lieu of time resolved simulations. This thesis has several aims; among them is to validate the earlier discussion that places DFT/MRCI as a method that treats a mix of dynamic and static correlation. Furthermore, this thesis aims to prove that DFT/MRCI is a technique that can not only simulate the spectroscopies of molecules as large as DMABN quickly, but also with accuracy and an appropriate treatment of the molecule's charge transfer states.

1.6 Computational Methodology

There are a number of specific parameters that were used to simulate spectroscopies using DFT/MRCI as implemented in GRaCI. The required KS MOs and integrals were computed using the PySCF package.[168,169] Two-electron integrals were calculated using the density fitting approximation.[170–172] All DFT/MRCI(2) calculations were performed using the aug-cc-pvdz basis set[173] unless otherwise specified. The DFT-MRCI-R2017 Hamiltonian was used for the calculation for valence excited states, with the application of the DFT/MRCI(2) method, parameterized for use using the QTP17 functional[123] for both valence and core excited states. The CVS approximation was used for all core excitations in XAS and XPS simulations. An energy-based configuration selection threshold of δEsel = 1.0Eh was used in both the DFT/MRCI and DFT/MRCI(2) calculations. In the construction of the DFT/MRCI(2) effective Hamiltonian, Nbuf = 10 buffer states per irreducible representation were used along with an Intruder State Avoidance (ISA) shift parameter of $5 * 10^3$ Eh. The implicit solvation method used is named the domain-decomposition Conductor Like Screening Model (dd-COSMO) solvation model;[168,174] wherein a static dielectric constant was used to simulate

the presence of solvent around the geometry in question.

To simulate valence and X-Ray photoelectron spectrum, excitations were computed between singlet valence excited states to doublet core ionized states or valence ionized states. Currently DFT/MRCI(2) does not have black box capability for the initial reference space for these doublet states, so by default, a small 2-particle/2-hole restricted active space was constructed by hand. In this active space, excitations were included from the HOMO-6 to the HOMO orbital range, to the LUMO up to the LUMO+17 orbital range. For excited state absorption calculations (necessary to evaluate interpolated paths in various portions of the report that use DFT/MRCI(2)), the active space was computed in a black box manner,[124,151] using a converging reference space based on several RASCI calculations.[141]

The other main electronic structure techniques used in this work were CASSCF and CASPT2, and by default all calculations were performed using the (14,13) active space, with the cc-pvdz basis set. All the excited state structures for DMABN were initially obtained from previous electronic structure calculations using CASSCF/CASPT2[142–144,146,175,176] with active spaces of (12,11)[7] and (14,13),[10] which were re-optimized a second time in OpenMolcas 21 with CASPT2 (14,13)[177] (except when otherwise explicly stated). These optimizations were performed without any symmetry constraints and were simulated in the gas phase, while the basis set used for these optimizations was also cc-pvdz.[173] The geometry optimization of the pTICT structure on S_1 achieved by Coto et al. using RASSCF/CASPT2 at (14,13) could not be reproduced using OpenMolcas 21 even at higher active spaces.[10,177] This structure is more closely examined in Chapter 2.3, and there the excited state structure used was taken directly from the coordinates provided by the paper from which the excited state structure was proposed.[10] The implicit solvation model used for CASSCF and CASPT2 was the polarizable continuum model (PCM) model as implemented in OpenMolcas 21. PCM as implemented in Molcas specifically refers to conductor-PCM (or C-PCM),[178–180] which like dd-COSMO considers the solute molecule as being surrounded at each atom by cavities, which are in turn surrounded by a dielectric medium defined by a dielectric constant.[181,182]

Using a scaling function, the effects of the dielectric medium on the energy of the system are determined using semi-empirical factors, and it is the choice of these semi-empirical factors that primarily separates C-PCM and dd-COSMO.[178,180,182–184] As shown further in this work (specifically Chapter 2.2), the effects of dd-COSMO were more drastic at simulating the effects of a solvent model on excitation energies than PCM, wherein PCM seemed to barely influence excited state energies for a given molecular system.

In this work, several linear interpolated paths in internal coordinates (LIICs) were computed between excited state minimum structures. In this work, the LIICs were computed by evaluating excitation energies for 100 to 200 intermediate nuclear geometries between the initial and target nuclear geometries. LIICs represent a thin one dimensional slice through the space spanned by potential energy surfaces, they can illustrate the variance of electronic character that a molecule experiences with changing nuclear coordinates on a broad level, but excited state minimums and transition states are best resolved through explicit excited state optimizations that consider vibrational modes of the molecule. For CASSCF and CASPT2, the paths were often discontinuous unless at each step, the previous step's orbitals were used as a starting guess for the next set of orbitals. Applying this change often meant that LIICs would be difficult to compute for some set of excited state structures that differed significantly in electronic character (for example, most LIICs involving the $\pi\sigma^*$ structure). Intermediate structures for linear interpolated paths in internal coordinates (LIICs) between structures of interest were computed using the chemcoord module.[185] Often these LIICs involved pre-computed transition state optimizations, which could only be performed by either CASSCF or CASPT2 (see Chapter 2.2) as GRaCI does not have this capability for DFT/MRCI as of yet. Optimizing transition states in solvent was not feasible when using the polarizable continuum model (PCM) model for excited states implemented in OpenMolcas 21,[186] so by default, the transition states themselves were not optimized in solvent. Transition states would be optimized in the gas phase, paths would be computed, and then a second set of paths would be computed based on the nuclear structures of the

"gas" path using the PCM model. In this case, the iterative process of using each previous step's orbitals as a guess could not be applied for interpolated paths calculated in solvent. The various approximations involved to determine the transition state barriers in solvent are important emphasize; this is a key focus of Chapter 2.2.

For all simulated spectrum determined using DFT/MRCI in this work, excitation or ionization energies were convoluted with a gaussian using an empirical full width half maximum (FWHW). These FWHWs were typically chosen based on a comparison to existing experimental data for each simulated spectroscopy (for UV/VIS, VPS, XAS/XPS, Chapters 3.1, 4 & 5), or they were chosen for illustration purposes to distinguish between many small excitations that may otherwise represent a large broad signal in experimental spectrum (for transient absorption, Chapter 3.2). Finally, at several points in this thesis, the molecular orbitals of the ground state minimum structure are referred to in order to interpret spectroscopic signals associated with various simulated excitations or ionizations, which can be found in Fig 4. In these types of representations of nuclear geometries throughout the thesis, blue atoms refer to nitrogen atoms, grey atoms refer to carbon atoms, white atoms refer to hydrogen atoms, and red atoms refer to oxygen atoms.

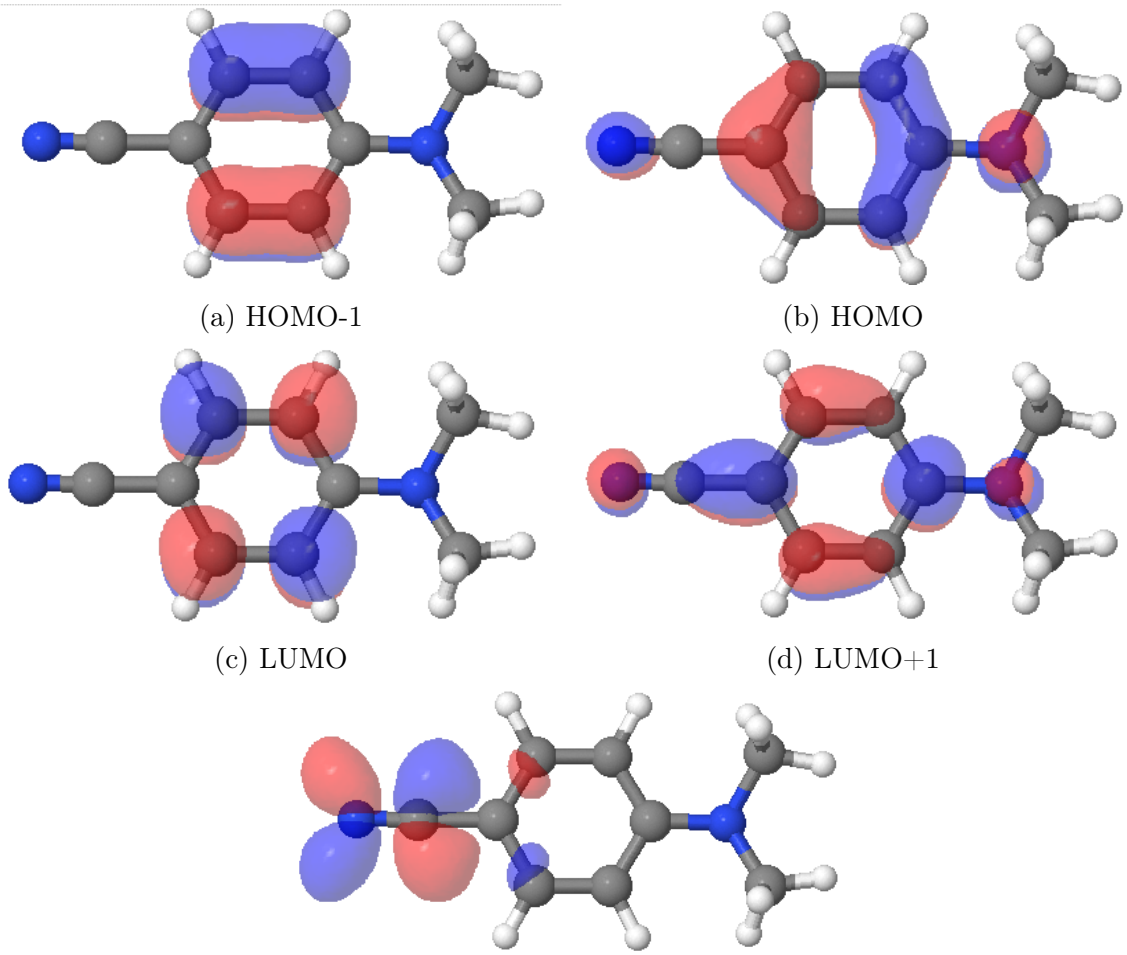

(a) HOMO-1

(b) HOMO

(c) LUMO

(d) LUMO+1

(e) LUMO+3

Figure 4: An overview of the molecular orbitals of the ground state minimum geometry of DMABN, calculated with DFT/MRCI(2), and visualized in jmol[6]

2 The Excited State Dynamics of DMABN

In this chapter, a working model for the excited state dynamics of DMABN is defined. This model is partly based on the model put forward by Gomez et al, but with many slight differences determined after a thorough electronic structure analysis of DMABN and its excited state structures. In this model, the main mechanism that determines the rate of CT formation is the magnitude of the transition barrier between the $S_1(\mathbf{R}_{LE})$ and $S_1(\mathbf{R}_{TICT})$ structures (Fig 2, its role has been previously discussed in other literature models, but typically not as a driver of CT formation).[4,5,8] High-level *ab initio* computations were used to characterize the relevant excited state potential energy surfaces, in which the structures in Fig 5 are employed to construct a dynamical model that will be the basis for all subsequent time-resolved spectroscopic analysis and simulation. These structures were determined by using initial guess geometries from various literature sources on DMABN where these excited state minimum structures claimed to be optimized using high level electronic structure methods. Then these xyz coordinates were reoptimized using CASPT2, with an active space of (14,13) and the cc-pvdz basis set in OpenMolcas 21, where snapshots of finalized structures are present in Fig 5.[177] The dynamical working model constructed in this section is denoted as the "two-state model", since only a pair of adiabatic excited states will be required to characterize the nonadiabatic dynamics that result after excitation to the lowest energy optically bright state, and it is these two states which are expected to have lifetimes long enough

to yield non transient signals in future spectroscopic techniques. A visual description of the two-state model can be found in Figure 6. Since early signals attributed to $S_1(\mathbf{R}_{TICT})$ formation are not well explained by the large transition-state barrier connecting the $S_1(\mathbf{R}_{LE})$ and $S_1(\mathbf{R}_{TICT})$ structures, a thorough analysis of the excited state dynamics immediately after absorption to the $S_2(\mathbf{R}_{PICT})$ structure and before the internal conversion from S_2 to S_1 is necessary. The size of the transition-state barrier itself is then characterized using linear interpolated paths in internal coordinates (LIICs) between the $S_1(\mathbf{R}_{LE})$ and $S_1(\mathbf{R}_{TICT})$ geometries, using several *ab initio* electronic structure methods. There exist other proposed excited states of DMABN which have not been included in this model; the pTICT or $\pi\sigma^*$ motifs specifically. The pTICT structure has been rarely explored in theoretical literature on DMABN, based mostly on experimental transient absorption signals,[10] and TDDFT calculations.[67,187] Likewise, the $\pi\sigma^*$ structure's role in the excited state dynamics of DMABN has also been disputed.[7,8,73] Using *ab initio* calculations, it is shown in this chapter that these structures play a negligible role in the excited state dynamics of DMABN, consistent with the two-state model.

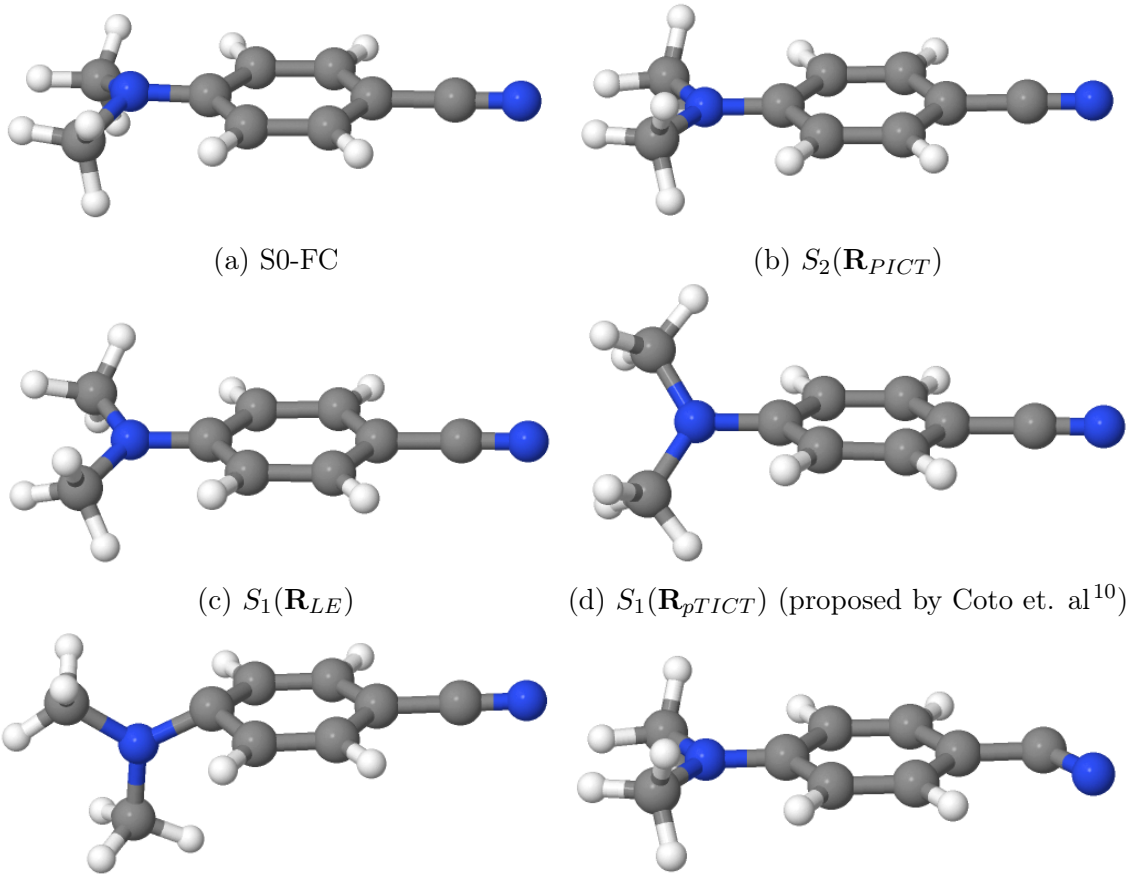

(a) S0-FC

(b) $S_2(\mathbf{R}_{PICT})$

(c) $S_1(\mathbf{R}_{LE})$

(d) $S_1(\mathbf{R}_{pTICT})$ (proposed by Coto et. al[10])

(e) $S_1(\mathbf{R}_{TICT})$

(f) $S_1(\mathbf{R}_{\pi\sigma*})$

Figure 5: An overview of the ground and excited state geometries of Dimethylamino benzonitrile (DMABN). (Nitrogen atoms are in blue, Carbon Atoms are in Grey)

2.1 The Role of the Planar Charge Transfer Structures

The lowest lying optically bright transition corresponds to excitation to the adiabatic S_2 state.[5,7,8,26,33] Directly after absorption to this state, excited state minimums computed on S_2 have been predicted to have charge transfer character, resembling the previously proposed PICT model.[4,8,13] Due to this excited state minimum appearing to resemble a charge transfer state, there has been speculation that a major contributor to TICT formation on S_1 is due to several proposed conical intersections between S_2 and S_1 (this conical intersection region is present in earlier literature models, Fig 2, but will be referred to specifically in the two-state model under the umbrella term CI.1, Fig 6). In this region, a handful of individual conical intersections have been optimized using various electronic structure methods in previous literature, but direct population of these conical intersections have not been tracked in time resolved studies.[4,5,8,9,13,62,85] This conical intersection region, CI.1, implies quick $S_1(\mathbf{R}_{TICT})$ formation in DMABN, instead of the actual $S_1(\mathbf{R}_{LE})$ to $S_1(\mathbf{R}_{TICT})$ gradual formation seen in DMABN in acetonitrile that takes place over a few picoseconds.[9,34] Early sporadic signals attributed to charge transfer formation in DMABN have actually been detected in simulation and in experiment (160-300 fs, in acetonitrile),[34,73] after the majority of the excited state population has evolved from S_2 to S_1 (30-100 fs),[4,7,34,72] but these are much lower in intensity than the set of signals that are attributed to $S_1(\mathbf{R}_{TICT})$ formation in the picosecond regime, indicating the $S_1(\mathbf{R}_{TICT})$ structure is more significantly populated at the longer picosecond timescale.[9,34] The main dynamical models in literature used to describe DMABN are insufficient to describe this phenomenon on their own.[9,10] Identifying how the $S_1(\mathbf{R}_{TICT})$ structure is populated early, but only for a brief period, is important when proving the applicability of the two-state model. To achieve this, the role of the $S_2(\mathbf{R}_{PICT})$ structure compared to the $S_1(\mathbf{R}_{TICT})$ structure must be closely examined, as well as the mechanism of internal conversion from S_2 to S_1.

The excited states accessible at the nuclear geometries ($S_2(\mathbf{R}_{PICT})$ and $S_1(\mathbf{R}_{TICT})$) in

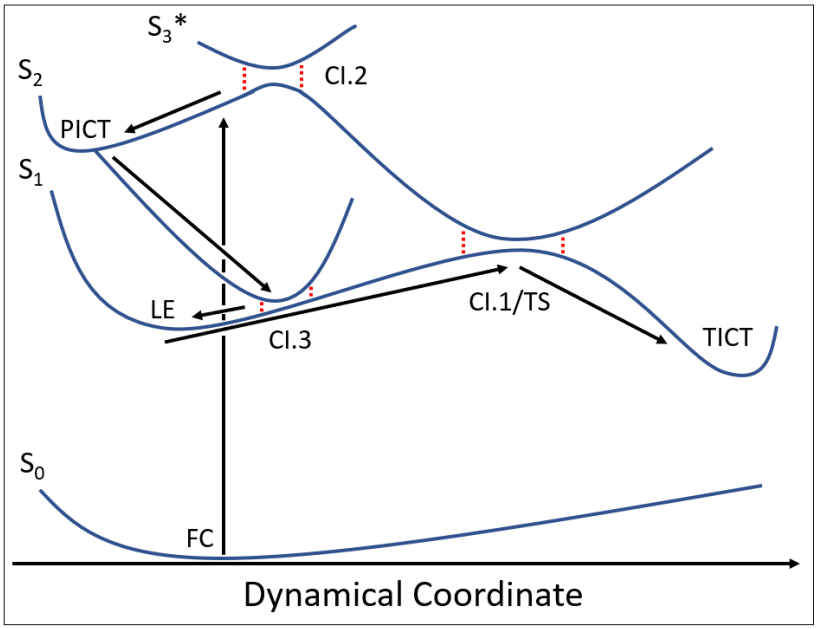

Figure 6: Proposed two-state model of the excited state dynamics of DMABN, based on the conclusions made in Chapter 2 of this text. At t = 0 there is ground state absorption to S_2, followed by relaxation into $S_2(\mathbf{R}_{PICT})$, interstate decay to $S_1(\mathbf{R}_{LE})$ through a conical intersection region (dubbed CI.3), and finally conversion to $S_1(\mathbf{R}_{TICT})$ through a transition state (TS) on S_1. This transition state should lie near the conical intersection region (CI.1) as there is a significant change in electronic character after this transition state barrier is overcome. Some excited state population may proceed through a separate pathway, overcoming a transition state barrier on S_2, which also represents a conical intersection region between S_2 and one or several higher lying adiabatic states (S_3*). After overcoming this barrier, excited state population may proceed to S_1 via the conical intersection region established in previous literature studies (CI.1), leading to early $S_1(\mathbf{R}_{TICT})$ formation (Fig 2). The dynamical coordinate is defined the same way as Fig 2.

Fig 5 were visualized using their NTOs to evaluate their electronic character (Fig 7 to Fig 10). These NTOs were generated from the ground and excited state wavefunctions computed by DFT/MRCI in the gas phase, at the nuclear geometry specified and the excited electronic states required (e.g. for the $S_1(\mathbf{R}_{TICT})$ structure, the NTOs represent changes in electron density, using the hole-electron formalism, from the S_0 to S_1 electronic states at the TICT nuclear structure).[7,73,154,158] The DFT/MRCI(2) method used in the next several sections is benchmarked against other electronic structure methods and experimental data elsewhere, and has reasonable agreement with respect to vertical excitation energies computed at various excited state minimum structures compared to other high level *ab initio* methods such

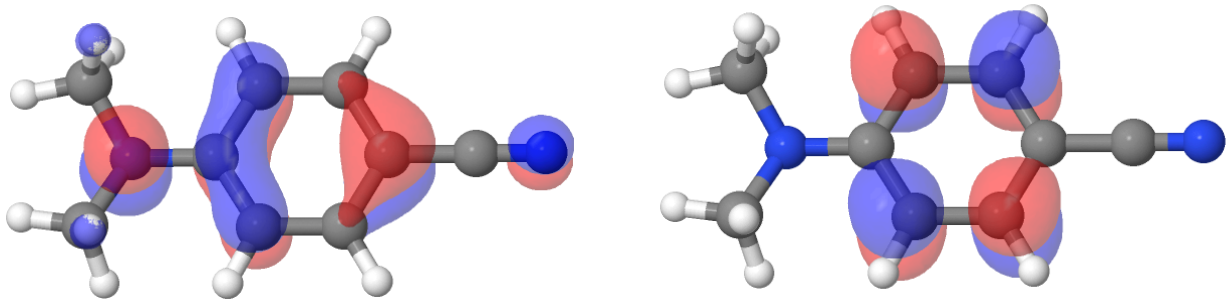

(a) Major contribution (83.3%)

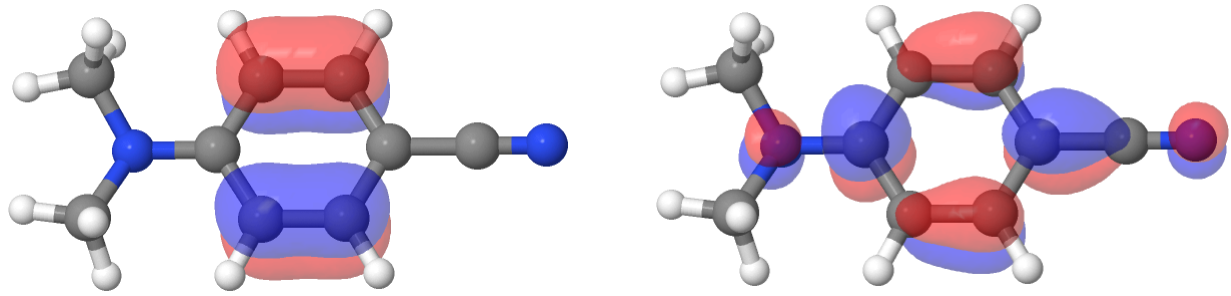

(b) Minor contribution (16.7%)

Figure 7: Dominant NTO pairs, absorption at the Ground State Minimum to S_1, at the $S_1(\mathbf{R}_{LE})$ excited state minimum geometry[5,7,8]

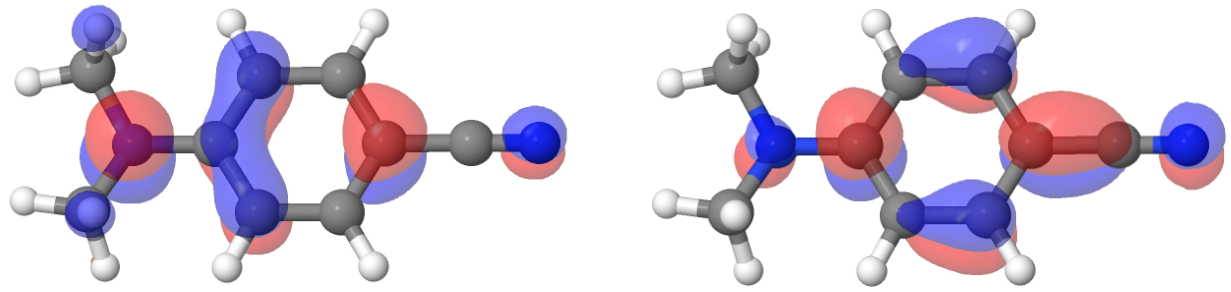

(a) Major contribution (98.5%)

Figure 8: Dominant NTO pairs, absorption at the Ground State Minimum to S_2, at the $S_2(\mathbf{R}_{PICT})$ excited state minimum geometry[5,7,8]

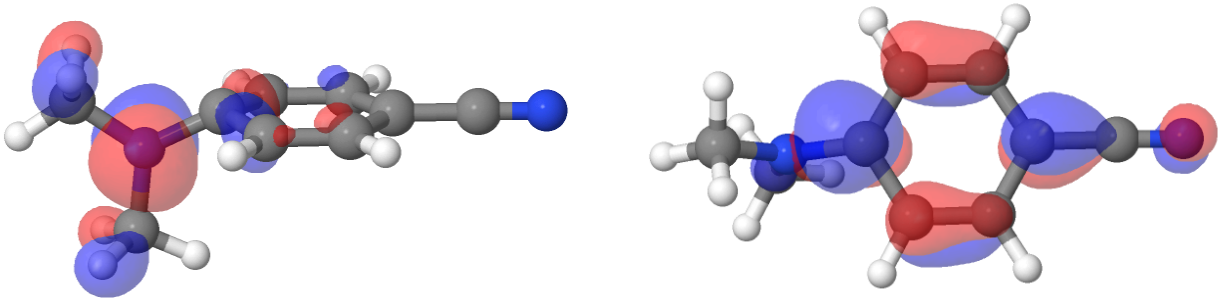

(a) Major contribution (99.0%)

Figure 9: Dominant NTO pairs, absorption at the Ground State Minimum to S_1, at the $S_1(\mathbf{R}_{TICT})$ excited state minimum geometry[5,7,8]

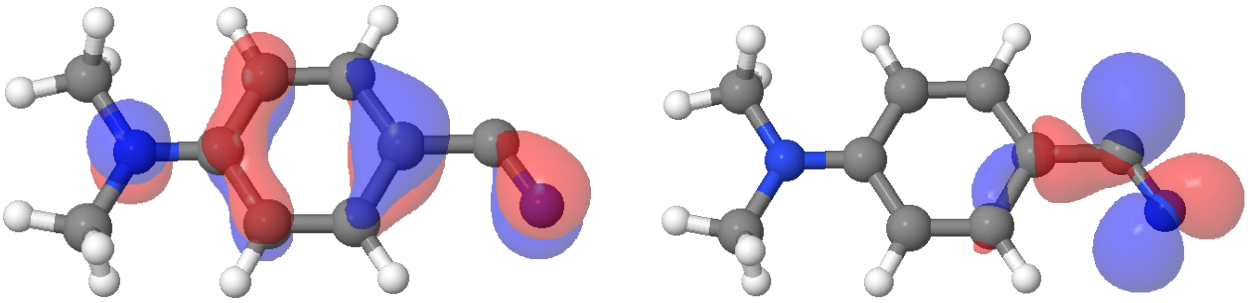

(a) Major contribution (95.6%)

Figure 10: Dominant NTO pairs, absorption at the Ground State Minimum to S_1, at the $S_1(\mathbf{R}_{\pi\sigma*})$ excited state minimum geometry[7]

as CASPT2 or MRCI (Appendix, A.1). Fig 7 to Fig 10 show the dominant natural transition pairs for various excited state minimums of DMABN (consistent with previous literature in their description of the $S_1(\mathbf{R}_{TICT})$ and $S_1(\mathbf{R}_{LE})$ structures).[5,7,8] A localized orbital around the nitrogen develops as the HOMO at the $S_1(\mathbf{R}_{TICT})$ structure which is not the same as the HOMO at the $S_2(\mathbf{R}_{PICT})$ or $S_0(\mathbf{R}_{Min})$ structures, providing evidence that the electronic character at the $S_1(\mathbf{R}_{TICT})$ and $S_2(\mathbf{R}_{PICT})$ structures is fundamentally different. This would imply a high lying conical intersection between the S_2 and S_3 adiabatic states (this hypothetical conical intersection region will be dubbed CI.2, Fig 6). In the diabatic representation, this would imply that two diabatic states corresponding to TICT and PICT character cross at a point which must be accessed through a small barrier on S_2 from the geometry at t = 0. This is because a barrierless transition to CI.2, and by extension CI.1, is inconsistent with the aforementioned timescales of $S_1(\mathbf{R}_{TICT})$ formation). This is in contrast to the model proposed by Druzhinin et al,[85] which if converted to the diabatic basis such that the derivative couplings between the S_2 and the S_1 adiabatic states was reduced at the conical intersection shown in said model, would imply that the $S_2(\mathbf{R}_{PICT})$ and $S_1(\mathbf{R}_{TICT})$ structures represented the same diabatic state. Depending on which model is true, the excited state dynamics at the S_2 adiabatic state has far reaching implications for how the $S_1(\mathbf{R}_{TICT})$ structure is accessed at early timescales, and the overall dynamical model.

The separate diabatic states hypothesis requires further verification besides the use of NTOs. First, it was important to verify the role of the $S_2(\mathbf{R}_{PICT})$ structure, and whether or not the structure constituted a minimum as others have determined.[4,62] Appendix A.2 contains the result of an optimization on S_2 from the ground state geometry (using CASPT2), that led to the optimized $S_2(\mathbf{R}_{PICT})$ structure. With harmonic frequency analysis (observation of the excited state hessian yielded vibrational frequencies, returned at the end of the aforementioned CASPT2 optimization with OpenMolcas 21), it was determined that this structure actually represents a first order saddle point on the S_2 excited state surface instead of an excited state minimum. After perturbing the $S_2(\mathbf{R}_{PICT})$ excited state minimum

geometry along the mode associated with the imaginary frequency of the first order saddle point, a conical intersection was found between S_2 and S_1 at an LE-like structure with a twisting angle of 22 degrees, for which descent into the $S_1(\mathbf{R}_{LE})$ structure was concluded to be the most probable outcome (this conical intersection region will be referred to as CI.3, Fig 6). This process is barrierless, and since there is only slight amplitude motion between the $S_2(\mathbf{R}_{PICT})$ and $S_1(\mathbf{R}_{LE})$ structures, this process is consistent with the timescale attributed to the S_2 to S_1 decay in previous works.[10,34,72,75] Immediately after relaxation from S_2 to S_1 through the CI.3 structure, the transition barrier between CI.3 and the $S_1(\mathbf{R}_{TICT})$ structure is smaller than the transition barrier separating the $S_1(\mathbf{R}_{LE})$ and $S_1(\mathbf{R}_{TICT})$ structures, potentially explaining the early signals attributed to the $S_1(\mathbf{R}_{TICT})$ structure.[10,34,75] Alternatively, early signals could also be explained by any residual excited state population that does not sink into the $S_2(\mathbf{R}_{PICT})$ saddle point, and instead overcomes some transition state barrier on S_2 to proceed to the other two conical intersections (CI.2 and CI.1). Note that the early population of the $S_1(\mathbf{R}_{TICT})$ structure (160-300 fs) has only been observed in polar solvent, and the analysis of the internal conversion mechanism from S_2 to S_1 was performed in the gas phase. In the gas phase, the size of the transition-state barrier on S_1 leading to $S_1(\mathbf{R}_{TICT})$ formation from CI.3 may be too large, leading to no early $S_1(\mathbf{R}_{TICT})$ formation in the gas phase.[34] So far the analysis of the $S_2(\mathbf{R}_{PICT})$ and $S_1(\mathbf{R}_{TICT})$ structures using NTOs and a harmonic frequency analysis of the former structure implies that at least 3 conical intersection structures/regions exist in order to fit with the timescales offered by experimental spectroscopies. In the absence of dynamics simulations or excited state optimizations at such high lying adiabatic states, diabatic linear interpolated paths in internal coordinates (LIICs) were computed between the $S_1(\mathbf{R}_{TICT})$ and $S_2(\mathbf{R}_{PICT})$ geometries (Fig 11, see Chapter 1.4.3 for a review of p-BDD and how diabatic states are computed using DFT/MRCI as implemented in GRaCI).[154,156]

Fig 11 uses the initial adiabatic/diabatic states computed at the TICT geometry, to estimate the final diabatic states at the PICT geometry, by the iterative computation of

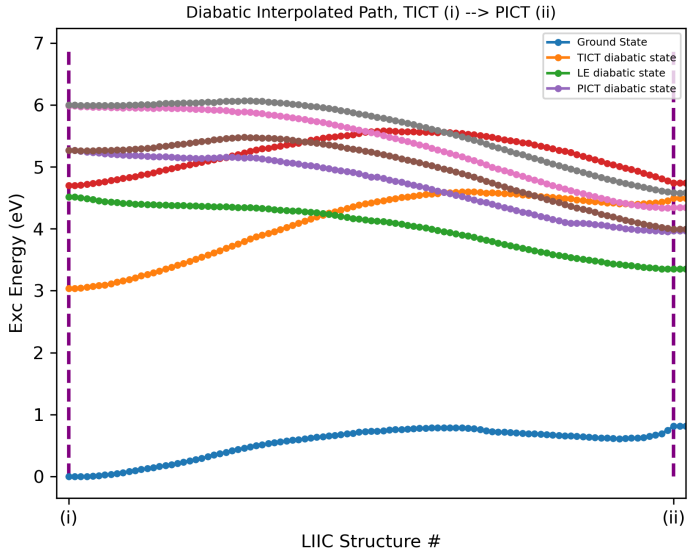

Figure 11: Diabatic LIIC between optimized CASPT2 i) $S_1(\mathbf{R}_{TICT})$ and ii) $S_2(\mathbf{R}_{PICT})$ geometries, energies of diabatic states computed using p-BDD/DFT/MRCI(2), where the initial set of diabatic states was determined based on the vertical excitation energies at the optimized $S_1(\mathbf{R}_{TICT})$ structure computed using DFT/MRCI(2), and was used to estimate further diabatic states at subsequent geometries using p-BDD. At either ends of this LIIC, there exist two separate diabatic charge transfer states at S_1, indicating that there are two charge transfer states for DMABN present in the molecule's excited state dynamics. The orange curve represents the TICT diabatic state ($S_D(\mathbf{R}_{TICT})$), at S_1 at the TICT geometry, and at S_5 at the PICT geometry. The purple curve represents the PICT diabatic state ($S_D(\mathbf{R}_{PICT})$), at S_1 at the PICT geometry, and at S_4 at the TICT geometry.

diabatic states from the initial adiabatic states computed by DFT/MRCI(2) at the TICT geometry. Starting from the TICT geometry, the diabatic state at S_1 appears to be a local minimum (orange curve, $S_D(\mathbf{R}_{TICT})$). Assuming this state is responsible for charge transfer in DMABN as has been implied by the TICT hypothesis, this charge transfer state remains at S_1 at geometries that possess a high twisting angle of the dimethylamino group. However, as the LIIC indicates, when moving from the TICT geometry to the PICT geometry, $S_D(\mathbf{R}_{TICT})$ moves to S_2, and then at the PICT geometry, it eventually represents the S_5 adiabatic state. Meanwhile, at the PICT geometry, the S_1 state is represented by the green curve, and the S_2 state is represented by a purple curve (diabatic state, $S_D(\mathbf{R}_{PICT})$) that has dropped in energy from its initial placement at S_4 at the TICT geometry. At the PICT geometry,

the S_1 state is attributed to the LE diabatic state (assuming the conventional dynamics models associated with DMABN, see Fig 6, referred to from here as $S_D(\mathbf{R}_{LE})$), so this S_2 state at the PICT geometry represents the initial charge transfer state probed by ground state absorption. Therefore, there are two charge transfer diabatic states of importance in the excited state dynamics of DMABN. $S_D(\mathbf{R}_{PICT})$ is probed by ground state absorption (purple curve), but in later stages of the excited state dynamics, as the population at the LE geometry is converted to the TICT geometry, a new charge transfer state ($S_D(\mathbf{R}_{TICT})$) drops down to S_1, distinct from the one initially absorbed to. This would imply that after initial excitation at the ground state to S_2, direct relaxation to the $S_1(\mathbf{R}_{TICT})$ structure is unlikely (through CI.2 and CI.1). This is supported by the fact that a few small barriers exist between the $S_D(\mathbf{R}_{PICT})$ and other diabatic curves which represent the CI.2 region of conical intersection structures. Therefore, the excited state population likely proceeds by internal conversion from the $S_2(\mathbf{R}_{PICT})$ structure to the $S_1(\mathbf{R}_{LE})$ structure (through CI.3) instead. After the majority of the excited state population reaches S_1, the intersection between the $S_D(\mathbf{R}_{TICT})$ and $S_D(\mathbf{R}_{LE})$ diabatic states represents a conical intersection region (CI.1), which doubles as a transition state barrier on S_1 which allows for conversion from the latter to the former.

More work is required in this area to establish whether the intersection between the $S_D(\mathbf{R}_{TICT})$ and $S_D(\mathbf{R}_{PICT})$ diabatic states is actually accessed in the excited state dynamics of DMABN. Analysis using p-BDD is heavily dependent on the choice of the initial adiabatic/diabatic states used to construct the ADT matrix, so it's difficult to establish the actual size of the transition state barrier using this method. It is reasonable at this point to say that it could be a cause for those early sporadic $S_D(\mathbf{R}_{TICT})$ signals detected in experiment were the barrier very small, however for now it is estimated that the transition state barrier on S_1 is the primary factor that guides $S_1(\mathbf{R}_{TICT})$ formation, at least with regard to the long lived signals that are attributed to the $S_1(\mathbf{R}_{TICT})$ structure at more than 1 picosecond.[9,34,73] When measuring the source of the long lived signals attributed to the $S_1(\mathbf{R}_{TICT})$

structure, the conical intersection between the $S_D(\mathbf{R}_{TICT})$ and $S_D(\mathbf{R}_{PICT})$ diabatic states is considered to be minorly contributing, and will be mostly disregarded in the context of the two-state model put forward in subsequent chapters of this thesis.

Present in the Appendix (A.3) are a series of other diabatic LIICs taken between the various nuclear structures of DMABN; several of these LIICs disagree with the hypothesis established from Fig 11, and indicate that the $S_D(\mathbf{R}_{PICT})$ and $S_D(\mathbf{R}_{TICT})$ diabatic states are the same. However, as previously mentioned (See Chapter 1.4.3), this is likely due to the initial choice of adiabatic/diabatic states at the first geometry. Since the $S_D(\mathbf{R}_{TICT})$ diabatic state is high lying at the ground state geometry, these diabatic LIICs lose accuracy when not starting from the $S_1(\mathbf{R}_{TICT})$ geometry, as the initial guess of diabatic states will not include the $S_D(\mathbf{R}_{TICT})$ diabatic state at other geometries. Furthermore, since the $S_D(\mathbf{R}_{PICT})$ and $S_D(\mathbf{R}_{TICT})$ diabatic states are both charge transfer states from the dimethylamino group to the cyano group, in certain diabatic LIICs, with a poor guess of initial diabatic states, the diabatic state at S_1 at the TICT geometry is often mistaken for the $S_D(\mathbf{R}_{PICT})$ state. Especially for larger molecules (see Chapter 2.2, DIABN electronic structure calculations), the similarity in the electronic character of these two diabatic states makes excited state optimizations often difficult, and is likely a contributing factor to the interpretation of these two states as the same in other pieces of literature.[5,8] One diabatic LIIC that is unfortunately missing from this section due to computational difficulties is a diabatic LIIC between the TICT and ground state geometries, which may yield more information as to the size of the transition barrier separating the $S_D(\mathbf{R}_{PICT})$ and $S_D(\mathbf{R}_{TICT})$ diabatic states at t = 0, compared to the barrierless transition that occurs on S_2 from the ground state geometry to the PICT geometry. Further diabatic LIICs performed on this system could also consider the explicit role of the S_1 transition states optimized in Chapter 2.2).

In summary, the $S_D(\mathbf{R}_{PICT})$ and $S_D(\mathbf{R}_{TICT})$ diabatic states were found to be distinct. It is likely that the crossing between the two diabatic states (a conical intersection in the adiabatic representation, CI.2) requires a small amount of energy to access after initial

absorption to S_2 at t = 0, representing a minor transition state barrier. Therefore, after initial absorption from S_0 to S_2, the majority of the excited state population will instead see relaxation to the $S_2(\mathbf{R}_{PICT})$ minimum, followed by internal conversion to the $S_1(\mathbf{R}_{LE})$ structure through a conical intersection structure with a slight, 22 degree twist (CI.3). Early $S_1(\mathbf{R}_{TICT})$ signals (160-300 fs) found in experiment may be attributed to a number of causes, either the overcoming of the conical intersection region at S_2 (CI.2), or the slightly smaller transition state barrier on S_1 accessible after relaxation to S_1 through a conical intersection (CI.3) but before the $S_1(\mathbf{R}_{LE})$ minimum is populated.[34] These early signals are sporadic and do not involve the majority of the excited state population which instead accesses the $S_1(\mathbf{R}_{LE})$ minimum after the CI.3 conical intersection structure. The primary mechanism of $S_1(\mathbf{R}_{TICT})$ formation is hypothesized to be through the transition-state barrier separating the $S_1(\mathbf{R}_{LE})$ and $S_1(\mathbf{R}_{TICT})$ structures, occurring over a few picoseconds (Fig 6).[7,9,73,85]

2.2 The Character and Height of the transition-state barrier

The height of the transition-state barrier separating the $S_1(\mathbf{R}_{LE})$ and $S_1(\mathbf{R}_{TICT})$ structures is important to characterize so that the specific rate of charge transfer formation in DMABN can be ascertained. To find the height of the transition-state barrier, the explicit transition state structure on S_1 involved must be optimized using *ab initio* electronic structure methods. That is to say, an intermediate nuclear structure between the $S_1(\mathbf{R}_{LE})$ and $S_1(\mathbf{R}_{TICT})$ structures must be determined with an excited state hessian yielding one imaginary frequency. At the first stages of researching this topic, basic LIICs were calculated between the excited state structures of DMABN and optimized transition states determined using two electronic structure methods, CASSCF and CASPT2 (see Appendix, A.4 for the results of these LIICs). It was quickly found that when evaluating the same LIICs using DFT/MRCI(2) based on structures optimized using CASPT2, that the shape of DFT/MRCI(2) LIICs and CASPT2 LIICs resembled each other quite closely. When using a transition state optimized with CASPT2, computing CASPT2 LIICs between the $S_1(\mathbf{R}_{LE})$ and $S_1(\mathbf{R}_{TICT})$ structures would

yield a maximum on S_1 associated with that transition state. Using DFT/MRCI(2) excitation energies, and using the same nuclear structures from the CASPT2 LIICs would result in a maximum on S_1 at a similar location along the DFT/MRCI(2) LIIC (see Appendix, A.4 for the results of these LIICs). This was indicative of how the two methods yield similar potential energy surfaces, at least for the molecular system being studied (DMABN), and therefore transition state structures optimized with DFT/MRCI(2) should resemble transition state structures optimized with CASPT2. Since DFT/MRCI(2) as implemented in GRaCI does not yet have the capability to optimize transition states, this allowed for the use of CASPT2 optimized transition states to be used as quasi DFT/MRCI(2) transition states, with the necessary stipulation that there would be minor inaccuracies intrinsic to this approach. Analytical gradients are not implemented for CASPT2, leading to computationally expensive transition state optimizations with numerical gradients. Therefore, in order to find the height of the transition-state barrier, a three pronged approach was used: the CASSCF, CASPT2, and DFT/MRCI(2) electronic structure methods. Optimization of the transition states was successful using the relatively inexpensive CASSCF method, but was only rarely so using the more expensive CASPT2 method (optimization cycles typically exceeded the time and resources available, and were often too computationally expensive unless smaller active spaces were used, (12,11) for DMABN transition state instead of the typical (14,13) active space selected for optimizing the excited state minimum structures). The transition states that were successfully optimized with CASPT2 were then used to estimate the size of the transition-state barrier for DFT/MRCI(2), for which transition-state optimization is not currently implemented. Furthermore, LIICs adjacent to the gas phase LIICs were computed using implicit solvation models to simulate the effects of acetonitrile. None of the electronic structure methods discussed yielded reliable transition state optimizations in acetonitrile, therefore the best approach was to obtain the transition state optimized structures computed in the gas phase, and use them to estimate the barrier heights associated with the transition states in acetonitrile using LIICs, where the excitation energies

were at least computed with the implicit solvent models available in GRaCI and Molcas. This procedure likely led to the overestimation of the true barrier heights associated with the acetonitrile transition states, and slight mischaracterizations of the nuclear structure of the transition states in acetonitrile.

Fig 12 shows a summary of the excited state energies found after calculating a series of interpolated paths between the relevant excited state minimum structures, and the transition state optimized with CASSCF, CASPT2, or estimated for DFT/MRCI(2) using the CASPT2 optimized transition state structure, for DMABN. The interpolated paths themselves can be found in the Appendix (A.4), along with images of the nuclear structure of the transition states optimized with each method. In this energy level diagram, and all others in this chapter, zero point energy at each excited state is not considered, that is the focus of the Rice-Ramsperger-Kassel-Marcus (RRKM) analysis further in this chapter.

In Figure 12, CASSCF predicts a large transition state barrier that is difficult to overcome even with the >1 eV of internal energy available at the $S_1(\mathbf{R}_{LE})$ structure after relaxation from S_2 to S_1. CASPT2 lowers the absolute energy of all excited states compared to CASSCF, but specifically lowers the absolute energy of the charge transfer states such that the character of the transition state barrier is entirely different than the description provided by CASSCF. A consequence of the charge transfer states being lower in energy is that CASPT2 predicts that the transition state barrier is trivial to overcome in the gas phase and in acetonitrile, with the internal energy available at the $S_1(\mathbf{R}_{LE})$ structure after relaxation from S_2 to S_1. DFT/MRCI acts as a middle ground between the two description offered by the other two electronic structure methods, lowering the absolute energies of the charge transfer states relative to CASSCF, but also predicting a larger transition state barrier compared to CASPT2. However, since this transition state was optimized using CASPT2 and not DFT/MRCI(2), it should be noted that the estimated barrier in Fig 12 for DFT/MRCI(2) is an upper bound to the true transition state barrier, and a transition state optimized with gradients computed with DFT/MRCI(2) would be lower in absolute energy. Using polariz-

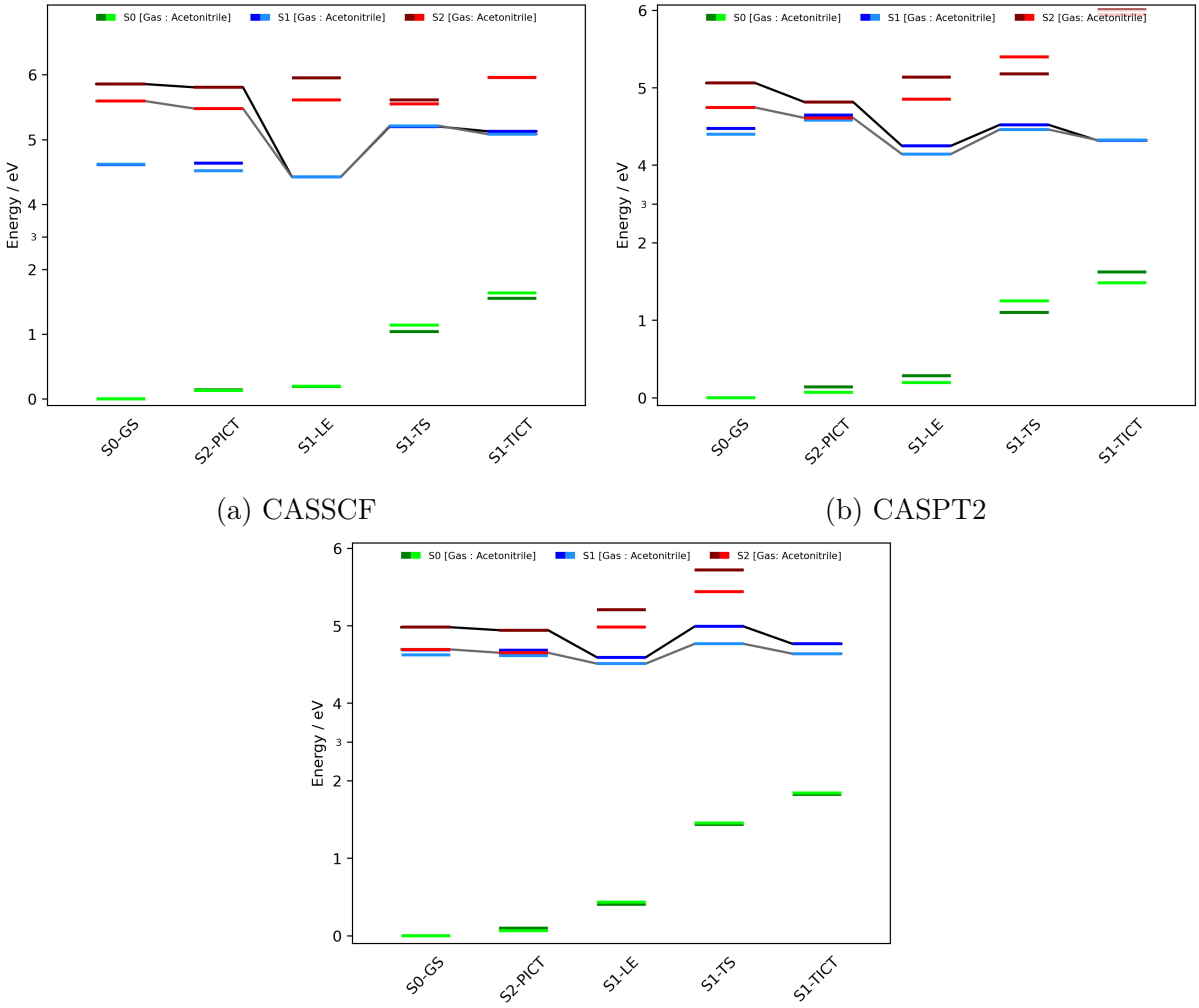

(a) CASSCF

(b) CASPT2

(c) DFT/MRCI(2), excited state energies on top of CASPT2 optimized structures

Figure 12: Energy Level Diagrams, excited state energies at relevant excited state geometries of DMABN, optimized at several levels of electronic structure theory. To summarize, the absolute energy of the charge transfer states are high lying under the CASSCF description, reduced significantly in the CASPT2 description, and DFT/MRCI(2) represents a middle ground. Likewise, the size of the transition state barrier separating the $S_1(\mathbf{R}_{LE})$ and $S_1(\mathbf{R}_{TICT})$ structures decreases significantly under CASPT2, and only slightly for DFT/MRCI(2), compared to CASSCF. Results were simulated in the gas phase and in acetonitrile, where the effect of the implicit solvation model is more pronounced for calculations conducted with DFT/MRCI(2) due to the implicit solvation method chosen. Solid black/grey (gas/acetonitrile) lines in this case track the expected pathway for the majority of the excited state population after initial absorption to S_2 at t = 0, see Fig 6.

able continuum model (PCM) for CASSCF/CASPT2 and domain-decomposition Conductor Like Screening Model (ddCOSMO) for DFT/MRCI(2) to simulate the effects of polar solvent results in a small reduction in the excited state energies of all structures studied. The use of an implicit solvation model had a series of expected and unexpected effects on the excited state energies calculated. Firstly, the absolute energy of the $S_1(\mathbf{R}_{TICT})$ structure did not fall below the absolute energy of the $S_1(\mathbf{R}_{LE})$ structure when using any electronic structure method. Therefore, unlike experimental data would suggest, none of the implicit solvation models implied that the molecule would reach the TICT excited state minimum structure in acetonitrile or in the gas phase as the $S_1(\mathbf{R}_{TICT})$ structure did not represent an absolute minimum on S_1. Secondly, the two implicit solvation models used had entirely separate effects on the excited state energies of the $S_2(\mathbf{R}_{PICT})$ structure and the transition states optimized. While both implicit solvation methods decreased the relative energy of the $S_2(\mathbf{R}_{PICT})$ structure, and slightly decreased the relative energy of the $S_1(\mathbf{R}_{LE})$ structure relative to the gas phase, only ddCOSMO used with DFT/MRCI(2) decreased the relative energy of the transition state compared to the energy of the $S_1(\mathbf{R}_{LE})$ structure, increasing the rate of charge transfer in acetonitrile.

The nuclear character of the transition states optimized by CASSCF and CASPT2 warrants discussion, since the two methods find entirely separate nuclear structures after geometry optimization. This difference is significant especially since CASSCF predicts a much larger transition state barrier than the other two methods CASPT2 and DFT/MRCI(2). In the two-state model, the $S_1(\mathbf{R}_{TICT})$ structure is accessed via nuclear displacements along two primary coordinates: the amino dihedral angle and the out of plane bend at the carbon atom of the benzene ring bonded to the nitrogen atom of the amino group. The CASSCF transition state structure exists at a geometry that has a significant twist of the dimethylamino group, but the dimethylamino group is not bent out of plane significantly. Meanwhile, the CASPT2 transition state structure exists at a geometry that is very similar to the proposed $S_1(R_{pTICT})$ excited state minimum,[10] however the dimethylamino group is slightly out of

plane with the benzene ring. A harmonic frequency analysis of both structures indicate that they both exist as an unstable maximum (imaginary frequency) at a vibrational mode that appears to control the level of pyramidalization around the dimethylamino group. In order to overcome the transition state barrier and reach the transition state, the excited state hessian of the CASSCF transition state implies that the dimethylamino group must first twist nearly 90 degrees, while the excited state hessian of the CASPT2 transition state imples that the de-pyramidalization can occur much earlier, at a structure closer to the proposed $S_1(R_{pTICT})$ state.[10] Therefore, CASSCF indicates the $S_1(\mathbf{R}_{LE})$ to $S_1(\mathbf{R}_{TICT})$ transition is sequential, where the dimethylamino group must be almost fully twisted before the local nuclear structure around the dimethylamino nitrogen can change, while CASPT2 indicates that both the twist and bend of the dimethylamino group happen simultaneously as the dimethylamino nitrogen becomes de-pyramidalized. It is difficult to say at the outset which transition state optimization yielded a geometry closest to the true transition state; this will require an interrogation of these transition-state barriers against experimental spectroscopies (see Chapter 4).

In previous work on DMABN, it was observed that the rate of charge transfer could be controlled by increasing the size of the carbon chains on the dimethylamino group.[13] For this reason, diisopropyl aminobenzonitrile (DIABN) and aminobenzonitrile (ABN) have been examined in the past.[5,13,188,189] Whereas charge transfer has been observed both in polar solvent and in the gas phase for DIABN, charge transfer has not been observed in either environment for the ABN.[5,13,188,189] The two molecules are particularly useful analogues to compare with DMABN. Based on previous literature, it is expected that the transition state barrier should decrease with respect to DMABN for DIABN, and increase with respect to DMABN for ABN.[13] The two-state model was assumed to be valid when studying these analogues, under the justification that the actual nuclear structural changes are minimal; the donor-acceptor model coupled with a conjugated ring is still intact, and so the character of the DIABN $S_1(\mathbf{R}_{TICT})$ and $S_1(\mathbf{R}_{LE})$ structures should be similar compared to their DMABN

equivalents. The same diabatic analysis performed in Chapter 2.1 could not be performed for DIABN due to computational difficulties incurred by the molecule's size, it is difficult to say at this juncture whether the two-state model will hold for the molecule without further analysis. Regardless, the transition-state barriers were evaluated with CASSCF, CASPT2, and DFT/MRCI(2) for both DIABN and ABN. In the Appendix (A.5), the nuclear geometries of the excited state minimum structures optimized using CASPT2 for DIABN and ABN are present. Note that CASPT2 transition state optimizations and excited state optimizations were exceptionally computationally expensive for DIABN, requiring active spaces of at maximum (8,7) as opposed to the typical (14,13), for all transition state optimizations. However all excited state energies yielded by CASSCF/CASPT2 in LIICs conducted on the molecule were performed with (14,13) active spaces.

Fig 13 and Fig 14 show a summary of key points along the LIICs computed for DIABN and ABN, analogous to Fig 12. The interpolated paths themselves from which these are based can be found in the Appendix (A.4), along with images of the nuclear structure of the transition states optimized with each method.

The electronic structure methods CASSCF, CASPT2, and DFT/MRCI(2) treat the analogues in this section similarly to DMABN. For instance, the relative energy of the charge transfer state energies computed by CASSCF for DIABN are higher lying then their equivalents in CASPT2 and DFT/MRCI(2). Furthermore, the smallest transition state barrier is computed with CASPT2, while DFT/MRCI(2) computes a moderate transition state barrier compared to the other two computed by CASSCF and CASPT2. The main difference between the calculations on DIABN and those of DMABN is that for the calculations performed with CASPT2 and DFT/MRCI(2), the absolute energy of the $S_1(\mathbf{R}_{TICT})$ structure is consistently lower than the $S_1(\mathbf{R}_{LE})$ structure. Furthermore, using all three electronic structure methods, the relative energy of the transition state compared to the $S_1(\mathbf{R}_{LE})$ structure is lower for the DIABN calculations compared to those computed on DMABN. The reverse is true for ABN; the $S_1(\mathbf{R}_{TICT})$ structure is very high lying across all electronic structure meth-

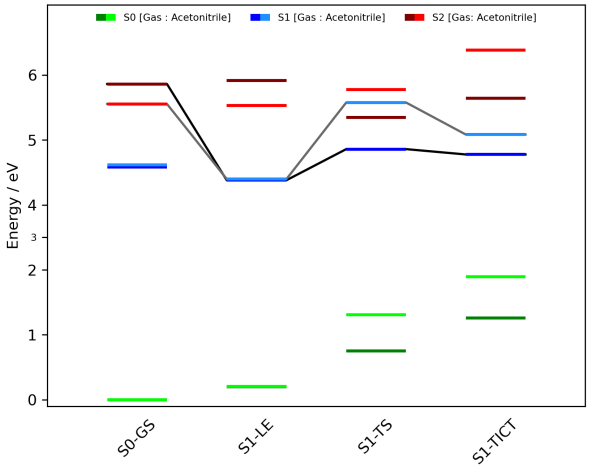

(a) CASSCF

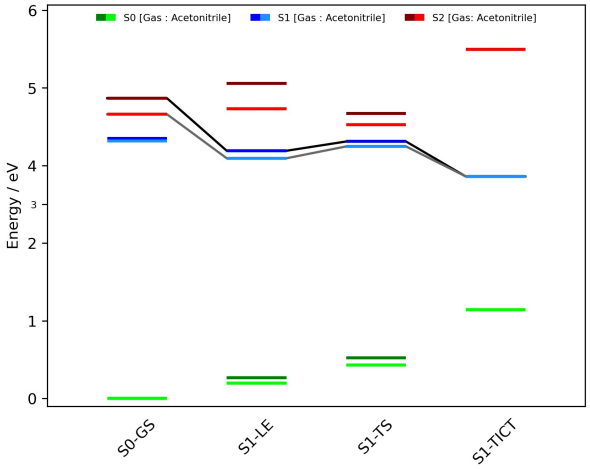

(b) CASPT2

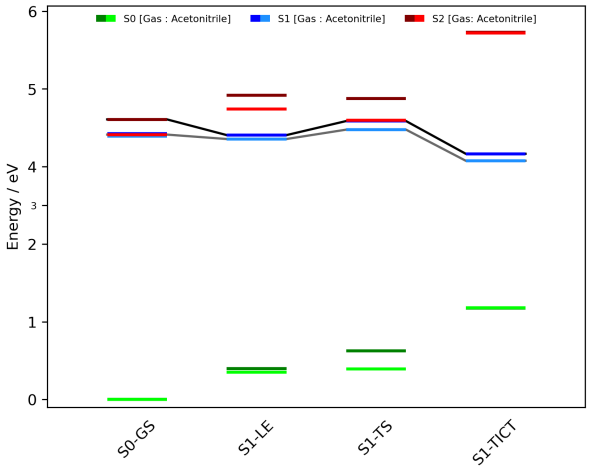

(c) DFT/MRCI(2), excited state energies on top of CASPT2 optimized structures

Figure 13: Energy Level Diagrams, excited state energies at relevant excited state geometries of DIABN, optimized at various levels of electronic structure theory. In comparison to the results obtained for DMABN (Fig 12), the absolute energy of the $S_1(\mathbf{R}_{TICT})$ structure is consistently lower than the absolute energy of the $S_1(\mathbf{R}_{LE})$ structure. Furthermore, an excited state minimum associated with the $S_2(\mathbf{R}_{PICT})$ structure could not be successfully optimized with the molecule. Solid black/grey (gas/acetonitrile) lines in this case track the expected pathway for the majority of the excited state population after initial absorption to S_2 at t = 0.

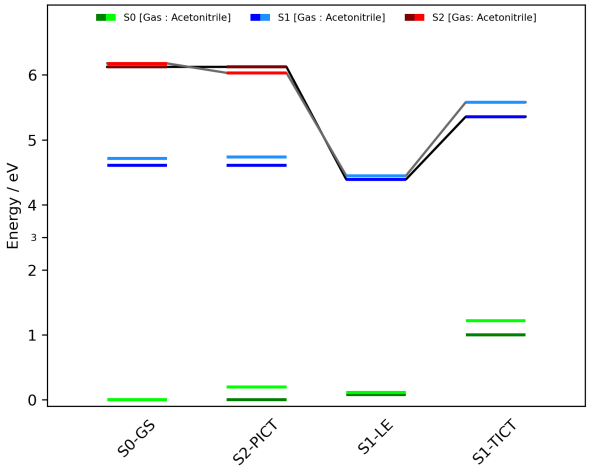

(a) CASSCF

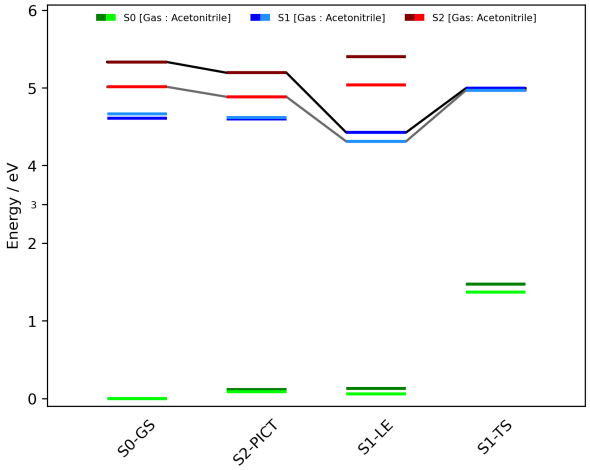

(b) CASPT2

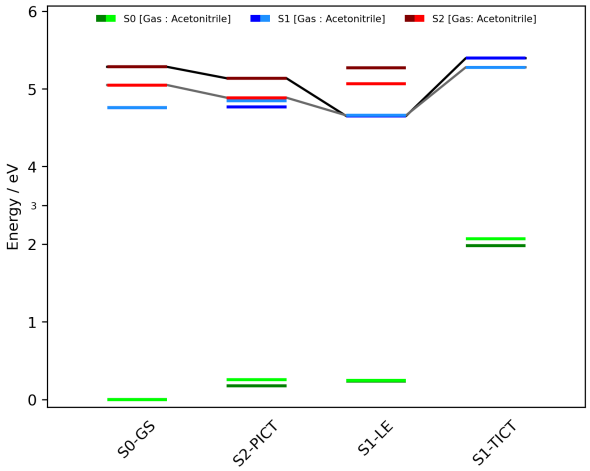

(c) DFT/MRCI(2), excited state energies on top of CASPT2 optimized structures

Figure 14: Energy Level Diagrams, excited state energies at relevant excited state geometries of ABN, optimized at various levels of electronic structure theory. In comparison to the results obtained for DMABN (Fig 12), the absolute energy of the $S_1(\mathbf{R}_{TICT})$ structure is consistently higher than the absolute energy of the $S_1(\mathbf{R}_{LE})$ structure. Both CASSCF and CASPT2 could not successfully optimize the $S_1(\mathbf{R}_{TICT})$ excited state minimum structure, and therefore a transition state between the $S_1(\mathbf{R}_{LE})$ and $S_1(\mathbf{R}_{TICT})$ states was not optimized either. Solid black/grey (gas/acetonitrile) lines in this case track the expected pathway for the majority of the excited state population after initial absorption to S_2 at t = 0.

ods, however the actual transition-state barrier could not be determined. This is because for ABN, CASPT2 and CASSCF could not successfully optimize the $S_1(\mathbf{R}_{TICT})$ structure, instead the energy of the state is approximated by using a structure with the same internal coordinates as DMABN in Fig 14. The $S_1(\mathbf{R}_{TICT})$ structure for ABN has claimed to be optimized using CASSCF and CASPT2 using previous works,[5] so it is likely the choice of basis set, convergence parameters, or initial guess affects the success rate of these optimizations significantly for ABN. This would indicate at least, that the $S_1(\mathbf{R}_{TICT})$ minimum for ABN represents a shallow minimum. A transition state could also not be successfully optimized with either CASSCF or CASPT2 for the molecule, and thus the size of the transition-state barrier could not be determined. Returning to DIABN, the transition state at the CASSCF and CASPT2 levels of theory both proved quite difficult to optimize due to what seems to be an exceptionally small transition state barrier between the $S_1(\mathbf{R}_{LE})$ and $S_1(\mathbf{R}_{TICT})$ structures. Transition state optimizations often found similar transition state structures for DIABN with similar absolute energies, but with broad differences in the twisting angle of the dimethylamino group. Therefore, in Fig 13, the transition state energies found at CASPT2 and CASSCF have a large degree of uncertainty attached to them. The $S_2(\mathbf{R}_{PICT})$ structure also proved difficult to optimize for DIABN, and in fact both CASSCF and CASPT2 found that the ground state structure of DIABN with a small twist was lower in absolute energy at S_2 than a planarized nuclear structure. Finally, similar to the calculations performed on DMABN, the use of an implicit solvent model to simulate the effects of acetonitrile for calculations performed on DIABN and ABN lowered the relative energy of the charge transfer states ($S_2(\mathbf{R}_{PICT})$ and $S_1(\mathbf{R}_{TICT})$). However the transition states themselves were not affected when using the PCM model, and only when using the ddCOSMO implicit solvation model were their absolute energies reduced. As others have argued, for polar solvents especially, the choice of semi-empirical factors in dd-COSMO is more appropriate for treating solvent effects on many body molecules (such as DMABN),[178,183] and so in this case it is likely that this model is more accurately describing the energy of the transition state in

acetonitrile, although it is difficult to say for certain considering the other approximations already made so far.

To better quantify the transition-state barriers studied so far, the Rice-Ramsperger-Kassel-Marcus (RRKM) kinetics theory was used. The use of a microcanonical transition state theory for an excited state picosecond process is typically not appropriate, since RRKM assumes that all nuclear structures with the same energy are equally probable and uniformly sampled on a time scale faster than the rate at which the transition state barrier is overcome. Despite this, RRKM is justified as a first approximation to the excited state dynamics on S_1 since the geometries of the pre-transition state and post-transition state structures are well defined by specific geometric characteristics (twist, out of plane bend), and the excited state dynamics on S_1 are relatively simple (lack of significant competing pathways). Finally, the individual lifetimes of the $S_1(\mathbf{R}_{LE})$ and $S_1(\mathbf{R}_{TICT})$ structures are relatively long lived, with emissions persisting from both structures after hundreds of picoseconds, giving time for the internal energy to be sufficiently reorganized into the vibrational states of the $S_1(\mathbf{R}_{LE})$ and S_1 transition state structures.[9,13,34,75,85] Zero point energy corrections to the excited state energies at the $S_1(\mathbf{R}_{LE})$ and $S_1(\mathbf{R}_{TS})$ geometries based on available excited state hessians (CASSCF or CASPT2). The rate at which each transition state barrier on S_1 is overcome with the internal energy still available at the $S_1(\mathbf{R}_{LE})$ structure after decay from the $S_2(\mathbf{R}_{PICT})$ structure was estimated using RRKM. The excited state hessians at each transition state structure were readily available after transition state optimizations conducted for CASPT2 and CASSCF using OpenMolcas 21, and the internal energy available at the $S_1(\mathbf{R}_{LE})$ structure could be ascertained based on the difference between the energy required to absorb at S_2 from the ground state minimum, and the absolute energy of the $S_1(\mathbf{R}_{LE})$ structure. The rate constants were used in a first order rate law equation, to predict the time at which the final concentration of the reactant decreases to 50% of its initial concentration. The results of these calculations are present in Table 1 for DMABN and DIABN, using the electronic structure methods discussed in this work.

A number of shifts were applied to the excited state energies in Fig 12 and Fig 13 to find the rate constants in Table 1. These were significant for excited state energies computed with CASPT2, as the absolute energy of the S_2 state after ground state absorption was always large enough such that the transition state barrier was predicted to be overcome instantly (<50 fs), in the gas phase and in acetonitrile for both molecules. The basis of these shifts were comparisons to experimental results which detected the rise time of the charge transfer signal in DMABN in acetonitrile,,[9] as well as experimental results supposedly detecting the rise of a charge transfer signal in DIABN in the gas phase (discussed in detail in Chapter 4). It was determined that in order for CASPT2 to accurately recreate a rise time of the charge transfer signal consistent with experimental data, a shift of about -0.58 eV needed to be applied to absolute energy of the $S_2(\mathbf{R}_{GS})$ structure. That is to say, the amount of internal energy at the $S_1(\mathbf{R}_{LE})$ structure after decay from S_2 to S_1 is presumed to be overestimated by CASPT2. Since this internal energy was so high, the transition state barriers for DMABN/DIABN in the gas phase and acetonitrile were predicted to be overcome near instantaneously, which is inconsistent with the aforementioned experimental data available, necessitating the aforementioned shift. Furthermore, the PCM model in electronic structure calculations in Fig 12 provided a description of the charge transfer process that was inconsistent with experimental data. At the $S_2(\mathbf{R}_{PICT})$ and $S_2(\mathbf{R}_{GS})$ structures, their absolute energies decreased significantly compared to their gas phase absolute energies, but since the energy of the transition state structure was unaffected by the PCM implicit solvation model for CASSCF and CASPT2 calculations, RRKM predicted that the charge transfer process would be slower in acetonitrile for both DMABN and DIABN. Hence, all calculations using the PCM model were not included in Table 1; it appears as if dd-COSMO is the preferred implicit solvation model to treat molecules of this size and for extremely polar solvents, due to the aforementioned semi empirical parameters used in its implementation. Finally, the DFT/MRCI(2) description of DMABN and DIABN in acetonitrile was vastly different from their gas phase description. For example, for DMABN the S_2 and S_1

adiabatic states were nearly degenerate at the ground state geometry, meaning the transition state barrier was impossible to overcome in acetonitrile for DMABN due to a lack of internal energy. A final shift of +0.07 eV was applied to the internal energy at the $S_1(\mathbf{R}_{LE})$ structure for all DFT/MRCI(2) calculations in acetonitrile (dd-COSMO), to better match with experimental data. The process of multiple shifts further illustrates the inaccuracies inherent to this method, in addition to further inaccuracies such as those caused by the differences between excited state optimizations performed in the gas phase compared to those in acetonitrile, which were neglected in this study. Moreover, using the energy at the $S_2(\mathbf{R}_{GS})$ structure plus/minus an empirical shift to estimate the internal energy available at the $S_1(\mathbf{R}_{LE})$ structure is only applicable as a first guess, and yet this parameter is very important to the description of the excited state dynamics provided by RRKM analysis. Part of the analysis used to determine the empirical shifts to the internal energy in each case was done by constructing RRKM curves based on a variable amount of internal energy and the transition state barriers previously computed, these RRKM curves are presented in the Appendix (A.6).

An RRKM analysis (with shifts to excited state energies returned from CASPT2) can lead to rise times that are consistent with other experimental studies on DMABN and DIABN.[9] However, as shown elsewhere (Appendix, A.4), the DIABN LIIC that exists between the $S_1(\mathbf{R}_{LE})$ and $S_1(\mathbf{R}_{TICT})$ structures is sufficient on its own without the explicit optimization of a transition state in demonstrating that charge transfer should occur for this molecule, because the $S_1(\mathbf{R}_{TICT})$ structure is significantly more low lying in energy than the $S_1(\mathbf{R}_{LE})$ structure, which is not the case for the adjacent LIICs computed for DMABN. LIICs computed without transition states are a good first guess compared to the LIICs computed with explicit transition states in this section, and can yield important information about whether charge transfer is likely for a DMABN-type molecule. Determining the specific rise and decay times of the charge transfer process is best determined through experimental time resolved studies; as observed in this work and others,[73] current electronic structure calculations per-

Table 1: Rate Constants k(E) and corresponding transition times for the $S_1(\mathbf{R}_{LE}) \rightarrow S_1(\mathbf{R}_{TICT})$ conversion in DMABN and DIABN, determined using different *ab initio* levels of theory.

Molecule	Method	Solvent	Shift applied to $S_2(\mathbf{R}_{GS})$ absolute energy	k(E) (s^{-1})	decay/rise time (picoseconds)
DMABN	CASSCF	Gas	0	2.2 * 10^6	3.1*10^5
	CASPT2	Gas	-0.58	$\sim$0	$\sim \infty$
	DFT/MRCI(2)	Gas	0	$\sim$0	$\sim \infty$
	DFT/MRCI(2)	Acetonitrile	+0.07	2.5 * 10^8	2.8
DIABN	CASSCF	Gas	0	5.5 * 10^8	1.3
	CASPT2	Gas	-0.58	1.7 * 10^8	4.0
	DFT/MRCI(2)	Gas	0	2.4 * 10^8	2.8
	DFT/MRCI(2)	Acetonitrile	+0.07	3.7 * 10^9	0.2

formed on DMABN with some *ab initio* methods such as CASPT2 underestimate the rise time of the charge transfer states responsible for dual fluorescence. However, DFT/MRCI(2) requires no shift in the gas phase to reproduce time constants that were consistent with previous experimental data on DIABN in the gas phase (see Chapter 4), even with the use of CASPT2 excited state structures. Therefore, in order to further develop this thesis, the simulation of spectroscopies is encouraged for the excited state structures of DMABN and its analogues using DFT/MRCI(2) exclusively, such that if charge transfer formation is likely for a given molecule, distinct signals attributed to the $S_1(\mathbf{R}_{TICT})$ structure can be identified in a time resolved study. The focus of future sections (Chapter 3 onwards), is thus to benchmark the electronic structure method of choice, DFT/MRCI(2), against experimental data. Once this is done, DFT/MRCI(2) may be applied to estimate new unperformed spectroscopies, as a first guess for future time resolved studies. Before all of this can be done, a few minor alternate hypothesises for the excited state dynamics of DMABN must be addressed.

2.3 The Proposed Role of the Partially Twisted Charge Transfer and $\pi\sigma*$ states

The two-state model introduced in Fig 6 excludes the proposed $S_1(\mathbf{R}_{pTICT})$ and $S_1(\mathbf{R}_{\pi\sigma*})$ structures, which in literature have often been used to explain experimental spectroscopic signals.[8,10] In this section, linear interpolated paths in internal coordinates (LIICs) are computed utilizing DFT/MRCI(2) to demonstrate that the $S_0(\mathbf{R}_{Min}) \rightarrow S_2(\mathbf{R}_{PICT}) \rightarrow S_1(\mathbf{R}_{LE})$ $\rightarrow S_1(\mathbf{R}_{TICT})$ mechanism in Fig 6 best describes the excited state dynamics of DMABN, and that the $S_1(R_{pTICT})$ and $S_1(\mathbf{R}_{\pi\sigma*})$ structures do not play a significant role. While this topic has already been considered numerous times by other studies, it is important to address for this thesis because the electronic structure method used to compute spectroscopies, DFT/MRCI(2), has not been used to tackle this problem, and it is relevant to see if the method describe these structures significantly differently than CASPT2, CASSCF, etc. Equivalent LIICs computed using CASPT2, or with solvent, can be found elsewhere

(Appendix, A.7).

LIICs involving the $S_1(\mathbf{R}_{\pi\sigma*})$ structure were difficult to compute using CASPT2. This is because CASPT2 LIICs often have discontinuities unless neighbouring geometries have adiabatic states that do not change significantly in their electronic character, which often requires orbitals from one step in an LIIC to be used as a guess for future steps in an LIIC. Further discontinuities arrive if the electronic character of the adiabatic states considers changes significantly from step to step, as is the case for paths including the $S_1(\mathbf{R}_{\pi\sigma*})$ structure, since orbitals describing the excited states accessible at the PICT geometry will differ significantly from the orbitals describing the excited states accessible at the $\pi\sigma*$ geometry.

The role of the $S_1(\mathbf{R}_{pTICT})$ structure is often disputed due to the inability of electronic structure methods to find an excited state minimum with unique electronic character at the partially twisted geometry.[7,8] Similarly to CASPT2, DFT/MRCI(2) finds that at the pTICT geometry, the S_2 and S_1 states are nearly degenerate (Fig 15). Therefore the nuclear structure of DMABN at the partially twisted geometry will relax to either the $S_1(\mathbf{R}_{LE})$ or $S_1(\mathbf{R}_{TICT})$ geometries. Fig 15 implies that the $S_1(\mathbf{R}_{LE})$ structure requires about 0.27 eV to overcome the transition barrier required to reach the $S_1(\mathbf{R}_{pTICT})$ geometry, and similarily there is a small 0.20 eV barrier preventing direct population of the $S_1(\mathbf{R}_{TICT})$ structure from the $S_1(\mathbf{R}_{pTICT})$ structure. The presence of a conical intersection near the $S_1(\mathbf{R}_{pTICT})$ geometry is significant, and has been found in previous work on DMABN.[8] Here, these adiabatic LIICs are consistent with the diabatic LIIC shown earlier in this discussion (Fig 11), which indicate that this conical intersection represents a degeneracy between the diabatic $S_D(\mathbf{R}_{TICT})$ and $S_D(\mathbf{R}_{LE})$ states (CI.1), and therefore the pTICT geometry is not a source of transient excited state signals.[10]

As shown by the potential energy curves in Fig 16 and Fig 17, the $S_1(\mathbf{R}_{\pi\sigma*})$ structure is unlikely to play a significant role in the excited state dynamics of DMABN. Fig 16a and Fig 16b demonstrate that with or without forced planarization of the $S_1(\mathbf{R}_{LE})$ structure to the PICT nuclear structure, a barrier persists separating the $S_1(\mathbf{R}_{LE})$ and $S_1(\mathbf{R}_{\pi\sigma*})$ excited

state minimums, and the size of the barrier is primarily due to the bending vibrational motion of the cyano group (0.37 eV). In the previous section (Fig 12), it was established that DFT/MRCI(2) predicts that 0.29 eV of internal energy is available after ground state absorption and internal conversion to S_1, hence it is unlikely that this transition-state barrier will be overcome, and the $S_1(\mathbf{R}_{\pi\sigma*})$ structure will be populated. However, a transition state may exist that reduces the size of the transition-state barrier between the $S_1(\mathbf{R}_{LE})$ and $S_1(\mathbf{R}_{\pi\sigma*})$ structures, although optimizations so far have been unsuccessful with all of the electronic structure methods in Chapter 2.2.

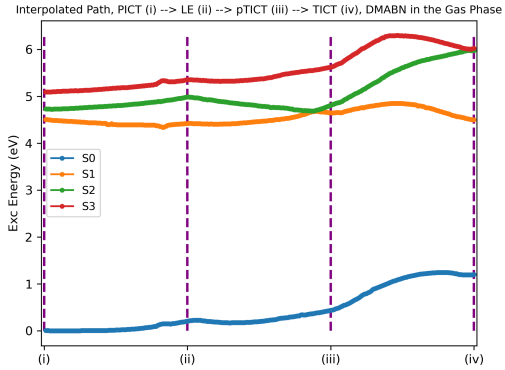

Figure 15: LIIC of DMABN, through the following nuclear geometries, PICT $\rightarrow$ LE $\rightarrow$ pTICT $\rightarrow$ TICT. Energies are computed by DFT/MRCI(2), in the Gas Phase. Legend refers to adiabatic states, S_0, S_1, S_2, etc.

Assuming that the $S_1(\mathbf{R}_{\pi\sigma*})$ structure can be populated via a transition state that lowers the transition-state barrier between the $S_1(\mathbf{R}_{\pi\sigma*})$ structure and $S_1(\mathbf{R}_{LE})$ structures, the $S_1(\mathbf{R}_{\pi\sigma*})$ structure is still unlikely to contribute to $S_1(\mathbf{R}_{TICT})$ formation. Fig 17 illustrates the various potential sequential pathways that could lead to $S_1(\mathbf{R}_{TICT})$ formation. The LIIC that represents the smallest transition-state barrier between the $S_1(\mathbf{R}_{\pi\sigma*})$ and $S_1(\mathbf{R}_{TICT})$ structures requires an immediate reversal of the bending of the cyano group. Any other structural change leads to a larger transition-state barrier of upwards of 0.8 eV, which is not surpassable with the internal energy available on S_1 after the aforementioned S_2 to S_1 internal conversion process.

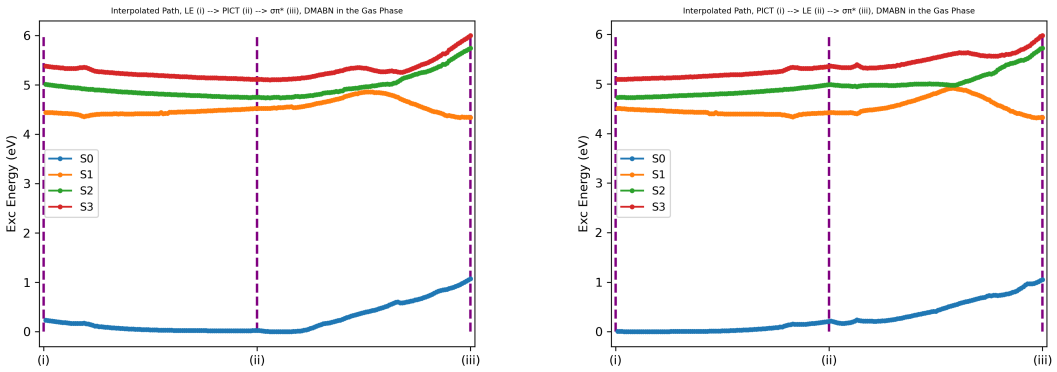

(a) LE $\rightarrow$ PICT $\rightarrow$ $\pi\sigma^*$ (b) PICT $\rightarrow$ LE $\rightarrow$ $\pi\sigma^*$

Figure 16: LIICs of DMABN, evaluating the transition-state barrier of the population of the $S_1(\mathbf{R}_{\pi\sigma*})$ structure. Energies computed by DFT/MRCI(2), in the Gas Phase. Legend refers to adiabatic states, S_0, S_1, S_2, etc.

Overall, the $S_1(\mathbf{R}_{\pi\sigma*})$ structure is unlikely to contribute to $S_1(\mathbf{R}_{TICT})$ formation, and so it was not included in the description of the two-state model (see Fig 6). Without an explicit transition state optimized between the $S_1(\mathbf{R}_{LE})$ and $S_1(\mathbf{R}_{\pi\sigma*})$ structures, it is difficult to ascertain the true height of the transition-state barrier between the two. However, even if the transition state barrier between the $S_1(\mathbf{R}_{\pi\sigma*})$ and $S_1(\mathbf{R}_{LE})$ structures is surpassed, since the $S_1(\mathbf{R}_{\pi\sigma*})$ structure cannot contribute towards $S_1(\mathbf{R}_{TICT})$ formation, it is best characterized as the endpoint of a competing pathway to $S_1(\mathbf{R}_{TICT})$ formation, and does not necessarily disprove the two-state model (yet it would reduce the overall $S_1(\mathbf{R}_{TICT})$ yield). In order to evaluate whether the $S_1(\mathbf{R}_{LE}) \rightarrow S_1(\mathbf{R}_{\pi\sigma*})$ pathway is competing with the main two-state model pathway significantly, $S_1(\mathbf{R}_{LE}) \rightarrow S_1(\mathbf{R}_{TICT})$, existing experimental data must be evaluated, and new spectroscopies must be simulated, which can detect signals attributed to the $S_1(\mathbf{R}_{LE})$, $S_1(\mathbf{R}_{\pi\sigma*})$, and $S_1(\mathbf{R}_{TICT})$ structures.

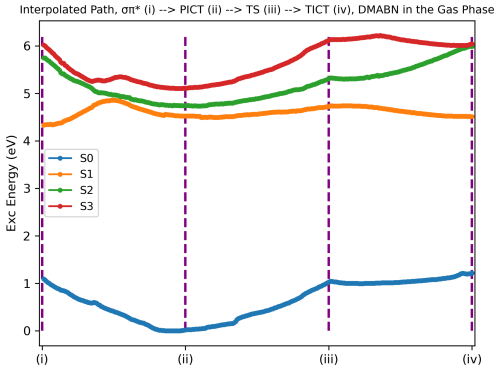

(a) $\pi\sigma^* \rightarrow$ PICT $\rightarrow$ pTICT $\rightarrow$ TICT

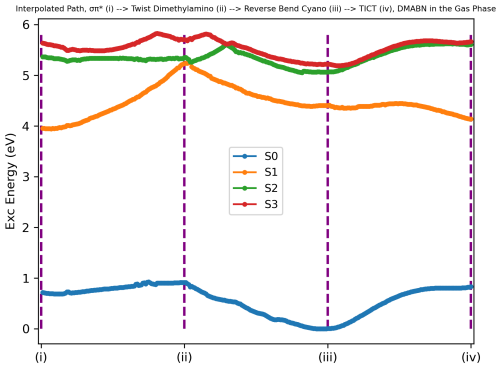

(b) $\pi\sigma^* \rightarrow$ Dimethylamino Twist $\rightarrow$ Reverse Cyano Bend $\rightarrow$ TICT

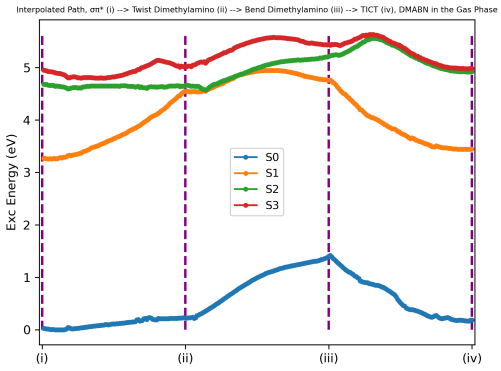

(c) $\pi\sigma^* \rightarrow$ Dimethylamino Twist $\rightarrow$ Dimethylamino Bend $\rightarrow$ TICT

Figure 17: LIICs of DMABN, evaluating the transition barriers of the population of the $S_1(\mathbf{R}_{TICT})$ structure from the $S_1(\mathbf{R}_{\pi\sigma*})$ structure. Energies computed by DFT/MRCI(2), in the Gas Phase. Legend refers to adiabatic states, S_0, S_1, S_2, etc.

3 Time Resolved Spectroscopies of DMABN in Solution

3.1 UV/VIS Absorption: Benchmarking Quantum Chemical Methods

In order to validate and utilize the two-state model by predicting various excited state spectroscopies, it is important to first establish that the quantum chemistry method of choice, DFT/MRCI(2), can reproduce basic experimental spectrum. The absorbance/fluorescence spectrum of DMABN has been evaluated in a number of studies,[9,10,13,26,29,40,83,85] and has been essential to benchmark other electronic structure methods including CASSCF and CASPT2 (Appendix, A.8). Figure 18 displays simulated absorbance/fluorescence spectrum of DMABN computed with DFT/MRCI(2), compared to experimental spectrum, while also including the (theoretical) fluorescence of the $S_1(\mathbf{R}_{\pi\sigma*})$ structure. The $S_1(\mathbf{R}_{\pi\sigma*})$ structure is presumed to not be responsible for any of the experimental fluorescing bands, but it is included here because the structure is significant enough that signals attributed to the structure will be simulated in all future simulated spectroscopies in this thesis. The experimental spectrum being compared to in Figure 18 is the one produced by Druzhinin[9] that evaluated DMABN in acetonitrile, where relative oscillator strengths calculated with DFT/MRCI(2) in acetonitrile have all been scaled upwards to better compare specific emitting wavelengths. In the experimental spectrum, the assignment of peaks to GS, LE and

CT absorptions/emissions is based on the conventional dual fluorescence theory advocated by Druzhinin et al, which states that in acetonitrile, the two signals present are attributed to the LE structure and CT structure.[9] Not every absorbance/fluorescence spectrum taken in literature has spotted an emission correlated to the LE structure for DMABN in acetonitrile, with many experimental UV/Vis spectrum solely spotting the CT structure in acetonitrile, and solely the LE structure in the gas phase.[10,29] In this section, the purpose is primarily to establish whether DFT/MRCI(2) estimates the relative excited state energies of each potentially emitting structure in the excited state dynamics of DMABN in a manner consistent with experimental assignments. Establishing at the outset where simulated spectroscopies differ with basic experimental spectroscopies allows for easier interpretations of inconsistencies that may arise when repeating the process for more advanced experimental spectroscopies elsewhere in this thesis. There is less emphasis on comparing the specific intensities of individual emissions to experimental data, since the implicit solvation model (dd-COSMO) does not significantly alter the intensities of excited state emissions relative to equivalent gas phase calculations. For example, dd-COSMO is unable to predict the strong fluorescence of the $S_1(\mathbf{R}_{TICT})$ structure in acetonitrile, and instead predicts a weak fluorescence of the structure similar to equivalent gas phase calculations. Equivalent spectra to Figure 18, conducted in the gas phase, are present elsewhere (Appendix, A.8). Spectrum conducted in this section are convoluted with a Gaussian using a 1000 cm^{-1} full width half maximum to better compare with experimental UV/Vis spectrum.

In Figure 18, it is evident that the three visible experimental peaks can be associated with the simulated ground state absorption to the bright S_2 state, and the simulated fluorescence of the $S_1(\mathbf{R}_{LE})$ and $S_1(\mathbf{R}_{TICT})$ structures, similar to the assignments produced by other electronic structure methods (Appendix, A.8). When an absolute shift is applied to the DFT/MRCI(2) absorbance and fluorescence energies, the relative energies of the ground state and $S_1(\mathbf{R}_{TICT})$ energies compare well to the first and third bands in experiment, but the $S_1(\mathbf{R}_{LE})$ peak is relatively blue shifted (higher in energy, eV) compared to the

second band in experiment. Therefore, DFT/MRCI(2) is able to qualitatively identify the relative energies of the $S_0(\mathbf{R}_{FC})$ absorption, $S_1(\mathbf{R}_{LE})$ and $S_1(\mathbf{R}_{TICT})$ emissions, except in the case of the $S_1(\mathbf{R}_{LE})$ structure which is slightly shifted such that it is calculated to have a higher relative absorbance energy than expected (which necessitates a higher fluorescing energy in eV in Figure 18). The electronic character of the $S_1(\mathbf{R}_{LE})$ structure is defined by several weakly contributing configuration state functions (CSFs) (see Fig 7), so this is indicative of the method slightly struggling to describe the necessary static correlation for this excited state minimum structure. The nature of the shifts applied here assume that the relative description of the ground state and $S_1(\mathbf{R}_{TICT})$ structures are correct, and the relative description of the $S_1(\mathbf{R}_{LE})$ structure is incorrect, but the reverse may be true. However, it seems more likely that DFT/MRCI(2) is struggling to describe the electronic character of the $S_1(\mathbf{R}_{LE})$ structure, since it requires a more complex description than the ground state of DMABN, and the $S_1(\mathbf{R}_{TICT})$ structure, which is described by a simple HOMO to LUMO transition from S_0 to S_1.

When comparing the spectrum simulated with DFT/MRCI(2) to the experimental UV/Vis spectrum, it is inconclusive whether the two-state kinetic model is apt at describing the excited state dynamics of DMABN. The fluorescence bands attributed to the $S_1(\mathbf{R}_{\pi\sigma*})$ and $S_1(\mathbf{R}_{TICT})$ structures overlap, so a definitive accounting of the excited state dynamics of DMABN is not possible on the basis of static absorption spectroscopy alone. More excited state spectroscopies are necessary to prove the validity of the two-state model, specifically spectroscopic methods that are dependent on changes in the electronic and nuclear character of the states being studied, which are simulated with increasing complexity in subsequent chapters.

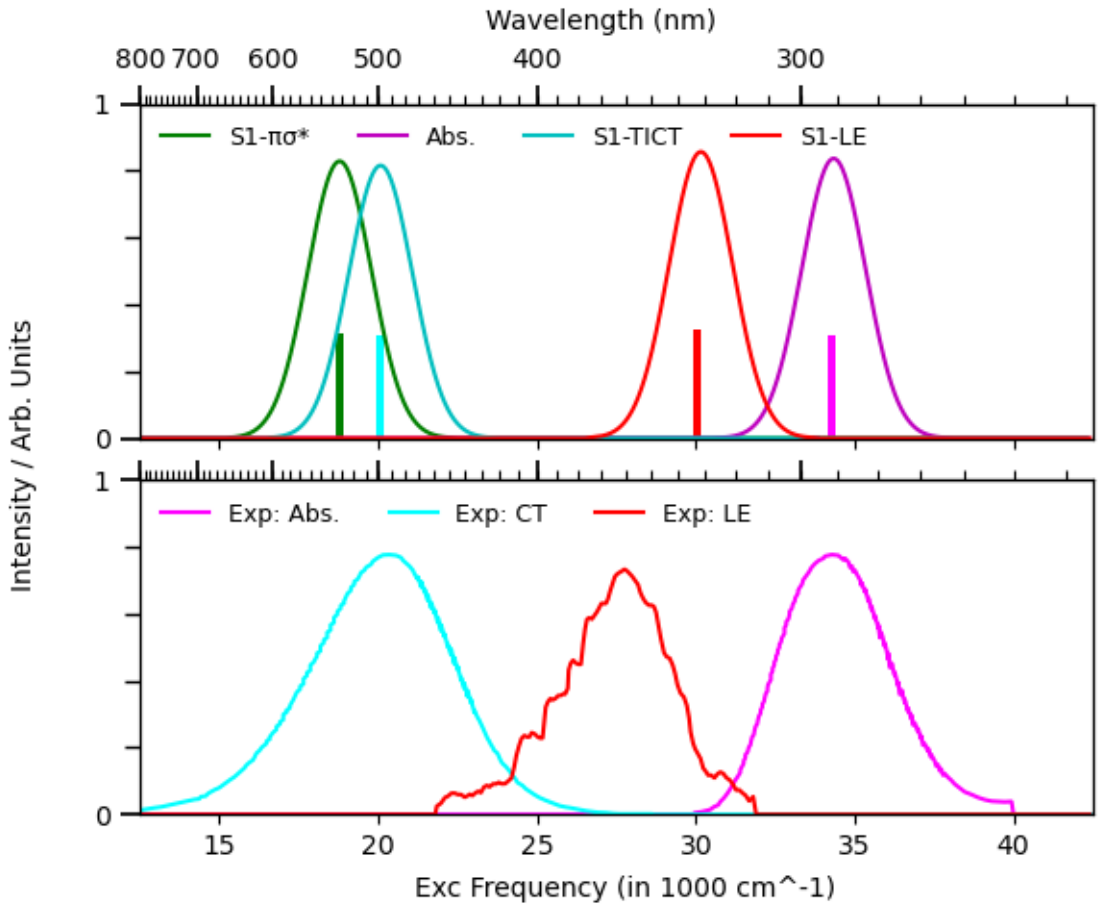

Figure 18: UV/Vis absorption spectrum of DMABN in Acetonitrile. Top: Spectrum computed with DFT/MRCI(2). Bottom: Experimental spectrum.[9] The following oscillator strengths were altered for better visibility: $S_1(\mathbf{R}_{TICT})$(Osc Str x400), $S_1(\mathbf{R}_{LE})$(Osc Str x35), $S_1(\mathbf{R}_{\pi\sigma*})$ (Osc Str x6500), Exp-LE(Osc Str x25). A final shift of -0.27 eV was applied to all excitation energies obtained with DFT/MRCI(2) (or alternatively, the absolute energy of the $S_0(\mathbf{R}_{GS})$ structure was increased by 0.27 eV), to better match with experiment (however even after this shift, there exists a slight discrepancy between the experimental and simulated energies for the $S_1(\mathbf{R}_{LE})$ structure.

3.2 Transient Absorption Spectroscopy: Simulation and interpretation

There have been two key studies that have performed transient absorption spectroscopy on DMABN and have yielded entirely different models of charge transfer formation, based on their separate interpretations of their respective spectra. The first spectrum, proposed by Druzhinin et al.[9] was interpreted in a way similar to the two-state model; it assumed that the transient excited state signals were attributed to the $S_1(R_{LE})$ and $S_1(\mathbf{R}_{TICT})$ structures.[9,85] The second, proposed by Coto et al., was interpreted to assume that the $S_1(R_{pTICT})$ and $S_1(\mathbf{R}_{\pi\sigma*})$ structures represented excited state minima that are populated after initial absorption.[10] The setup of the two studies is similar; both induce charge transfer by studying the molecule in a polar solvent (acetonitrile), and with slightly different pump wavelengths used to initially excite the molecule (290 nm[9,85] vs 267 nm,[10] the former choice of wavelength allowing for easier population of the S_2 adiabatic state due to being higher in energy).[9,10,85] The Coto et al. study probes the sample using a white light continuum (WLC) of 330-750 nm, while the Druzhinin et al. study uses a WLC of 260-1040 nm, and both proceed to probe the molecule at short and long timescales, from 0.2 to 24.5 ps and to 64 ps respectively.[9,10,85] The Coto et al. study measures the excited state dynamics at more frequent intervals, while the Druzhinin et al. study uses a broader white light continuum probe pulse to measure a longer range of excited state absorption signals.[9,10,85] Overall, the setup of the two studies is similar, and the transient absorption spectrum have similar time evolutions of their excited state signals.[9,10,85]

The experiment by Druzhinin et al. explicitly accounts for the effects of stimulated emission via the subtraction of the previously mentioned reference spectrum obtained by experimental UV/Vis spectrum (Fig 18).[190,191] Assuming a model where the $S_1(\mathbf{R}_{LE})$ structure is populated first, followed by the $S_1(\mathbf{R}_{TICT})$ structure, Druzhinin et al. subtracts the simulated emission from the transient absorption spectrum by estimating the time resolution

of the two peaks attributed to the structures based on the dielectric solvent relaxation times of the solvent. In other words, Druzhinin et al. predicts that at low timescales the fluorescent band attributed to the $S_1(\mathbf{R}_{LE})$ structure dominates, and subtracts intensity from the transient absorption spectrum at the location where this fluorescent band is located in the UV/Vis spectrum. The intensity of the emission band being subtracted at each point in time is based partly on the gas phase UV/Vis spectrum, which slowly decreases in intensity as the population is converted from the $S_1(\mathbf{R}_{LE})$ structure to the $S_1(\mathbf{R}_{TICT})$ structure. Druzhinin et al. at each point in time also subtracts a stimulated emission component related to the fluorescing band in the UV/Vis spectrum attributed to the $S_1(\mathbf{R}_{TICT})$ structure, where the intensity of this subtraction starts out small, but gets progressively larger as it is assumed that there is a conversion from the $S_1(\mathbf{R}_{LE})$ structure to the $S_1(\mathbf{R}_{TICT})$ structure, where the maximum intensity is dictated by the intensity of the second fluorescing band in the UV/Vis spectrum (Fig 18).[190,191] For DMABN, it is necessary to account for stimulated emission in order to obtain the excited state absorption spectrum; there is a significant difference between the transient absorption and excited state absorption spectrum if the contribution of stimulated emission is non negligible.[9,190,191] For this reason, simulated results are compared solely to the results of Druzhinin et al., since the excited state absorption spectrum computed by *ab initio* electronic structure methods inherently will not reproduce stimulated emission contributions.[190,191] As for other components which contribute to the transient absorption spectrum of DMABN, such as the ground state bleach signals, these lie mostly outside of the wavelength range of interest (<300 nm), and do not significantly interfere with resolution of the excited state signals attributed to each excited state structure.

The electronic structure method used to estimate the excited state absorption (ESA) spectrum in this thesis is the aforementioned DFT/MRCI(2) that was used to estimate the static UV/Vis spectrum in an earlier section. To compare directly with experimental results by Druzhinin et al,[9] the excited state absorption spectra of DMABN are simulated using an implicit solvent model with a dielectric constant set to that of acetonitrile in Fig 19, for

each of the excited state structures mentioned previously that constitute a minima on S_1. The spectrum are convoluted with a Gaussian using a 6.00 nm full width half maximum, computed using the implementation of DFT/MRCI(2) in GRaCI.[154] To compare against the experimental ESA spectrum, we will measure against excited state signals attributed to early timescales ($S_1(\mathbf{R}_{LE})$ structure), and excited state signals attributed to late timescales ($S_1(\mathbf{R}_{TICT})$ structure). That way, signals computed using DFT/MRCI(2) can be directly compared against experimental excited state signals with the relative populations of the two structures being neglected. Additional spectra taken in the gas phase, including $S_1(R_{pTICT})$ and $S_2(\mathbf{R}_{PICT})$ contributions, can be found in the Appendix (A.8) along with additional NTOs detailing the character of the excited state absorptions simulated here (A.9).

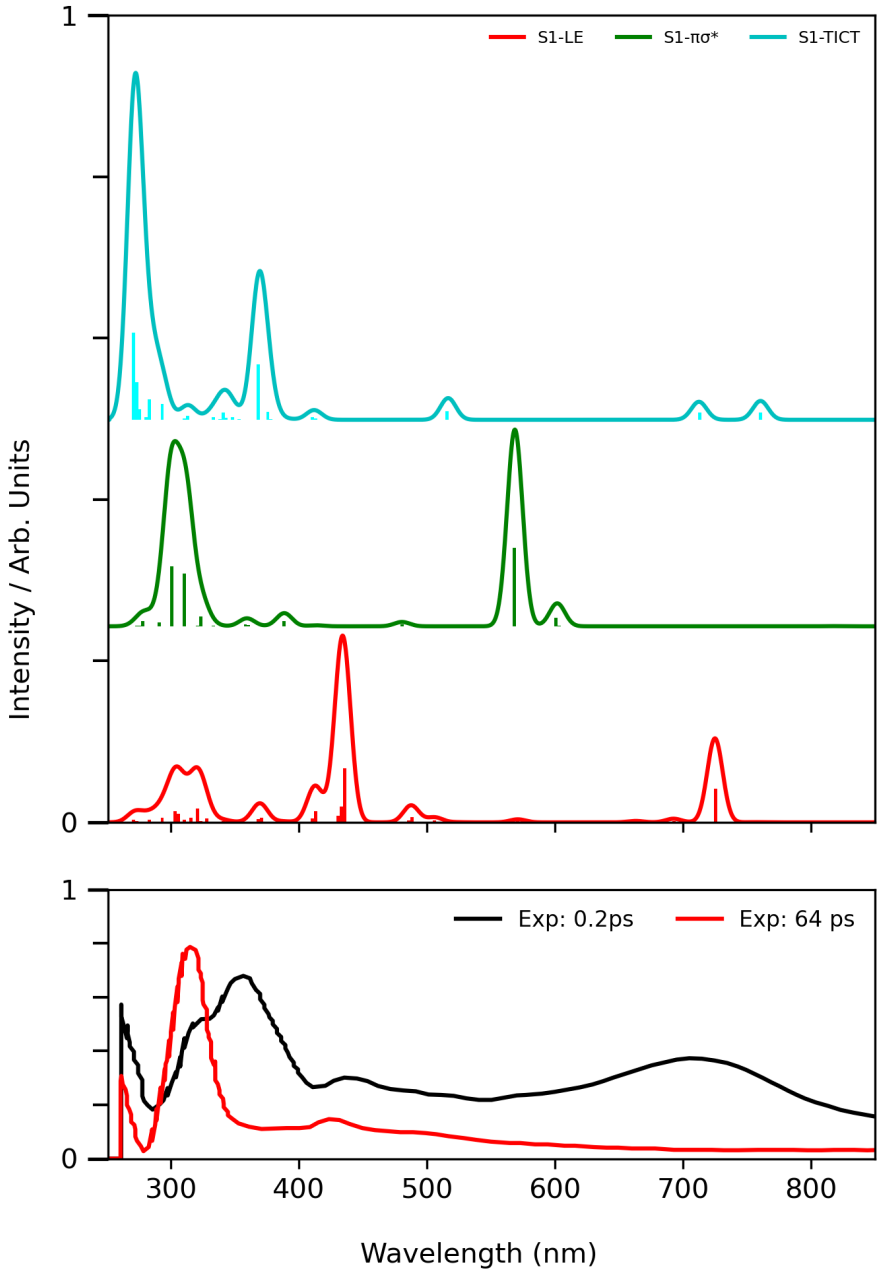

Figure 19: Excited state absorption spectrum of DMABN in acetonitrile. Top: Spectrum computed with DFT/MRCI(2). Bottom: Experimental excited state absorption spectrum,[9] The following osc strengths were altered for better visibility: $S_1(\mathbf{R}_{TICT})$(Osc Str x2), $S_1(\mathbf{R}_{LE})$(Osc Str x2)

The experimental excited state absorption (ESA) spectrum provided by Druzhinin et al. indicates the presence of two main peaks observed at early (0.2 ps) timescales, and one peak observed at late (64 ps) timescales. The first of these three peaks is in the high wavelength region (450 to 700 nm); the peak in the simulated spectrum (725 nm) can be assigned to a major ESA signal at 710 nm, associated with absorptions from the $S_1(\mathbf{R}_{LE})$ structure. Therefore the simulated spectrum interprets the Druzhinin et al. spectrum to be detecting a large amount of $S_1(\mathbf{R}_{LE})$ population at early timescales. The character of this excitation is from one of the partially occupied molecular orbitals at the $S_1(\mathbf{R}_{LE})$ structure to another partially occupied molecular orbital, and its breadth in experiment is likely due to the shallow well that the $S_1(\mathbf{R}_{LE})$ structure represents (see Chapter 2), as well as the multiconfigurational character of the $S_1(\mathbf{R}_{LE})$ structure. Simulated ESA spectra of the $S_1(\mathbf{R}_{\pi\sigma*})$ structure indicate that were the $S_1(\mathbf{R}_{\pi\sigma*})$ structure to be populated, it would be expected that a signal in the 500-550 nm region would exist in the experimental spectrum. At early and at late timescales, Druzhinin et al. does not detect an ESA signal in this region, so it is unlikely that the $S_1(\mathbf{R}_{\pi\sigma*})$ structure is being populated in this experiment at either early or late timescales. The character of this excited state absorption is localized at the cyano nitrogen, which is singly occupied at the $S_1(R_{\pi\sigma*})$ structure. Therefore, it makes sense why there is a low likelihood of this state being accessed from the $S_1(R_{LE})$ or $S_1(R_{TICT})$ states, since they do not share this single occupation. In the 300-400 nm region there exist two experimental signals, at 355 nm and 315 nm (at early and late timescales respectively). Simulated ESA of the excited states of interest predict an analogous set of signals at 435 nm and 369 nm, associated with excited state absorptions from the $S_1(\mathbf{R}_{LE})$ and $S_1(\mathbf{R}_{TICT})$ structures in the simulated spectra. This assignment is consistent with the characterization of the experimental peak at 710 nm to an absorption from the $S_1(\mathbf{R}_{LE})$ structure, and would indicate that since the only two structures that are populated are the $S_1(\mathbf{R}_{LE})$ and $S_1(\mathbf{R}_{TICT})$ structures, the two-state model is necessary to describe the excited state dynamics of DMABN. The character of the excitation of the $S_1(\mathbf{R}_{LE})$ structure is

very similar to the earlier excitation at 725 nm, but possesses some Rydberg character. The character of the excitation of the $S_1(\mathbf{R}_{TICT})$ structure on the other hand is difficult to interpret, as it fully represents an excitation to a Rydberg molecular orbital.

A sizeable shift is present when comparing the results of DFT/MRCI(2) to the experimental data at lower wavelengths, yet the qualitative nature of the experimental ESA spectrum is still recreated by simulation. This shift is expected; as previously demonstrated (Chapter 3.1), DFT/MRCI(2) like other *ab initio* electronic structure methods experiences a small shift of about 0.5 eV or less, compared to vertical excitation energies determined from experimental spectroscopies (Appendix, A.1). There is a mismatch in oscillator strengths when comparing simulated data to experimental spectrum; the simulated peaks at 725 nm and at 435 nm have similar oscillator strengths to their experimental equivalents at 710 nm and 435 nm, however the simulated peak at 315 nm is weaker than expected when compared to its experimental equivalent at 369 nm. This is due to the fact that the $S_1(\mathbf{R}_{LE})$ structure will represent a shallow minimum on S_1 (see LIICs in Chapter 2), leading to broad signals for absorptions and for emissions in experiment, that are not seen in these simulations which only study one optimized geometry. If several geometries similar to the $S_1(\mathbf{R}_{LE})$ excited state minimum were included in the calculation of the ESA spectrum with varying weights according to the shallowness of the LE minimum, calculations would better match with experimental spectrum for this state. Therefore, in experiment, $S_1(\mathbf{R}_{TICT})$ peaks will have higher oscillator strengths than broad peaks attributed to the $S_1(\mathbf{R}_{LE})$ state (as seen in the spectrum by Druzhinin et al), but in the simulated spectra in Fig 19, it appears as if excited state absorptions from the $S_1(\mathbf{R}_{LE})$ structure have stronger oscillator strengths than excited state absorptions from the $S_1(\mathbf{R}_{TICT})$ structure.

In summary, evaluating the excited state absorptions of DMABN in comparison to experiment solidifies that the role of the $S_1(\mathbf{R}_{\pi\sigma*})$ structure is minimal, and that the principal mechanism for charge transfer in DMABN must be through the transition barrier separating the $S_1(\mathbf{R}_{LE})$ and $S_1(\mathbf{R}_{TICT})$ structures.

4 Gas Phase Time-Resolved Photoelectron Spectroscopy

Time-resolved photoelectron spectroscopy (TRPES) is an experimental technique in which the ionization of valence electrons via femtosecond pulses is used to probe the time-evolution of molecular wave packets.[86,92] Changes in the electronic and nuclear character of a molecular wavepacket leads to differences in their ionization cross-sections and vertical ionization potentials, leading to different kinetic energies of ejected electrons.[86,92] Since ionization processes cannot be forbidden by a mismatch of the symmetries of the initial and final excited states like absorption processes, TRPES does not suffer from low cross-sections due to symmetry forbidden transitions.[86,92] Therefore, TRPES is aptly suited to study DMABN and DIABN in the gas phase, both being systems with large amplitude motion in their respective proposed charge transfer processes, and with proposed excited state structures that differ greatly in electronic and nuclear character.

As shown in Chapter 2 it is expected under the two-state model that the charge transfer process ($S_1(\mathbf{R}_{LE}) \rightarrow S_1(\mathbf{R}_{TICT})$) is favourable in DIABN and not DMABN. If the two states have significantly different electronic character, two separate signals would be expected in the TRPES spectrum of DIABN corresponding to the LE and TICT states, and one signal is expected in the TRPES spectrum of DMABN corresponding to the LE state. If the contribution of the $S_1(\mathbf{R}_{\pi\sigma*})$ structure is significant, than a signal attributed with the structure could also be present. In 2004, a series of unpublished TRPES spectra were taken

of both DMABN and DIABN.[192] These spectra were conducted with varying pump (260-325 nm)and probe (200 nm) wavelengths, and the excited state dynamics of the molecules were monitored over ∼20 ps. In this section, these experimental spectra will be directly compared with a set of static simulated valence photoelectron spectra to establish whether the signals present in the experimental spectra can be associated with certain excited state emissions. Furthermore, the time constants estimated using RRKM in Chapter 2 with respect to DMABN and DIABN allow for the derivation of simulated TRPES spectrum, which will also be compared to experimental TRPES spectra.

Fig 20 shows a summary of the experimental TRPES studies conducted on DMABN and DIABN. The most notable result in these spectrum can be found in Figure 20b; for DIABN there are two distinct signals at about 2.2 eV and 1.8 eV, that are directly correlated (as one rises, the other falls at a proportional rate). The presence of two distinct signals that occur at least 3 ps apart implies the presence of a transition barrier. Earlier in this work, the role of the $S_2(\mathbf{R}_{PICT})$ structure in facilitating the method of internal conversion from the S_2 to S_1 adiabatic states was considered. This decay is a barrierless one (Fig 6), and therefore the $S_2(\mathbf{R}_{PICT})$ structure is not expected to have a long lived signal in time resolved spectroscopies, meaning the decay from the $S_2(\mathbf{R}_{PICT})$ to $S_1(\mathbf{R}_{LE})$ structures would not be the cause of the 3 ps delay before the second signal in Fig 20b. Based on the *ab initio* calculations performed so far (Chapter 2), these signals can only be attributed to either the $S_1(\mathbf{R}_{LE})$ and $S_1(\mathbf{R}_{\pi\sigma*})$ structures, or the $S_1(\mathbf{R}_{LE})$ and $S_1(\mathbf{R}_{TICT})$ structures. This is because in the previous analysis, it is only these two choices of two structures that involve a transition state barrier of some kind consistent with the resolution between the two signals shown in the TRPES spectrum of DIABN. Similar to DMABN, the $S_1(\mathbf{R}_{LE}) \rightarrow S_1(\mathbf{R}_{\pi\sigma*})$ pathway and the $S_1(\mathbf{R}_{LE}) \rightarrow S_1(\mathbf{R}_{TICT})$ pathway are both theoretically possible for DIABN due to the presence of small transition state barriers predicted by DFT/MRCI(2) (see Appendix, A.10, and Chapter 2.2). However, DMABN does not reveal two separate signals, and therefore its single signal can be associated with the $S_1(\mathbf{R}_{LE})$ structure. The

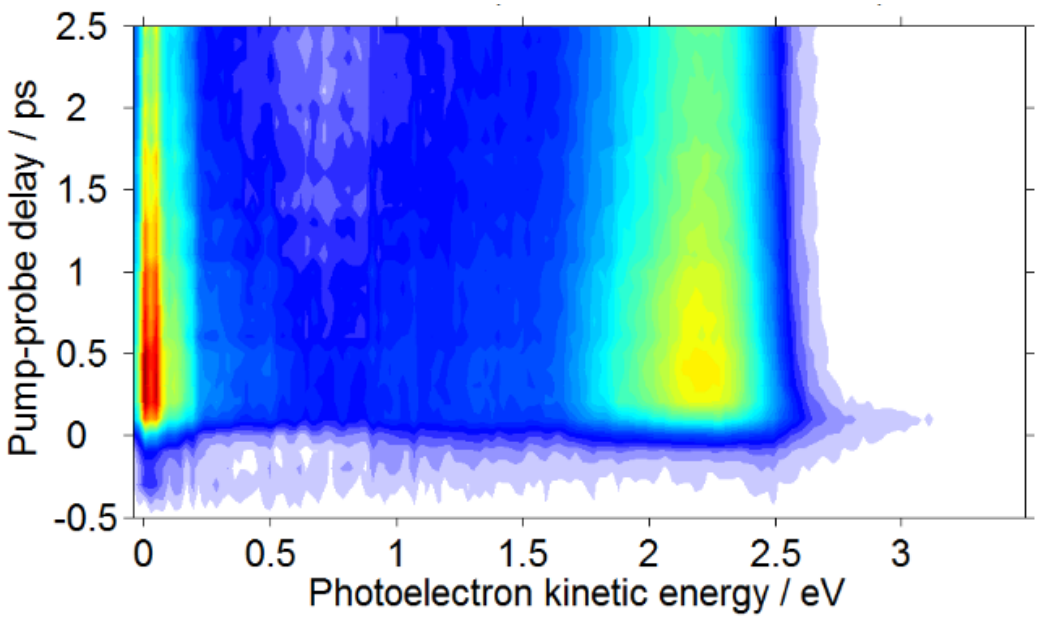

(a) DMABN

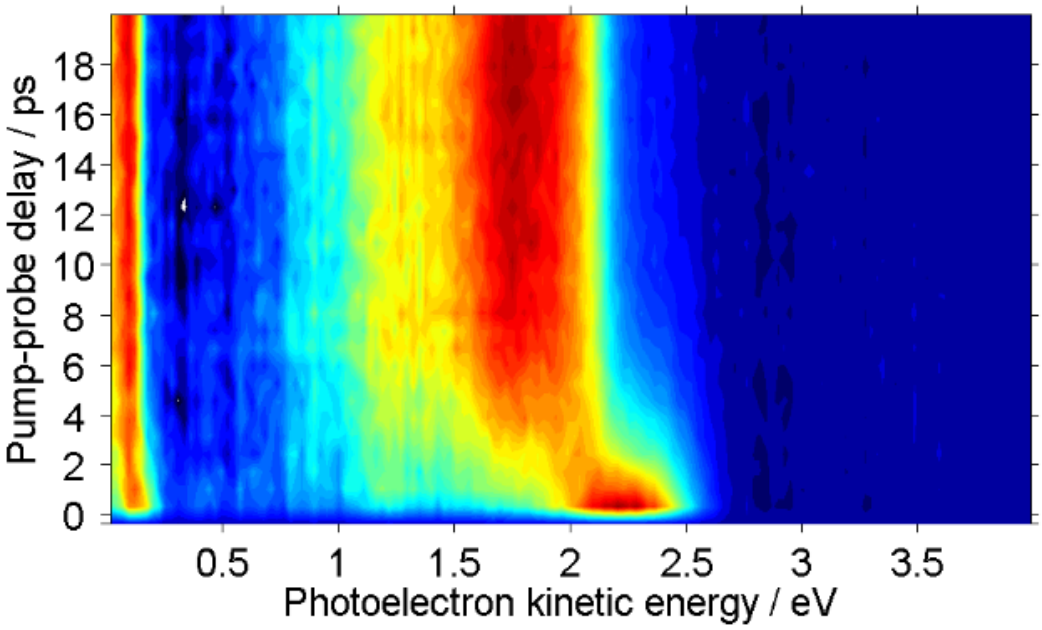

(b) DIABN

Figure 20: Experimental TRPES spectrum of DMABN and DIABN in the gas phase.

first excited state occupied on S_1 for DMABN and its derivatives has unambiguously been determined to be the $S_1(\mathbf{R}_{LE})$ structure by this work (see Chapter 2) as well as other theoretical studies on the molecule,[7,8,13] and as of yet there is no discovered mechanism by which the $S_1(\mathbf{R}_{\pi\sigma*})$ structure or the $S_1(\mathbf{R}_{TICT})$ structure can be populated directly after ground state absorption to the $S_2(\mathbf{R}_{PICT})$ structure.

In Chapter 2, the transition-state barrier between the $S_1(\mathbf{R}_{LE})$ and $S_1(\mathbf{R}_{TICT})$ structures was quantified and the structure of the transition state was characterized. By using DFT/MRCI(2) to compute excited state energies on top of CASPT2 excited state minimum structures, no shift was necessary to correlate the rise time of the charge transfer signal of DIABN in the gas phase, to the experimental rise time of the second excited state signal of DIABN in Fig 20. In Chapter 2, the rise time of the charge transfer state for DIABN was predicted to be 2.8 ps, and experimental data in Fig 20 see the rise of the second signal in around 3 ps. Furthermore, in DMABN, due to the size of the transition state barrier, the excited state energies provided by DFT/MRCI(2) suggested that charge transfer would not occur for DMABN in the gas phase. This is also consistent with the experimental data in Fig 20 that only sees the existence of one persistent signal (presumably attributed to the $S_1(\mathbf{R}_{LE})$ structure). The correlation of computed RRKM decay/rise times to experimental decay/rise times indicate that DFT/MRCI(2) under the two-state model is providing the best descriptor of the transition states of DMABN and DIABN. Since the transition states were explicitly optimized with CASPT2, this implies that the transition between the $S_1(\mathbf{R}_{LE})$ and $S_1(\mathbf{R}_{TICT})$ structures is not happening in multiple steps, but the de-pyramidalization and twisting of the dimethylamino group are both actions that happen simultaneously (see Chapter 2.2). To confirm that the previous assignment of the transient signals in the experimental spectrum is correct, simulated TRPES spectra (Fig 21) for both molecules are predicted based on the aforementioned charge transfer rise times determined in Chapter 2, and static valence photoelectron spectrum for the $S_1(\mathbf{R}_{LE})$ and $S_1(\mathbf{R}_{TICT})$ structures computed using DFT/MRCI(2). To clarify, these are not on-the-fly dynamical simulations, but

are an extrapolation of time independent photoelectron spectrum at several excited state structures of DMABN and DIABN, based on the rise and decay of the charge transfer state estimated in Chapter 2 using RRKM determined from the height of the transition state barrier found using DFT/MRCI(2). Static valence photoelectron spectrum were computed, and according to the rise/decay times computed in Chapter 2, the signals attributed to the $S_1(\mathbf{R}_{LE})$ structure were gradually scaled down, and the signals attributed to the $S_1(\mathbf{R}_{TICT})$ structure were gradually scaled upwards from 0. The decay time of the $S_2(\mathbf{R}_{PICT})$ structure and the rise time of the $S_1(\mathbf{R}_{LE})$ structure was also considered, assumed to be about 50 fs[34,72,81] To analyze these time resolved spectra in more detail, the static valence photoelectron spectrum that are the basis for Fig 21 must be evaluated individually, and by structure.

Static valence photoelectron spectra of DMABN, DIABN, and ABN were taken at the $S_1(\mathbf{R}_{LE})$, $S_1(\mathbf{R}_{TICT})$, and $S_1(\mathbf{R}_{\pi\sigma*})$ structures, convoluted with a Gaussian using a 0.10 eV full width half maximum to match with the bandwidth of the previously discussed experimental TRPES signals. Although ABN does not have experimental TRPES data that accompanies this spectrum, the static valence photoelectron spectrum of the molecule were still included to round out this study (See Appendix, A.11). To better compare these results to experimental data, a similar pump-probe setup to those used in other studies has been adopted, such that the binding energies of the electrons returned by GRaCI have been converted to the kinetic energies of the electrons after the photoemission.[88,89] To do this, the kinetic energy of the electron is estimated by subtracting the absorption energy of the excited state of interest and the returned binding energies, from the sum of the pump and probe energies, leading to the images in Fig 22.

Note that because simulated methods tend to overestimate the excitation energies of the $S_1(\mathbf{R}_{LE})$ and $S_1(\mathbf{R}_{TICT})$ structures (Appendix, A.1), the wavelengths in Figure 20 cannot be used to solve for the kinetic energies in Figure 22. For instance, a pump photon of 277 nm is not sufficiently energetic to access S_2 in DMABN according to DFT/MRCI(2) and

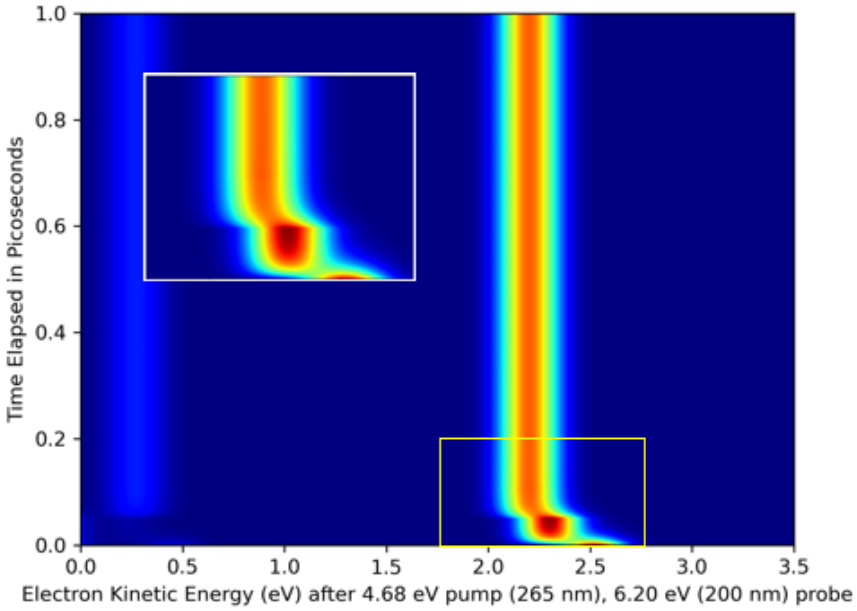

(a) DMABN. Inset: Early excited state dynamics, $S_0(\mathbf{R}_{Min}) \rightarrow S_2(\mathbf{R}_{PICT}) \rightarrow S_1(\mathbf{R}_{LE})$. Main figure: Persistent excited state signal, $S_1(\mathbf{R}_{LE})$.

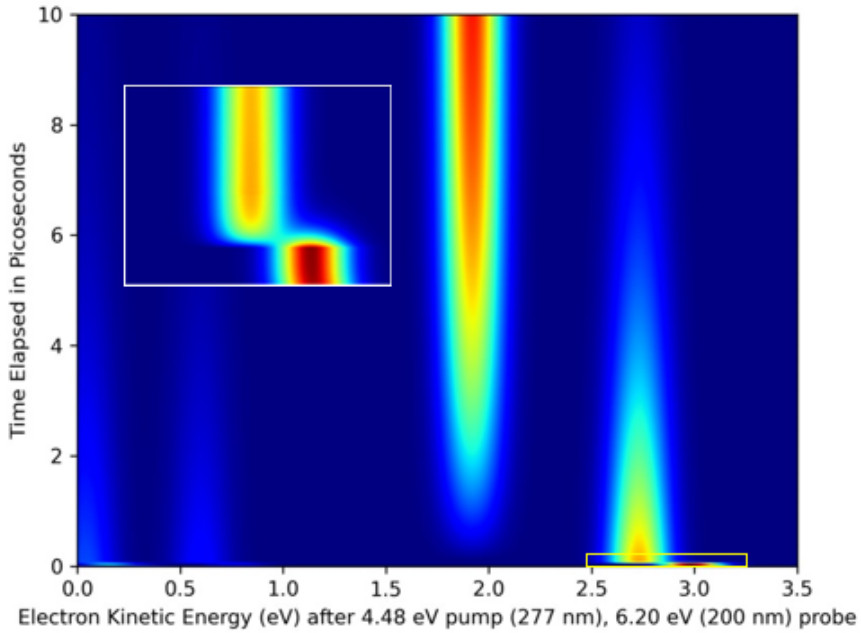

(b) DIABN. Inset: Early excited state dynamics, $S_0(\mathbf{R}_{Min}) \rightarrow S_1(\mathbf{R}_{LE})$. Main figure: Persistent excited state signal, $S_1(\mathbf{R}_{LE}) \rightarrow S_1(\mathbf{R}_{TICT})$.

Figure 21: Simulated TRPES spectrum, based on transition-state barriers and static photoelectron spectrum predicted by DFT/MRCI(2) (Table 1 and Fig 22)

CASPT2, but it is sufficient according to the experimental data available which detects fluorescence from excited state minimum, implying that S_2 has been accessed by ground state absorption (Fig 20). Therefore, to make sure that the static valence photoelectron spectra are directly comparable to the experimental TRPES spectrum, a series of shifts were applied. Assuming the same pump and probe energies as the analogous experimental TRPES spectrum (DMABN and DIABN), for each valence photoelectron spectrum it is assumed that the S_0 to S_2 barrier can be overcome, even if the pump energy of the experimental spectrum is less than the calculated S_0 to S_2 absorption energy. Next, a shift of -0.5 to -0.8 eV, is applied to each spectrum in Figure 22, to better match the results there with Figure 20. To be specific, for the TRPES spectrum attributed to DMABN, the sole non transient peak is matched in location to the simulated peak attributed to the $S_1(\mathbf{R}_{LE})$ structure in Figure 22 using a -0.8 eV shift applied to all signals in Figure 22. Likewise for DIABN, a shift of -0.5 eV is applied to all signals in order to match the simulated $S_1(\mathbf{R}_{LE})$ structure emission to the rightmost non transient peak in the experimental TRPES spectrum for DIABN. In Figure 22, the intensity of each ionization channel is represented by Dyson Norms, which are the norms of dyson orbitals representing overlaps of the wavefunction of the initial state and the final ionized state.[158,193] Note that the Dyson Norms in Figure 22 have not been modified, pointing to one of the advantages of TRPES over other forms of spectroscopy, as the $S_1(\mathbf{R}_{TICT})$ structure is predicted to be just as likely to be ionized compared to the other excited states according to DFT/MRCI(2), allowing the population of all excited states to be measurable in a time resolved study. Finally, equivalent spectrum to Fig 22, taken in acetonitrile, can be found in the Appendix, along with dyson orbitals describing each major excitation (A.12).

The spectra in Fig 22 across the analogues evaluated are simple to interpret; there exists one high intensity emission from each excited state structure on S_1. Furthermore, the character of each excitation is straightforward. The lowest energy excitation from the $S_1(\mathbf{R}_{LE})$ structure corresponds to an ejection of an electron from the LUMO ground state orbital,

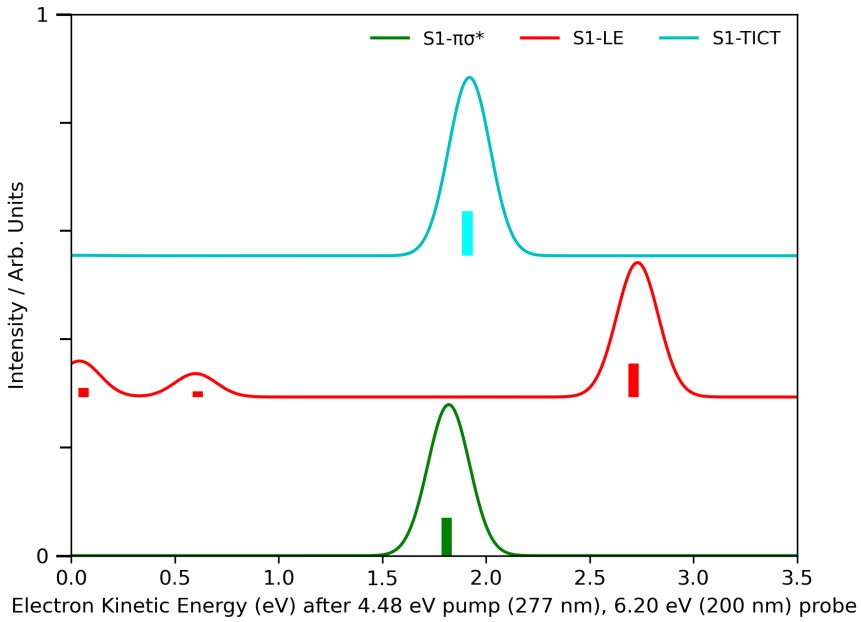

(a) DIABN (Shifted by -0.5 eV)

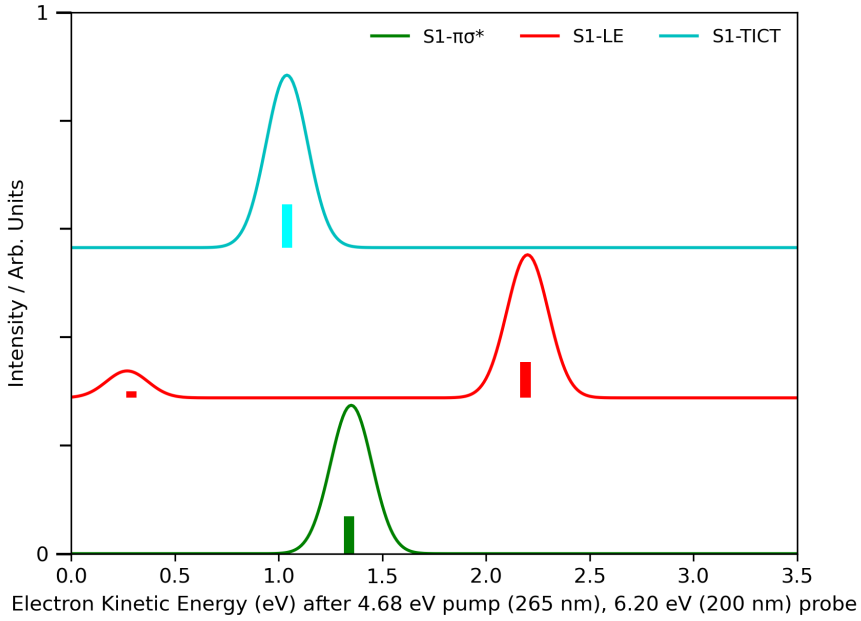

(b) DMABN (Shifted by -0.8 eV)

Figure 22: Simulated valence photoelectron spectrum of the excited states of DMABN and its analogues with DFT/MRCI(2) in the gas phase.

and the lowest energy excitation from the $S_1(\mathbf{R}_{TICT})$ state corresponds to ejection from the LUMO+1 ground state orbital (see Fig 4). Immediately, the difference in electronic character is apparent; the former dictates that an electron is ejected from within the benzene ring, and the latter dictates that an electron is ejected from a delocalized orbital not exclusively in the benzene ring. These are the orbitals that see an increase in occupation at S_1 compared to S_0, so it is intuitive that electrons from these orbitals are those which electrons are ejected from after the initial pulse is applied (see Fig 10). The $S_1(\mathbf{R}_{\pi\sigma*})$ structure sees excitation from a σ^* orbital, befitting the name.

The static spectra in Fig 22 are useful in identifying the source of the two excited state signals found with DIABN in the experimental TRPES study conducted (Fig 20b). The energy gap between the LE and TICT valence photoelectron peaks computed by DFT/MRCI(2) is about 0.7 eV (Fig 22a and Fig 21), which is close to the 0.4 eV energy gap between the two excited state signals attributed to the $S_1(\mathbf{R}_{LE})$ and $S_1(\mathbf{R}_{TICT})$ structures in the experimental TRPES spectrum. The cause of this discrepancy is similar to the slight +0.3 eV rightward shift attributed to the fluorescing energy of the $S_1(\mathbf{R}_{LE})$ structure in the UV/Vis spectrum (i.e., the absolute energy of the $S_1(\mathbf{R}_{LE})$ structure is overestimated, see Chapter 3). The $S_1(\mathbf{R}_{\pi\sigma*})$ signals unfortunately lie at a similar kinetic energy to the signals attributed to the $S_1(\mathbf{R}_{TICT})$ structure, meaning that the two-state model cannot be conclusively proven using TRPES. From an electronic structure perspective, the transition-state barrier between the $S_1(\mathbf{R}_{LE})$ and $S_1(\mathbf{R}_{\pi\sigma*})$ structures for DIABN is estimated to be similar in size to that of DMABN (see Appendix, A.10 and Chapter 2.3), while the transition barrier between the $S_1(\mathbf{R}_{LE})$ and $S_1(\mathbf{R}_{TICT})$ structures is smaller for DIABN than is its equivalent barrier for DMABN (See Chapter 2.2). The two-state model thus remains the most likely explanation for the experimental TRPES signals. However, the exact size of the transition-state barrier separating the $S_1(\mathbf{R}_{LE})$ and $S_1(\mathbf{R}_{\pi\sigma*})$ structures could not be ascertained due to a lack of successful transition state optimizations, so it remains unclear whether or not the $S_1(\mathbf{R}_{LE})$ $\rightarrow S_1(\mathbf{R}_{\pi\sigma*})$ process is competing with the charge transfer process.

Overall, by comparing experimental TRPES, and simulating new TRPES with *ab initio* electronic structure methods, some uncertainty persists regarding the two-state model. The overlap of signals attributed to the $S_1(\mathbf{R}_{\pi\sigma*})$ and $S_1(\mathbf{R}_{TICT})$ structures means that one cannot unambiguously determine that charge transfer occurs in DIABN, and not DMABN. However, this is the most likely outcome, considering that the transition state analysis done previously indicates that the rate of charge transfer should significantly increase in DIABN compared to DMABN, as the size of the transition-state barrier between the $S_1(\mathbf{R}_{LE})$ and $S_1(\mathbf{R}_{TICT})$ structures is only overcome for DIABN in the gas phase. To determine unambiguously whether the two-state model is a valid model that explains the excited state dynamics of DMABN, spectroscopies are required which separate the signals attributed to the $S_1(\mathbf{R}_{LE})$, $S_1(\mathbf{R}_{\pi\sigma*})$ and $S_1(\mathbf{R}_{TICT})$ structures individually.

5 Proposals for the Application of X-ray Spectroscopy to DMABN and other charge transfer systems

In the previous section, it was possible to resolve the $S_1(\mathbf{R}_{LE})$ and $S_1(\mathbf{R}_{TICT})$ structures of DMABN, DIABN, and ABN using TRPES spectroscopy. A definitive characterization of the excited state dynamics via spectroscopy, however, will likely require a multi-modal approach, since it is unlikely a single method will be able to differentiate between all the possible dynamical pathways. Indeed, simulation predicts that TRPES will not be able to resolve the $S_1(\mathbf{R}_{\pi\sigma*})$ and $S_1(\mathbf{R}_{TICT})$ channels as the predicted spectra from these structures strongly overlap such that is difficult to determine how much the $S_1(\mathbf{R}_{\pi\sigma*})$ structure is actually populated, and whether or not population of the state competes with the charge transfer process. Therefore, new spectroscopies are still necessary to evaluate the excited state dynamics of DMABN, such that in a time resolved study, independent signals attributed to all three states are distinguishable. Developments in the ability to generate femtosecond pulses of X-ray light, both at XFELs and in the laboratory, have enabled time resolved X-ray absorption and X-ray photoelectron (XAS/XPS) spectroscopies, along with their simulated equivalents

which have had their equivalent theoretical advances/developments.[112,123–129,131–136] In order to provide another metric by which to prove the two-state model and simultaneously measure the rate of potential $S_1(\mathbf{R}_{\pi\sigma*})$ and $S_1(\mathbf{R}_{TICT})$ formation, a series of simulated XAS and XPS spectroscopies were performed on DMABN. Using XAS/XPS, one can energetically resolve transitions involving different atoms, providing a local probe of electronic character, which may allow for signals attributed to different excited states to be better resolved compared to other excited state spectroscopies. The charge transfer process in DMABN has rarely been explored past the molecule's immediate structural derivatives like DIABN and ABN. In order to investigate the utility of these new X-ray spectroscopies, or motivate new time resolved experiments or simulations, a series of simulated spectroscopies over a range of DMABN-type molecules were conducted. By determining which derivatives have the most favourable charge transfer processes, and which derivatives have the best resolved signals attributed to the $S_1(\mathbf{R}_{TICT})$ structure, the most effective potential time resolved studies can be chosen. Nearly all of the DMABN-type compounds explored in the next sections have been evaluated experimentally,[13] and with minor deviations, all are likely to follow a similar set of excited state dynamics as per DMABN (excited state minimum optimizations have proven successful at the CASPT2 level for the $S_1(\mathbf{R}_{LE})$ and $S_1(\mathbf{R}_{TICT})$ structures for all structures analyzed in Chapter 5.

5.1 DMABN

5.1.1 X-ray Absorption Spectroscopy

Figure 23 shows a summary of X-ray absorption spectrum computed for relevant excited state structures of DMABN using DFT/MRCI(2) at the Carbon and Nitrogen K-Edges (that is to say, only including excitations from the 1s orbitals at Carbon and Nitrogen atoms of the molecule respectively). Extended spectra that include contributions from other excited states can be found in the Appendix (A.13). These spectra are trimmed past the core

ionization potential at each edge.[154] Significant particle NTOs for each of the major peaks in the spectrum are also included in the Appendix (A.13).[158] For the XAS/XPS spectrum conducted in this section, and the following sections, they are all convoluted with a Gaussian using a 0.30 eV full width half maximum, as is consistent with the approximate signal widths in previous simulated XAS/XPS studies.[194]

XAS spectrum simulated at the Carbon K-Edge (Figure 23a) indicate a large degree of overlap between excitations from the ground state minimum and the various excited state structures. In these cases, the excited state signals would not be visible in a time resolved experiment. Similar to transient absorption, a time resolved pump-probe XAS study will yield negative signals attributed to the ground state bleach.[195–197] At t = 0, a number of ground state molecules are excited to a valence electronic excited state by a pump pulse, and hence at any point t > 0, the amount of ground state molecules and signals associated with the ground state will be smaller than at t = 0.[195–197] Ground state XAS signals will also be very strong at t = 0, but at any point t > 0, the intensity of these signals will decrease and negative signals attributed to the ground state core excited states will be expected in a time resolved XAS study, and will bleach overlapping XAS signals attributed to excited state structures.[195–197] Excited state absorptions to the left of the spectrum are mostly from core electrons from carbons in the benzene ring, while further excitations from other carbons on the cyano group and the dimethylamino group exist to the right of the spectrum (determined from the NTOs of each core excitation, see Appendix (A.13)). Overall, most absorptions from excited state structures overlap with the ground state contributions, especially for absorptions from the $S_1(\mathbf{R}_{TICT})$ structure. For the $S_1(\mathbf{R}_{LE})$ and $S_1(\mathbf{R}_{\pi\sigma*})$ structures, there exist small tails in the 283-284 eV region which would not overlap with ground state absorptions, yet overlap with each other significantly. For the $S_1(\mathbf{R}_{LE})$ structure, this small tail is due to the existence of 3-4 partially occupied orbitals in its excited state description (See Fig 7), leading to absorptions that are low in probability, but that occur at lower energies in the spectrum. Conversely, absorptions from the $S_1(\mathbf{R}_{TICT})$ structure are close in

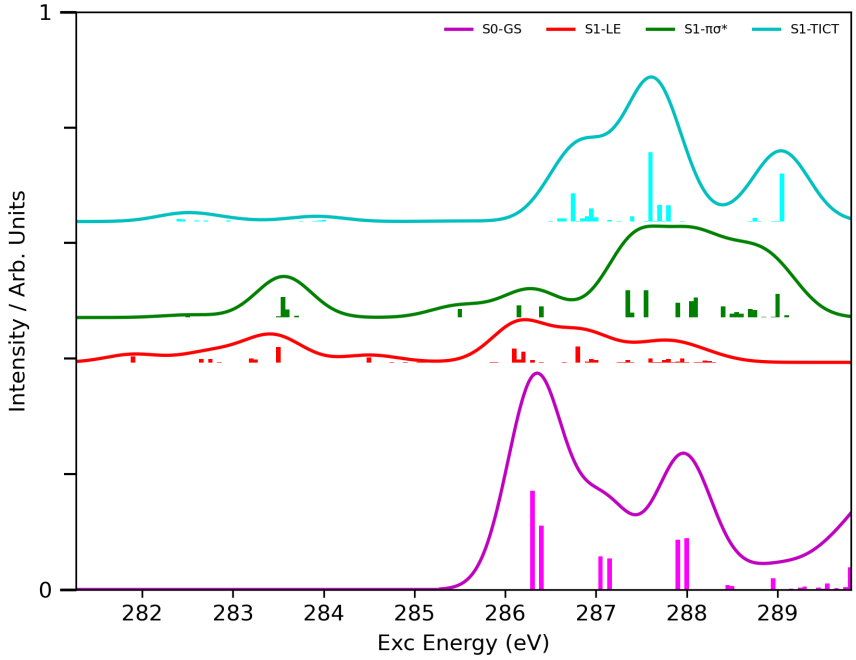

(a) Carbon K-Edge

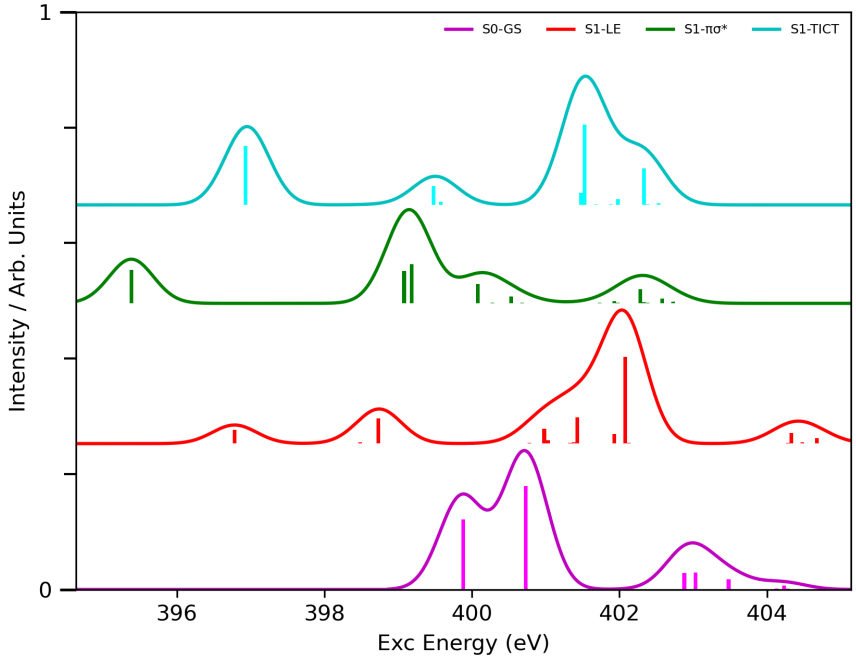

(b) Nitrogen K-Edge

Figure 23: Simulated X-ray absorption spectrum of DMABN with DFT/MRCI(2)

energy, and occur at higher energies in the spectrum due to the $S_1(\mathbf{R}_{TICT})$ structure being described by two higher lying singly occupied orbitals, which require more energy for a core electron to access, yet with a higher absorbing probability (Fig 9). The signals attributed to the $S_1(\mathbf{R}_{\pi\sigma*})$ structure weakly absorb due to the electronic character of the state at this structure. The $S_1(\mathbf{R}_{\pi\sigma*})$ structure possesses a singly occupied orbital centralized around the cyano group (Fig 10), but this makes the absorption probability for core electrons centralized on carbons in the benzene ring weak due to the inter-nuclear distance between the hole and particle orbitals. Only near the end of the spectrum (at high energy) do highly absorbing excitations occur from the $S_1(\mathbf{R}_{\pi\sigma*})$ structure, attributed to excitations from the carbon in the cyano group.

At the N K-Edge, (Figure 23b) the separation of the signals is significantly improved, this time all excitations from the excited state structures evaluated are distinct from the ground state absorptions. The $S_1(\mathbf{R}_{TICT})$ structure is well resolved owing to its first peak, which is attributed to an excitation from the nitrogen in the dimethylamino group to a localized molecular orbital centered around the same nitrogen. The $S_1(\mathbf{R}_{LE})$ structure is weakly resolved owing to its second peak, describing excitation into an orbital resembling the ground state HOMO (Fig 4) from the dimethylamino nitrogen core (the first peak describes the same excitation, except from the cyano nitrogen core). Finally, the $S_1(\mathbf{R}_{\pi\sigma*})$ structure is well resolved due to an early excitation to the singly occupied LUMO+3 ground state orbital, from an electron in the cyano nitrogen core. Overall, the N K-Edge spectrum of DMABN is particularly well suited to be evaluated over the course of a time resolved study; the two-state model used to analyze TICT formation in DMABN can been reinforced by directly measuring the rise and fall of the first $S_1(\mathbf{R}_{TICT})$ and $S_1(\mathbf{R}_{\pi\sigma*})$ excitations.

While experimental data does not exist for DMABN, recently XAS was applied at the Nitrogen K-Edge to the excited states of DMABN using EOM-CCSD, another *ab initio* electronic structure method.[114,126,132,194] When comparing the two spectrum, there is an absolute shift separating the results in this work by DFT/MRCI(2) and those evaluated with EOM-

CCSD. Specifically, the DFT/MRCI(2) results are left shifted by about -1.5 eV. The first calculated core absorptions from the ground state structure are at 399.8 eV or so, and the first excitations evaluated by Datar et al are at about 401.2 eV. Furthermore, DFT/MRCI(2) measures core absorptions attributed to the $S_1(\mathbf{R}_{LE})$ and $S_1(\mathbf{R}_{TICT})$ structures at 398.8 eV and 397.0 eV, which are shifted from their equivalent EOM-CCSD core absorptions at 400.7 eV and 398.9 eV (Note that DFT/MRCI(2) predicts an excitation attributed to the $S_1(\mathbf{R}_{LE})$ structure at 396.8 eV as well). As noted in Chapter 1.4.2 of this thesis, DFT/MRCI(2) is dependent on the use of Kohn Sham (KS) orbital energies to provide an approximation for the molecular orbital energies. This approximation is central to the compact nature of DFT/MRCI(2), but it is highly dependent on the functional used to initially generate the initial KS orbitals. For example, in a previous study that computed XAS spectra using DFT/MRCI(2), the BHLYP typically led to an absolute shift of about 3.2 eV compared to experimental core excited state energies, even if the relative placement of the energies matched well with the relative distance between experimental signals.[124] This absolute shift has been reduced in newer studies; owing to the use of the QTP17 functional which better recreates the ionization potential for core electrons, and the fact that the empirical parameters used to damp dynamic correlation were fit to relative excited state energies instead of absolute energies in the latest parameterization.[198] Now, DFT/MRCI(2) is expected to have a shift in its computed XAS results relative to experiment of about 0.5-1.0 eV. This makes the 1.5 eV shift in comparison with EOM-CCSD a predictable result, as typically the first major absorption of a EOM-CCSD core excitation spectra should not experience a large quantitative shift compared to experimental data.[199–201]

Overall, DMABN is well suited to a time resolved XAS study. The results at the Carbon K-Edge are mixed, but certainly at the Nitrogen K-Edge the $S_1(\mathbf{R}_{TICT})$ and $S_1(\mathbf{R}_{\pi\sigma*})$ structures can be well resolved owing to their peaks at 395.4 eV and 397.0 eV, nearly 1.5 eV apart. However, the $S_1(\mathbf{R}_{TICT})$ peak at 397.0 eV overlaps slightly with the lowly absorbing peak at 396.8 eV attributed to the $S_1(\mathbf{R}_{LE})$ structure, so time resolved XAS studies on their

own are not going to be enough to track the extent of charge transfer in DMABN.

5.1.2 X-ray Photoelectron Spectroscopy

Figure 24 describes the X-ray photoelectron spectrum computed using DFT/MRCI(2). Extended spectrum including contributions from other excited states can be found in the Appendix (A.14). Since electrons are ejected instead of excited in XPS, the nature of each transition is harder to elucidate as there exists no particle NTO. However a cursory understanding of the major emissions in the spectrum is found by using dyson orbitals implemented in the GRaCI package, which are localized around specific core atoms in the molecule (See Appendix, A.14). A time resolved XPS study works similarily to TRPES, ground state ionizations will bleach any excited state ionizations if they overlap. However unlike XAS, the ground state signals will have a high positive intensity, which will also make it difficult to resolve signals attributed to excited state structures.

This time, XPS provides much better separation of signals than previous spectra for distinguishing between the $S_1(\mathbf{R}_{LE})$ and $S_1(\mathbf{R}_{TICT})$ structures. At the Carbon K-Edge, (Figure 24a) nearly all emissions are overshadowed by emissions from the ground state structure, often being grouped together in small bands, similar to the XAS Carbon K-Edge. For the $S_1(\mathbf{R}_{TICT})$ structure, the first group of emissions at 290-291 eV is due to emissions from carbons in the benzene ring and the cyano group, while a smaller second group is due to emissions almost exclusively from carbons on the dimethylamino group. Like the XAS Carbon K-Edge, the emissions from the $S_1(\mathbf{R}_{LE})$ and $S_1(\mathbf{R}_{\pi\sigma*})$ structures are more scattered compared to emissions from the $S_1(\mathbf{R}_{TICT})$ structure, since the emissions from the dimethylamino group sometimes occur earlier, and emissions from the benzene group sometimes occur later. This behaviour is likely due to the decoupling of the dimethylamino group from the rest of the molecule at the $S_1(\mathbf{R}_{TICT})$ structure as a result of the twisted nuclear structure, which is a useful observation for designing molecules with suitable Carbon K-Edge resolution in the future.

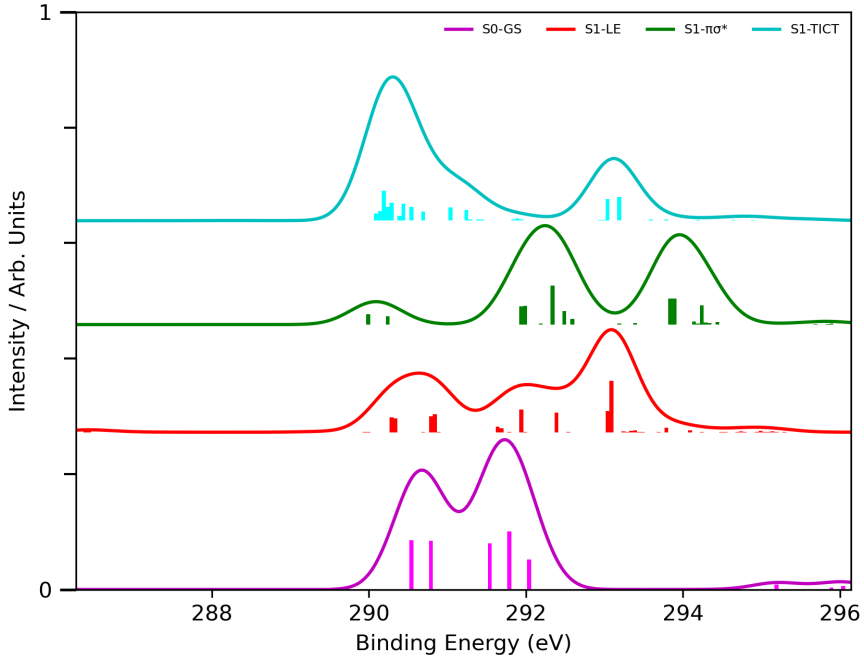

(a) Carbon K-Edge

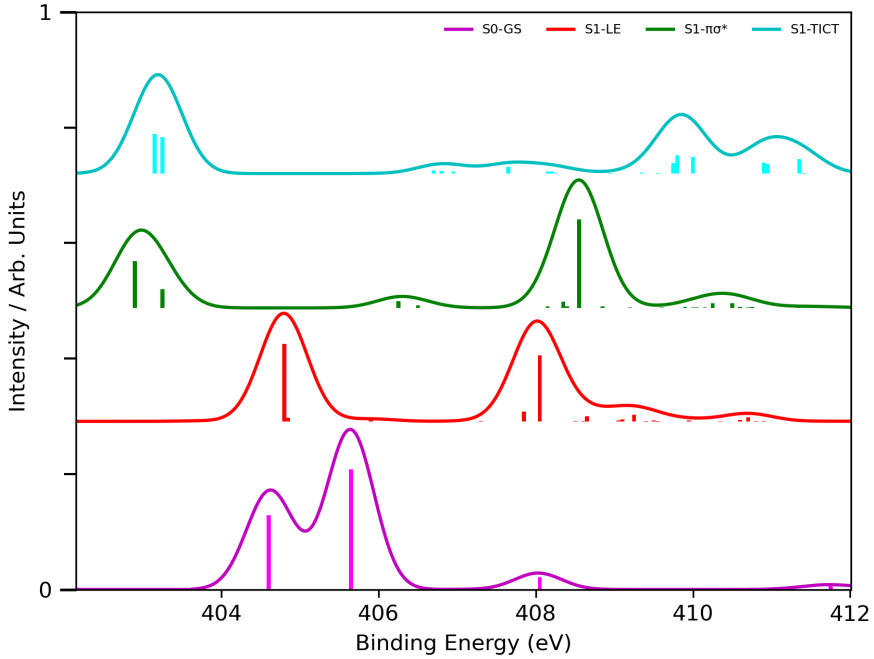

(b) Nitrogen K-Edge

Figure 24: Simulated X-ray photoelectron spectrum of DMABN with DFT/MRCI(2)

Results from the Nitrogen K-Edge (Figure 24b) are better resolved. In contrast to the Nitrogen K-Edge XAS spectrum, this time there is no overlap between the $S_1(\mathbf{R}_{LE})$ and $S_1(\mathbf{R}_{TICT})$ structures, but there is a large degree of overlap between the $S_1(\mathbf{R}_{TICT})$ and $S_1(\mathbf{R}_{\pi\sigma*})$ structures. The peaks are well ordered; emissions at 406 eV or earlier come from the cyano nitrogen, and emissions at 407 eV or later come from the dimethylamino nitrogen. In this case, the behaviour of the $S_1(\mathbf{R}_{TICT})$ and $S_1(\mathbf{R}_{\pi\sigma*})$ structures are similar, and their peaks overlap at about 406 eV. There is an intuitive reasoning for this; the $S_1(\mathbf{R}_{TICT})$ structure is defined by a movement of charge from the dimethylamino group to the cyano group (Fig 9), and the $S_1(\mathbf{R}_{\pi\sigma*})$ structure is defined by a movement of charge from the benzene ring to the cyano group (Fig 10), thus the chemical environment at the cyano nitrogen core is similar for the two states. Since XPS measures emissions, this relationship does not persist for the Nitrogen K-Edge XAS spectrum, as their absorption probabilities are dependent on the orbital that is populated as well as the initial core orbital. Both structures are well resolved at the Nitrogen K-Edge XPS from the $S_1(\mathbf{R}_{LE})$ structure, since at the $S_1(\mathbf{R}_{LE})$ structure, the electron density is centralized in the center of the benzene ring instead of at the cyano nitrogen (Fig 7). The $S_1(\mathbf{R}_{TICT})$ and $S_1(\mathbf{R}_{\pi\sigma*})$ structures are thus well resolved from the $S_1(\mathbf{R}_{LE})$ structure, however, in the 409.8-411.4 eV region, there is a series of unique emissions attributed to the $S_1(\mathbf{R}_{TICT})$ structure. No other $S_1(\mathbf{R}_{LE})$ or $S_1(\mathbf{R}_{\pi\sigma*})$ structure emissions in this region were found with significant strength.

Therefore, out of all the potential time resolved XAS/XPS experiments, Nitrogen XPS spectrum provide the best separation of signals between the relevant excited state structures necessary to track in a time resolved experiment. Contrary to the Nitrogen XAS spectrum, the direct rise and fall of the $S_1(\mathbf{R}_{\pi\sigma*})$ and $S_1(\mathbf{R}_{TICT})$ structures could be compared in a time resolved study, owing to the first $S_1(\mathbf{R}_{\pi\sigma*})$ emissions at 403 eV, and the series of $S_1(\mathbf{R}_{TICT})$ emissions in the 410 eV region. Furthermore, XAS at the Nitrogen K-Edge provides another means by which to detect the rise and fall of the $S_1(\mathbf{R}_{\pi\sigma*})$ structure owing to early absorptions at 395 eV. Unfortunately, the $S_1(\mathbf{R}_{LE})$ structure is rarely well resolved.

However, coordinating XAS/XPS studies on DMABN can allow for the rise of the $S_1(\mathbf{R}_{TICT})$ signal to be tracked at 410 eV in the Nitrogen XPS spectrum, which can be measured against the Nitrogen XAS $S_1(\mathbf{R}_{TICT})$ structure peak at 397 eV, to determine the rate of $S_1(\mathbf{R}_{LE})$ population at the same region.

5.2 DIABN and ABN

Figure 25 and 26 show the Nitrogen K-Edge XAS and XPS spectra for ABN and DIABN. The similarities with the DMABN X-ray spectra are readily apparent. The general shape of the XAS Nitrogen K-Edge spectra for ABN and DIABN matches the shape of the XAS Nitrogen K-Edge spectra for DMABN for all the relevant excited state structures. However, DMABN remains the best molecule of the three to detect the $S_1(\mathbf{R}_{TICT})$ structure; the separation between the excited state signals of the $S_1(\mathbf{R}_{TICT})$ and $S_1(\mathbf{R}_{\pi\sigma*})$ structures is decreased for both ABN and DIABN, although the excited state structure signals still remain distinct enough such that they don't overlap. DIABN presents a helpful case, while the separation of the excited state signals for the $S_1(\mathbf{R}_{TICT})$ and $S_1(\mathbf{R}_{\pi\sigma*})$ structures decreases, the separation between the $S_1(\mathbf{R}_{LE})$ and $S_1(\mathbf{R}_{\pi\sigma*})$ structures increases, so the molecule is better suited for a time resolved XAS study at the Nitrogen K-Edge than DMABN with a unique $S_1(\mathbf{R}_{LE})$ signal at 398 eV. The XPS spectra for DIABN and ABN are also similar to the DMABN Nitrogen K-Edge spectra. For DIABN the results are simple, the $S_1(\mathbf{R}_{TICT})$ structure is still resolved well due to higher energy peaks in the 409 eV region similarly to DMABN, and the $S_1(\mathbf{R}_{TICT})$ and $S_1(\mathbf{R}_{\pi\sigma*})$ structures still overlap. For ABN this relationship did not persist, the emissions in the expected late region occurred at lower energies for the $S_1(\mathbf{R}_{TICT})$ structure relative to other excited states, as opposed to the XPS spectra of DMABN. For ABN, every emission from an excited state overlaps significantly with either the ground state or another excited state emission.

A DIABN XAS/XPS time resolved study is certainly viable in the gas phase; the $S_1(\mathbf{R}_{TICT})$, $S_1(\mathbf{R}_{\pi\sigma*})$, and $S_1(\mathbf{R}_{LE})$ structures all have unique absorptions/emissions, unlike DMABN.

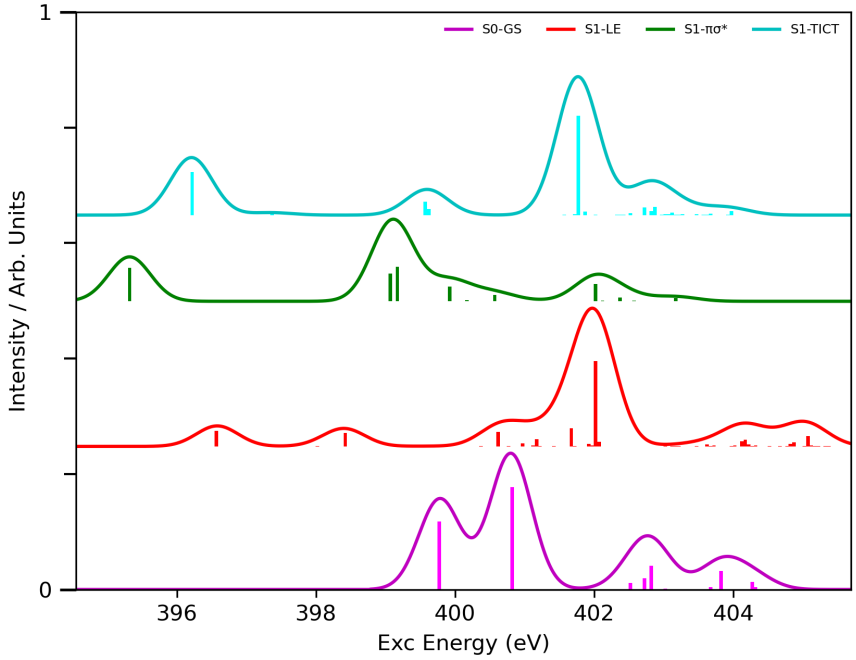

(a) Nitrogen K-Edge, ABN

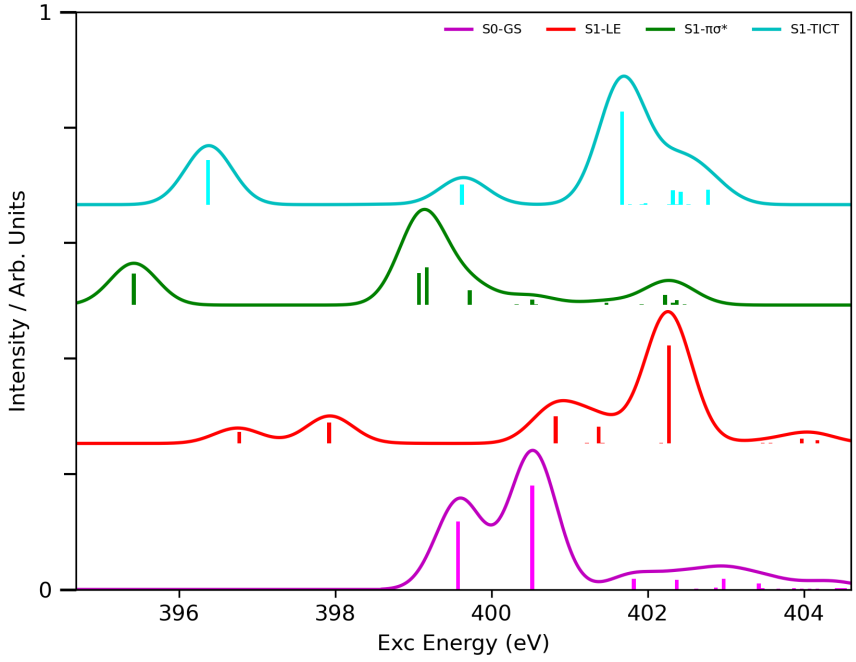

(b) Nitrogen K-Edge, DIABN

Figure 25: Simulated X-ray absorption spectrum of ABN and DIABN with DFT/MRCI(2)

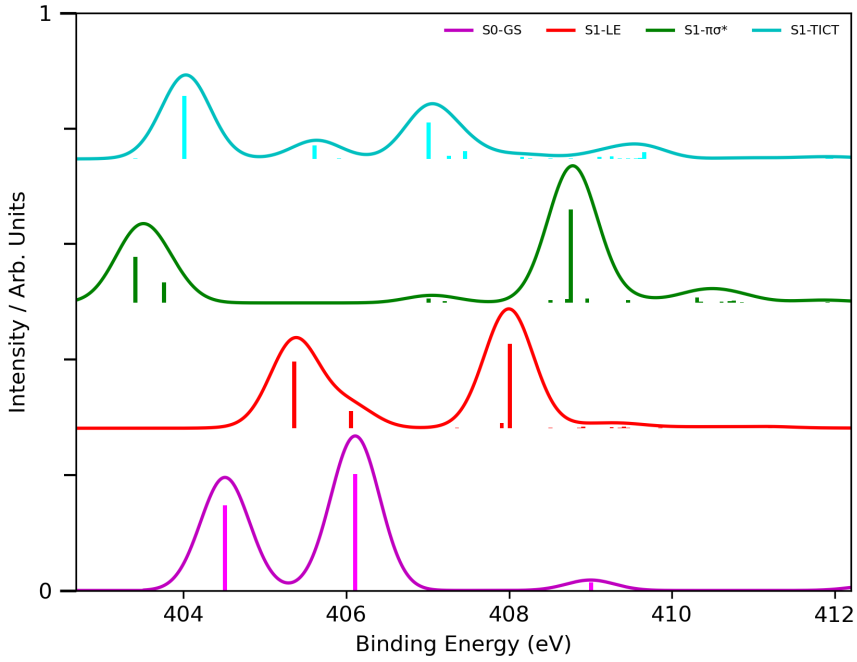

(a) Nitrogen K-Edge, ABN

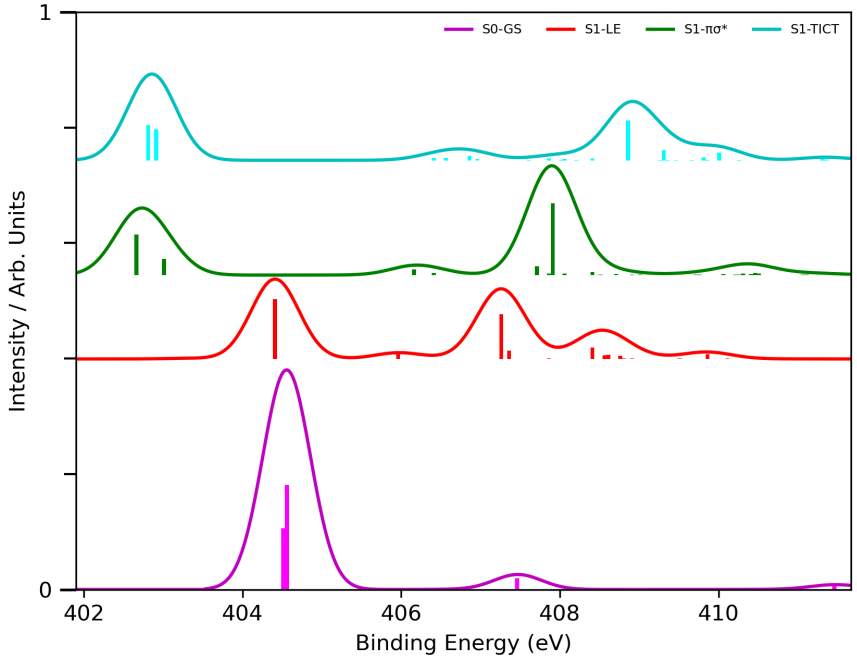

(b) Nitrogen K-Edge, DIABN

Figure 26: Simulated X-ray photoelectron spectrum of ABN and DIABN with DFT/MRCI(2)

An ABN study is less viable due to the separation in the excited state signals, but charge transfer has yet to be detected in ABN in gas phase or in solvent regardless.[5,13] While this work has provided evidence that a TRXAS/TRXPS study on DMABN and DIABN would be able to detect the extent of charge transfer formation in these molecules, the speed of DFT/MRCI(2), and its accuracy in recreating CASPT2 potential energy surfaces and experimental spectrum encourages further work in this region. Specifically, by studying several derivatives of DMABN at once using DFT/MRCI(2) to simulate XAS and XPS spectrum, it can be established that other analogues besides DMABN and DIABN would also be prime for a time resolved study.

5.3 Derivatives with different electron acceptors

Next, a series of derivatives of DMABN are evaluated, with the goal of determining under what conditions signals attributed to the $S_1(\mathbf{R}_{TICT})$ structure can be best resolved, and under what conditions the $S_1(\mathbf{R}_{TICT})$ structure is low enough in absolute energy to be populated in a time resolved experiment. Since XAS/XPS saw the best separation of the $S_1(\mathbf{R}_{LE})$ and $S_1(\mathbf{R}_{TICT})$ structures, these spectroscopies are used, in coordination with LIICs derived between the $S_1(\mathbf{R}_{LE})$ and $S_1(\mathbf{R}_{TICT})$ structures of each analogue. The interpolated paths themselves are found in the Appendix (A.15). Through this analysis, molecules that have a energetically favourable charge transfer state, and whose charge transfer state is readily observable using XAS/XPS, can be presented as optimal for a time resolved study.

One idea that was previously explored in experimental studies was to substitute the cyano group in DMABN with stronger electron withdrawing groups to increase the probability of the TICT process occurring.[13,187,202–204] A simplistic electron withdrawing group that does not introduce any other low lying electronic states can eliminate the $S_1(\mathbf{R}_{\pi\sigma*})$ hypothesis and help to confirm that the two-state model is necessary to induce $S_1(\mathbf{R}_{\pi\sigma*})$ formation. Figure 27 shows a sample of the groups with this quality that were evaluated, and Figure 28 & 29 show their respective XAS and XPS spectra at the Nitrogen and Oxygen K-Edges.

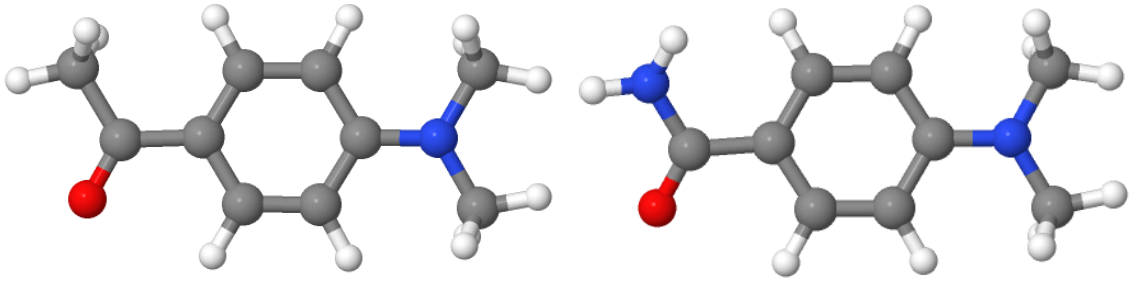

(a) Structure A1 (b) Structure A2

Figure 27: Overview of Derivatives of DMABN with different electron withdrawing groups. (Nitrogen atoms are in blue, Oxygen atoms are in Red, Carbon Atoms are in Grey)

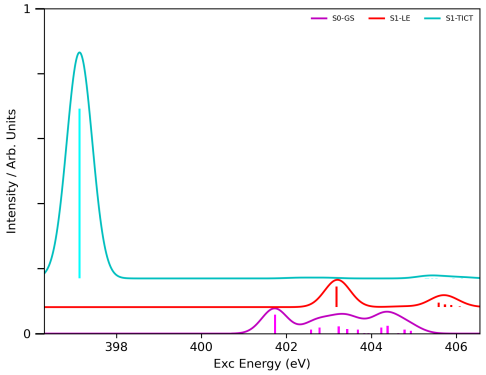

(a) Structure A1, Nitrogen K-Edge

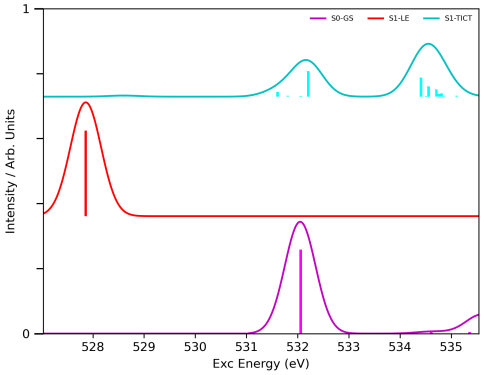

(b) Structure A1, Oxygen K-Edge

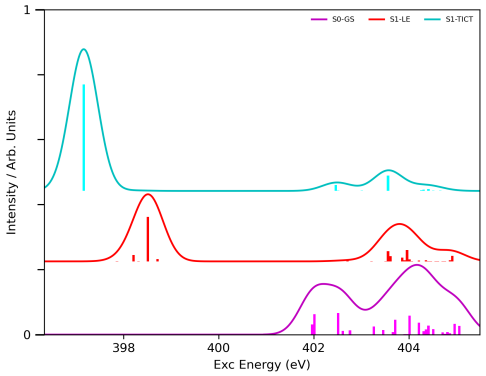

(c) Structure A2, Nitrogen K-Edge

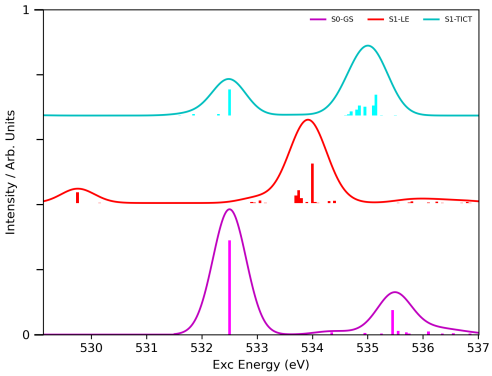

(d) Structure A2, Oxygen K-Edge

Figure 28: X-ray absorption spectrum of derivatives of DMABN with different electron withdrawing groups

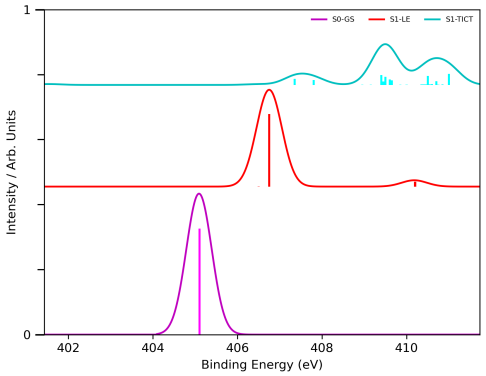

(a) Structure A1, Nitrogen K-Edge

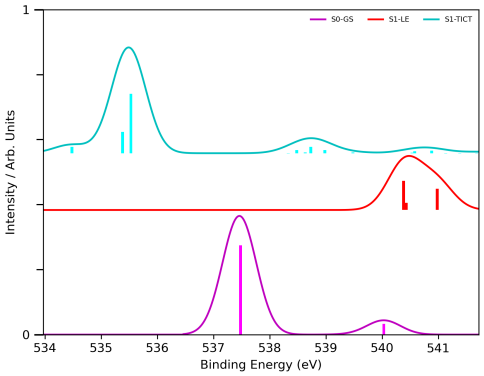

(b) Structure A1, Oxygen K-Edge

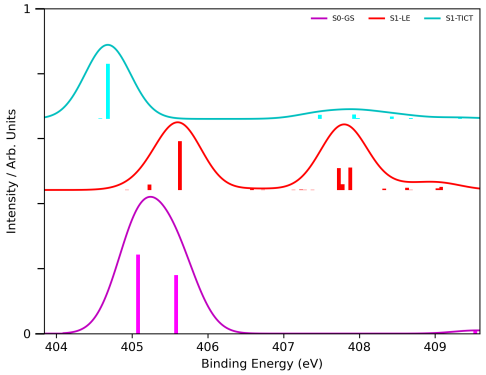

(c) Structure A2, Nitrogen K-Edge

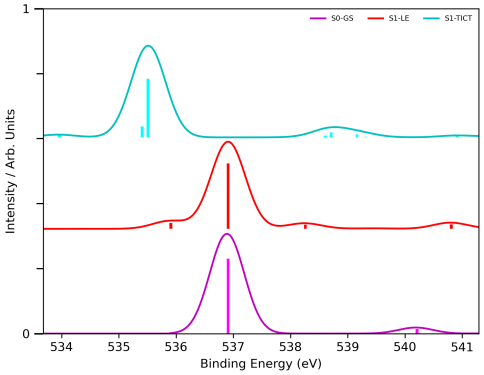

(d) Structure A2, Oxygen K-Edge

Figure 29: X-ray photoelectron spectrum of derivatives of DMABN with different electron withdrawing groups

The introduction of a unique electron withdrawing group like a carbonyl group, allows for another XAS/XPS set of spectra by which the $S_1(\mathbf{R}_{LE})$ and $S_1(\mathbf{R}_{TICT})$ structures can be distinguished. The advantages of this are evident in Figure 28 a) and b), where the use of the CH3O group allows for the $S_1(\mathbf{R}_{LE})$ and $S_1(\mathbf{R}_{TICT})$ spectra to be incredibly well resolved; one core excitation from the dimethylamino group responsible for the $S_1(\mathbf{R}_{TICT})$ peak at the Nitrogen K-Edge, and one core excitation from the carbonyl group responsible for the $S_1(\mathbf{R}_{LE})$ peak at the Oxygen K-Edge. The introduction of a simple withdrawing group that replaces the cyano group has the effect of changing the absorption energies of core excited states typical of DMABN-type molecules such that they can be more easily resolved. However, the actual probability of populating the $S_1(\mathbf{R}_{TICT})$ structure is also important to consider when analyzing derivatives of DMABN, and derivatives that sacrifice the cyano group for another withdrawing group do not appear to decrease the size of the transition barrier between the $S_1(\mathbf{R}_{LE})$ and $S_1(\mathbf{R}_{TICT})$ structures compared to DMABN (See Appendix, A.15).

5.4 Complex Derivatives

It was found after rigorous experimentation with several molecular designs present in previous works,[13] that an optimal electron withdrawing group to use in derivative design that reduces the absolute energy of the $S_1(\mathbf{R}_{TICT})$ structure, was an acetate ester as the withdrawing group. This group has rare experimental precedence,[13,205,206] but its application has often led to dual fluorescence and other properties consistent with DMABN derivatives. Figure 30 displays a few choice derivatives selected with this functional group. Structure B3 (Ethyl 4-(1H-pyrrol-1-yl)benzoate) is of particular importance; its design was influenced by previous work that used a pyrrole group as the electron donating group to detect charge transfer in similar derivatives of DMABN.[207] Figure 31 shows the most significant XAS and XPS spectra taken from these derivatives, specifically the Nitrogen K-Edge XAS, and the Oxygen K-Edge XPS. By using the principles of the previous section to split up excitations/emissions

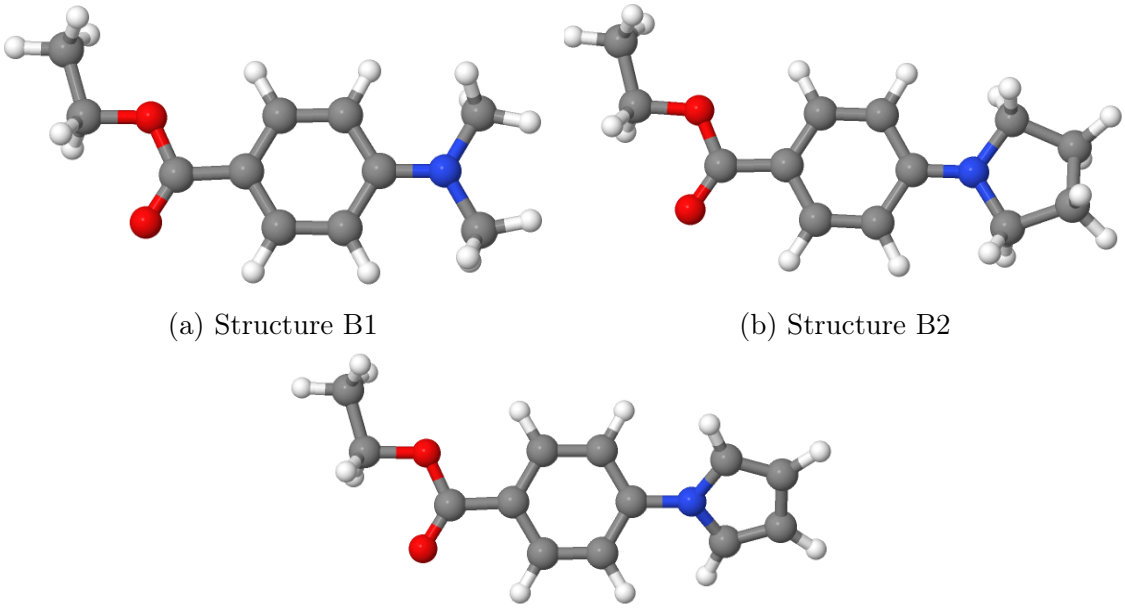

(a) Structure B1

(b) Structure B2

(c) Structure B3

Figure 30: Overview of Derivatives of DMABN that are benzoate esters

across different K-Edges through the selective choice of the electron withdrawing group, the $S_1(\mathbf{R}_{TICT})$ and $S_1(\mathbf{R}_{LE})$ excited state signals are separated by at least 1 eV. Also, there is a significant decrease in the size of the transition barrier (at least based on the LIICs estimated in the Appendix (A.15)), between the $S_1(\mathbf{R}_{LE})$ and $S_1(\mathbf{R}_{TICT})$ structures for these derivatives. For both B1 and B2, the S_1 and S_2 states are nearly degenerate at the ground state and $S_1(\mathbf{R}_{LE})$ structures, and the size of the transition barrier is less than 0.2 eV. In the case of these molecules, even though the transition-state barrier is quite small, it is unlikely that it will be overcome in a time resolved experiment owing to the lack of internal energy at the $S_1(\mathbf{R}_{LE})$ structure after decay from S_2.

Considering the B3 molecule, it is noted that the S_1, S_2, and S_3 states are all nearly degenerate at the ground state structure. DFT/MRCI(2) predicts that absorption will proceed from the S_0 to the S_3 state (which has PICT character), wherein the S_1 and S_2 states describe nearly degenerate, dark states from the ground state structure. Since the states are all closely linked in energy, ultrafast decay is likely to occur from the S_3 state, to the S_2 state, and then to the S_1 state. CASSCF optimized the $S_1(\mathbf{R}_{LE})$ and $S_1(\mathbf{R}_{TICT})$ structures

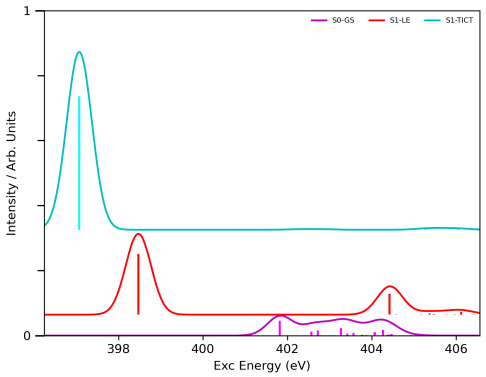

(a) Structure B1, Nitrogen Edge, XAS

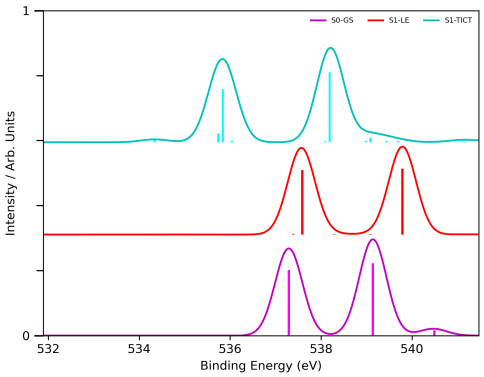

(b) Structure B1, Oxygen Edge, XPS

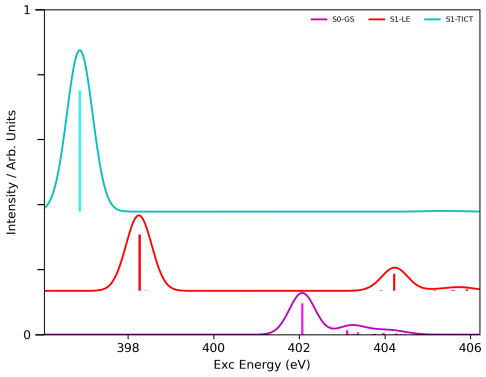

(c) Structure B2, Nitrogen Edge, XAS

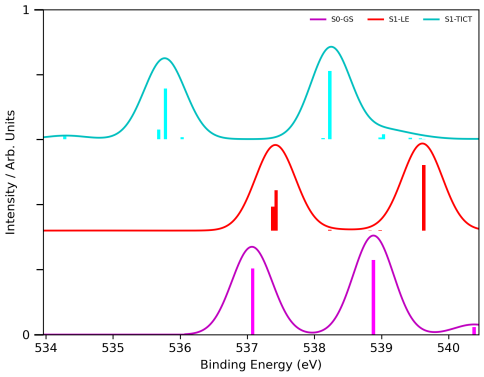

(d) Structure B2, Oxygen Edge, XPS

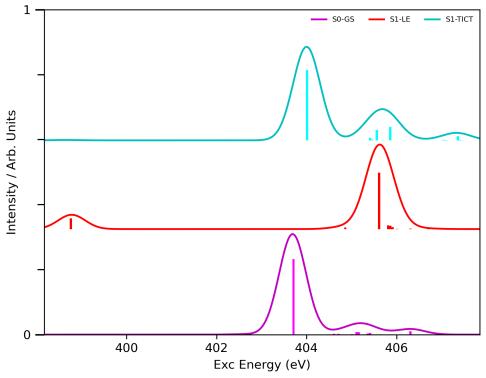

(e) Structure B3, Nitrogen Edge, XAS

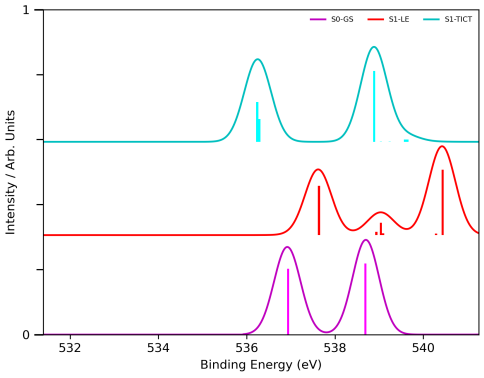

(f) Structure B3, Oxygen Edge, XPS

Figure 31: Various X-ray absorption/photoelectron spectrum of derivatives of DMABN that are benzoate esters

successfully, even though DFT/MRCI(2) predicts that the $S_1(\mathbf{R}_{LE})$ optimized structure may not represent a local minima. However from the ground state minimum structure, and the $S_1(\mathbf{R}_{LE})$ structure, DFT/MRCI(2) indicates that there is no transition-state barrier separating these states from the $S_1(\mathbf{R}_{TICT})$ structure. This is because the electronic character of the $S_1(\mathbf{R}_{TICT})$ structure for B3 is fundamentally different than the $S_1(\mathbf{R}_{TICT})$ structure studied for any other derivative studied so far. The Appendix (A.15) includes NTOs which describe the electronic character of the $S_1(\mathbf{R}_{TICT})$ structure of various compounds discussed in this section, of which B3 is included. There, it is shown how the NTOs associated with the $S_1(\mathbf{R}_{TICT})$ structure for this derivative are slightly different than those for DMABN, DIABN, etc. In this case, the hole orbital consists of π-$\pi*$ orbitals between carbons on the pyrrole ring instead of an orbital localized on solely the nitrogen. Effectively, these NTOs still describe a charge transfer state that has a minimum defined by a twisting of the electron donating pyrrole group, but it is still distinct from the typical $S_1(\mathbf{R}_{TICT})$ structure of DMABN. The electronic character of this state being distinct is readily apparent in the XAS and XPS spectra evaluated, where the $S_1(\mathbf{R}_{TICT})$, $S_1(\mathbf{R}_{LE})$, and ground state signals are typically shifted significantly such that across all the spectra evaluated, the $S_1(\mathbf{R}_{LE})$ and $S_1(\mathbf{R}_{TICT})$ structures have minimal separation, which limits the utilization of this compound for a time resolved study. A number of other similar studies on DMABN derivatives were also conducted over the course of this thesis, but these will be left to peruse in the Appendices for the curious reader (Appendix A.15 to A.19). In order to study advanced DMABN derivatives, the fundamental two-state model must first be definitively proven using new time resolved experimental spectroscopies such as XAS and XPS. After these are complete and the two-state model is proven, these derivatives can be returned to and experimented with to find ones with the best rate of charge transfer and the most spectroscopically resolved charge transfer states.

6 Concluding remarks

The TICT model of charge transfer that has been discussed at length in previous works, has still not been unambiguously proven, owing to the lack of experimental and simulated time resolved studies on the molecule that detect unique signals attributed to the $S_1(\mathbf{R}_{TICT})$ structure. For the time resolved studies that do exist, the signals associated with the $S_1(\mathbf{R}_{TICT})$ structure are not well separated compared to other relevant excited state signals, leading to confusion about the specific role of the $S_1(\mathbf{R}_{TICT})$ structure, even at picosecond timescales.[7,10,34,73] By simulating and interpreting the results of a series of spectroscopic techniques, this work determined that the charge transfer signal associated with DMABN is mostly likely attributed to the $S_1(\mathbf{R}_{TICT})$ structure, predicted by several *ab initio* electronic structure methods. The excited state dynamics of DMABN and its analogues were determined to be mostly likely governed by a two-state model. That is, quick excitation and relaxation from the ground state to the $S_2(\mathbf{R}_{PICT})$ structure, to the $S_1(\mathbf{R}_{LE})$ structure, followed by a significantly slower excited state population transfer through a transition barrier separating the $S_1(\mathbf{R}_{LE})$ and $S_1(\mathbf{R}_{TICT})$ structures. Other conical intersection structures proposed in this thesis and optimized in experimental studies may contribute to sporadic early $S_1(\mathbf{R}_{TICT})$ formation, but it is the aforementioned S_1 transition state barrier which more significantly controls the rate at which the $S_1(\mathbf{R}_{TICT})$ structure is populated. The role of the $S_1(\mathbf{R}_{\pi\sigma*})$ structure was examined directly using LIICs and comparison with experimental data; it was found that it would not contribute to the population of the $S_1(\mathbf{R}_{TICT})$ structure, but may be populated from the $S_1(\mathbf{R}_{LE})$ structure, acting as a competing pathway to the primary $S_1(\mathbf{R}_{LE})$ to $S_1(\mathbf{R}_{TICT})$ process. The two-state model was used to evaluate and interpret existing experimental UV/Vis, transient absorption, and time-resolved photoelectron spectrum, wherein signals associated with the $S_1(\mathbf{R}_{\pi\sigma*})$ structure calculated with DFT/MRCI(2) were often inconsistent with experimental data, while the $S_1(\mathbf{R}_{LE})$ and $S_1(\mathbf{R}_{TICT})$ structure signals could often be attributed to experimental

peaks at early and late timescales. There remained a degree of ambiguity regarding the role of the $S_1(\mathbf{R}_{\pi\sigma*})$ structure, which proved to be only resolvable with new simulated spectroscopies, which did not have experimental equivalents. Hence, DFT/MRCI(2) was applied to simulate never before seen X-ray absorption and X-ray photoelectron spectroscopies for DMABN and many of its analogues. It was found that for DMABN, the rise and fall of the $S_1(\mathbf{R}_{\pi\sigma*})$, $S_1(\mathbf{R}_{LE})$ and $S_1(\mathbf{R}_{TICT})$ structures could be tracked with combined XAS and XPS studies at the Nitrogen K-Edge. Therefore, a time resolved XAS/XPS experiment is the first spectroscopy uniquely suitable for determining whether or not the $S_1(\mathbf{R}_{\pi\sigma*})$ structure is actually populated, and can give unique insight into the rate of the charge transfer process for DMABN. Since DMABN is typically not expected to achieve dual fluorescence in the gas phase,[13,29] and does not see signals associated with charge transfer, the XAS and XPS spectra for molecules such as DIABN and ABN were also evaluated. DIABN is well suited for a time resolved XAS and XPS study, as the molecule retains the same separation between the $S_1(\mathbf{R}_{LE})$, $S_1(\mathbf{R}_{TICT})$, and $S_1(\mathbf{R}_{\pi\sigma*})$ structures via X-ray spectroscopies that DMABN does, and is expected to actually produce two signals instead of one in the gas phase according to the experimental TRPES spectrum of the molecule.

Finally, a series of future directions for those seeking to evaluate analogues of DMABN were proposed. Since XAS/XPS seemed to uniquely present well resolved excited state signals for the $S_1(\mathbf{R}_{LE})$ and $S_1(\mathbf{R}_{TICT})$ structures for DMABN, these spectroscopies in particular were chosen to evaluate a number of DMABN analogues. For example, eliminating the cyano group and evaluating the XAS and XPS of molecules with other strongly withdrawing groups could definitively prove whether the $S_1(\mathbf{R}_{\pi\sigma*})$ structure plays any role, given the $S_1(\mathbf{R}_{TICT})$ structure is low enough in absolute energy. On the other hand, if the goal of the time resolved study is to best resolve the $S_1(\mathbf{R}_{TICT})$ structure, the pyrrole ring proved particularly useful as an electron donating group to lower the absolute energy of the $S_1(\mathbf{R}_{TICT})$ structure greatly, although the resolution of this state in XAS/XPS is poor. Overall, in this thesis, the charge transfer dynamics of DMABN and its analogues were observed and

estimated without the actual presence of simulated excited state dynamics. It is encouraged that future studies on DMABN and its analogues take advantage of the excited state spectroscopies present here to present their own time resolved studies, that can directly validate the two-state model, and elucidate new details on the charge transfer process.

Supporting Information Available

The main Cartesian geometries, additional electronic structure results, several interpolated paths, and other important figures and analyses of DMABN are provided in the Appendix.

Appendix Part A: Valence Spectroscopies

A1: Excitation energies of the excited states of DMABN evaluated using DFT/MRCI(2) and other electronic structure methods

Table A1: DFT/MRCI(2) Absorption (Abs) and Fluorescence (Flu) Energies (eV) in Various Solvents, compared to other Electronic Structure Methods

Method (Basis Set, Solvent)	State (Abs or Flu)	Energy (eV)	Oscillator Strength
DFT/MRCI(2) (aug-cc-PVDZ, Gas Phase)	S0-GS (Abs to S1)	4.59	0.0157
	S0-GS (Abs to S2)	4.93	0.6056
	S1-LE (Flu to S0)	4.10	0.0156
	S1-pTICT (Flu to S0)	3.90	0.3356
	S1-TICT (Flu to S0)	2.96	0.0016
	S1-$\pi\sigma*$ (Flu to S0)	3.05	0.0001
DFT/MRCI(2) (aug-cc-PVDZ, Acetonitrile)	S0-GS (Abs to S1)	4.52	0.0144
	S0-GS (Abs to S2)	4.60	0.6421
	S1-LE (Flu to S0)	4.08	0.0192
	S1-pTICT (Flu to S0)	3.90	0.3356
	S1-TICT (Flu to S0)	2.83	0.0016
	S1-$\pi\sigma*$ (Flu to S0)	2.67	0.0001

DFT/MRCI(2) (aug-cc-PVDZ, Hexane)	S0-GS (Abs to S1)	4.57	0.0154
	S0-GS (Abs to S2)	4.81	0.6195
	S1-LE (Flu to S0)	4.12	0.0205
	S1-pTICT (Flu to S0)	4.04	0.3370
	S1-TICT (Flu to S0)	2.92	0.0016
	S1-$\pi\sigma*$ (Flu to S0)	2.91	0.0001
ADC(2) (TZVPP, Gas Phase)[208]	S0-GS (Abs to S1)	4.38	/
	S0-GS (Abs to S2)	4.64	/
	S1-LE (Flu to S0)	3.73	/
	S1-TICT (Flu to S0)	2.43	/
ADC(2) (TZVPP, Acetonitrile)[208]	S0-GS (Abs to S1)	4.26	/
	S0-GS (Abs to S2)	4.29	/
	S1-LE (Flu to S0)	3.37	/
	S1-TICT (Flu to S0)	2.39	/

ADC(2) (TZVPP, Hexane)[208]	S0-GS (Abs to S1)	4.32	/
	S0-GS (Abs to S2)	4.43	/
	S1-LE (Flu to S0)	3.64	/
	S1-TICT (Flu to S0)	2.20	/
TDDFT (TZVPP, Gas Phase)[33]	S0-GS (Abs to S1)	4.40	/
	S0-GS (Abs to S2)	4.67	/
	S1-LE (Flu to S0)	3.76	/
	S1-TICT (Flu to S0)	2.79	/
CASPT2 (12,11) (cc-pVTZ, Gas Phase)[79]	S0-GS (Abs to S1)	4.08	0.005
	S0-GS (Abs to S2)	4.34	0.418
	S1-LE (Flu to S0)	3.66	0.011
	S1-TICT (Flu to S0)	2.69	0.006

Experiment (Acetonitrile)[9]	S0-GS (Abs to S2)	∼4.2	/
	S1-LE (Flu to S0)	∼3.5	/
	S1-TICT (Flu to S0)	∼2.5	/
Experiment (Hexane)[9]	S0-GS (Abs to S2)	∼4.4	/
	S1-LE (Flu to S0)	∼3.7	/

A2: Evaluation of the S2-PICT state using MOLCAS

The S2-PICT minimum was optimized using OpenMolcas 21[177] with CASSCF using an active space of (12,11) (12 electrons, 11 orbitals). The Excited State Hessian computed at this geometry indicated the presence of one negative vibrational frequency, whose character is defined in Fig A2.1. Nudging the geometry of the optimized minima by the vibrational mode associated with this frequency resulted in a minimum on S2 being found at the geometry outlined in Fig A2.2 after optimization with OpenMolcas 21 once again. A DFT/MRCI(2) calculation was performed to evaluate the excited state energies at S1 and S2 at this nuclear structure, which were found to be 4.31 and 4.33 eV respectively, indicating that this nuclear structure is at a conical intersection between S2 and S1. Since this nuclear structure is quite similar to the S1-LE minimum, it is assumed that after this conical intersection is accessed, the majority of the excited state population sinks into occupying the S1-LE state.

```
++ Principal components of the normal modes
   ------------------------------------

   (Only contributions larger than 0.50 times the maximum are printed)


      Mode      1
        Frequency:          i40.59 cm-1
      --------------------------------
        Dihedral H5 C3 N2 C7     1.0000
        Dihedral C7 N2 C1 H21    0.9977
        Dihedral H6 C3 N2 C7     0.9888
        Dihedral H4 C3 N2 C7     0.9887
        Dihedral C7 N2 C1 H20    0.9866
        Dihedral C7 N2 C1 H19    0.9866
        Dihedral C1 N2 C3 H5     0.8865
        Dihedral C1 N2 C3 H6     0.8766
        Dihedral C1 N2 C3 H4     0.8765
        Dihedral C3 N2 C1 H21    0.8722
        Dihedral C3 N2 C1 H20    0.8624
        Dihedral C3 N2 C1 H19    0.8624
        Dihedral C1 N2 C7 C8    -0.6935
        Dihedral C1 N2 C7 C12   -0.6924
        Dihedral C3 N2 C7 C8    -0.6859
        Dihedral C3 N2 C7 C12   -0.6847
      --------------------------------
```

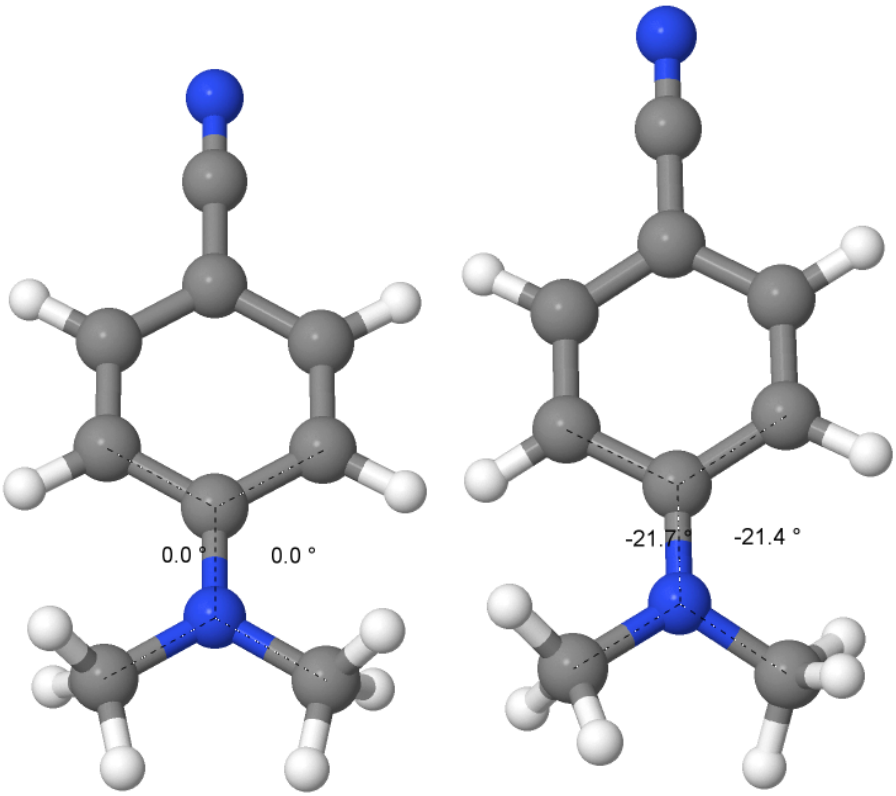

Figure A2.1: i) Character of the imaginary frequency at the S2-PICT optimized structure ii) Geometry of S2-PICT state iii) Geometry of optimized S2/S1 intersection, from applying vibrational mode displacement to the S2-PICT state

A3: Diabatic potential energy surfaces of DMABN with DFT/MRCI(2)

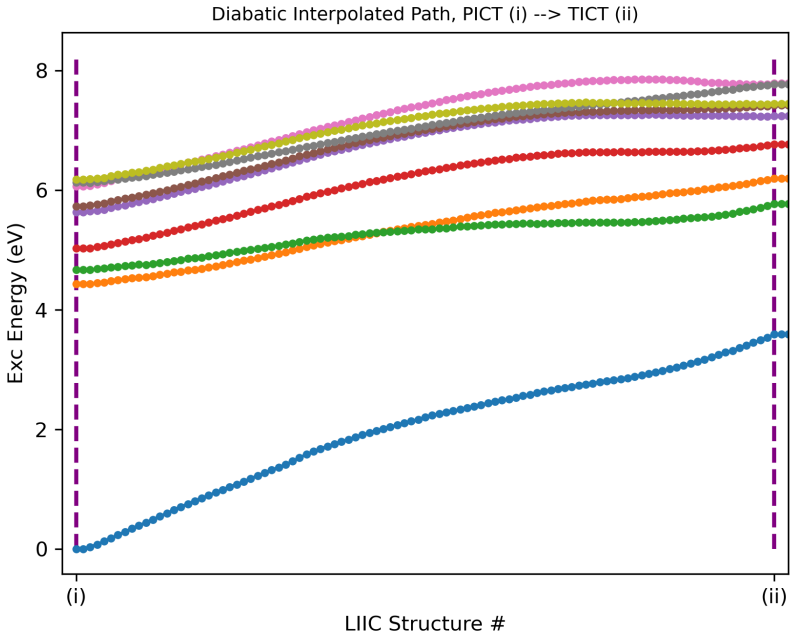

(a) PICT to TICT geometries

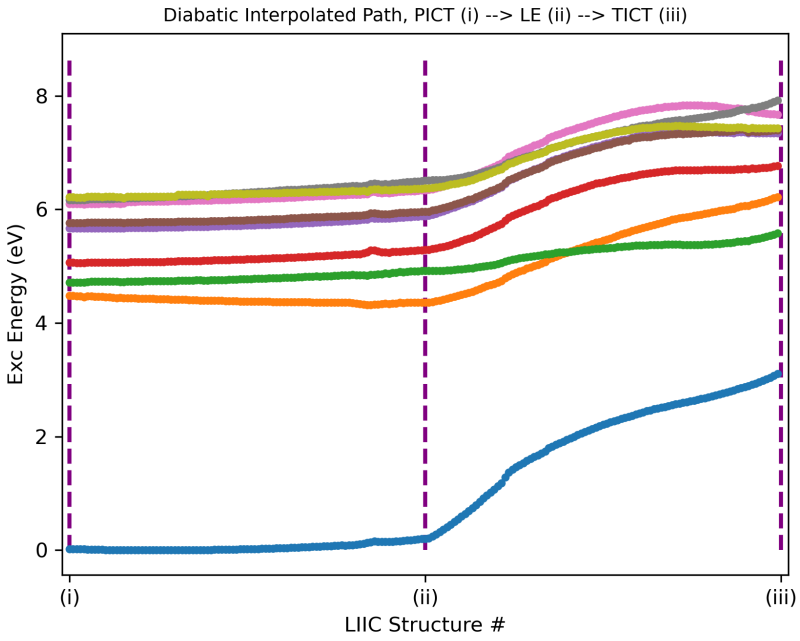

(b) PICT to LE to TICT geometries

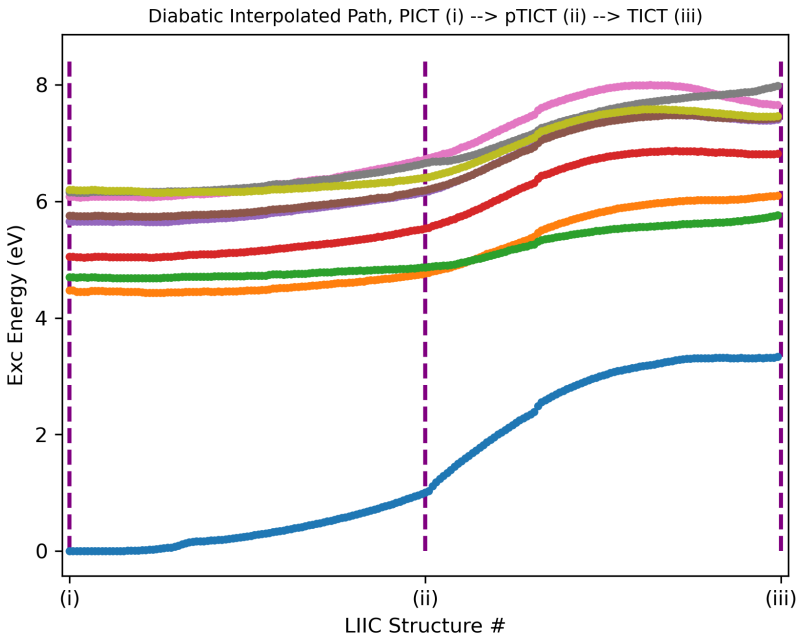

(c) PICT to pTICT[10] to TICT geometries

Figure A3.1: Diabatic Potential Energy Curves, initial guess of diabatic states at the PICT geometry

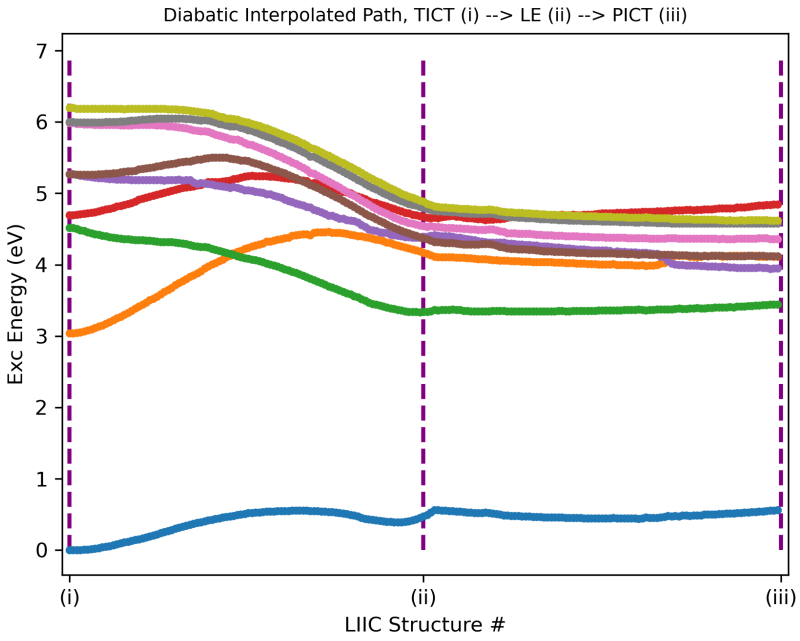

(a) TICT to LE to PICT geometries

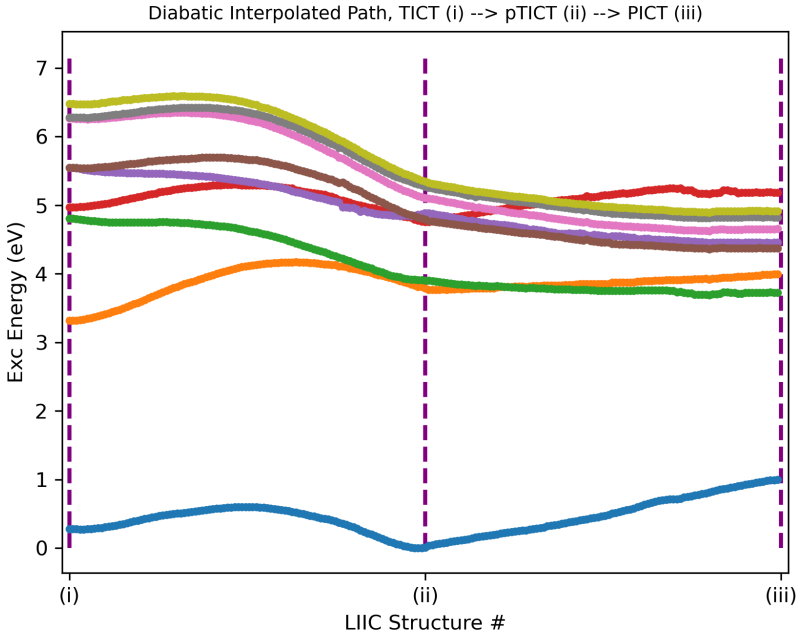

(b) TICT to pTICT[10] to PICT geometries

Figure A3.2: Diabatic Potential Energy Curves, initial guess of diabatic states at the TICT geometry

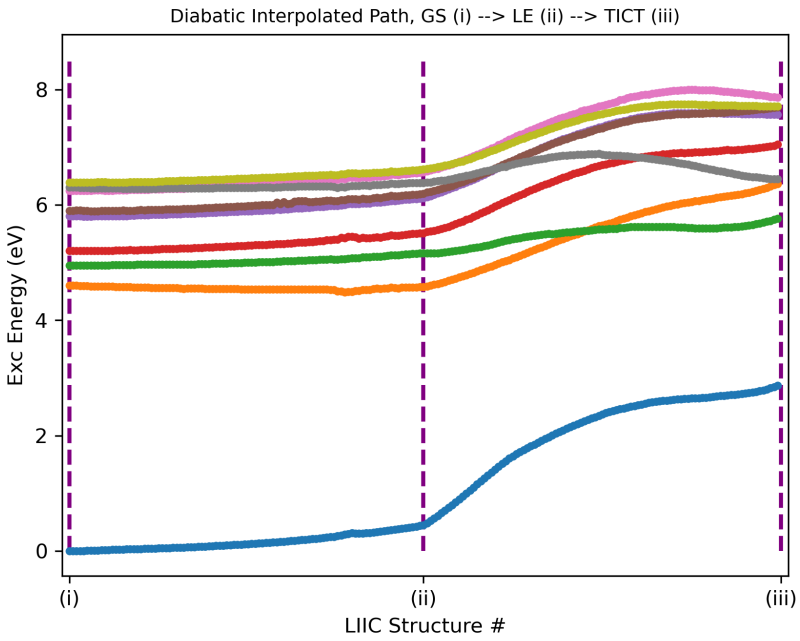

(a) GS to LE to TICT geometries

Figure A3.3: Diabatic Potential Energy Curves, initial guess of diabatic states at the ground state geometry

A4: Interpolated Paths from S1-LE to S1-TICT of the various DMABN derivatives through a transition state

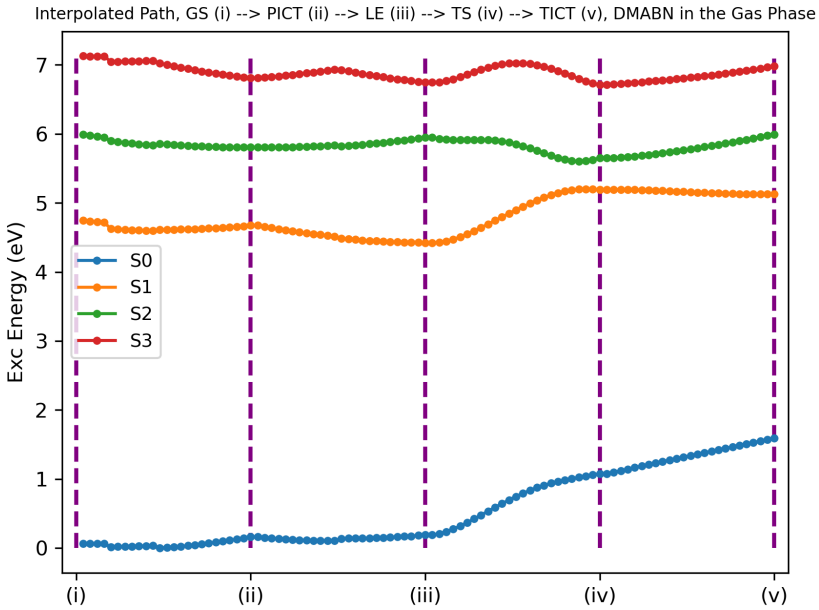

(a) CASSCF (12,11), Gas Phase

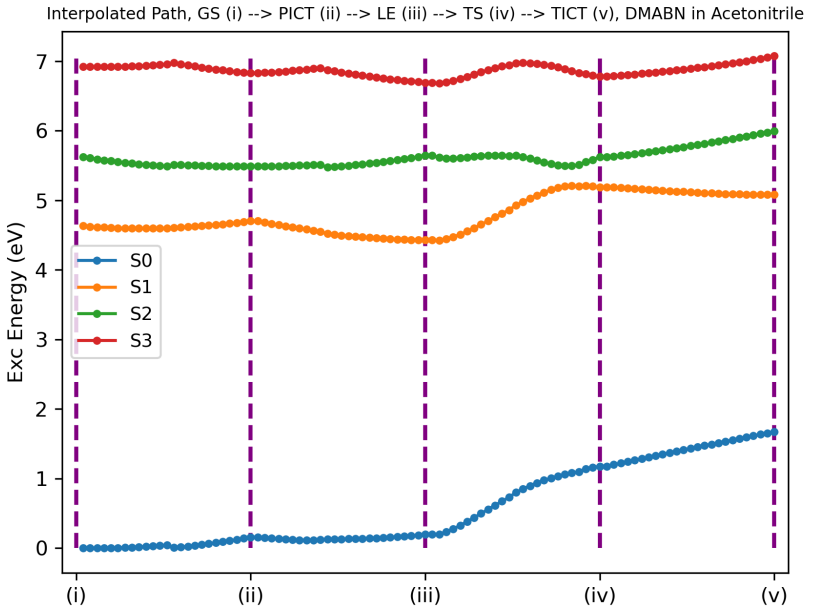

(b) CASSCF (12,11), Acetonitrile

Figure A4.1: Linear Interpolated Path of DMABN with CASSCF

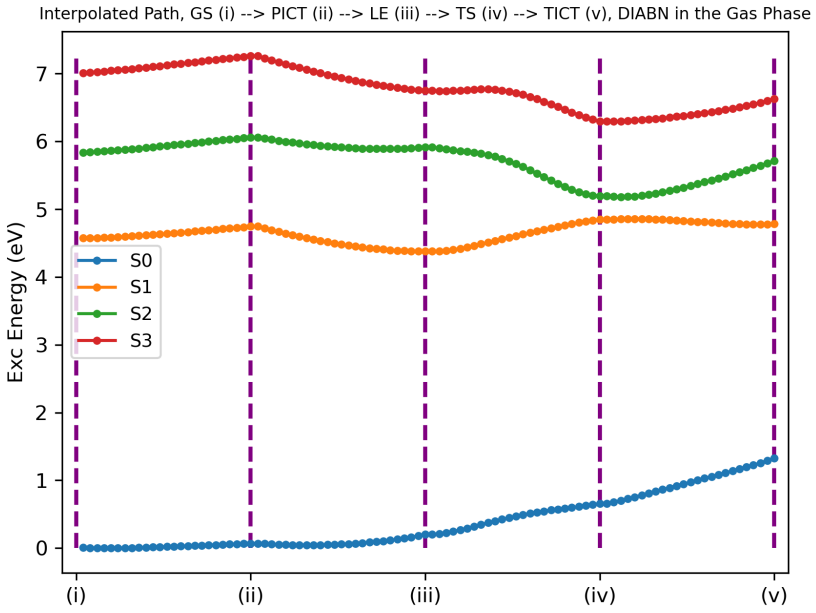

(a) CASSCF (12,11), Gas Phase

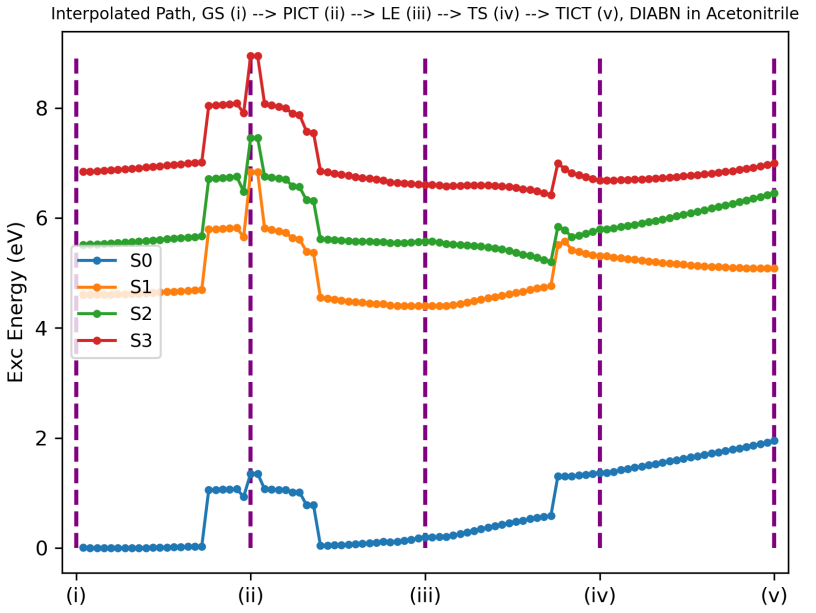

(b) CASSCF (12,11), Acetonitrile

Figure A4.2: Linear Interpolated Path of DIABN with CASSCF

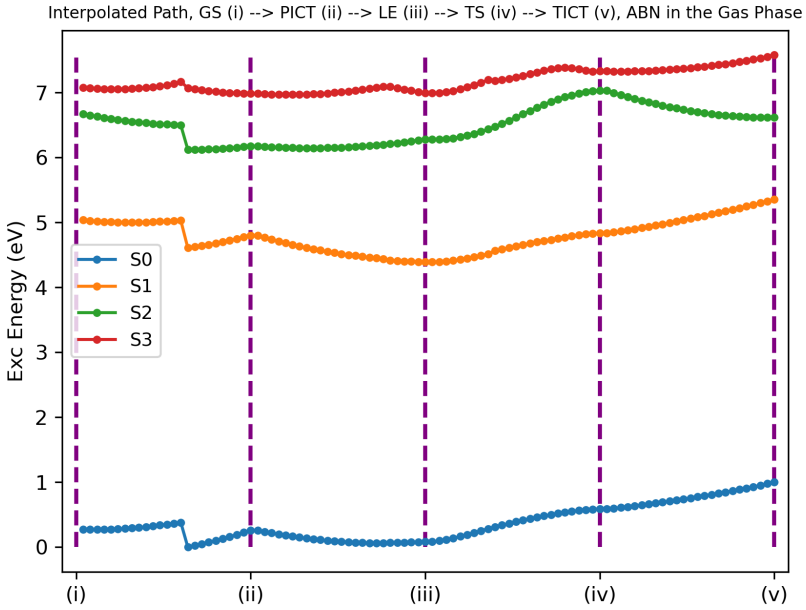

(a) CASSCF (12,11), Gas Phase

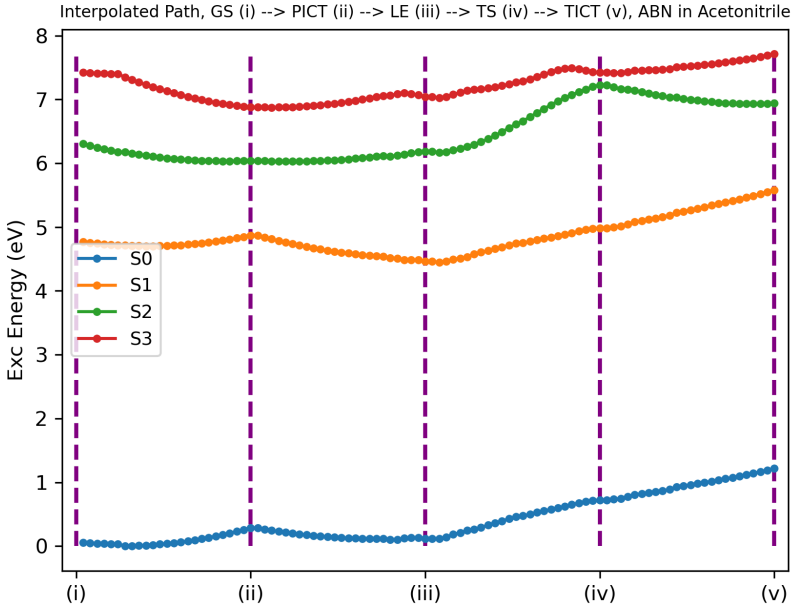

(b) CASSCF (12,11), Acetonitrile

Figure A4.3: Linear Interpolated Path of ABN with CASSCF (No transition state, S1-TICT not a minimum)

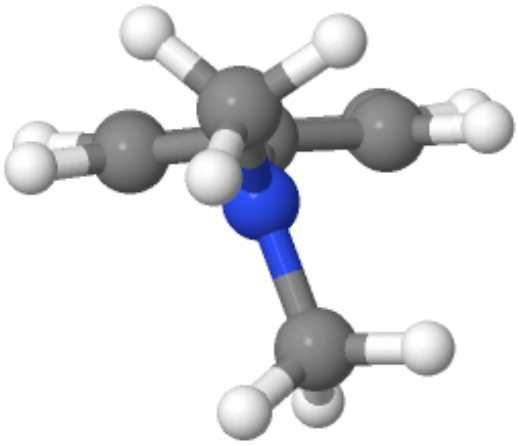

(a) Transition State for DMABN, optimized with CASSCF (12,11)

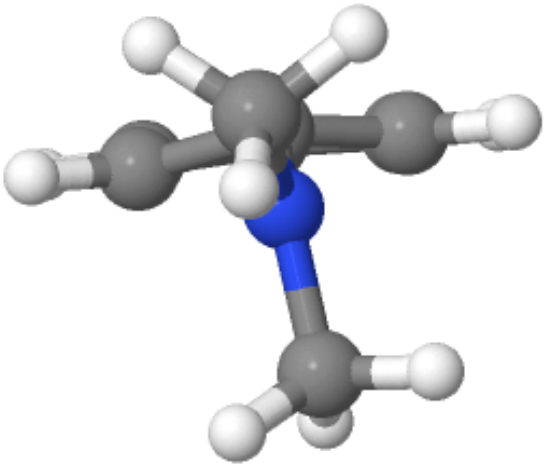

(b) Transition State for DMABN, optimized with CASSCF (12,11) nudged via its imaginary frequency

Figure A4.4: Transition State of DMABN, CASSCF(12,11)

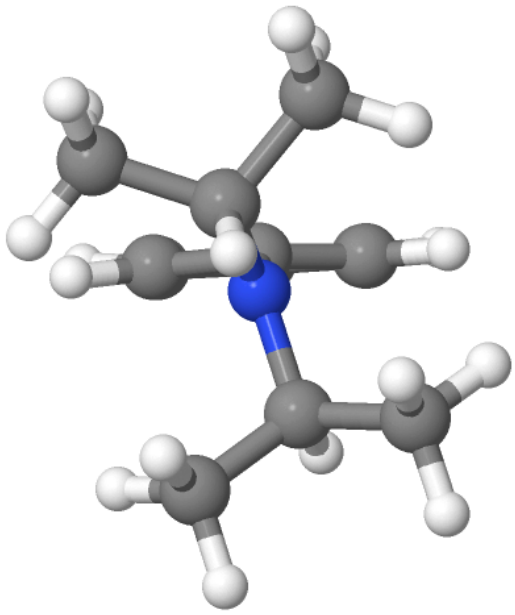

(a) Transition State for DIABN, optimized with CASSCF (12,11)

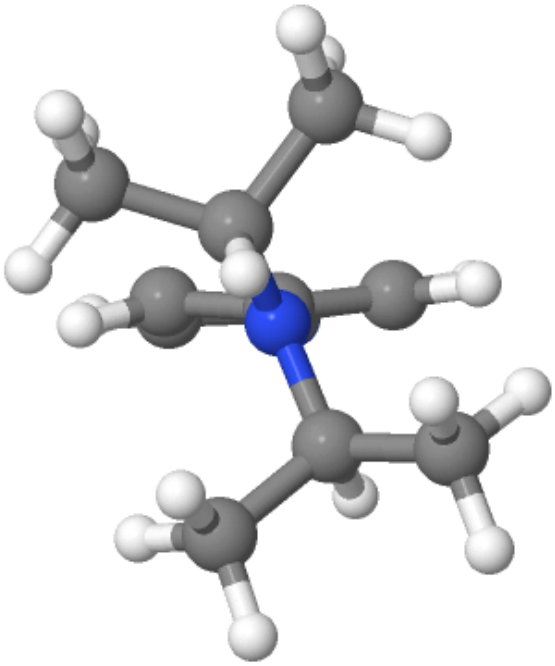

(b) Transition State for DIABN, optimized with CASSCF (12,11) nudged via its imaginary frequency

Figure A4.5: Transition State of DIABN, CASSCF(12,11)

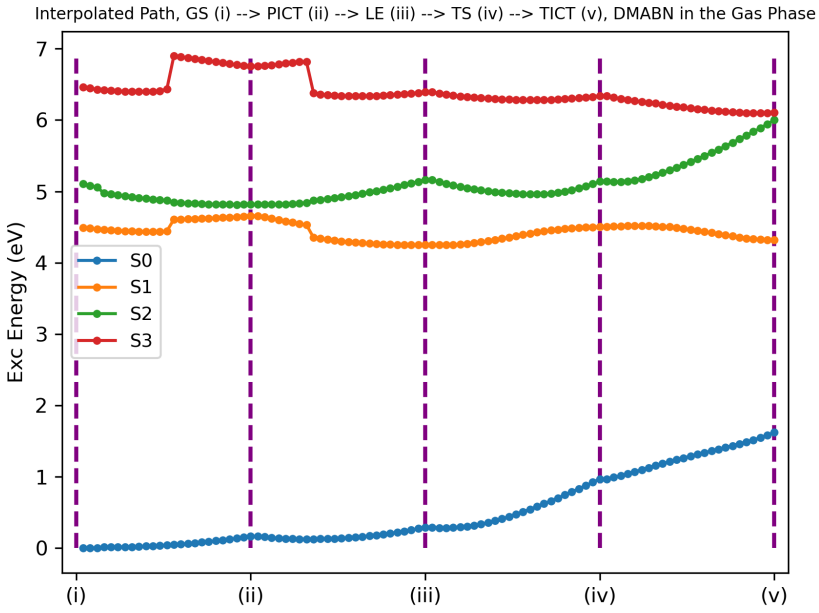

(a) CASPT2 (12,11), Gas Phase

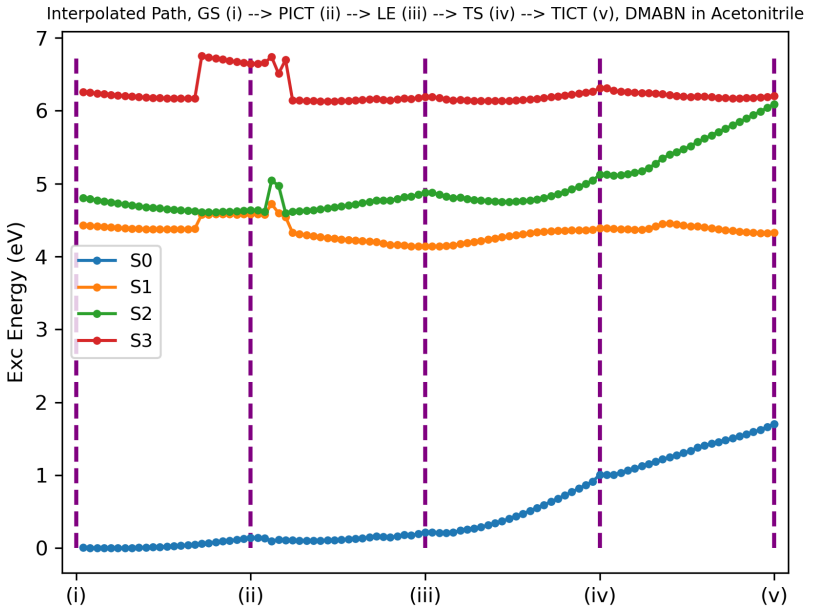

(b) CASPT2 (12,11), Acetonitrile

Figure A4.6: Linear Interpolated Path of DMABN with CASPT2

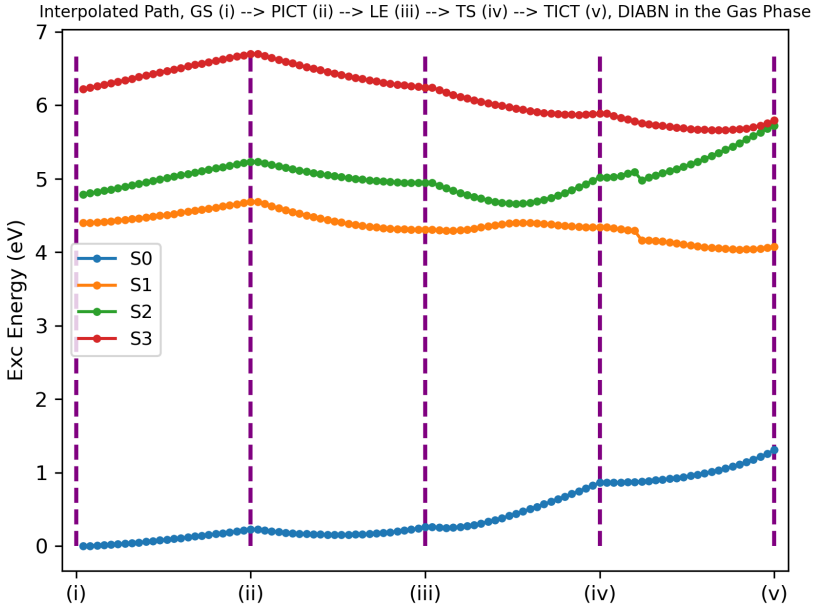

(a) CASPT2 (12,11), Gas Phase

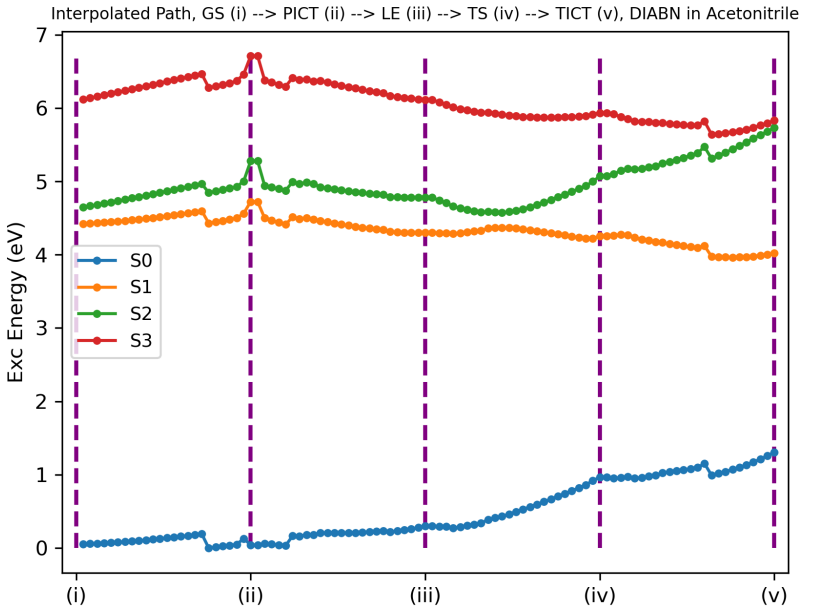

(b) CASPT2 (12,11), Acetonitrile

Figure A4.7: Linear Interpolated Path of DIABN with CASPT2

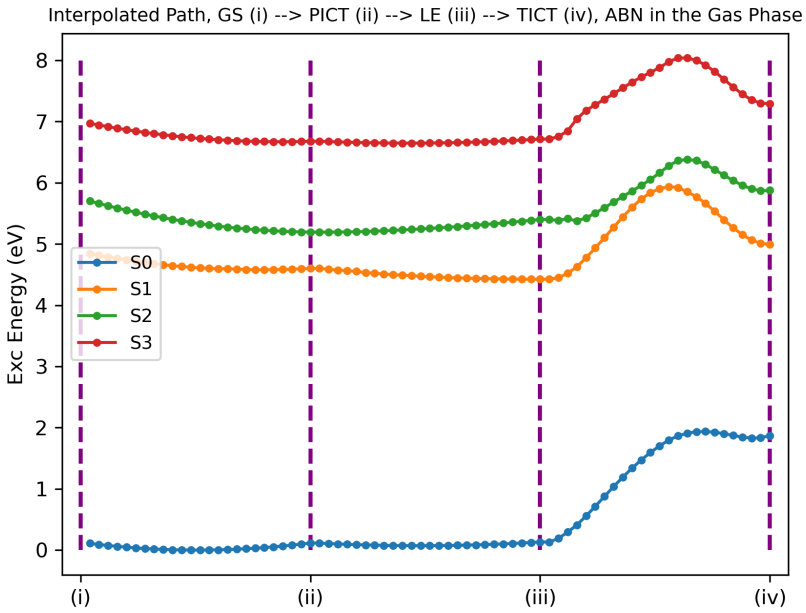

(a) CASPT2 (12,11), Gas Phase

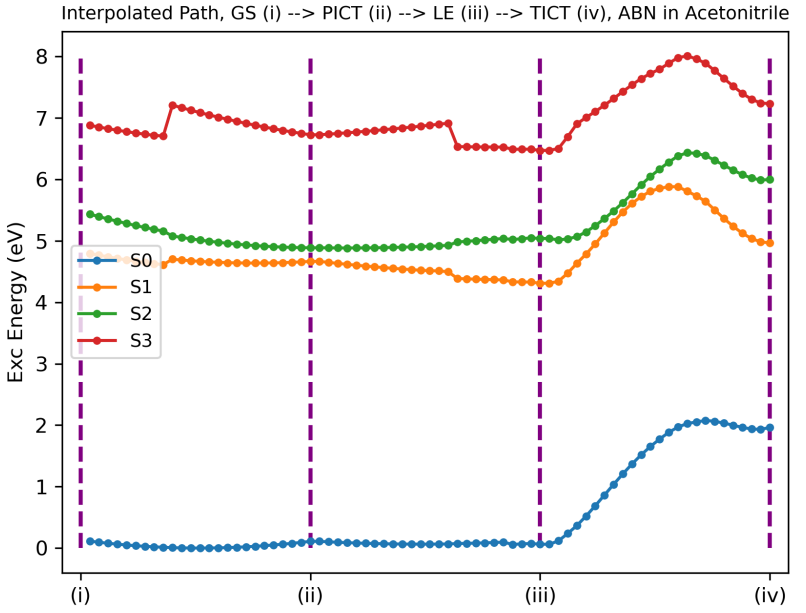

(b) CASPT2 (12,11), Acetonitrile

Figure A4.8: Linear Interpolated Path of ABN with CASPT2 (No transition state, S1-TICT not a minimum)

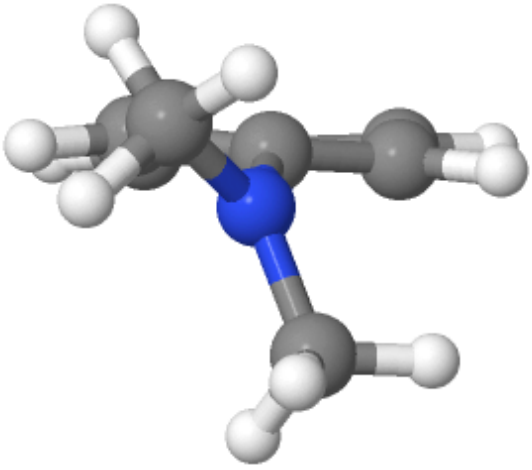

(a) Transition State for DMABN, optimized with CASPT2 (12,11)

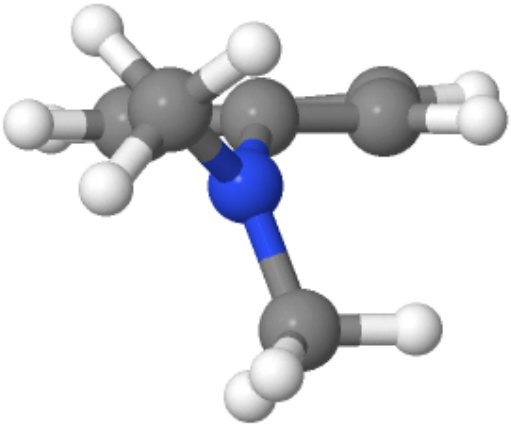

(b) Transition State for DMABN, optimized with CASPT2 (12,11) nudged via its imaginary frequency

Figure A4.9: Transition State of DMABN, CASPT2(12,11)

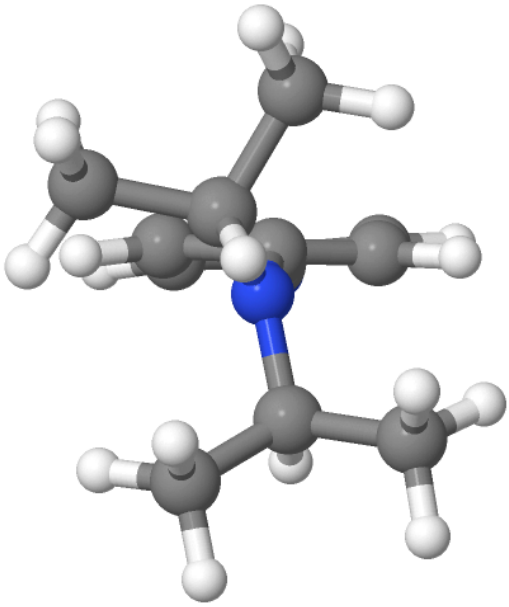

(a) Transition State for DIABN, optimized with CASPT2 (12,11)

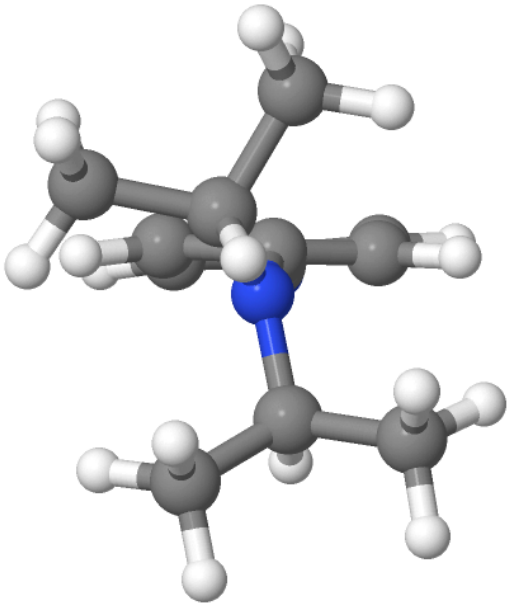

(b) Transition State for DIABN, optimized with CASPT2 (12,11) nudged via its imaginary frequency

Figure A4.10: Transition State of DIABN, CASPT2(12,11)

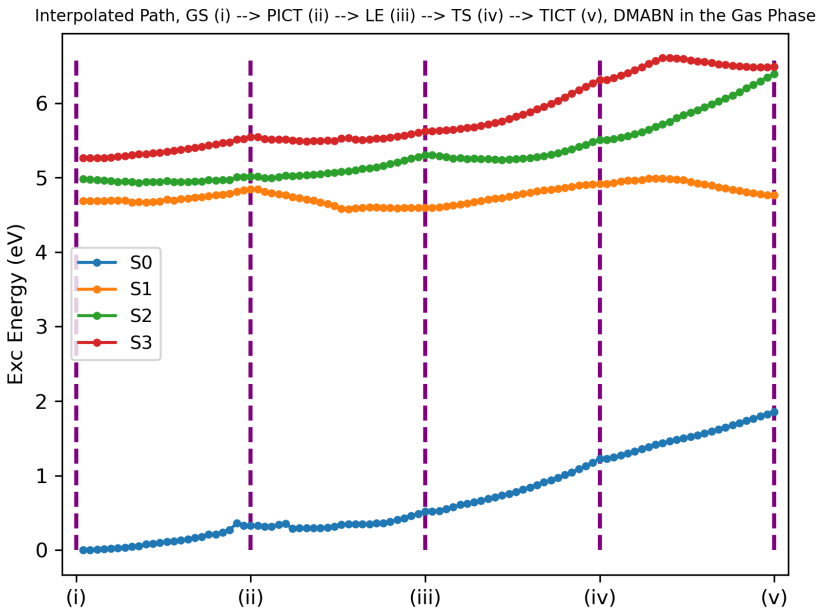

(a) DFT/MRCI(2), Gas Phase

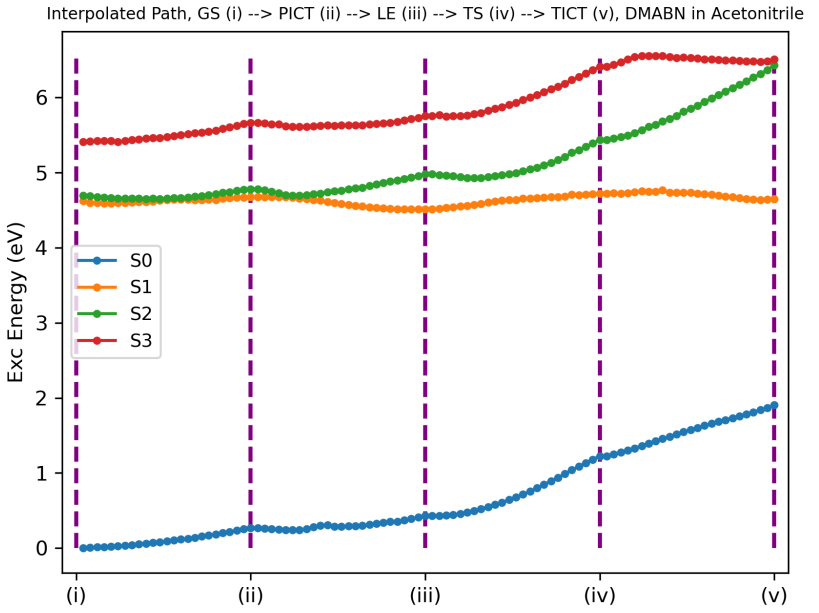

(b) DFT/MRCI(2), Acetonitrile

Figure A4.11: Linear Interpolated Path of DMABN with CASPT2 structures (energies eval. with DFT/MRCI(2)

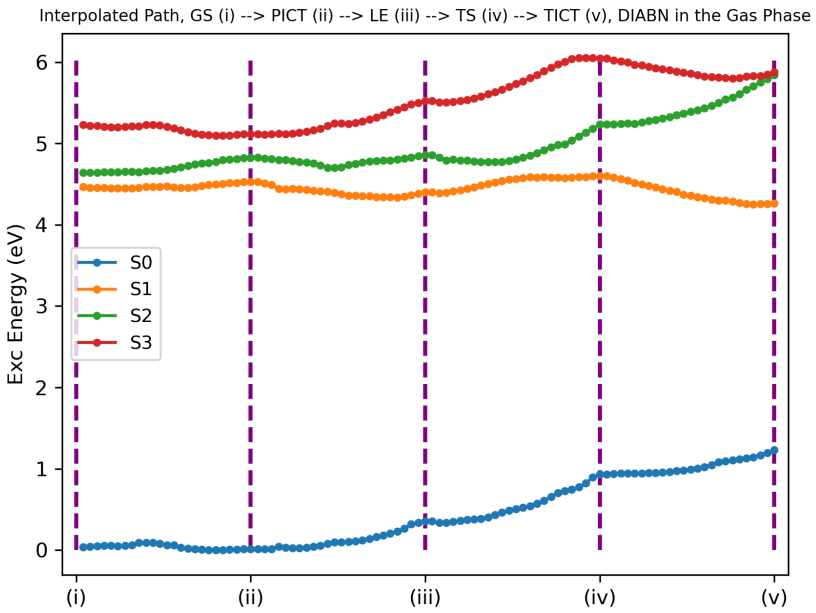

(a) DFT/MRCI(2), Gas Phase

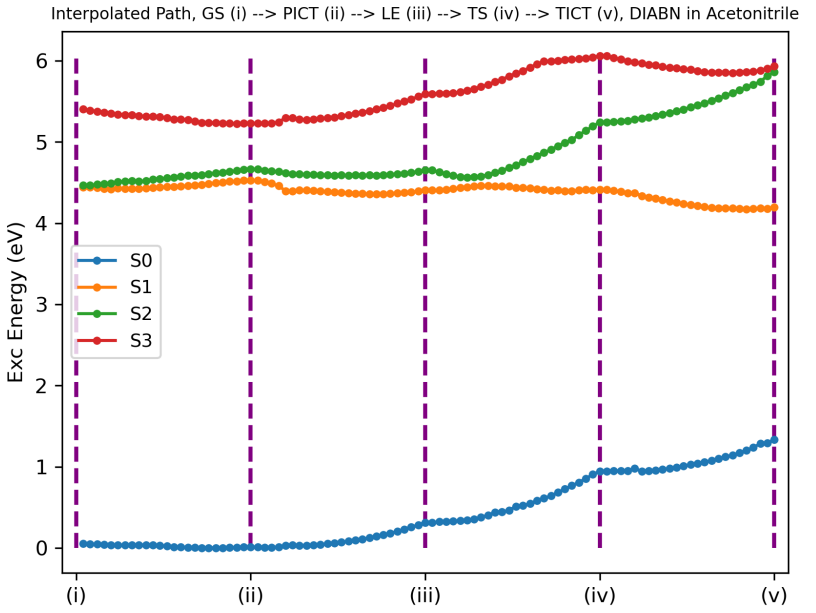

(b) DFT/MRCI(2), Acetonitrile

Figure A4.12: Linear Interpolated Path of DIABN with CASPT2 structures (energies eval. with DFT/MRCI(2)

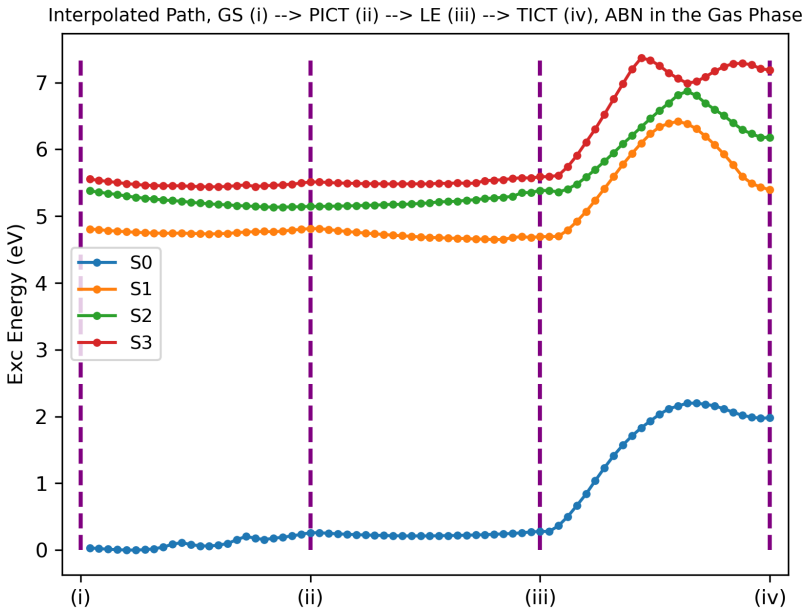

(a) DFT/MRCI(2), Gas Phase

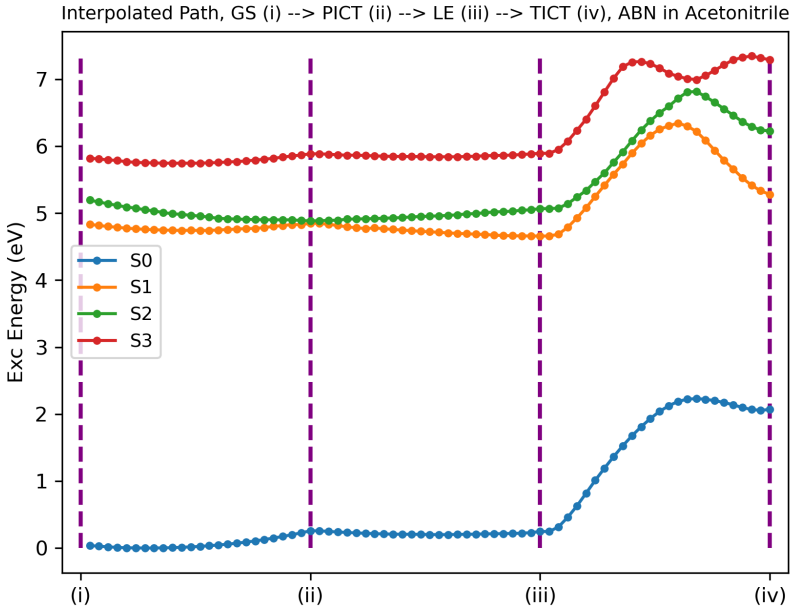

(b) DFT/MRCI(2), Acetonitrile

Figure A4.13: Linear Interpolated Path of ABN with CASPT2 structures (energies eval. with DFT/MRCI(2)

A5: Relevant excited state structures of DIABN and ABN

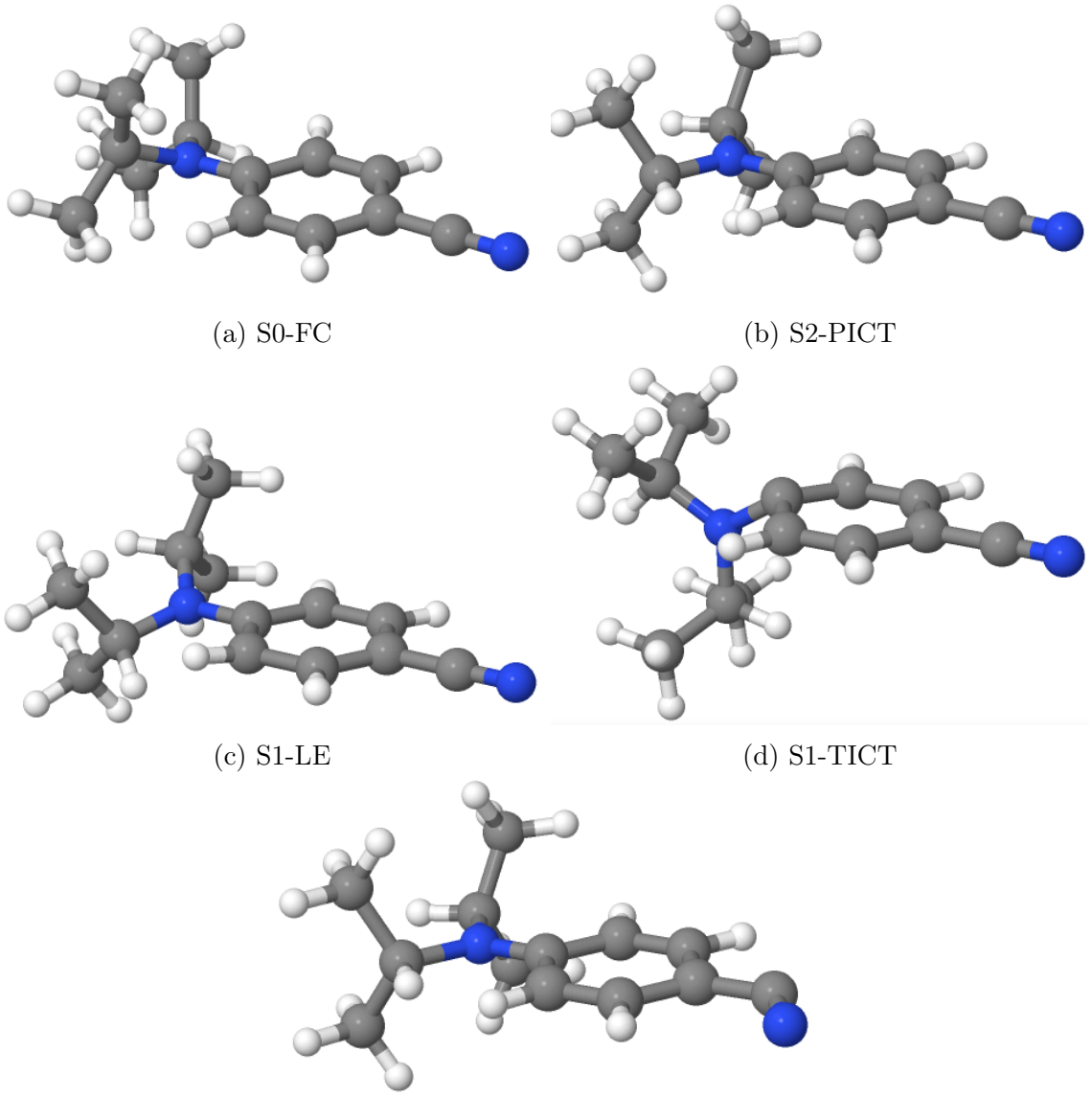

(a) S0-FC

(b) S2-PICT

(c) S1-LE

(d) S1-TICT

(e) S1-$\pi\sigma*$

Figure A5.1: An overview of the ground and excited state geometries of Diisopropylamino benzonitrile (DIABN)

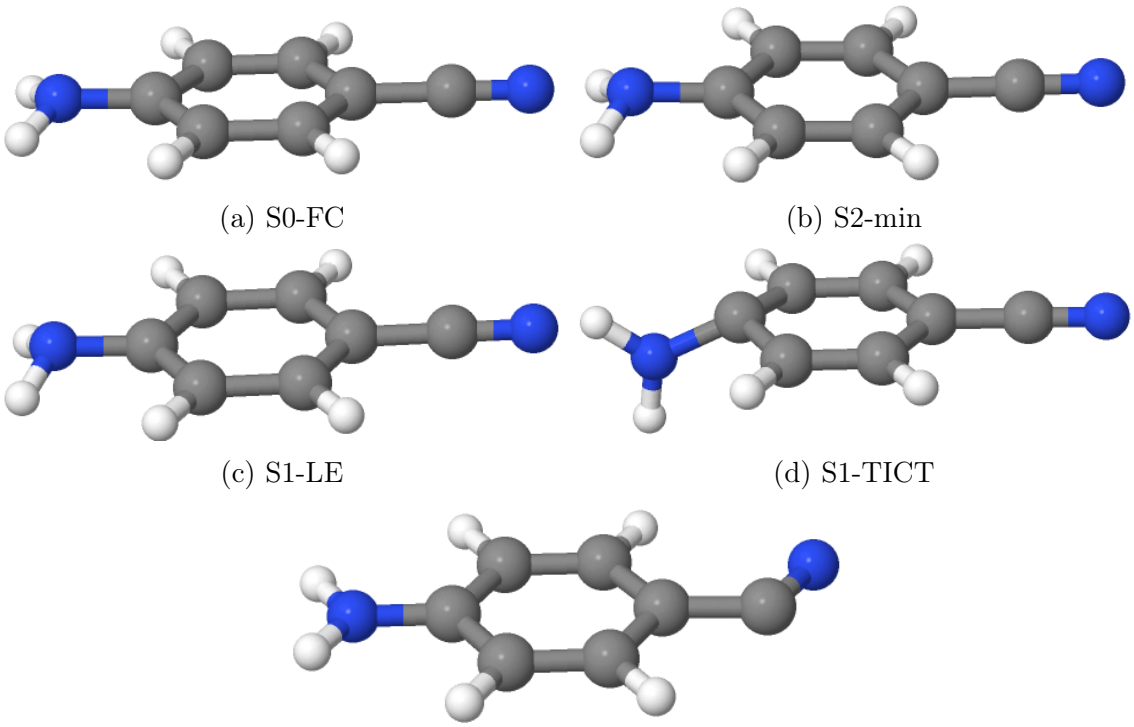

(a) S0-FC

(b) S2-min

(c) S1-LE

(d) S1-TICT

(e) S1-$\pi\sigma*$

Figure A5.2: An overview of the ground and excited state geometries of Aminobenzonitrile (ABN)

A6: RRKM curves. Change in charge transfer rate with internal energy available.

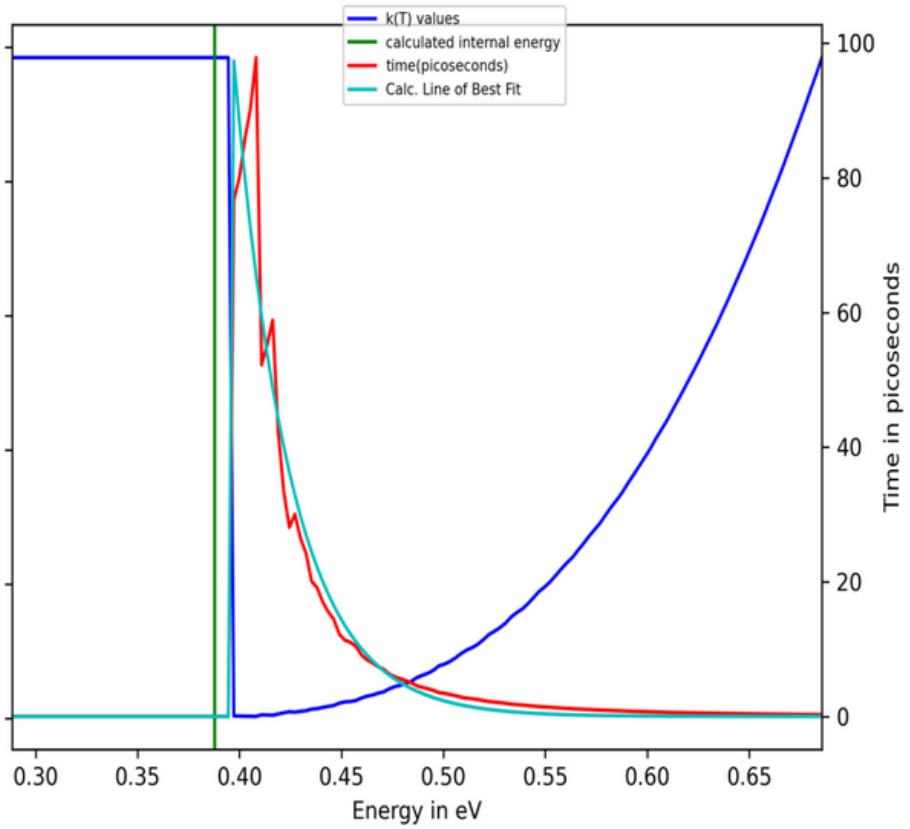

(a) DFT/MRCI(2), Gas Phase

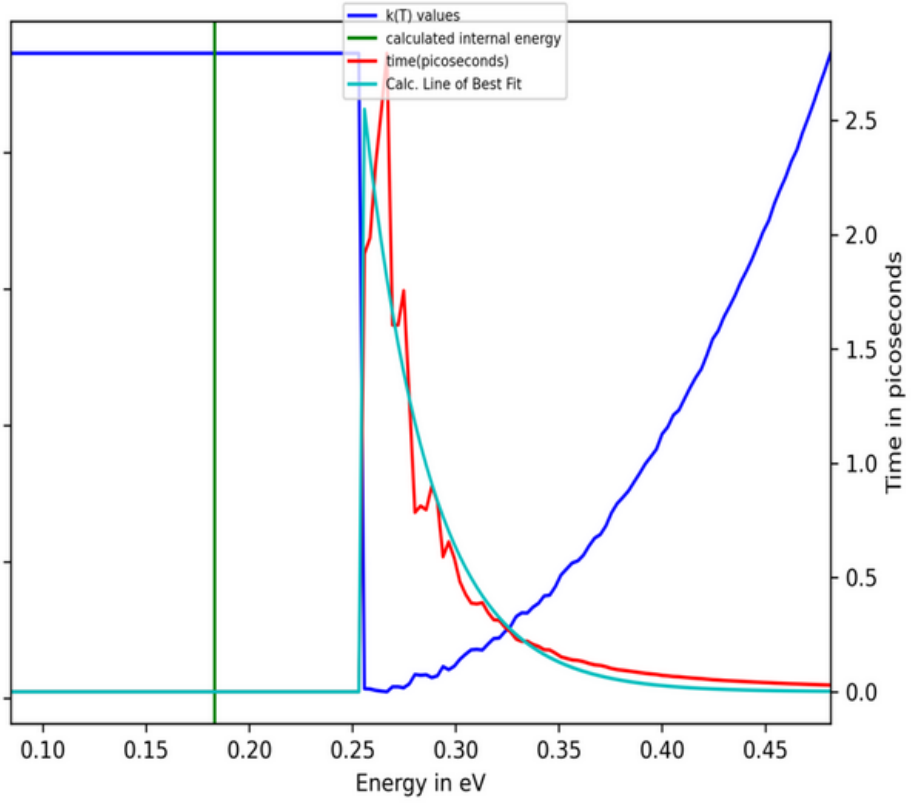

(b) DFT/MRCI(2), Acetonitrile

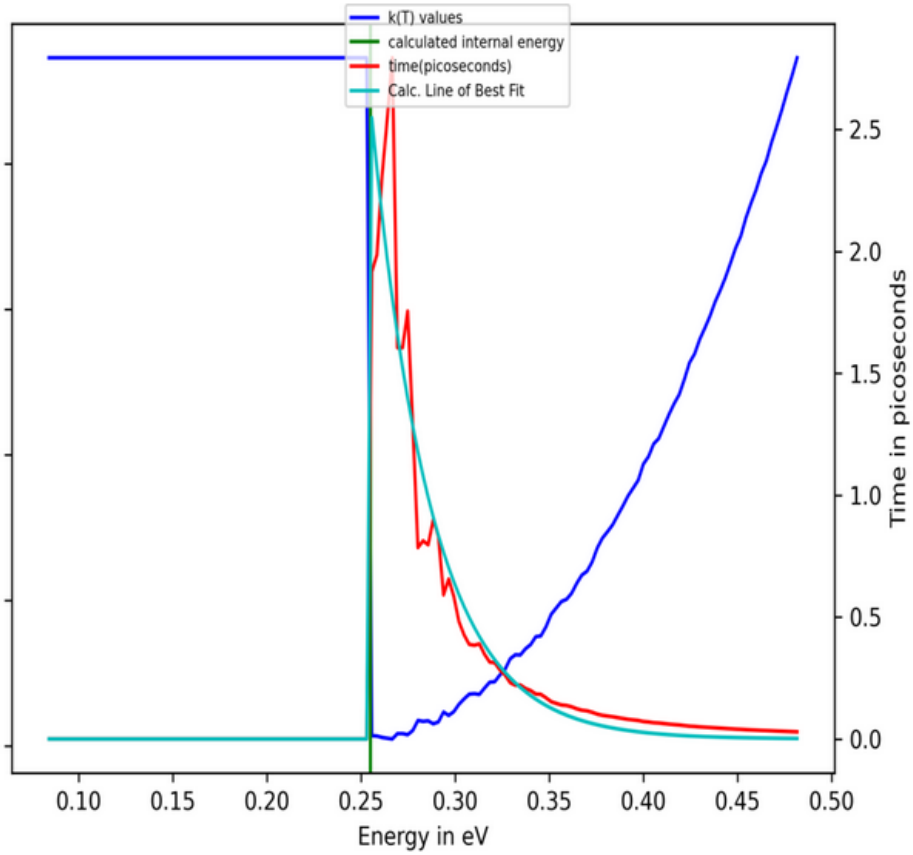

(c) DFT/MRCI(2), Acetonitrile (Shift of +0.07 eV)

Figure A6.1: RRKM Curves. DMABN, with DFT/MRCI(2).

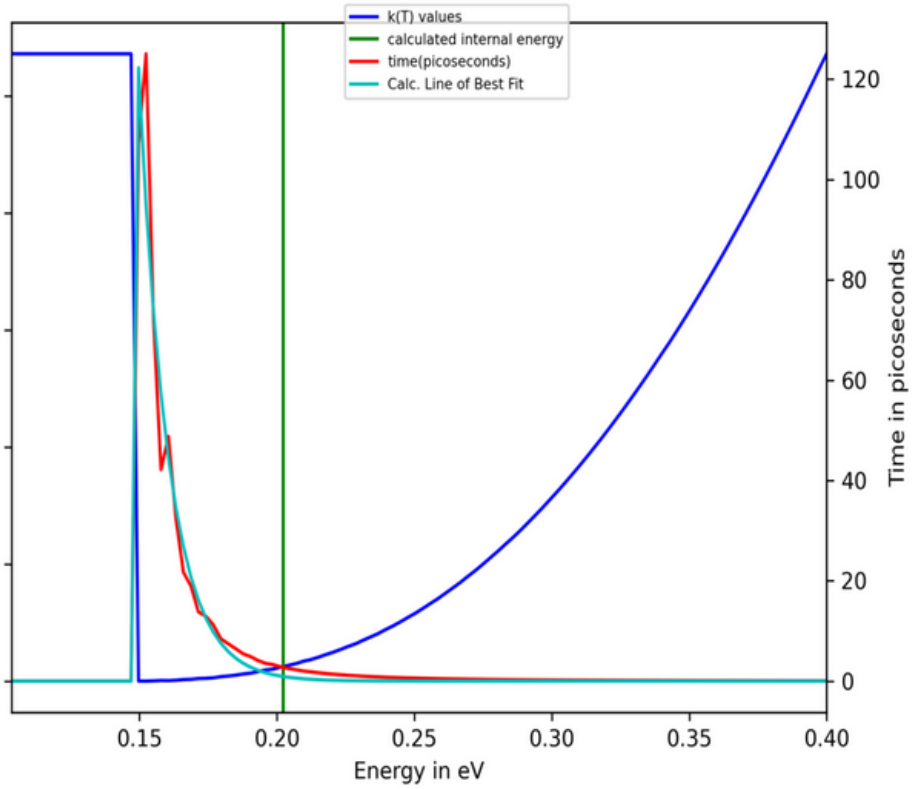

(a) DFT/MRCI(2), Gas Phase

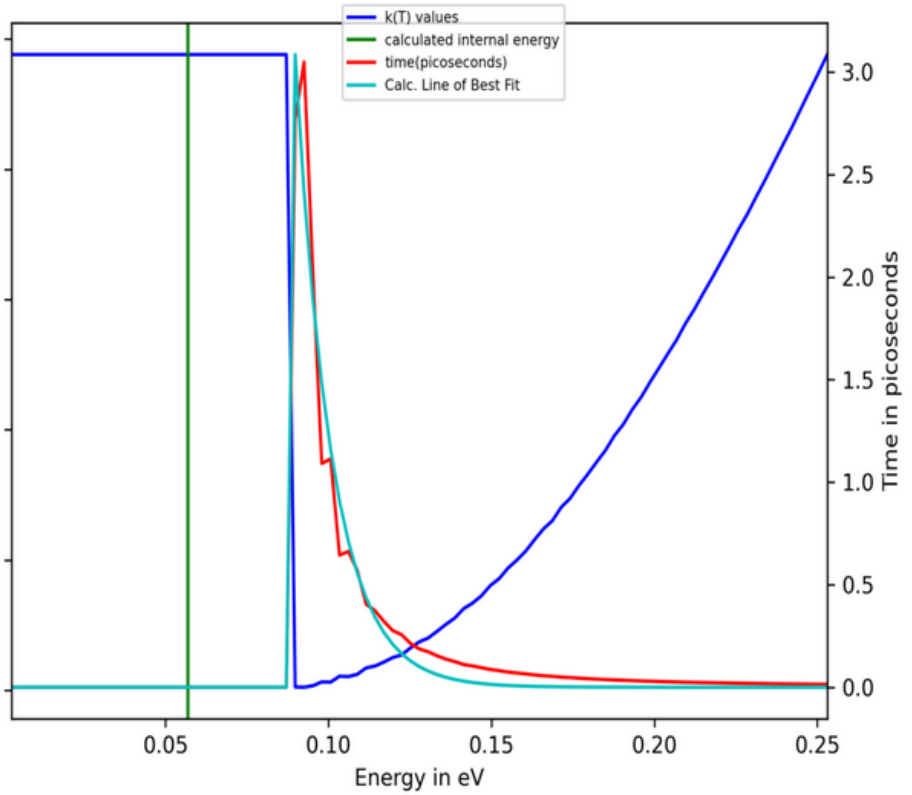

(b) DFT/MRCI(2), Acetonitrile

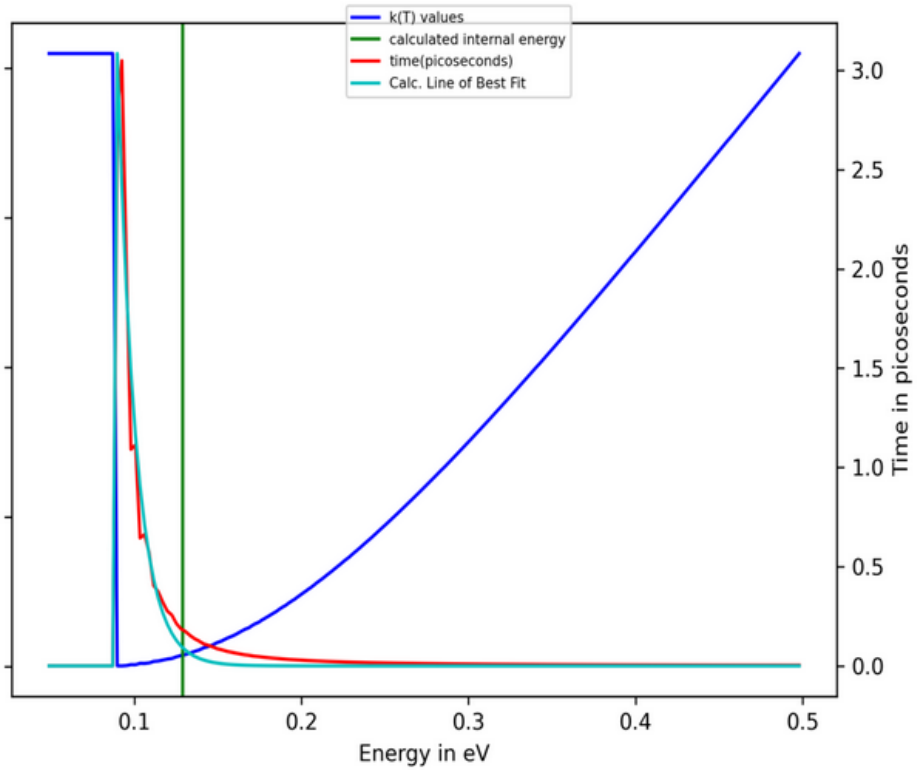

(c) DFT/MRCI(2), Acetonitrile (Shift of +0.07 eV)

Figure A6.2: RRKM Curves. DIABN, with DFT/MRCI(2).

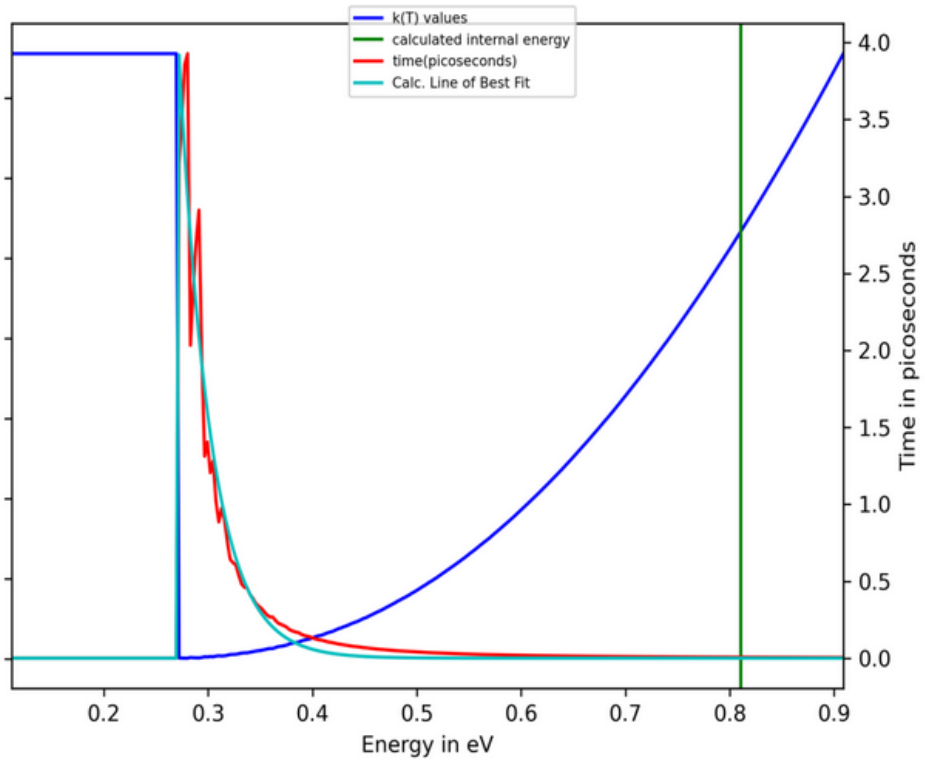

(a) CASPT2(12,11), Gas Phase

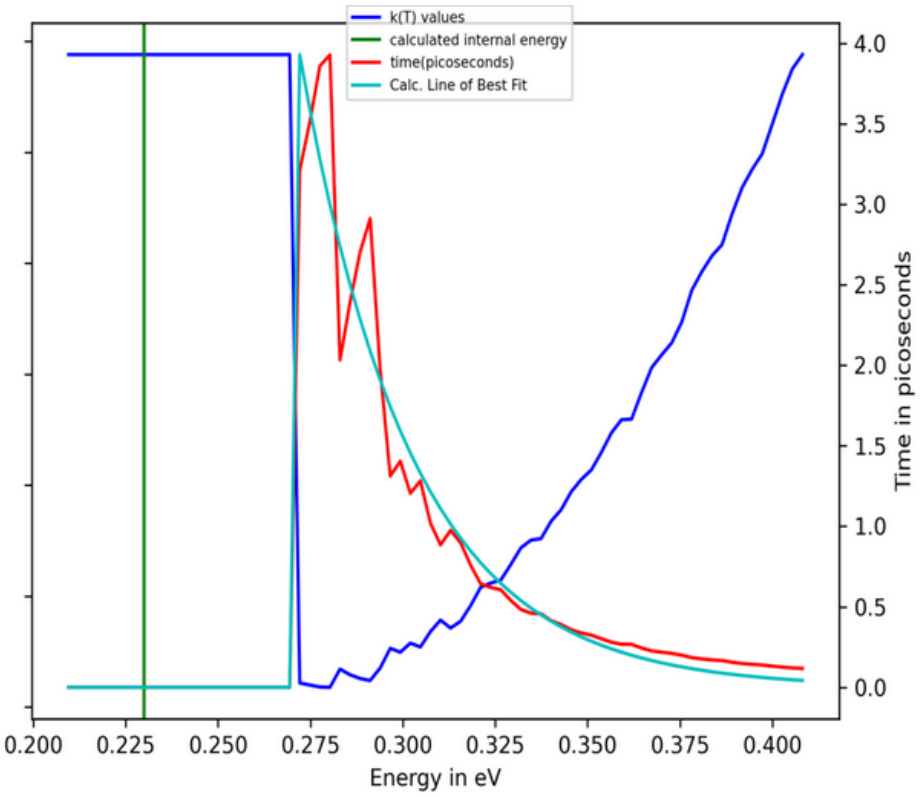

(b) CASPT2(12,11), Gas Phase (Shift of -0.58 eV)

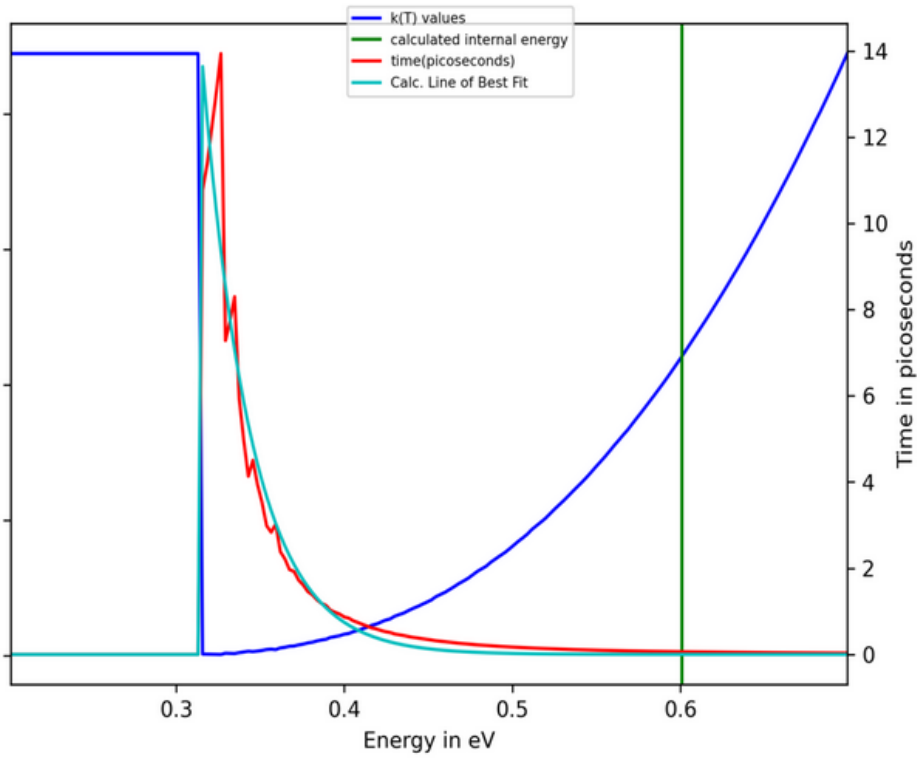

(c) CASPT2(12,11), Acetonitrile

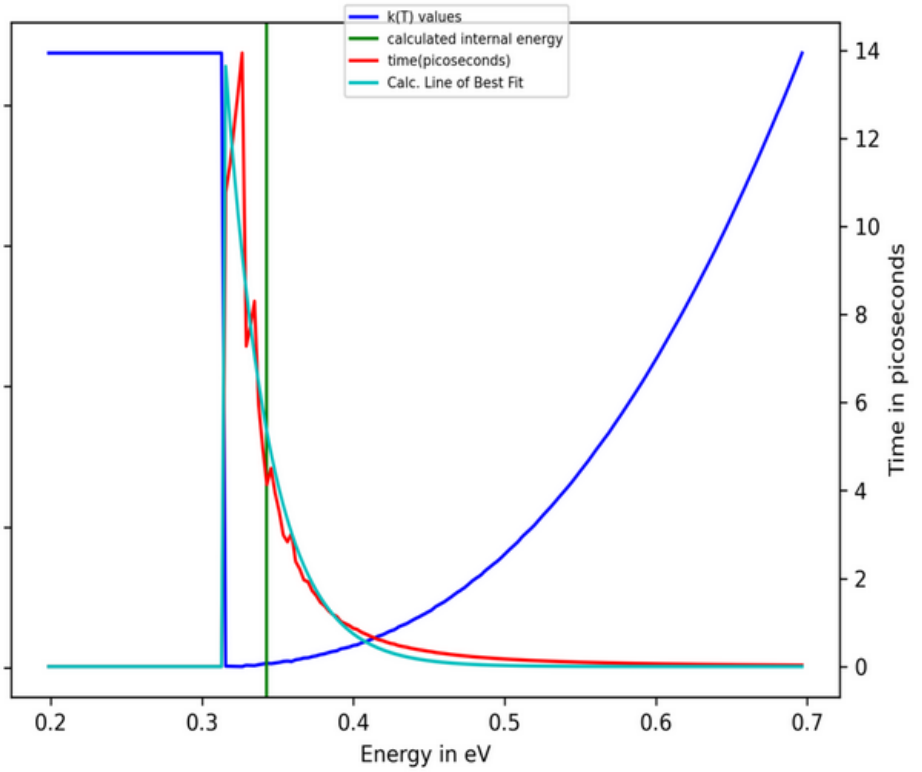

(d) CASPT2(12,11), Acetonitrile (Shift of -0.26 eV)

Figure A6.3: RRKM Curves. DMABN, with CASPT2.

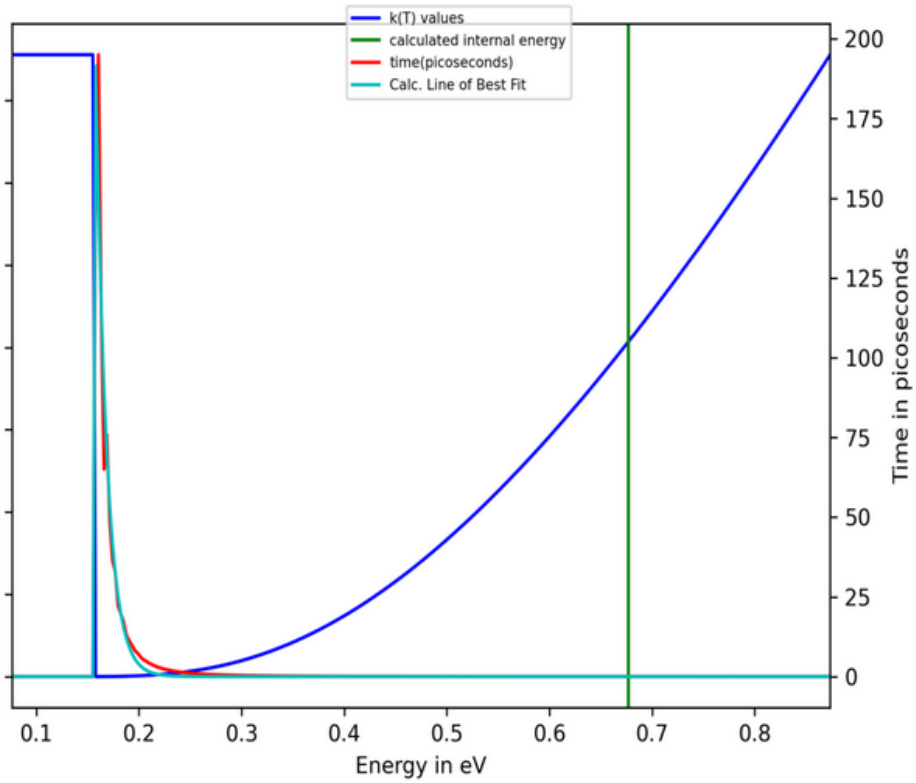

(a) CASPT2(12,11), Gas Phase

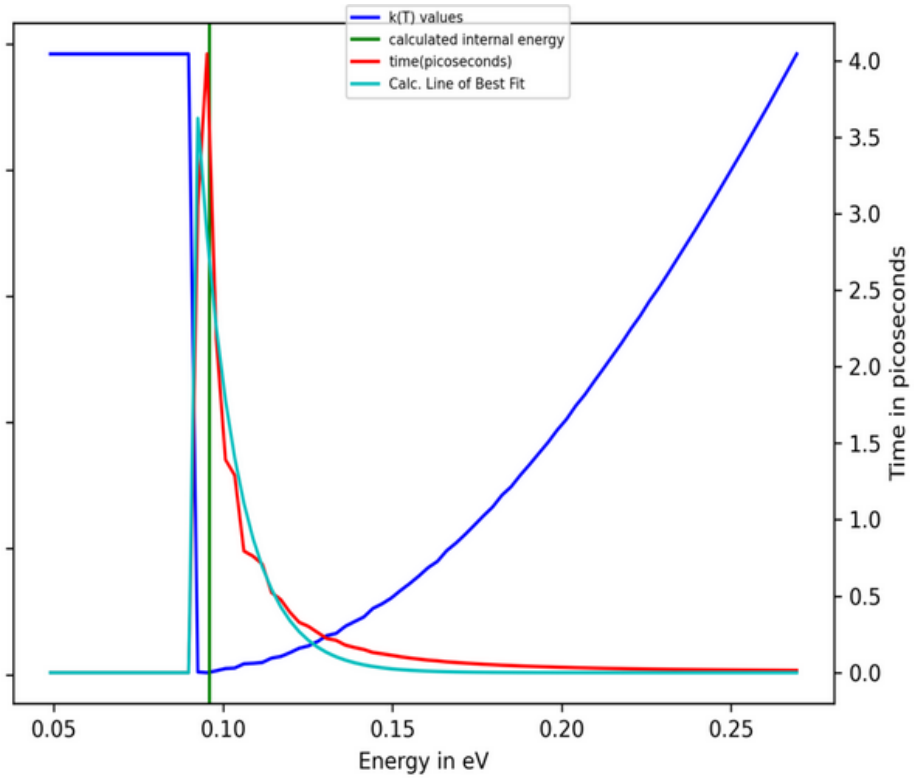

(b) CASPT2(12,11), Gas Phase (Shift of -0.58 eV)

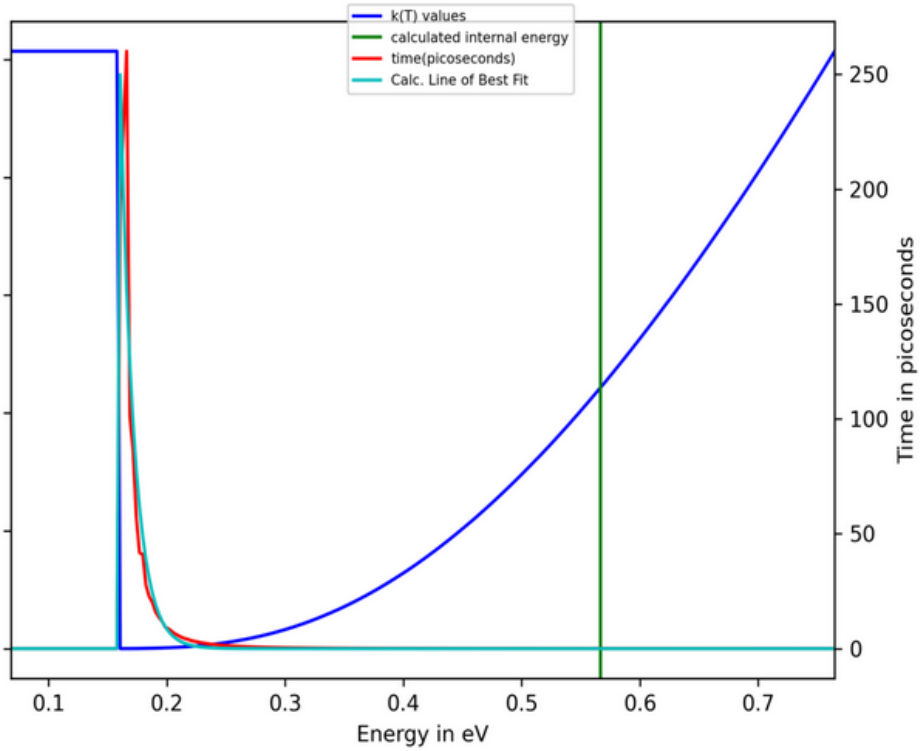

(c) CASPT2(12,11), Acetonitrile

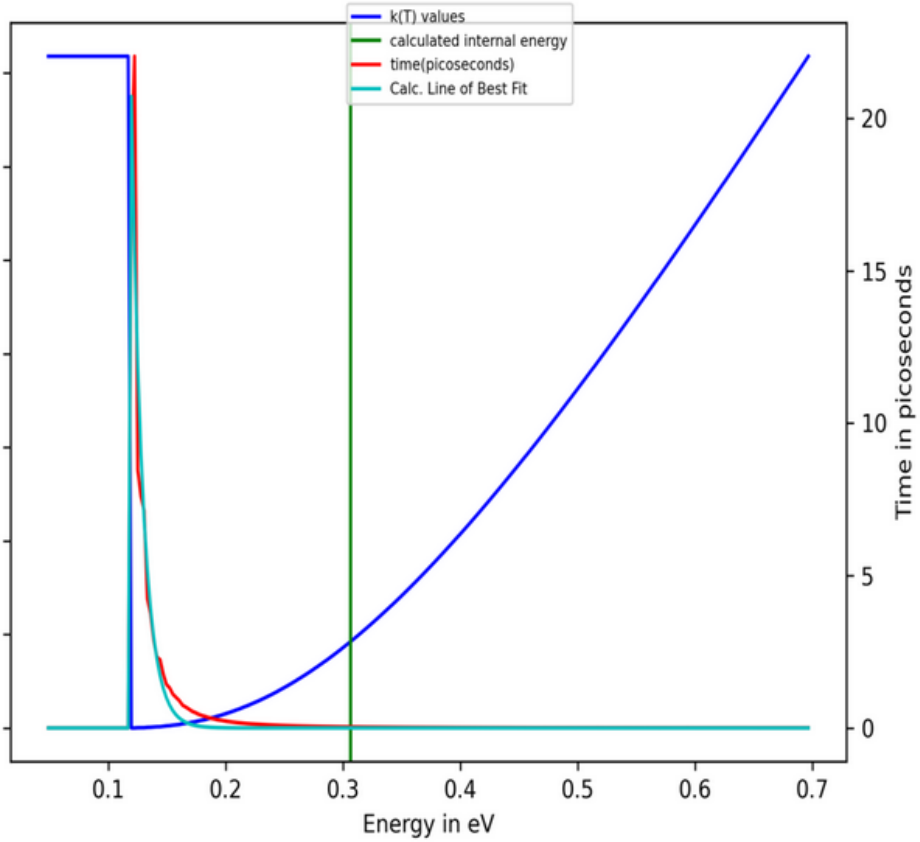

(d) CASPT2(12,11), Acetonitrile (Shift of -0.26 eV)

Figure A6.4: RRKM Curves. DIABN, with CASPT2.

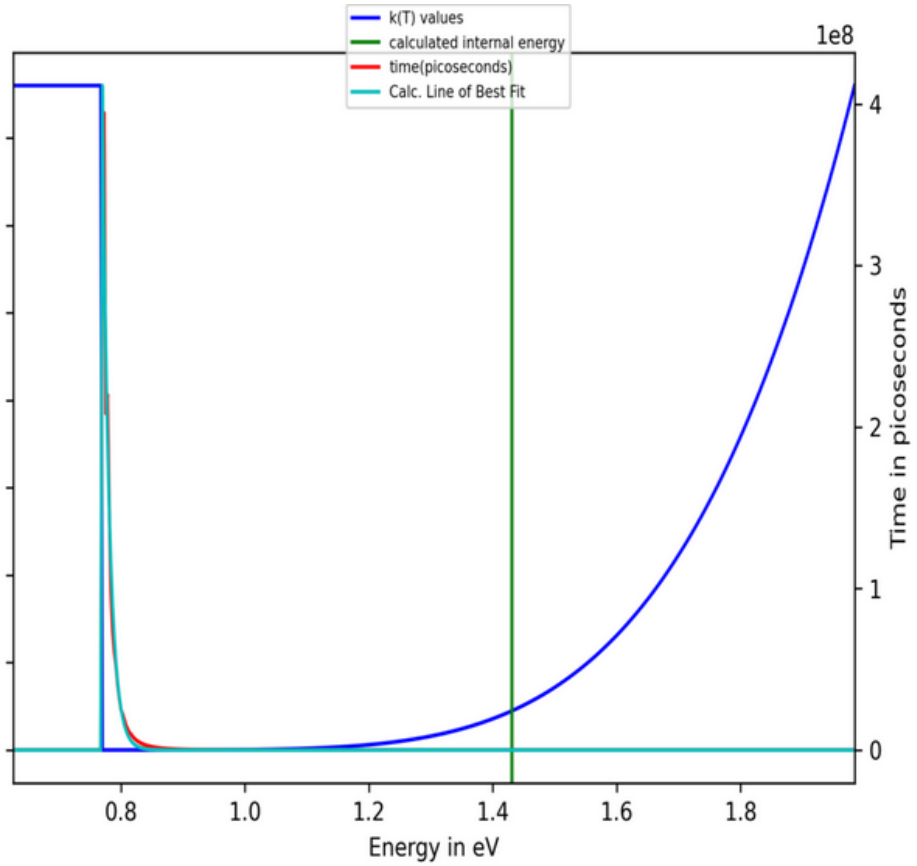

(a) CASSCF(12,11), Gas Phase

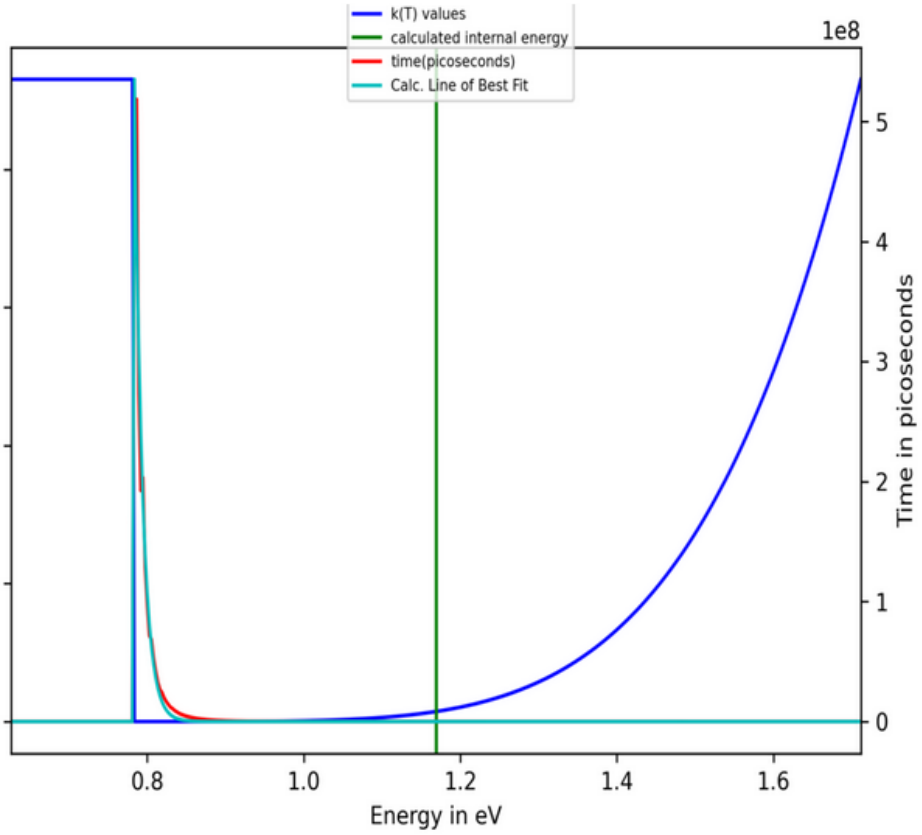

(b) CASSCF(12,11), Acetonitrile

Figure A6.5: RRKM Curves. DMABN, with CASSCF.

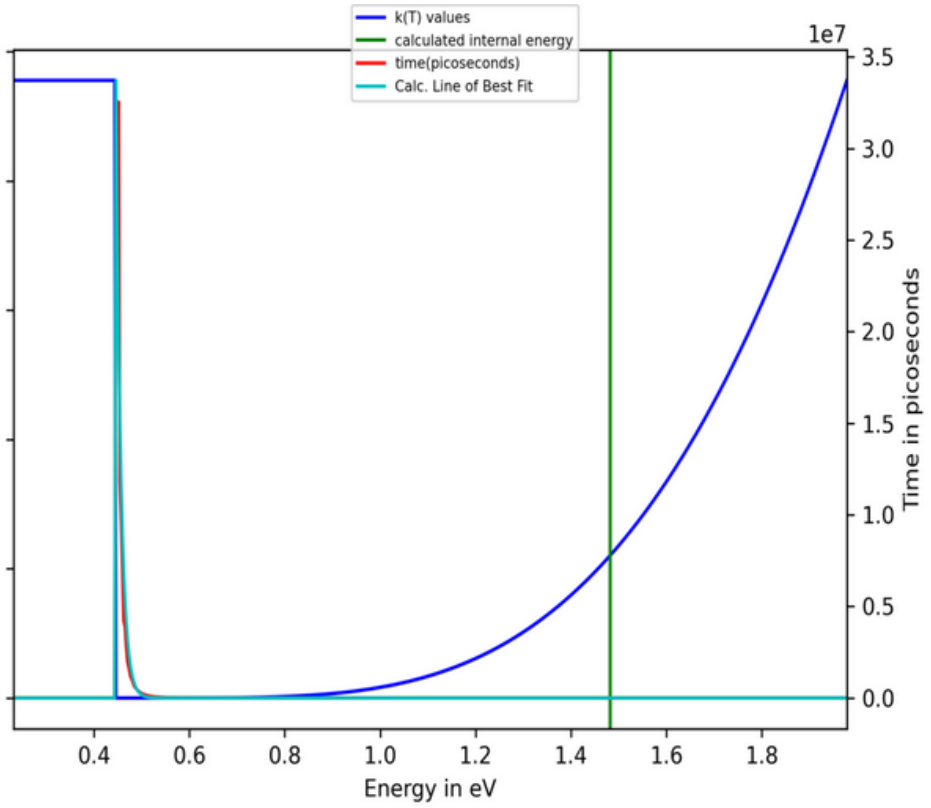

(a) CASSCF(12,11), Gas Phase

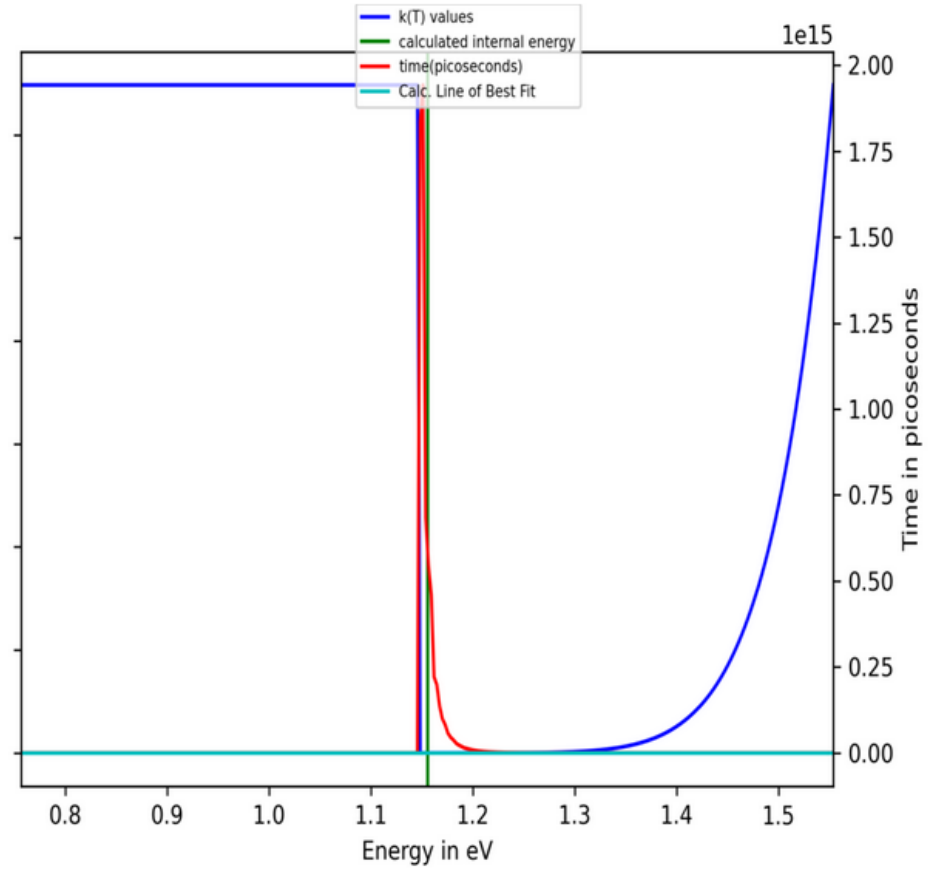

(b) CASSCF(12,11), Acetonitrile

Figure A6.6: RRKM Curves. DIABN, with CASSCF.

A7: Interpolated Paths between excited state structures of DMABN

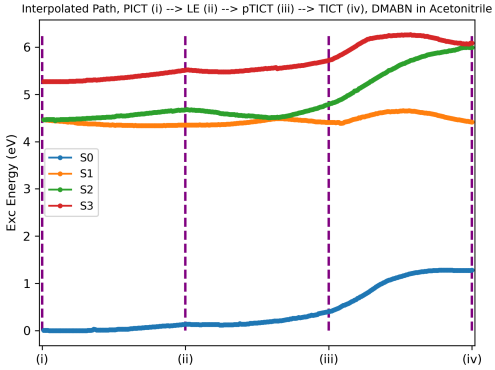

Figure A7.1: LIIC of DMABN, PICT $\rightarrow$ LE $\rightarrow$ pTICT $\rightarrow$ TICT. Energies computed by DFT/MRCI(2), in Acetonitrile.

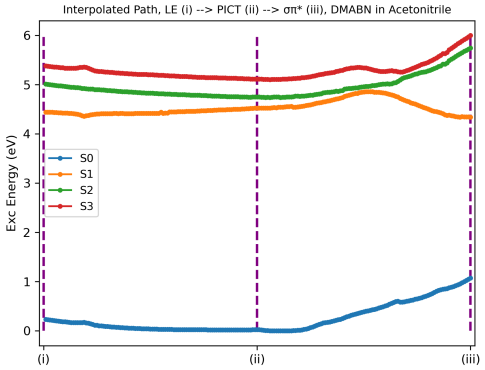

(a) LE → PICT → $\pi\sigma*$

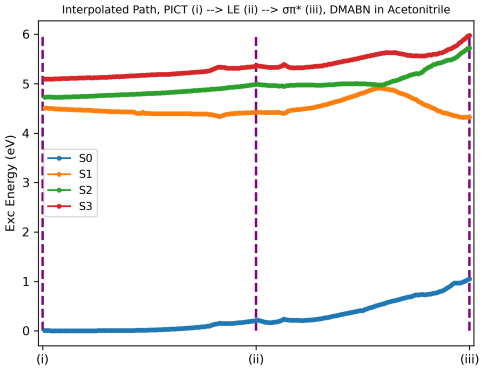

(b) PICT → LE → $\pi\sigma*$

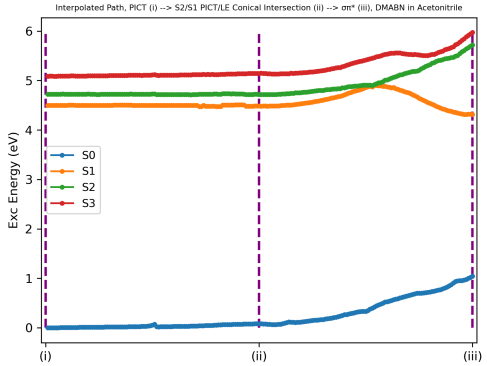

(c) PICT → S2/S1 CI → $\pi\sigma*$

Figure A7.2: LIICs of DMABN, evaluating the transition state barrier of the population of the $S_1(\mathbf{R}_{\pi\sigma*})$ state. Energies computed by DFT/MRCI(2), in Acetonitrile.

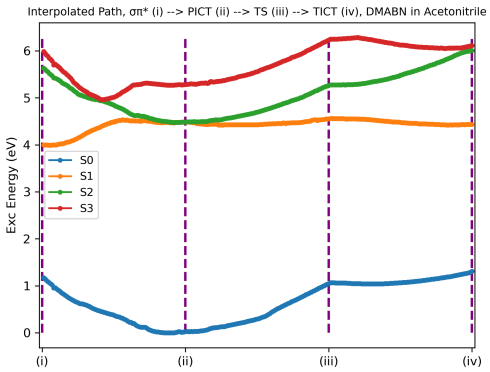

(a) $\pi\sigma*$ → PICT → pTICT → TICT

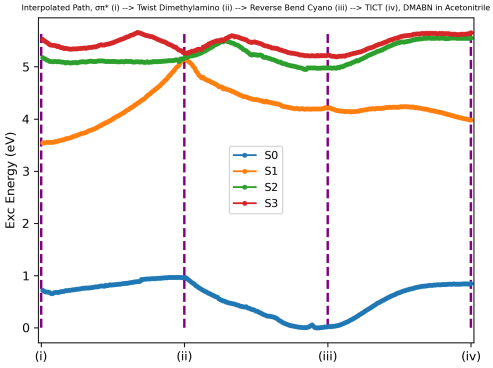

(b) $\pi\sigma*$ → Dimethylamino Twist → Reverse Cyano Bend → TICT

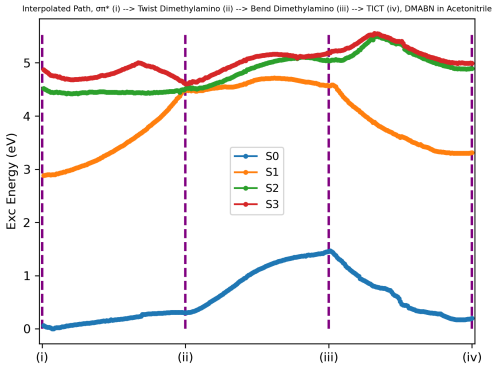

(c) $\pi\sigma*$ → Dimethylamino Twist → Dimethylamino Bend → TICT

Figure A7.3: LIICs of DMABN, evaluating the transition barriers of the population of the $S_1(\mathbf{R}_{TICT})$ state from the $S_1(\mathbf{R}_{\pi\sigma*})$ state. Energies computed by DFT/MRCI(2), in Acetonitrile.

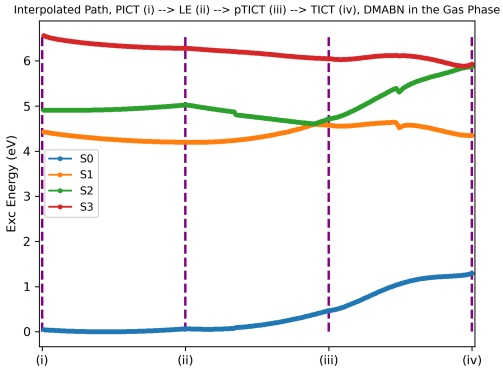

Figure A7.4: LIIC of DMABN, PICT → LE → pTICT → TICT. Energies computed by CASPT2, in the Gas Phase.

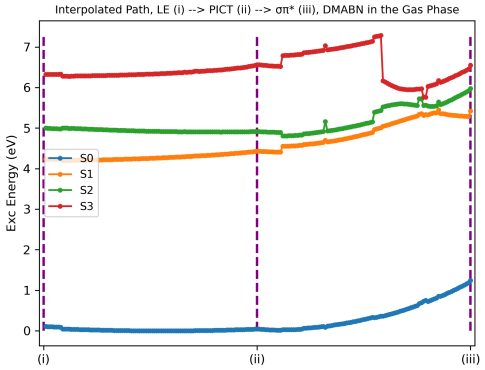

(a) LE $\rightarrow$ PICT $\rightarrow$ $\pi\sigma*$

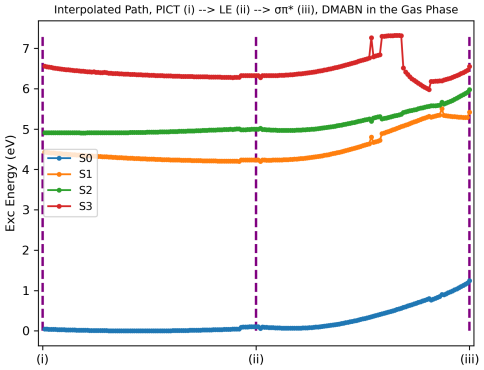

(b) PICT $\rightarrow$ LE $\rightarrow$ $\pi\sigma*$

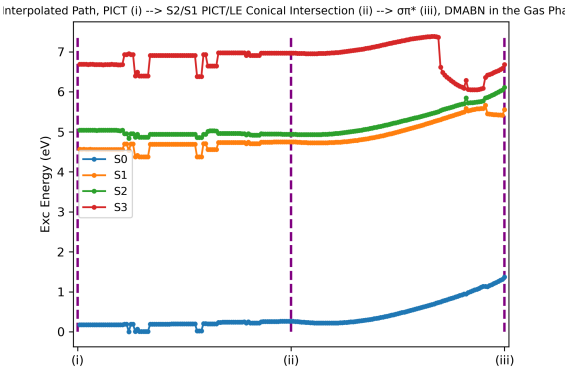

(c) PICT $\rightarrow$ S2/S1 CI $\rightarrow$ $\pi\sigma*$

Figure A7.5: LIICs of DMABN, evaluating the transition state barrier of the population of the $S_1(\mathbf{R}_{\pi\sigma*})$ state. Energies computed by CASPT2, in the Gas Phase.

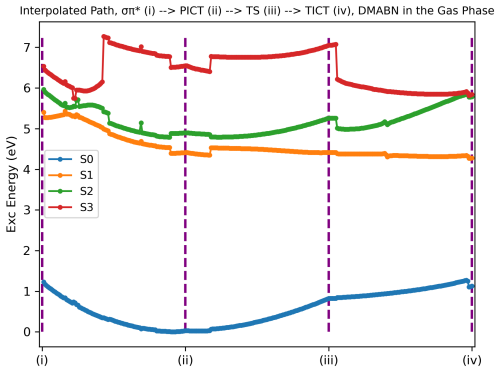

(a) $\pi\sigma*$ → PICT → pTICT → TICT

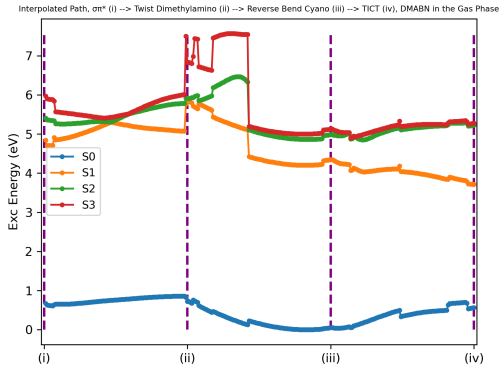

(b) $\pi\sigma*$ → Dimethylamino Twist → Reverse Cyano Bend → TICT

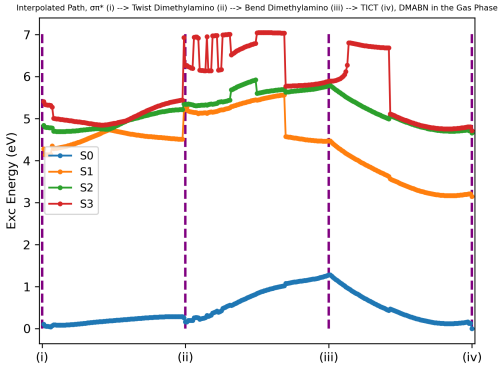

(c) $\pi\sigma*$ → Dimethylamino Twist → Dimethylamino Bend → TICT

Figure A7.6: LIICs of DMABN, evaluating the transition barriers of the population of the $S_1(\mathbf{R}_{TICT})$ state from the $S_1(\mathbf{R}_{\pi\sigma*})$ state. Energies computed by CASPT2, in the Gas Phase.

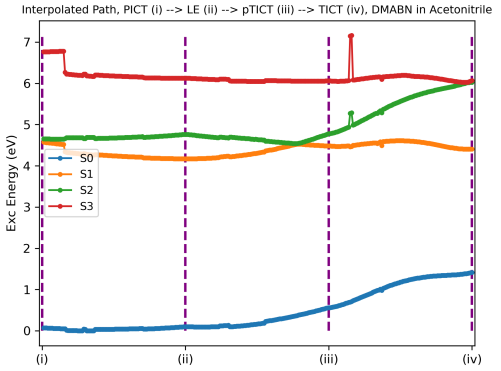

Figure A7.7: LIIC of DMABN, PICT → LE → pTICT → TICT. Energies computed by CASPT2, in Acetonitrile.

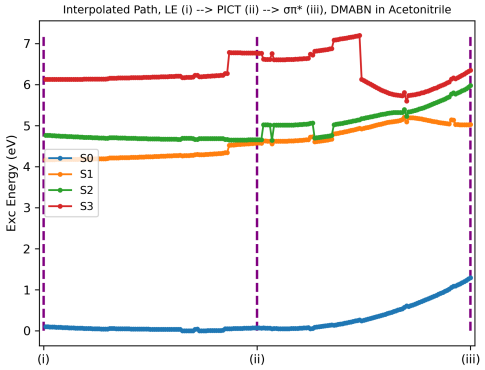

(a) LE → PICT → $\pi\sigma*$

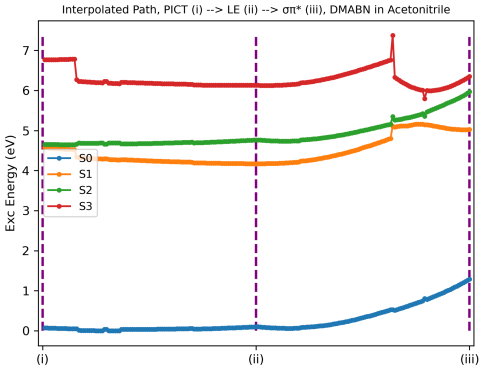

(b) PICT → LE → $\pi\sigma*$

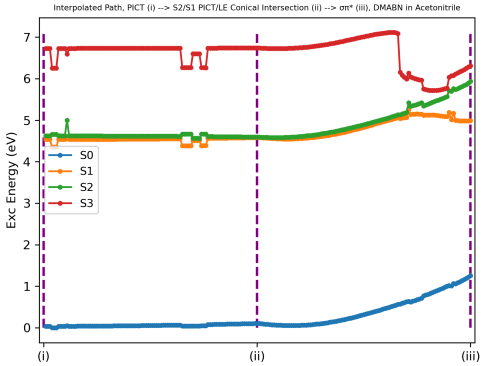

(c) PICT → S2/S1 CI → $\pi\sigma*$

Figure A7.8: LIICs of DMABN, evaluating the transition state barrier of the population of the $S_1(\mathbf{R}_{\pi\sigma*})$ state. Energies computed by CASPT2, in Acetonitrile.

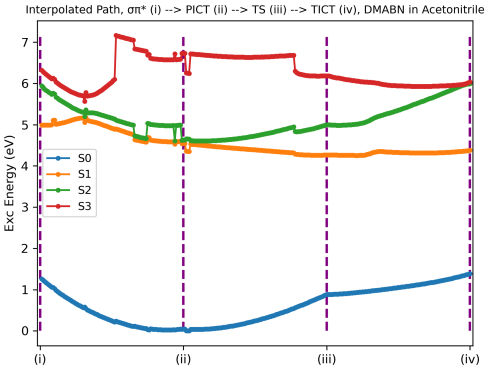

(a) $\pi\sigma*$ → PICT → pTICT → TICT

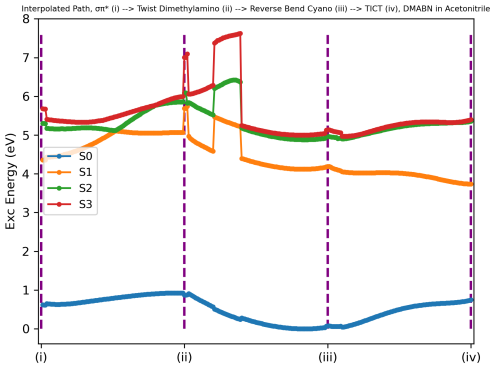

(b) $\pi\sigma*$ → Dimethylamino Twist → Reverse Cyano Bend → TICT

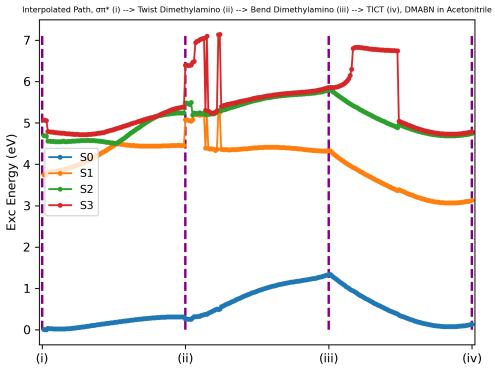

(c) $\pi\sigma*$ → Dimethylamino Twist → Dimethylamino Bend → TICT

Figure A7.9: LIICs of DMABN, evaluating the transition barriers of the population of the $S_1(\mathbf{R}_{TICT})$ state from the $S_1(\mathbf{R}_{\pi\sigma*})$ state. Energies computed by CASPT2, in Acetonitrile.

A8: Extended Absorbance/Fluorescence and Transient Absorption Spectrum, DMABN

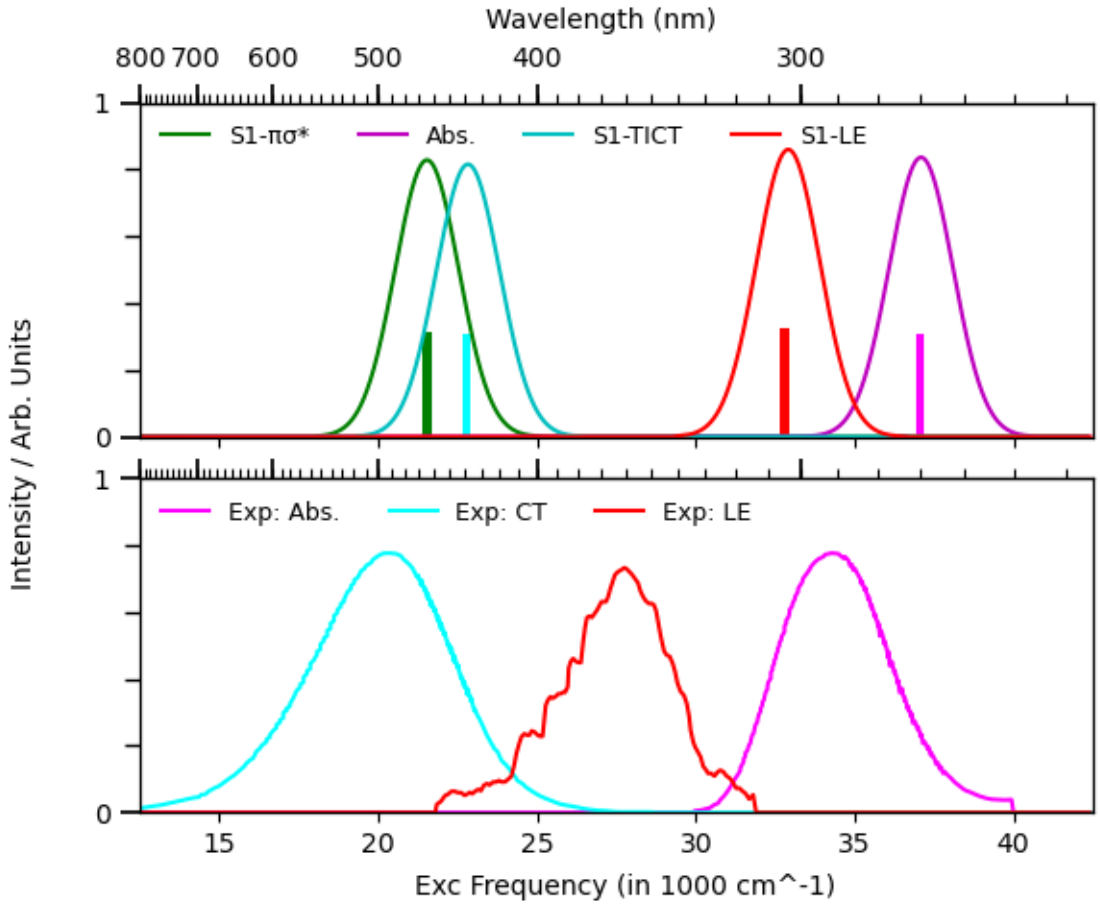

Figure A8.1: UV/Vis Absorption Spectrum of DMABN in Acetonitrile. Top: Spectrum computed with DFT/MRCI(2). Bottom: Experimental Spectrum.[9] The following osc strengths were altered for better visibility: S1-TICT(Osc Str x400), S1-LE(Osc Str x35), S1-$\pi\sigma*$ (Osc Str x6500), Exp-LE(Osc Str x25). The DFT/MRCI(2) results were unshifted.

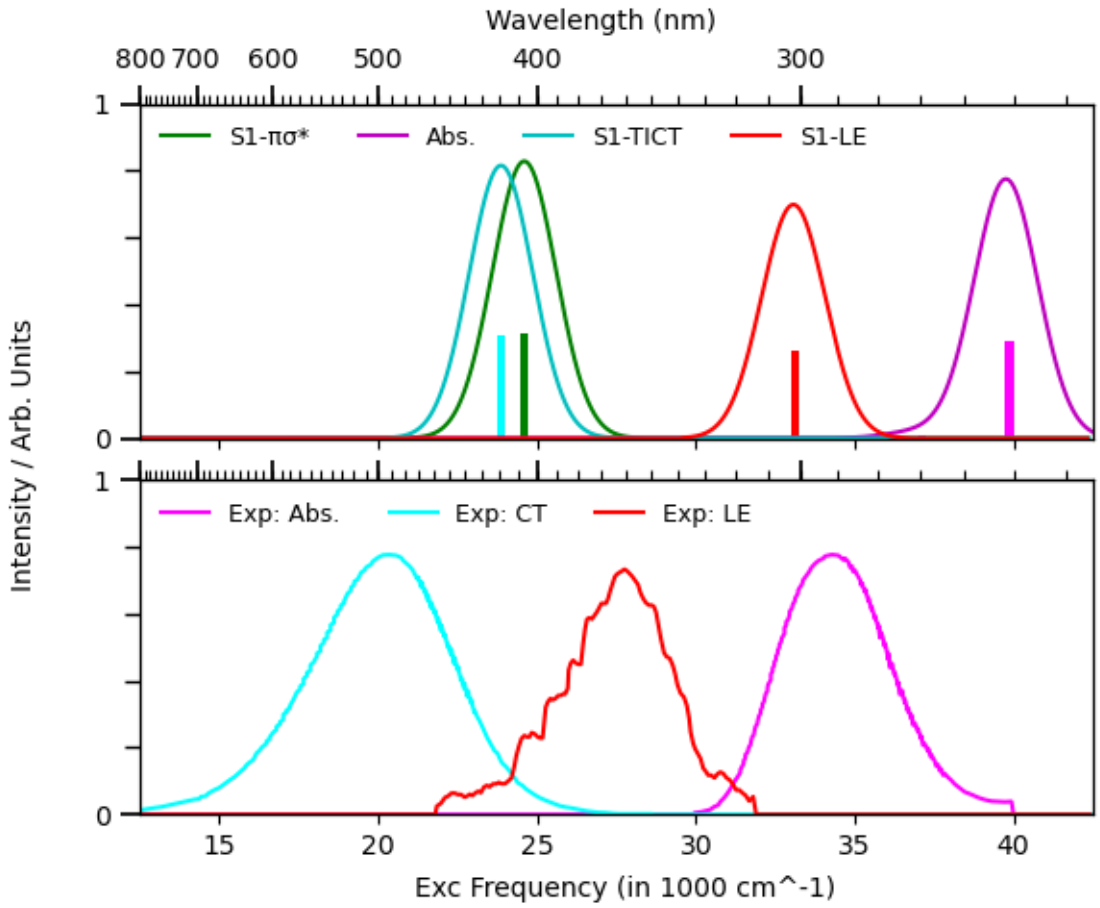

Figure A8.2: UV/Vis Absorption Spectrum of DMABN in the Gas Phase. Top: Spectrum computed with DFT/MRCI(2). Bottom: Experimental Spectrum.[9] The following osc strengths were altered for better visibility: S1-TICT(Osc Str x400), S1-LE(Osc Str x35), S1-$\pi\sigma*$(Osc Str x6500), Exp-LE(Osc Str x25). The DFT/MRCI(2) results were unshifted.

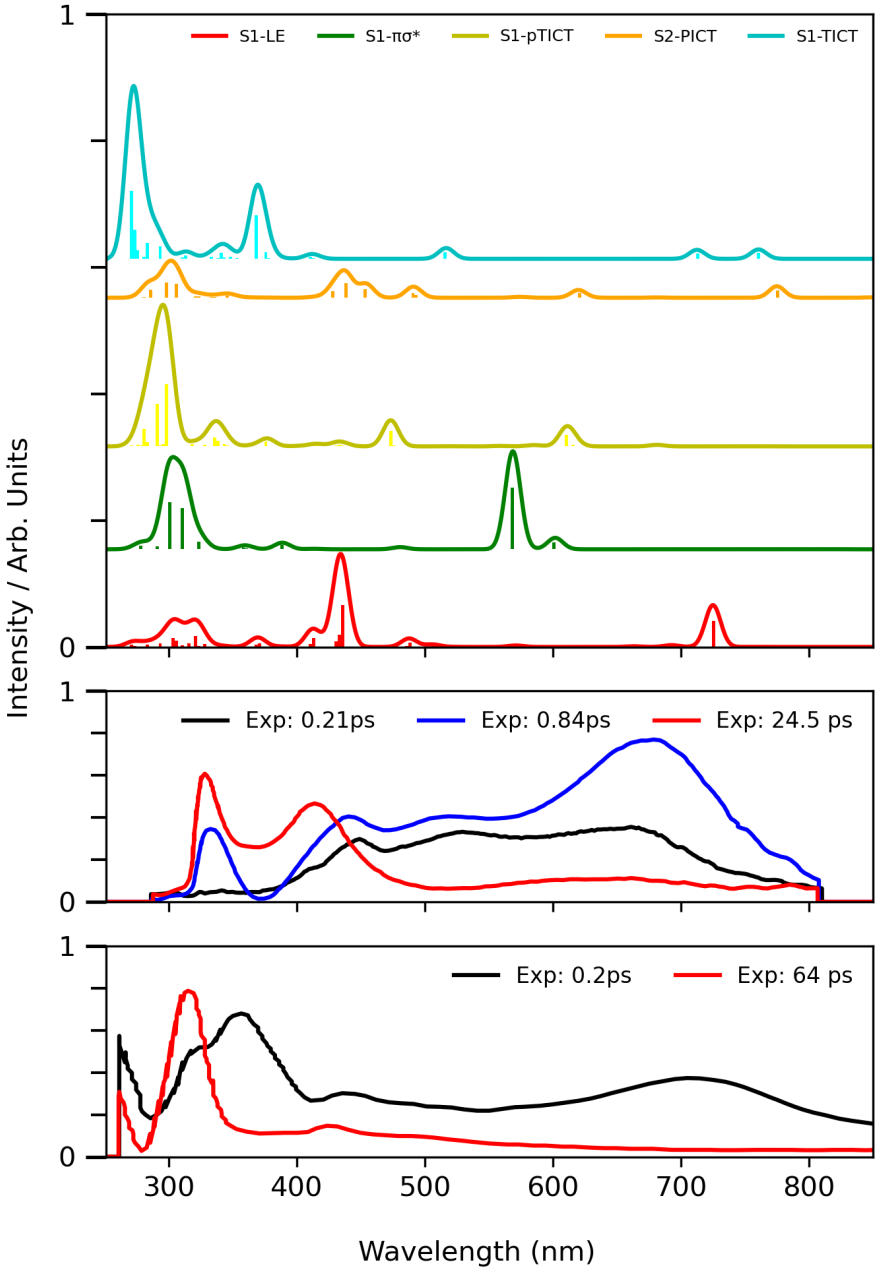

Figure A8.3: Excited State Absorption Spectrum of DMABN in acetonitrile. Top: Spectrum computed with DFT/MRCI(2). Middle: Experimental Transient Absorption Spectrum,.[10] Bottom: Experimental Transient Absorption Spectrum,[9] The following osc strengths were altered for better visibility: S1-TICT(Osc Str x2), S1-LE(Osc Str x2)

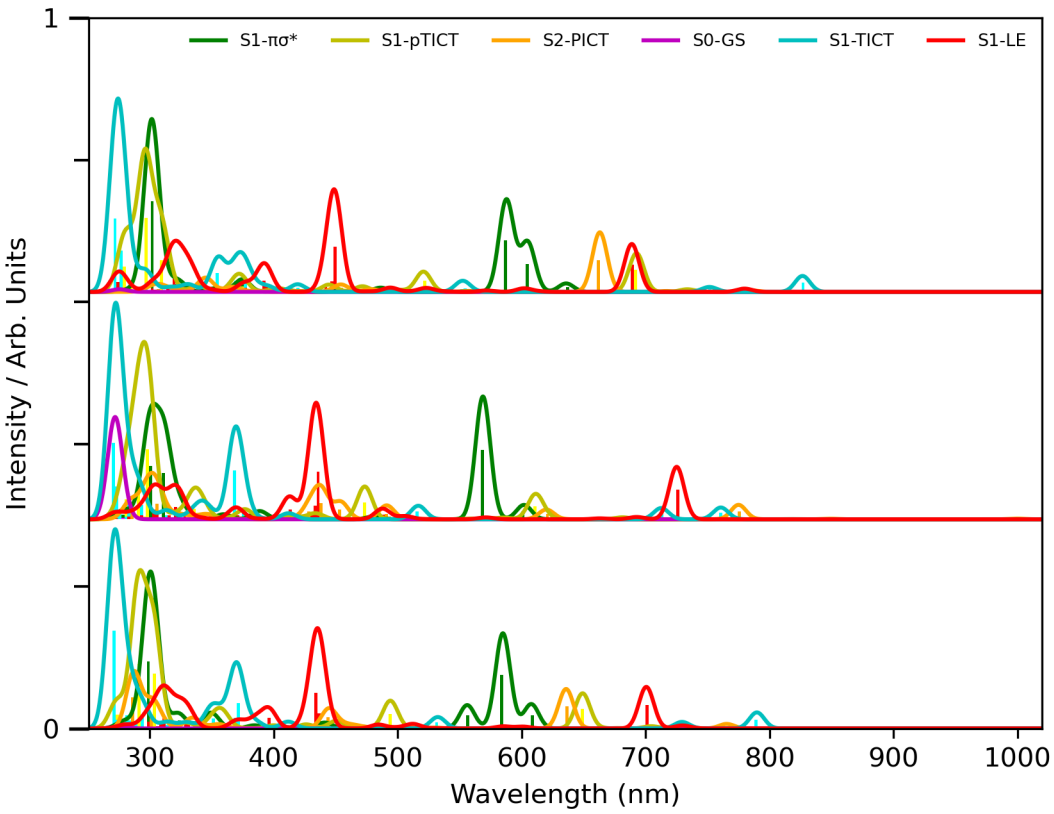

Figure A8.4: Extended Excited State Absorption Spectrum of DMABN with DFT/MRCI(2). From top to bottom: In the Gas Phase, In Acetonitrile, In n_hexane. The following osc strengths were altered for better visibility: S1-TICT(Osc Str x2), S1-LE(Osc Str x2), S0-GS(Osc Str x0.25)

A9: NTOs for significant excitations in the simulated excited state absorption spectrum of DMABN

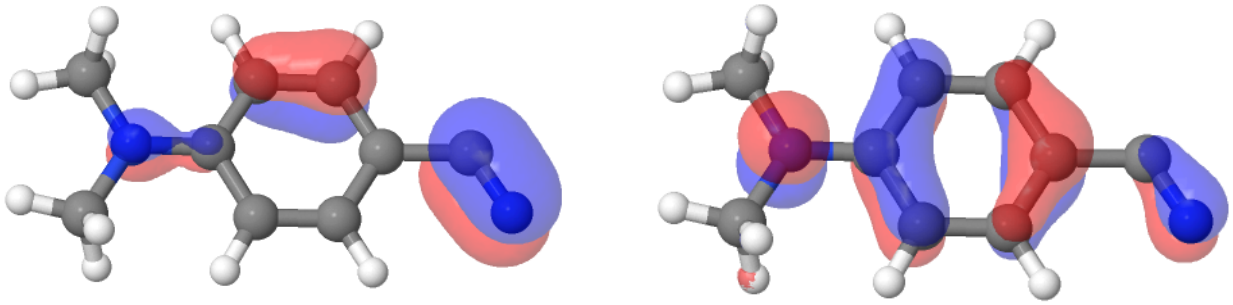

Figure A9.1: Dominant NTO pair (92.3%), Absorption at 558nm (Fig 19)) associated with the S1-$\pi\sigma*$ state

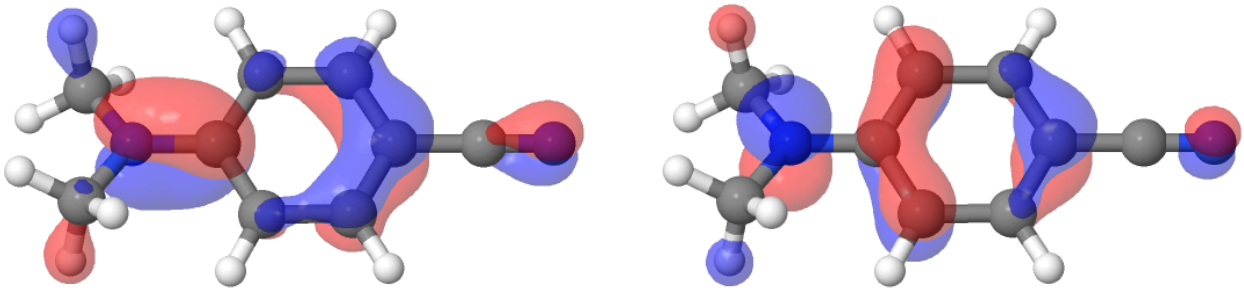

(a) Major contribution (89.2%)

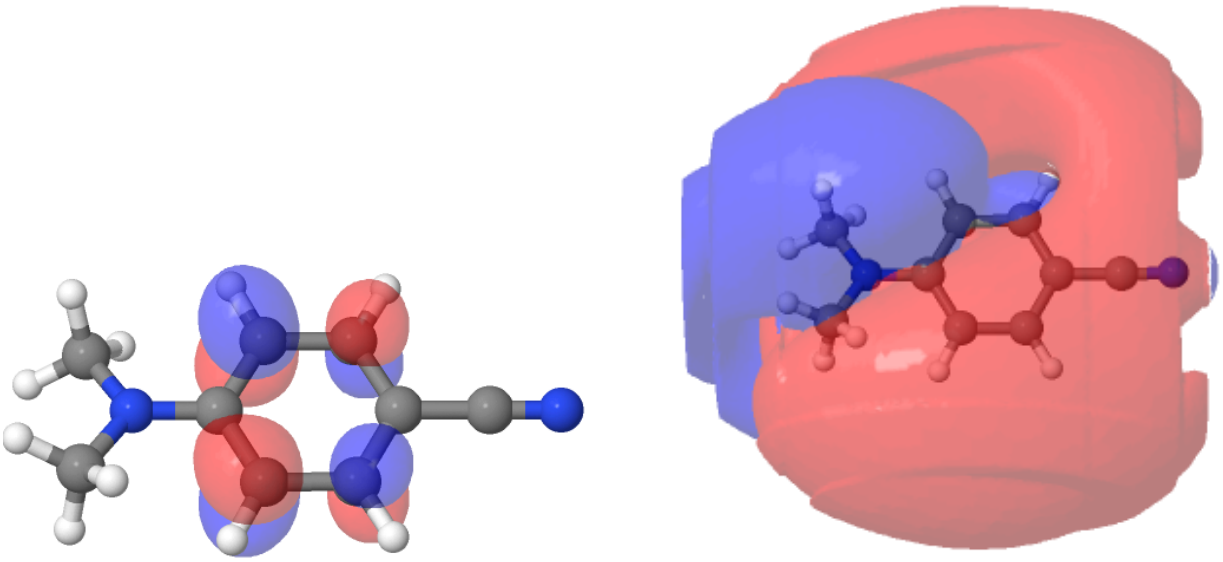

(b) Minor contribution (10.8%)

Figure A9.2: Dominant NTO pairs, Absorption at 725nm (Fig 19) associated with the S1-LE state

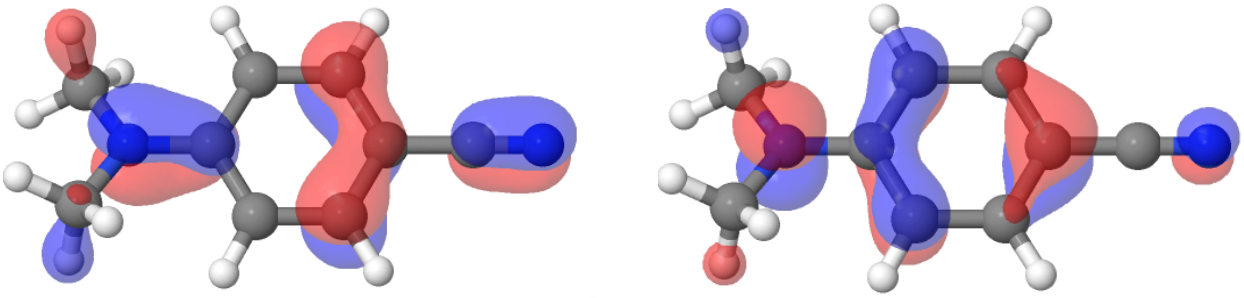

(a) Major contribution (50.7%)

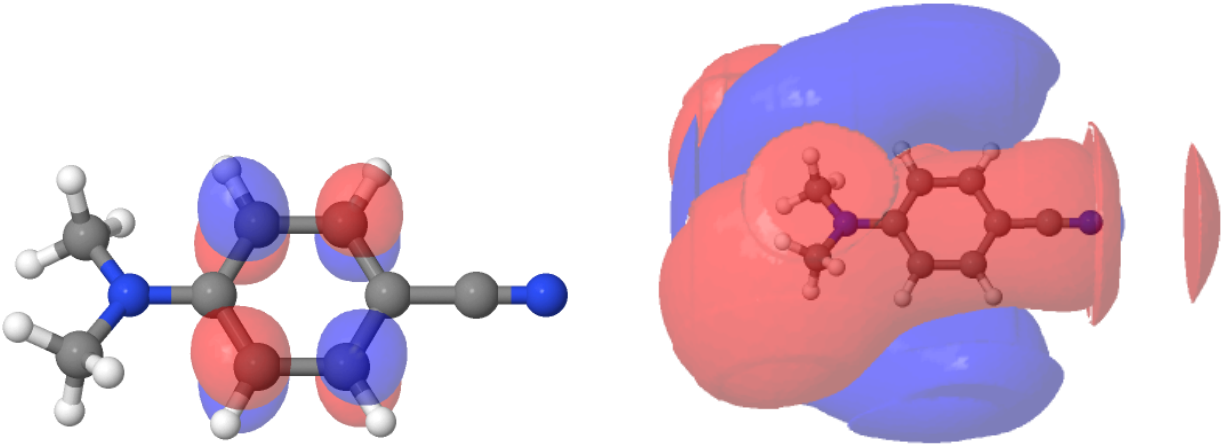

(b) Minor contribution (45.8%)

Figure A9.3: Dominant NTO pairs, Absorption at 435nm (Fig 19) associated with the S1-LE state

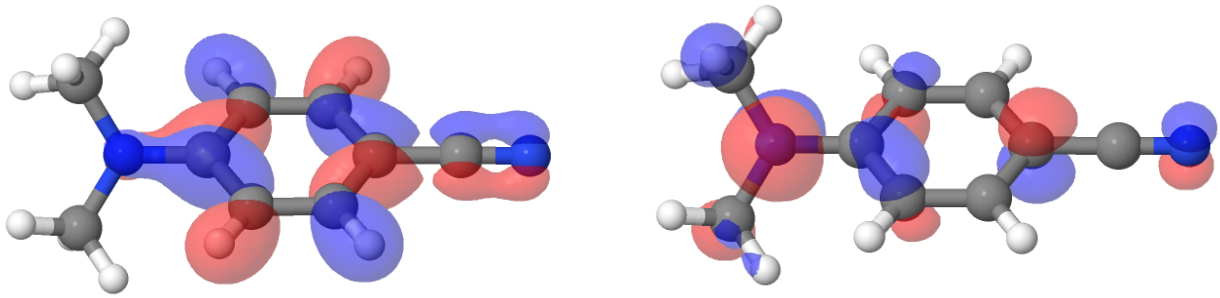

(a) Major contribution (68.6%)

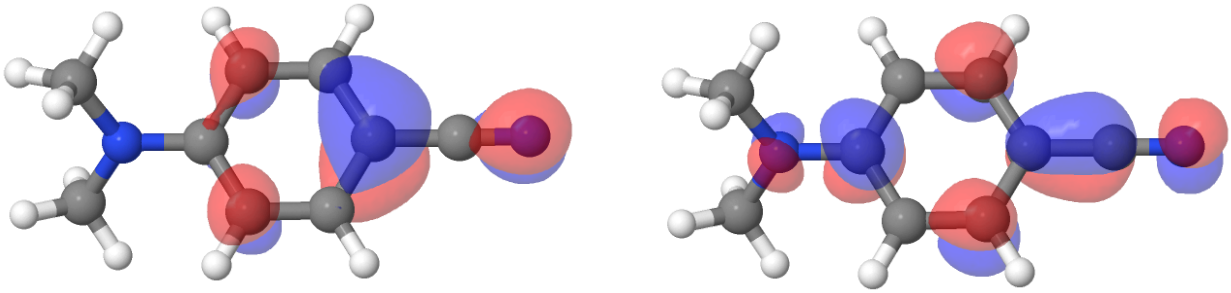

(b) Minor contribution (17.3%)

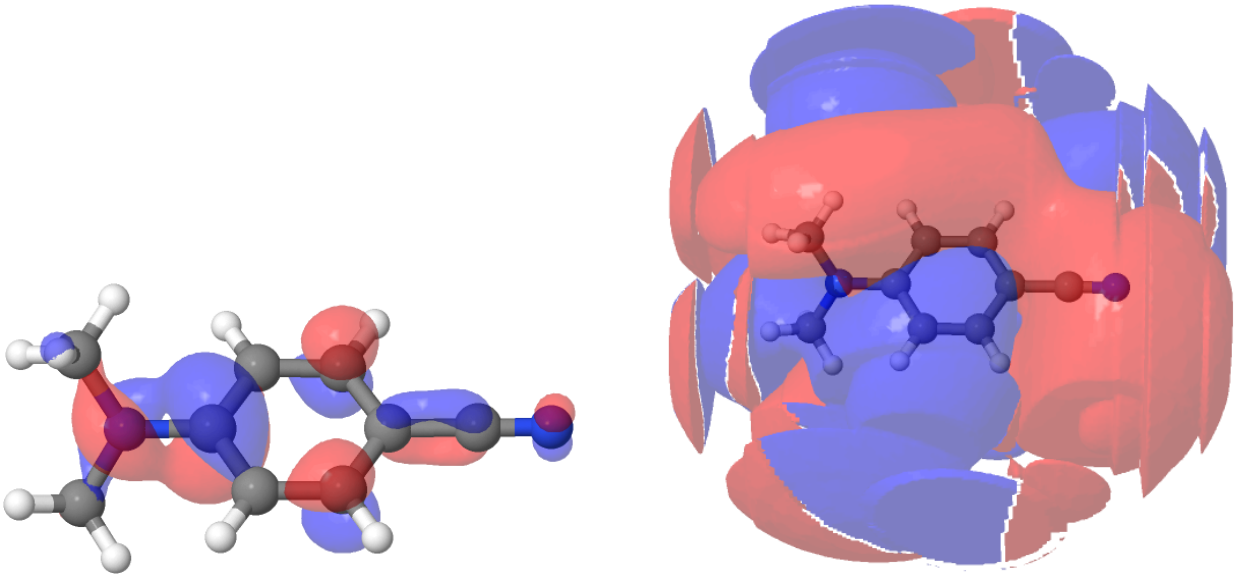

(c) Minor contribution (14.1%)

Figure A9.4: Dominant NTO pairs, Absorptions at 290-299nm (Acetonitrile, Fig A8.3) associated with the S1-pTICT state

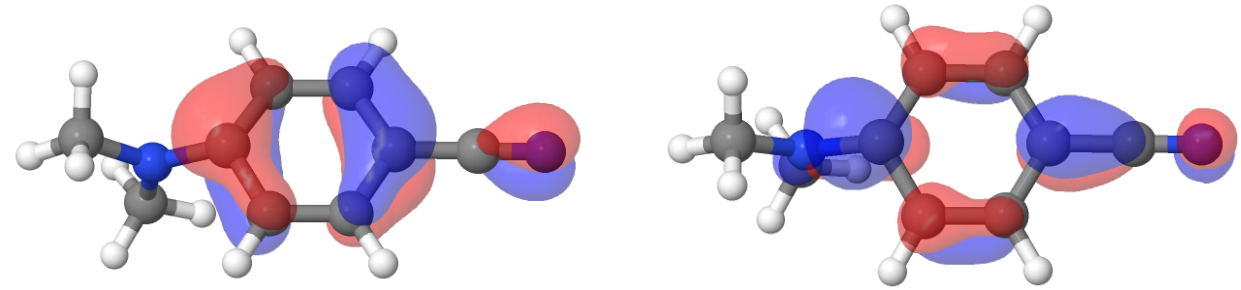

(a) Major contribution (75.8%)

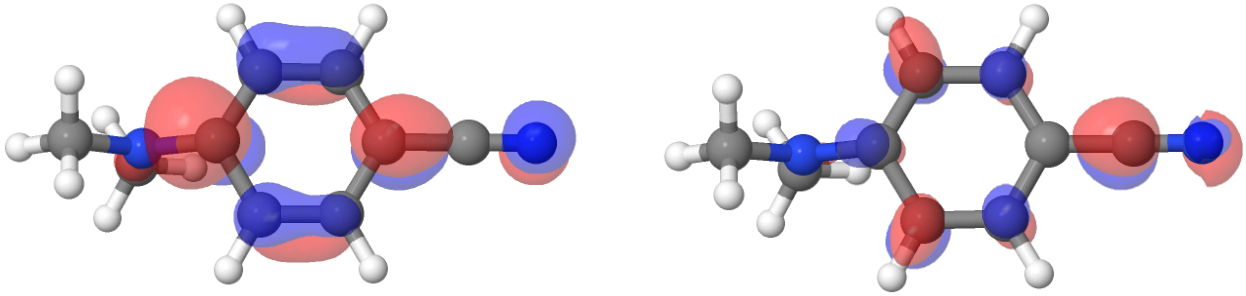

(b) Minor contribution (18.5%)

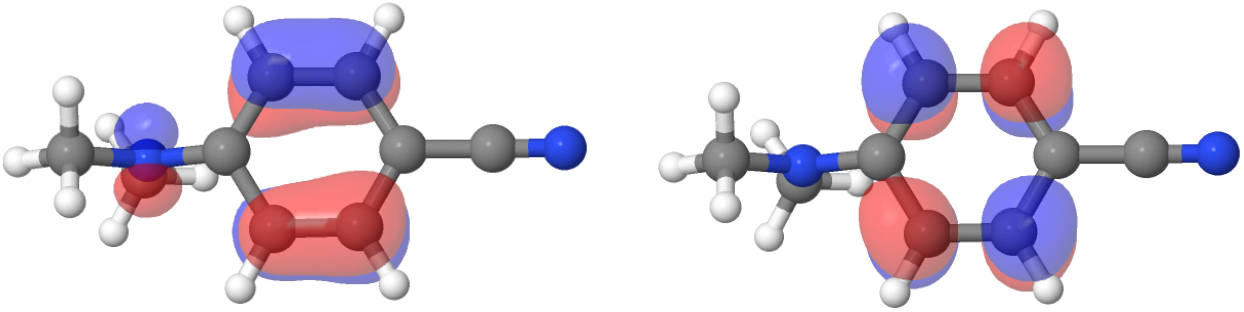

(c) Minor contribution (5.7%)

Figure A9.5: Dominant NTO pairs, Absorption at 271nm (Acetonitrile, Fig A8.4) associated with the S1-TICT state

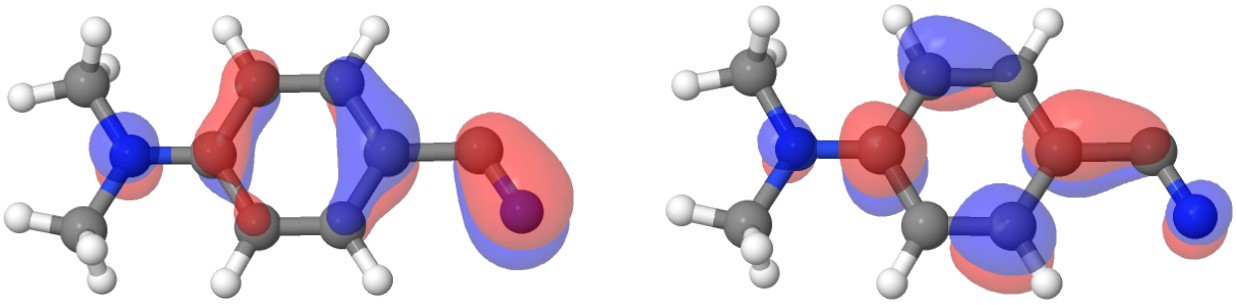

(a) Major contribution (88.8%)

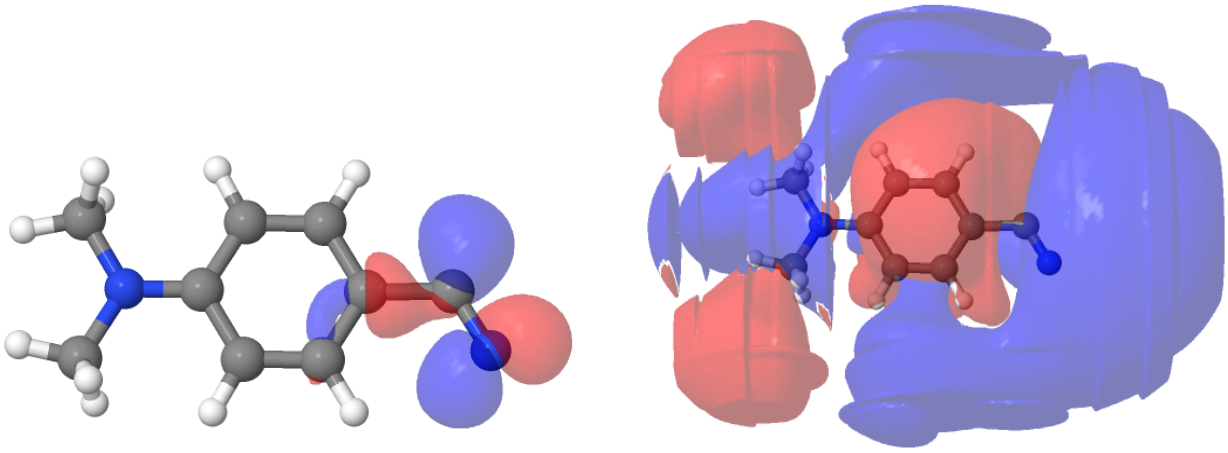

(b) Minor contribution (7.5%)

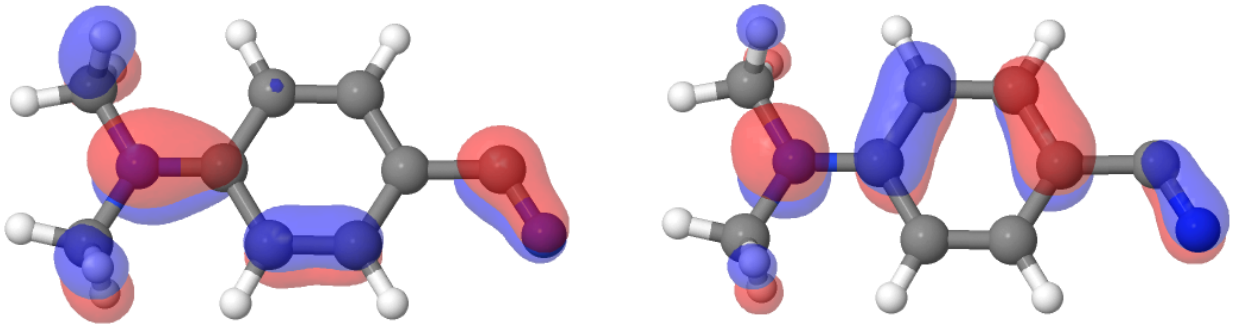

(c) Minor contribution (3.7%)

Figure A9.6: Dominant NTO pairs, Absorption at 291nm (Fig 19) associated with the S1-$\pi\sigma*$ state

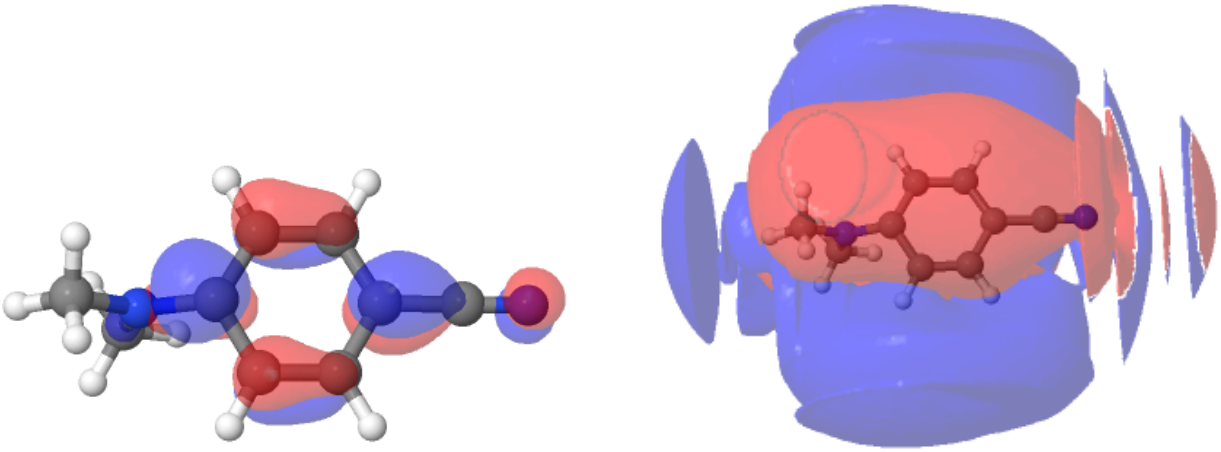

(a) Major contribution (90.4%)

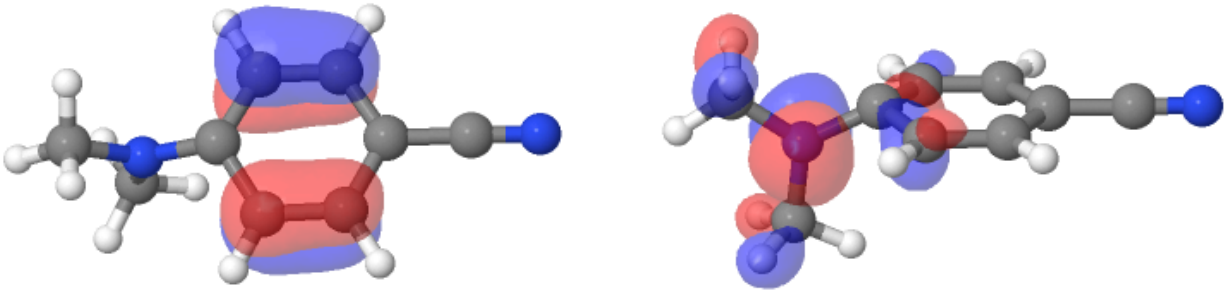

(b) Minor contribution (6.8%)

Figure A9.7: Dominant NTO pairs, Absorption at 369nm (Fig 19) associated with the S1-TICT state

A10: LIIC of DIABN: Estimating the size of the transition state barrier between the LE and $\pi\sigma*$ state

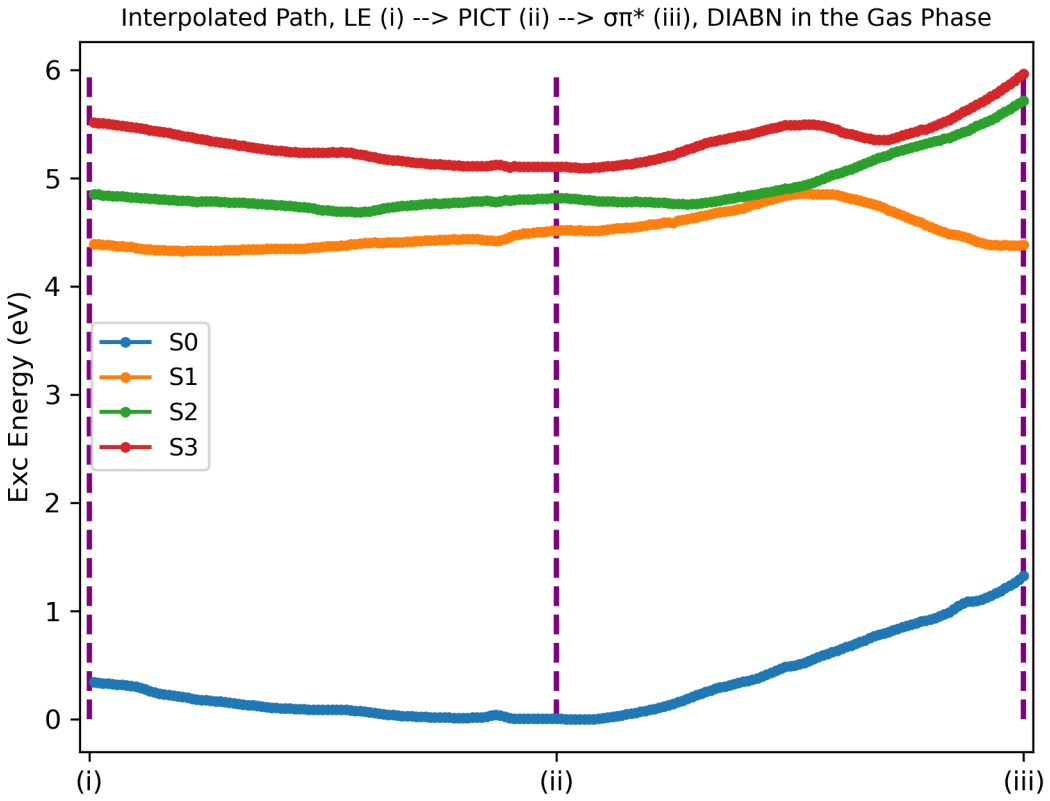

Figure A10.1: LIIC of DIABN, LE $\rightarrow$ PICT $\rightarrow$ $\pi\sigma*$. Energies computed by DFT/MRCI(2), in the Gas Phase.

A11: Simulated TRPES Spectrum of Aminobenzonitrile

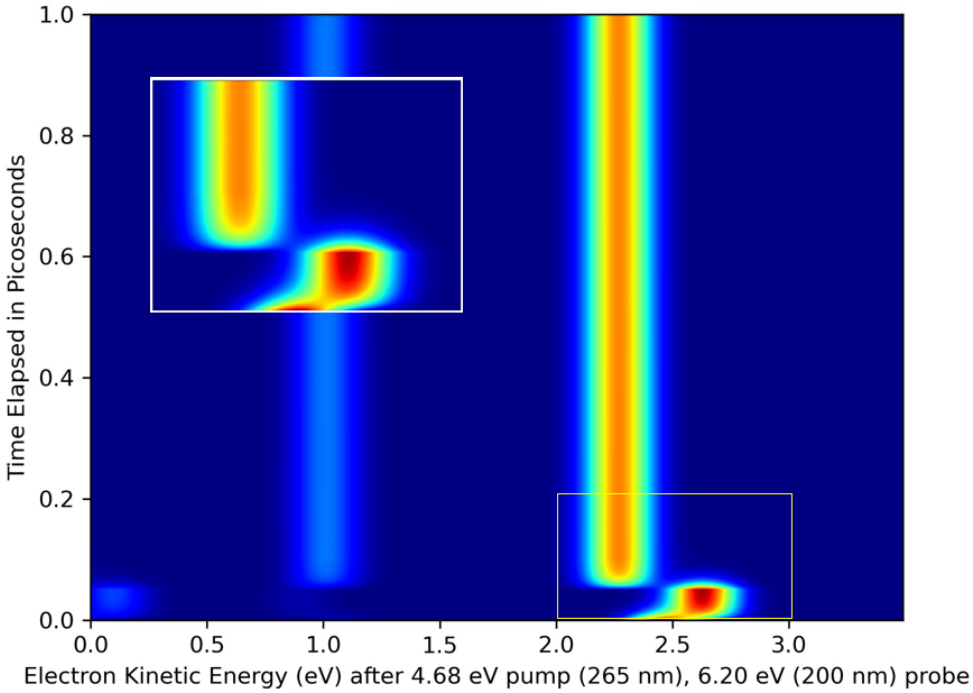

Figure A11.1: Simulated TRPES Spectrum of ABN, based on transition state barriers evaluated with various electronic structure methods (see A.3), and static photoelectron spectrum evaluated with DFT/MRCI(2) (see A.12). Inset: Early excited state dynamics, $S_0(\mathbf{R}_{Min}) \rightarrow S_2(\mathbf{R}_{PICT}) \rightarrow S_1(\mathbf{R}_{LE})$. Main figure: Persistent excited state signal, $S_1(\mathbf{R}_{LE})$.

A12: Extended Valence Photoelectron Spectrum and Dyson Orbitals, DMABN and its Derivatives

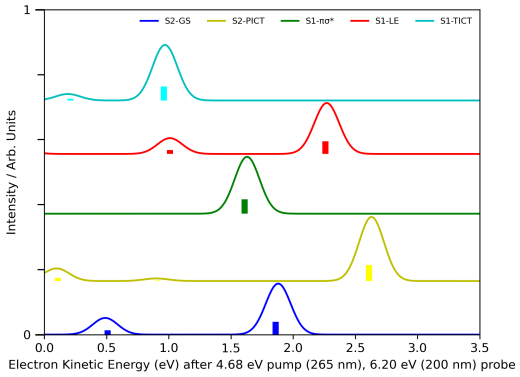

(a) ABN

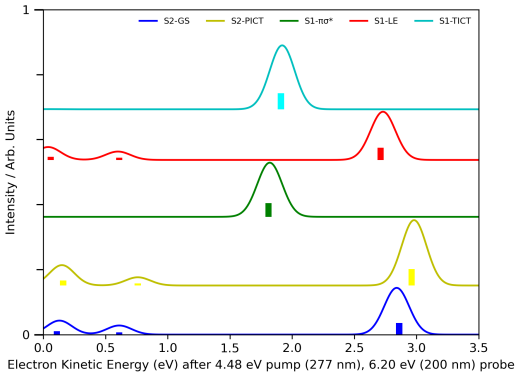

(b) DIABN (Left shifted by 0.5 eV)

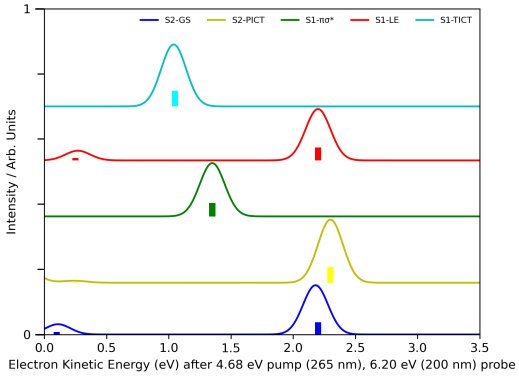

(c) DMABN (Left shifted by 0.8 eV)

Figure A12.1: Simulated Valence Photoelectron Spectrum of the excited states of DMABN and its analogues with DFT/MRCI(2) in the Gas Phase.

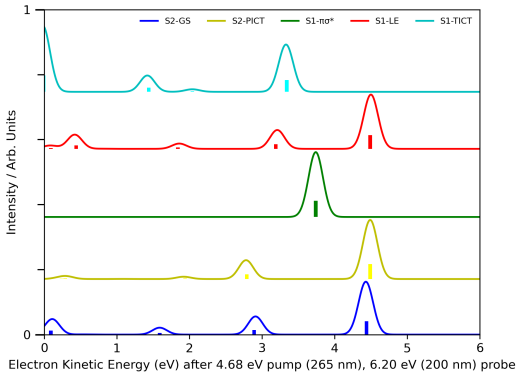

(a) ABN

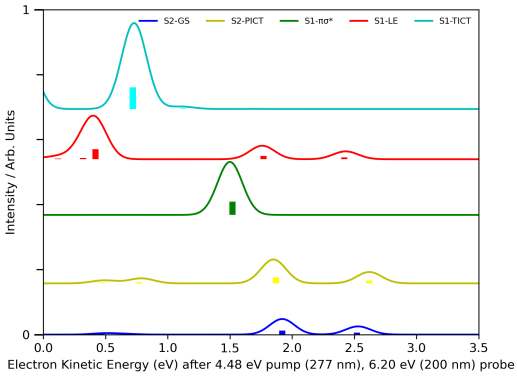

(b) DIABN (Left shifted by 0.5 eV)

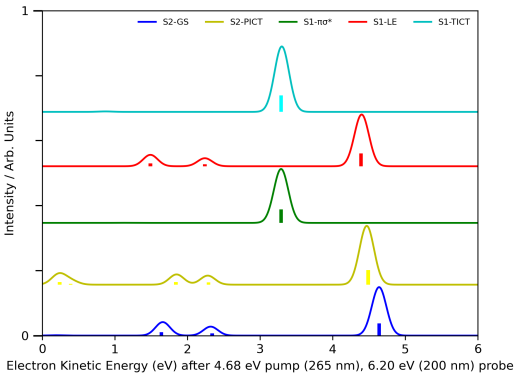

(c) DMABN (Left shifted by 0.8 eV)

Figure A12.2: Simulated Valence Photoelectron Spectrum of the excited states of DMABN and its analogues with DFT/MRCI(2) in Acetonitrile.

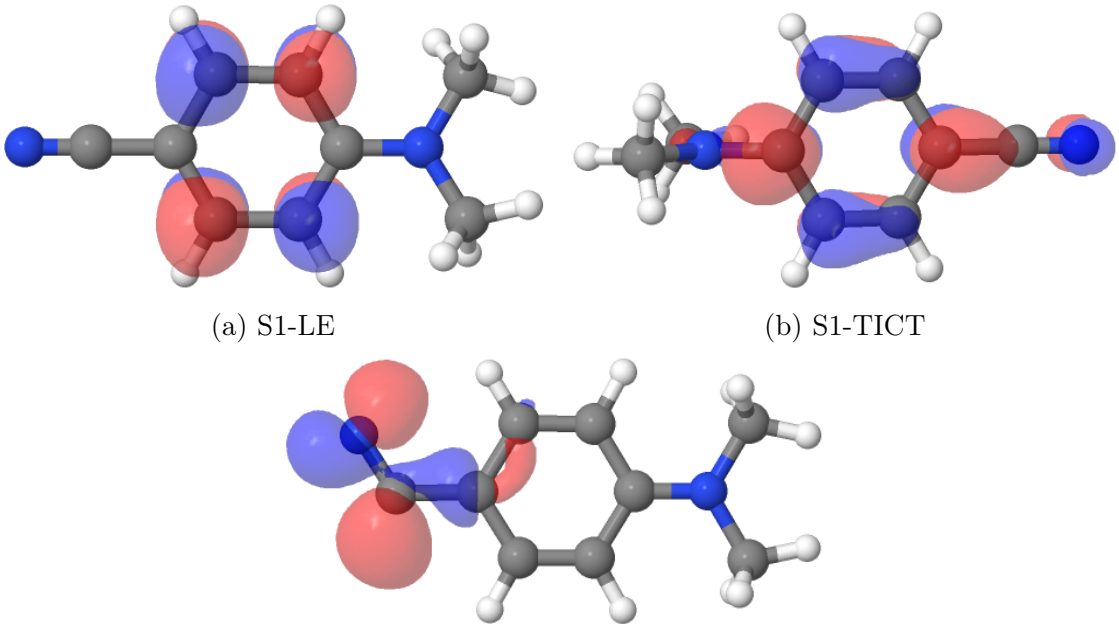

(a) S1-LE

(b) S1-TICT

(c) S1-$\pi\sigma*$

Figure A12.3: Dyson Orbitals for the each of the first major photoemissions in the static VPS spectrum.

Appendix Part B: X Ray Spectroscopies

A13: Extended XAS Spectrum, and NTOs for Significant Absorptions, DMABN

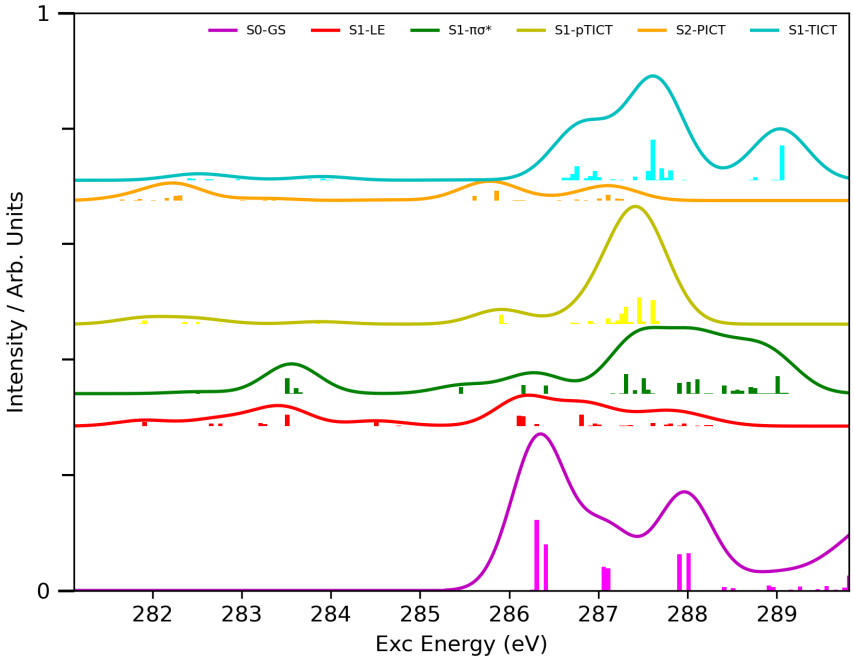

(a) Carbon Edge

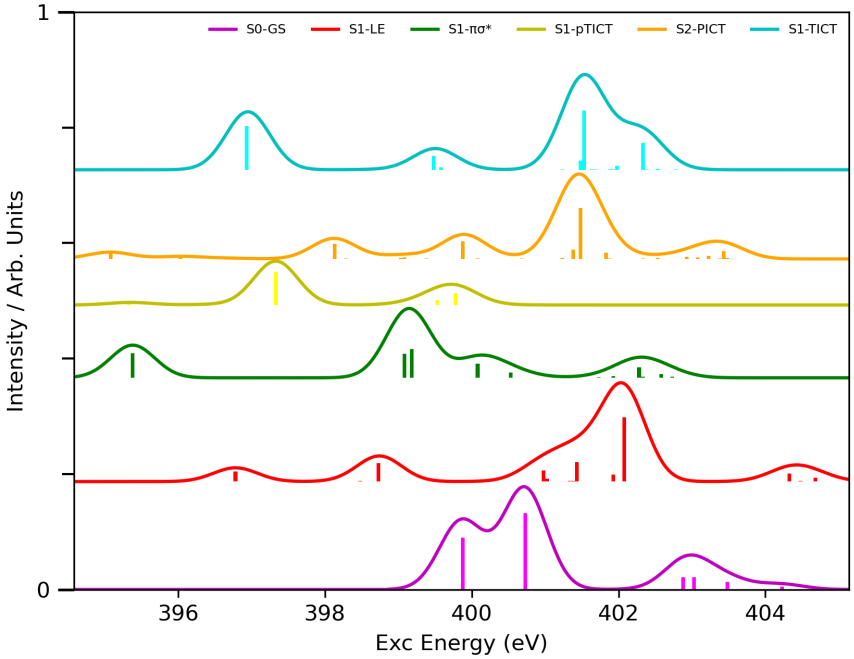

(b) Nitrogen Edge

Figure A13.1: Simulated X Ray Absorption Spectrum of DMABN with DFT/MRCI(2), all possible excited state contributions

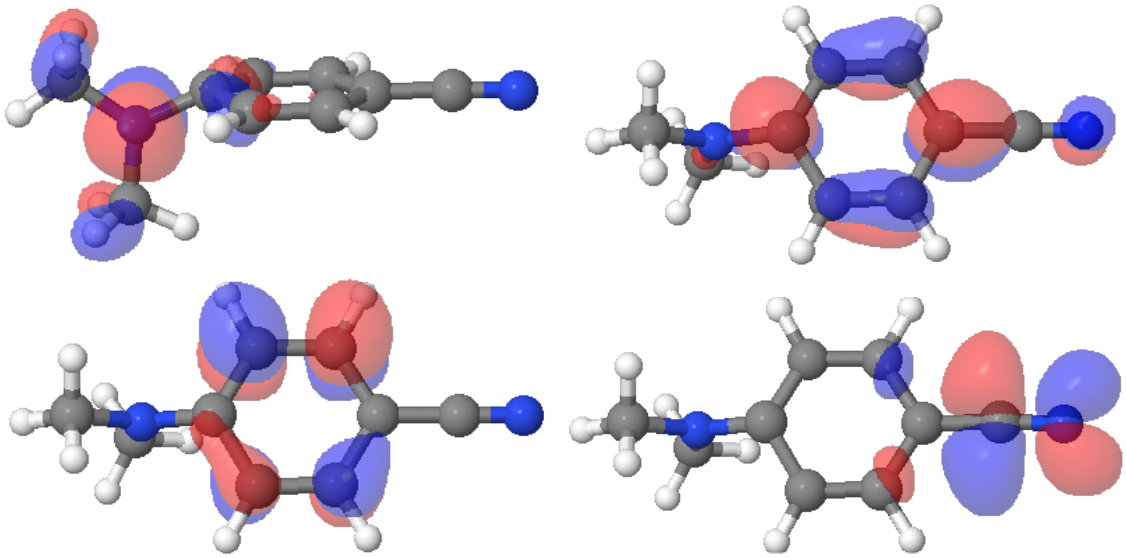

(a) S1-TICT state: Major excitations to orbitals at i) ∼ 282.4eV, ii) ∼ 286.6-287.0, 287.4eV, iii) ∼ 287.6-287.8eV, iv) ∼ 289.1 eV

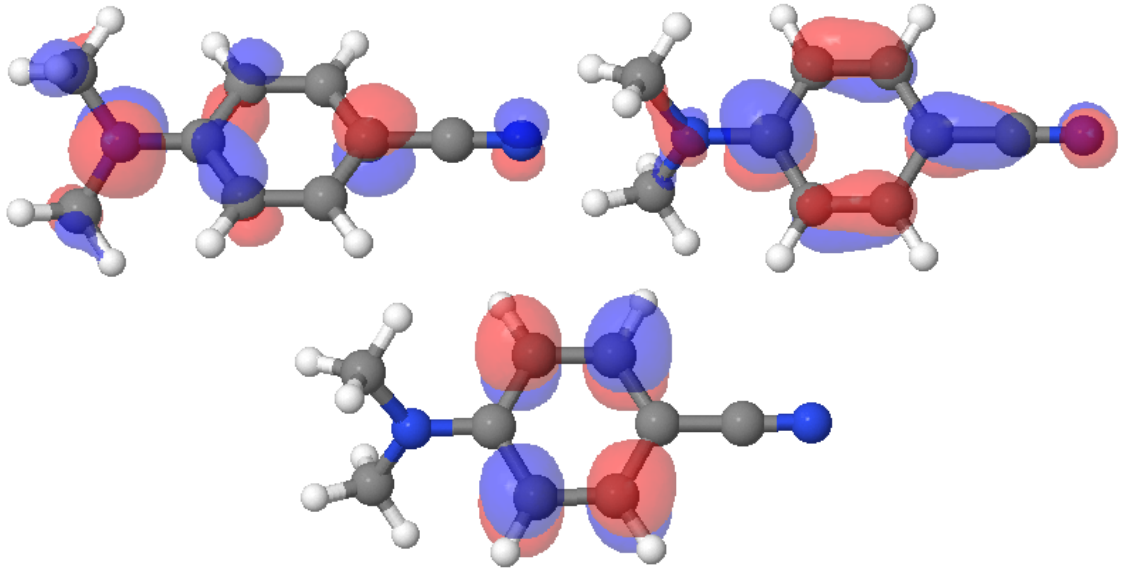

(b) S1-pTICT state: Major excitations to orbitals at i) ∼ 281.9, 282.3, 282.5, 283.9eV ii) ∼ 285.9, 286.7, 286.9, 287.1-287.3, 287.5eV, iii) ∼ 287.4, 287.6-287.7, 288.0eV

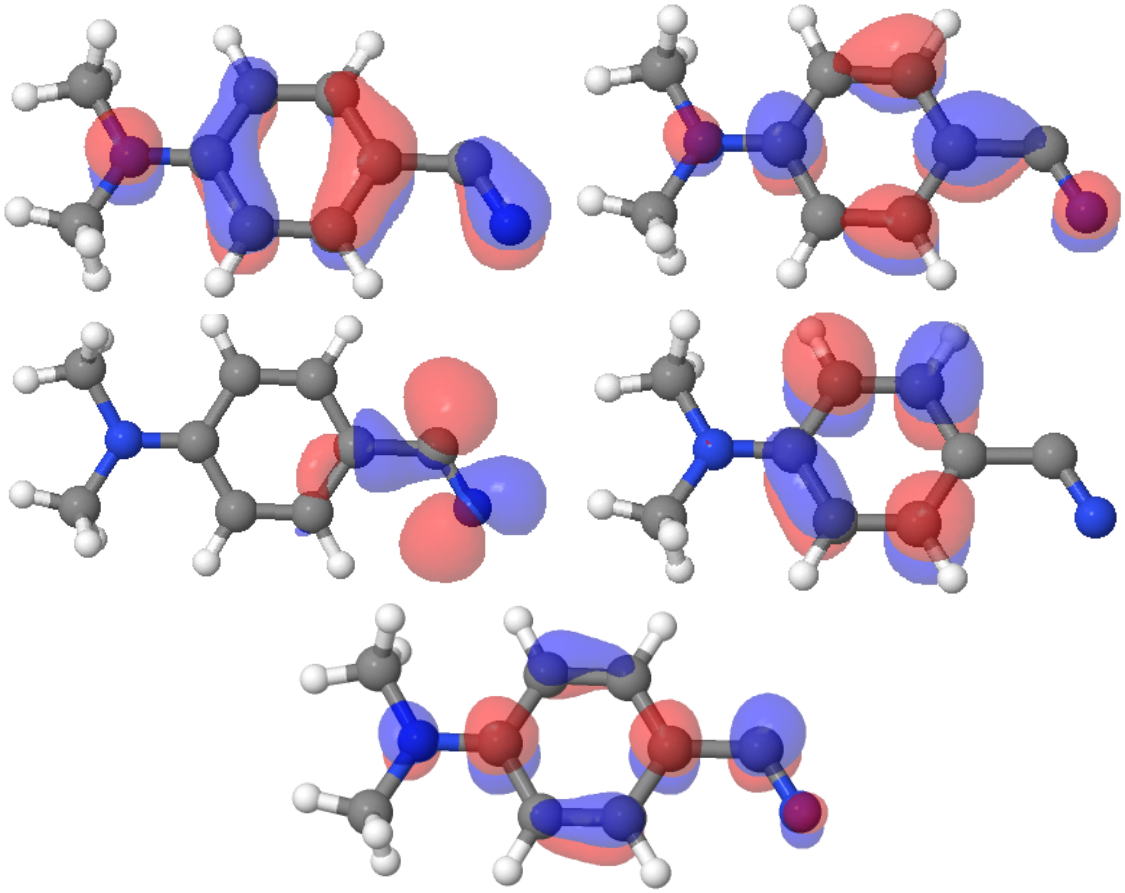

(c) S1-$\pi\sigma*$ state: Major excitations to orbitals at i) $\sim$ 282.5, 283.5-283.7, 285.5eV, ii) $\sim$ 286.2-286.5, 288.1, 288.5 eV, iii) $\sim$ 286.4eV, iv) $\sim$ 287.9-288.0, 288.4, 288.6-288.8eV v) $\sim$ 289.0 eV

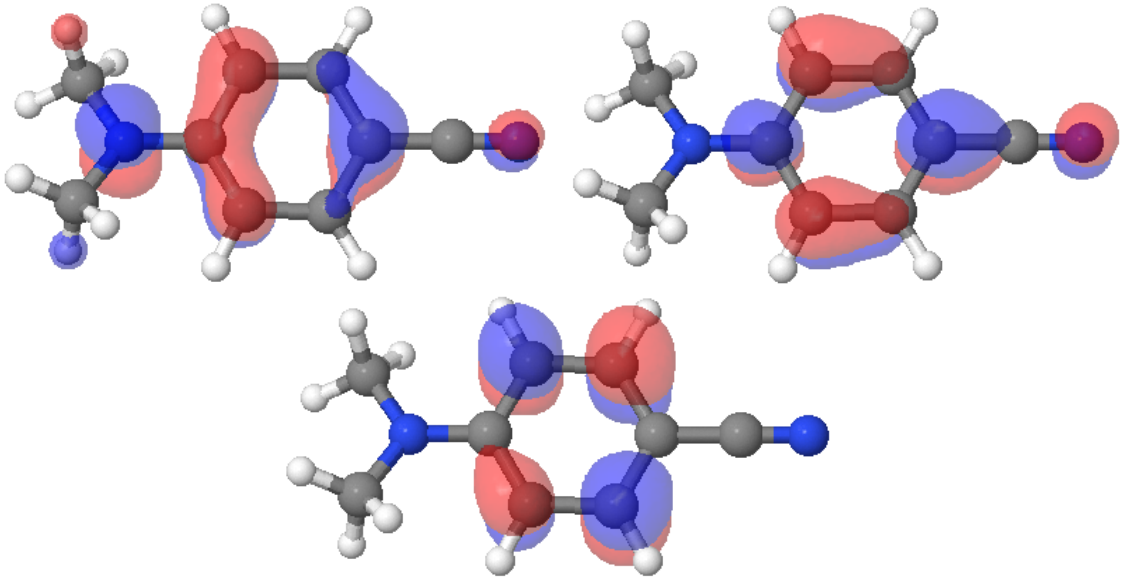

(d) S1-LE state: Major excitations to orbitals at i) $\sim$ 281.9, 283.2-283.3, 283.5, 284.5eV, ii) $\sim$ 282.7-282.8, 286.1-286.3, 287.8-288.0, 288.2-288.3eV, iii) 286.8, 287.0, 287.3, 287.6eV

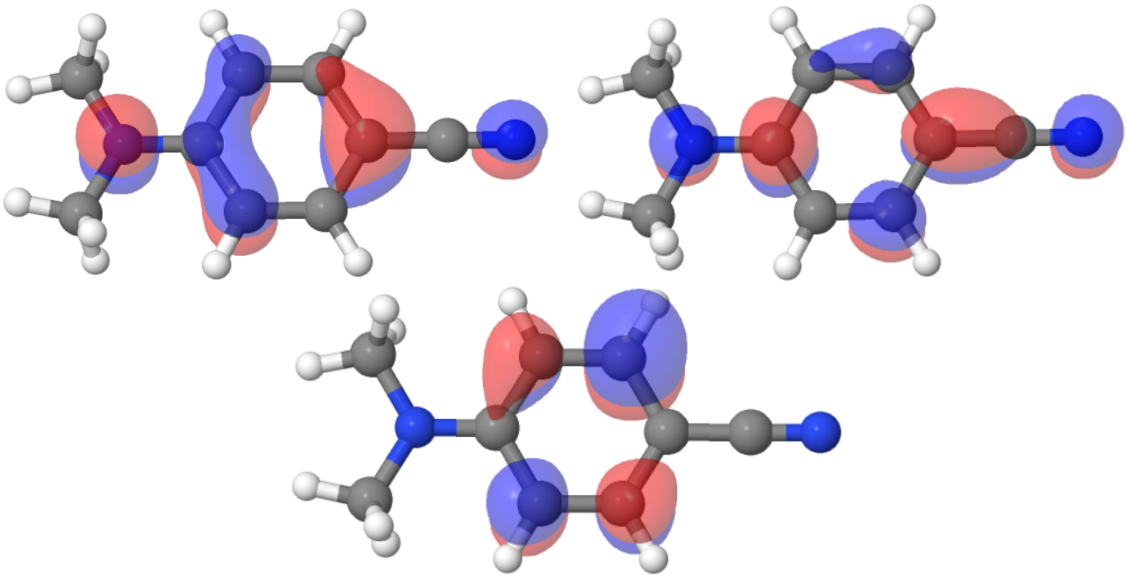

(e) S2-PICT state: Major excitations to orbitals at i) $\sim$ 281.7-281.8, 282.1-282.3eV, ii) $\sim$ 286.6, 286.8, 287.2eV, iii) 283.4, 285.6, 285.8, 287.0, 287.2eV

Figure A13.2: Particle NTOs corresponding to bright transitions in Fig A13.1a, XAS at C edge

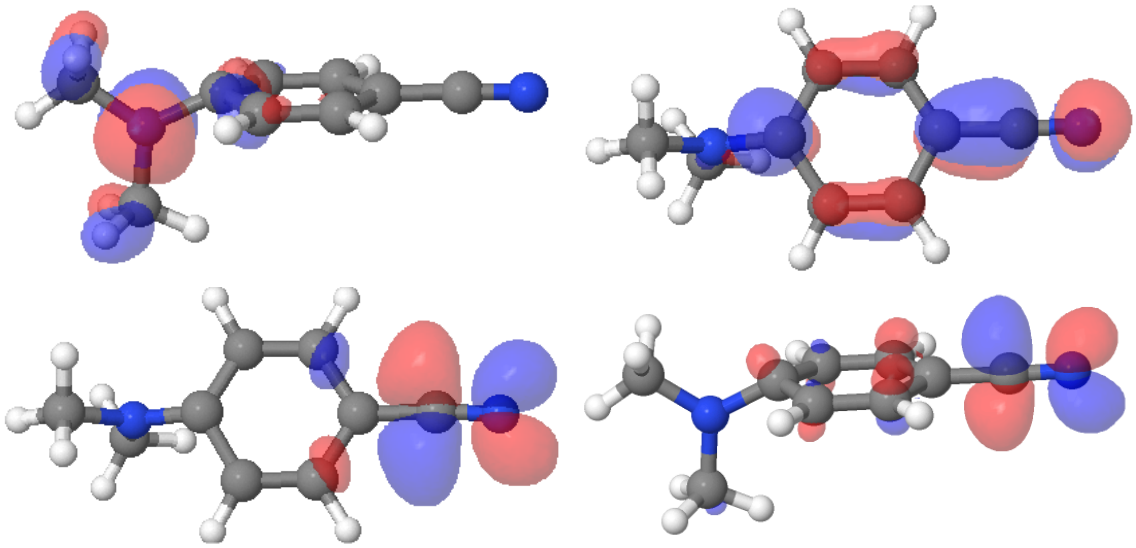

(a) S1-TICT state: Major excitations to orbitals at i) $\sim$ 397.0eV, ii) $\sim$ 399.5eV, iii) $\sim$ 401.5eV iv) 402.0, 402.3 eV

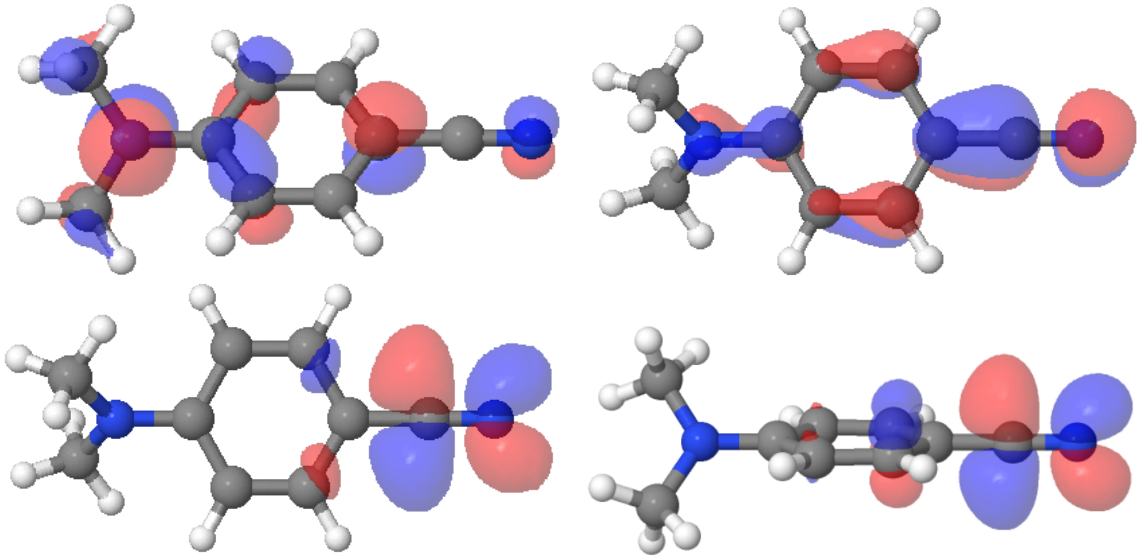

(b) S1-pTICT state: Major excitations to orbitals at i) $\sim$ 395.4, 397.3eV, ii) $\sim$ 399.5, 399.8eV, iii) $\sim$ 401.4-401.5eV, iv) $\sim$ 402.4, 402.6, 402.8, 403.0eV

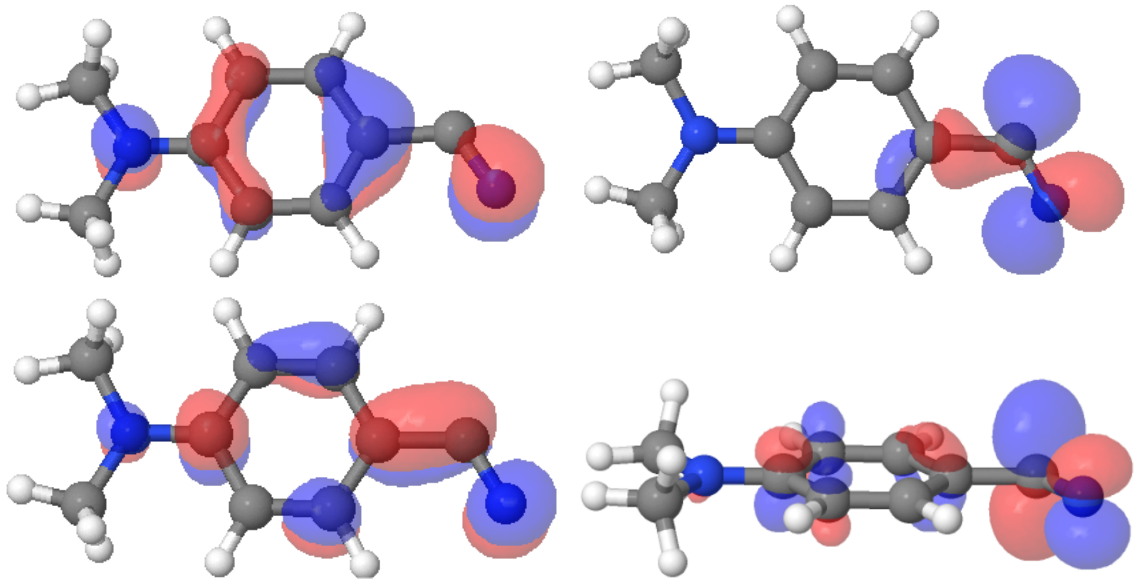

(c) S1-$\pi\sigma*$ state: Major excitations to orbitals at i) $\sim$ 395.4, 400.1eV, ii) $\sim$ 399.2, 403.8eV iii) $\sim$ 399.1, 400.5, 405.2eV, iv) $\sim$ 402.3, 402.6eV

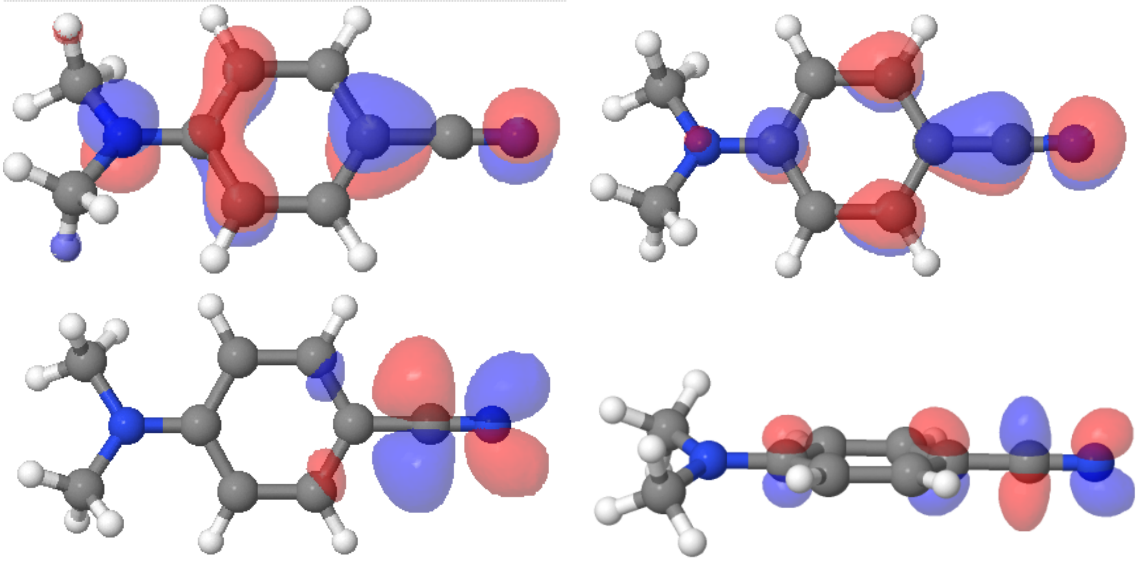

(d) S1-LE state: Major excitations to orbitals at i) $\sim$ 396.8, 398.8eV, ii) $\sim$ 401.0, 401.4eV, iii) $\sim$ 401.9, 402.1eV, iv) $\sim$ 404.3, 404.7eV

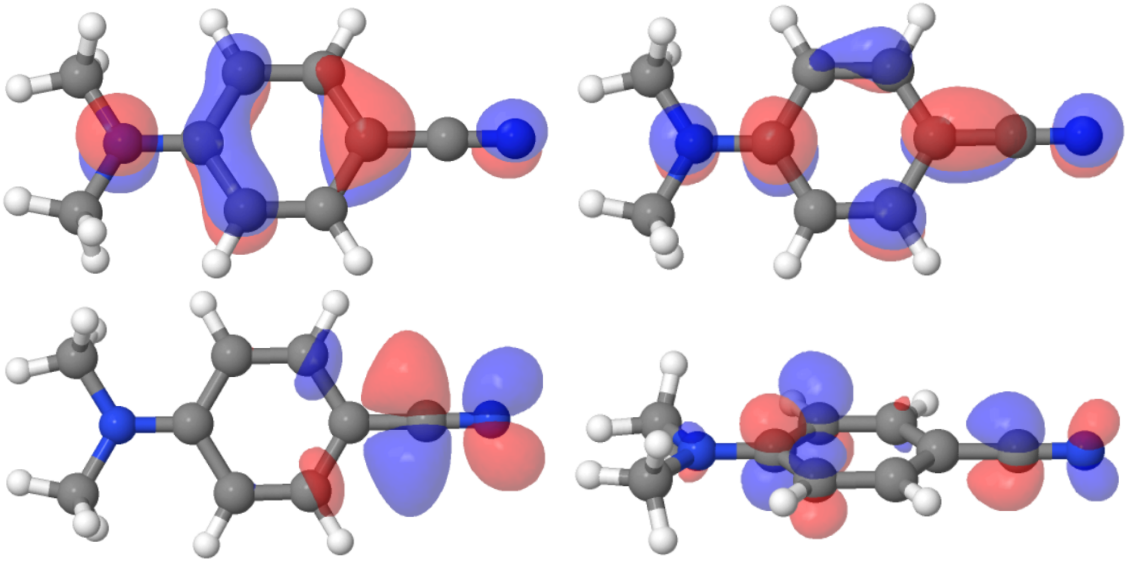

(e) S2-PICT state: Major excitations to orbitals at i) $\sim$ 395.1, 398.1eV, ii) $\sim$ 399.9, 404.0eV, iii) $\sim$ 401.4-401.5, 401.8eV, iv) $\sim$ 403.2, 403.4, 403.6eV

Figure A13.3: Particle NTOs corresponding to bright transitions in Fig A13.1b, XAS at N edge

A14: Extended XPS Spectrum, and Dyson Orbitals for significant emissions, DMABN

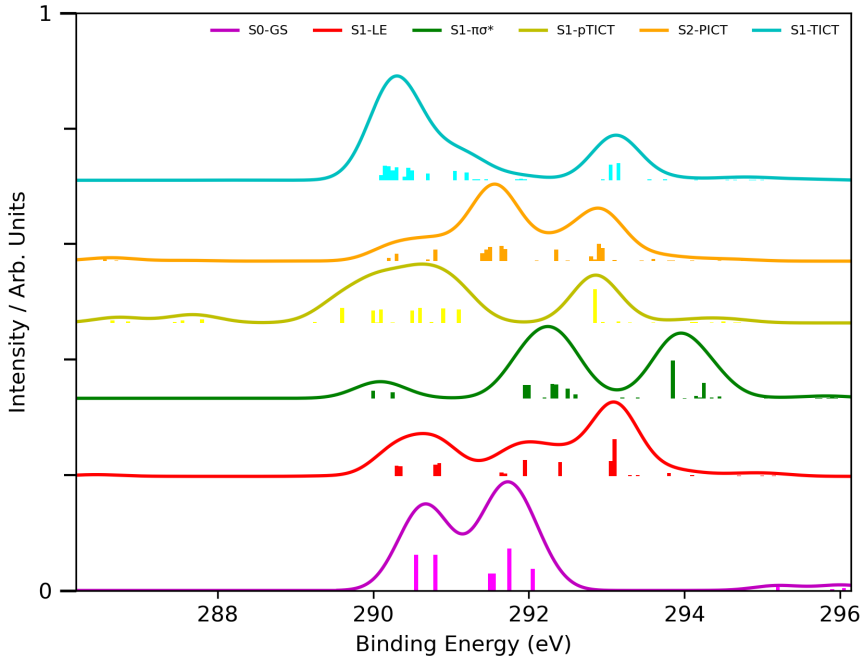

(a) Carbon Edge

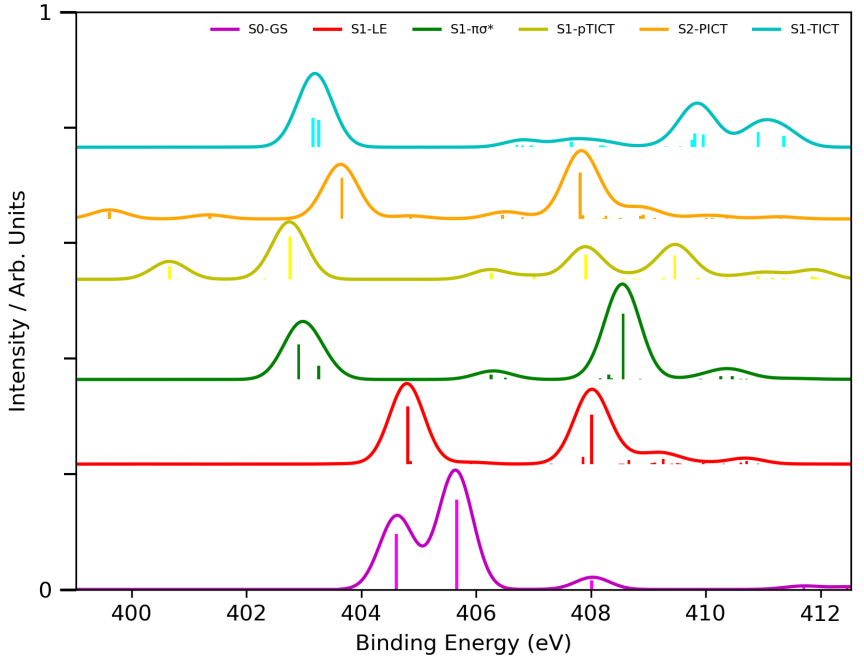

(b) Nitrogen Edge

Figure A14.1: Simulated X Ray Photoelectron Spectrum of DMABN with DFT/MRCI(2), all possible excited state contributions

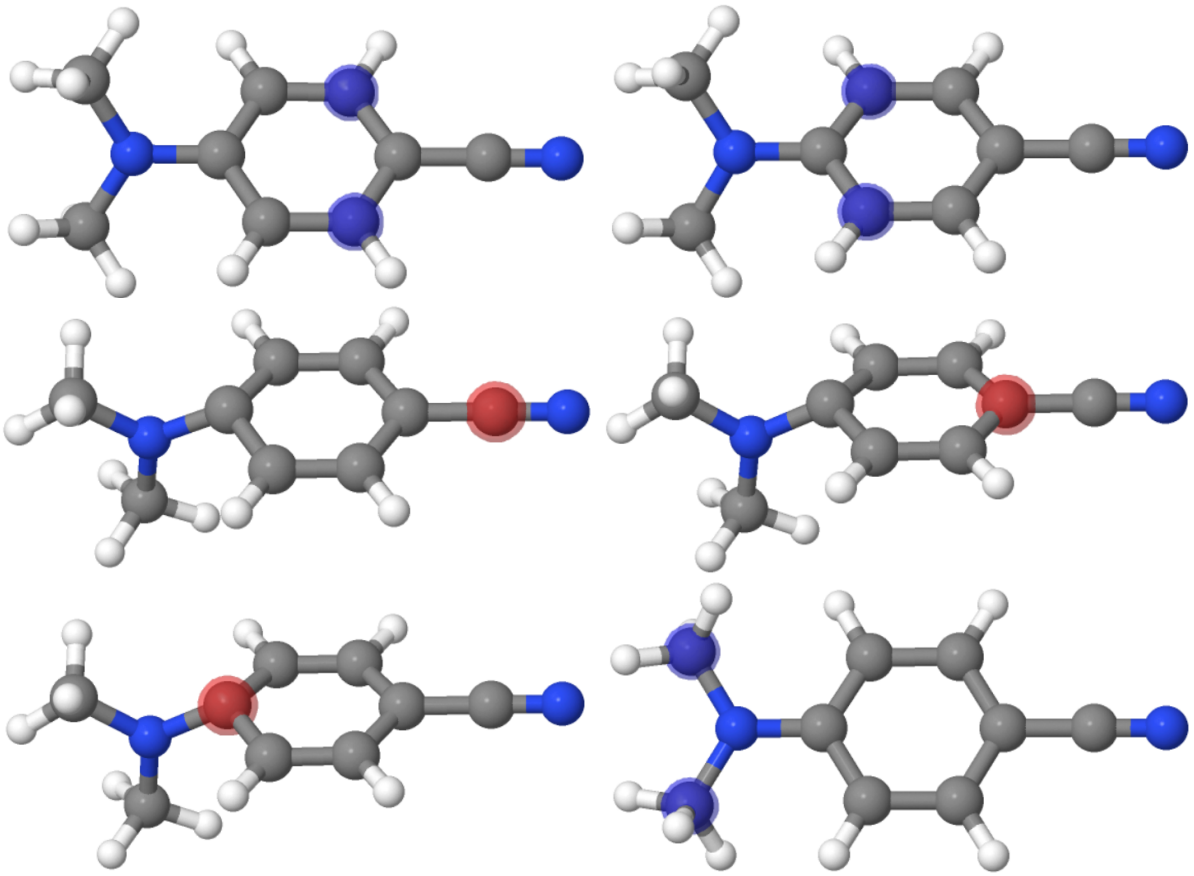

Figure A14.2: Dyson Orbitals describing bright transitions in Fig A14.1a, XPS at C edge: i) at 290-293 eV, ii) at 287, 290-292, 294 eV iii) at 288, 290-292 eV, iv) at 287-288, 290-293 eV, v) at 291-294 eV, vi) at 293-294 eV

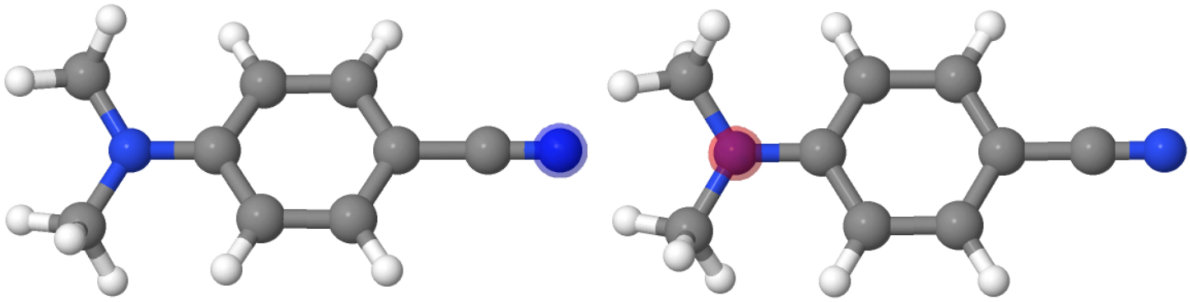

Figure A14.3: Dyson Orbitals describing bright transitions in Fig A14.1b, XPS at N edge: i) at 400-401, 403-407 eV, ii) at 408-412 eV

A15: Linear Interpolated Paths through Internal Coordinates (LIICs) of various DMABN derivatives

A collection of the LIICs discussed in the final portion of the paper. As a general rule, each path spans about 50-100 points, where the first point represents the ground state structure, the middle point represents the locally excited structure, and the final point represents the twisted intramolecular charge transfer structure. Analogous paths for DMABN, DIABN, and ABN are included as a point of comparison, even though the DMABN LIIC shown here is present elsewhere in the main text.

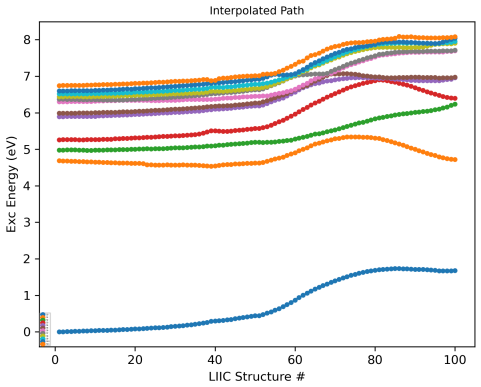

(a) DMABN

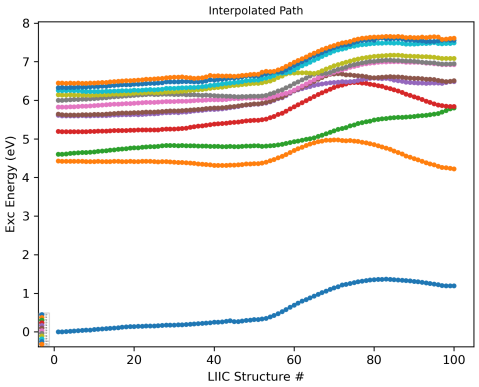

(b) DIABN

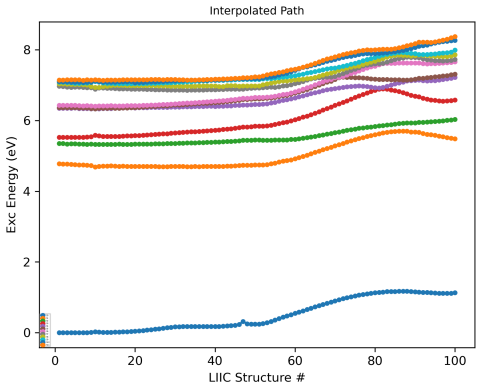

(c) ABN

Figure A15.1: LIICs between the ground state minimum, locally excited minimum (LE), and the twisted intramolecular charge transfer (TICT) minimum: Initial LIICs between previously evaluated derivatives

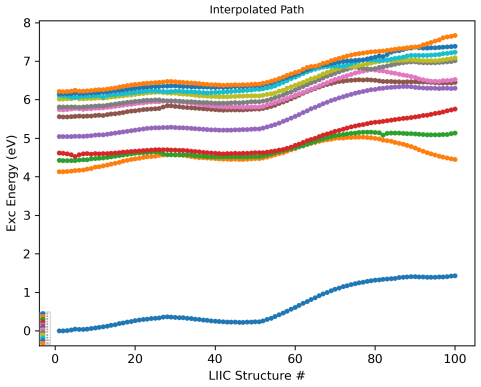

(a) A1

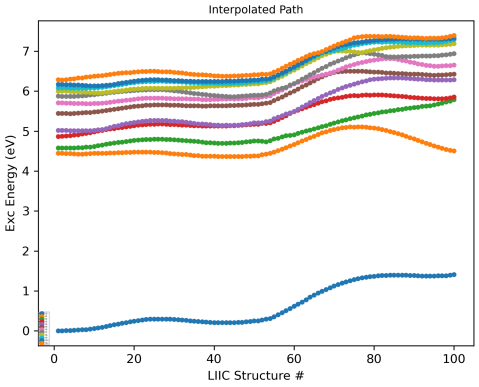

(b) A2

Figure A15.2: LIICs between the ground state minimum, locally excited minimum (LE), and the twisted intramolecular charge transfer (TICT) minimum: Derivatives with oxygen withdrawing groups

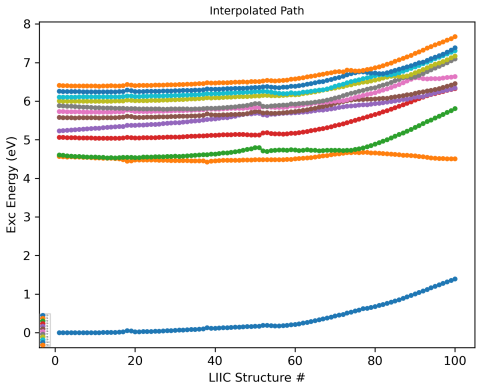

(a) B1

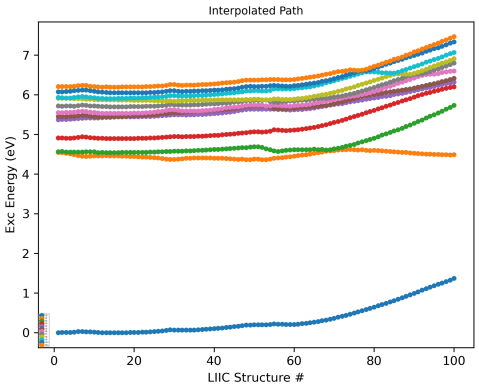

(b) B2

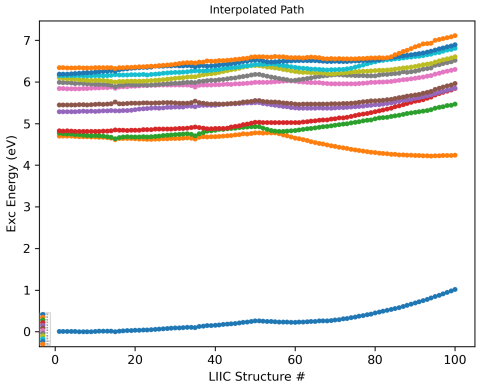

(c) B3

Figure A15.3: LIICs between the ground state minimum, locally excited minimum (LE), and the twisted intramolecular charge transfer (TICT) minimum: Complex Derivatives

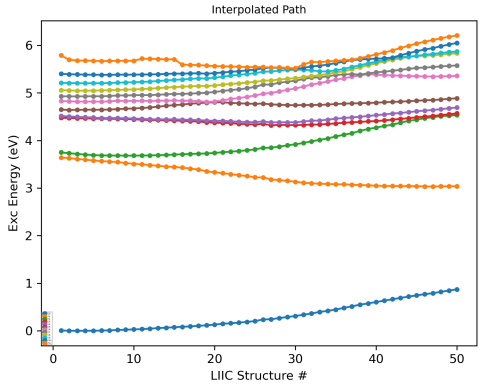

(a) C1. In this case, step 0 represents the ground state minimum, and step 50 represents the S1-TICT minimum (S1-LE does not represent a minimum for D3)

Figure A15.4: LIICs between the ground state minimum, locally excited minimum (LE), and the twisted intramolecular charge transfer (TICT) minimum: Charged Derivatives

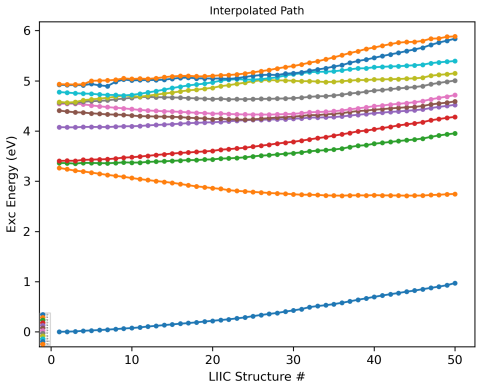

(a) D1, In this case, step 0 represents the ground state minimum, and step 50 represents the S1-TICT minimum

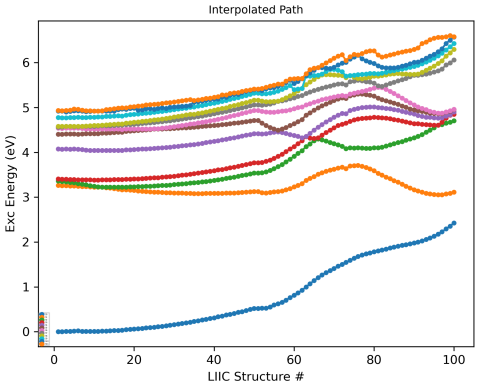

(b) D1, In this case, step 0 represents the ground state minimum, step 50 represents the S1-ESIPT-E minimum, and step 100 represents the S1-ESIPT-K minimum

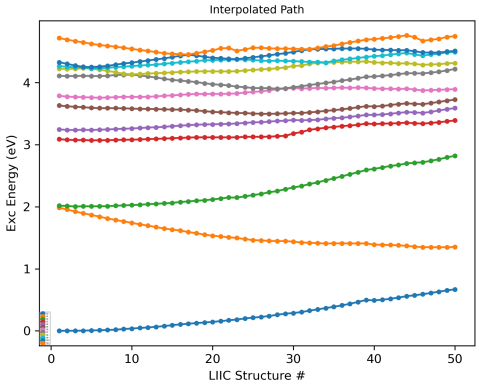

(c) D2, In this case, step 0 represents the ground state minimum, and step 50 represents the S1-TICT minimum

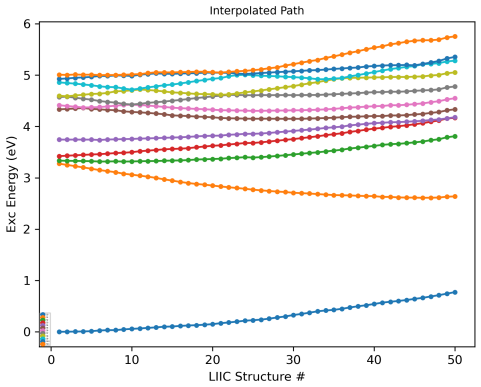

(d) D3, In this case, step 0 represents the ground state minimum, and step 50 represents the S1-TICT minimum

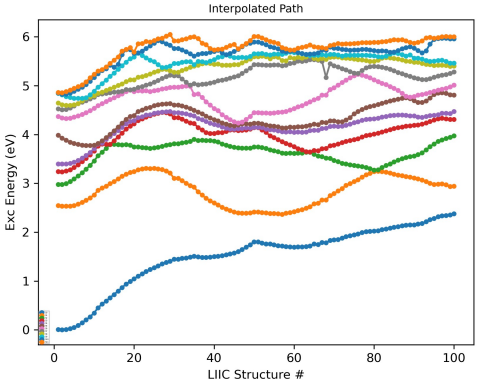

(e) D3, In this case, step 0 represents the S1-ESIPT-E minimum, step 50 represents the S1-ESIPT-K minimum, and step 100 represents the S1-ESIPT-K-TICT minimum

Figure A15.5: LIICs for important excited structures in DMABN derivatives that possess a significant ESIPT process (ESIPT TICT derivatives)

A16: DMABN Derivatives, Relevant NTOs of Charge Transfer States

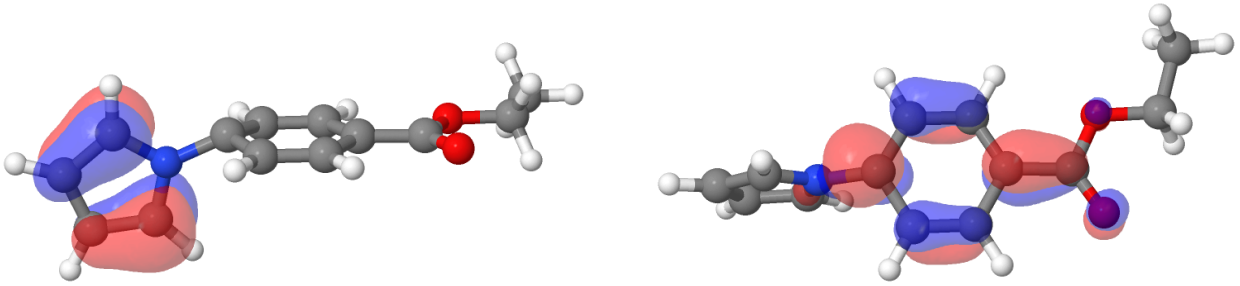

(a) S1-TICT, B3-TICT minimum

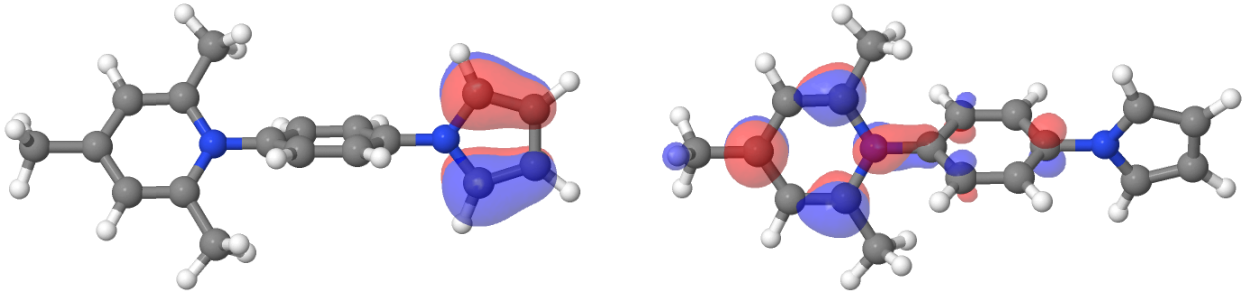

(b) S1-TICT, C1-TICT minimum

Figure A16.1: Dominant NTO pairs, some excited state descriptions of molecules evaluated in the Complex and Charged Derivatives sections

A17: Charged Derivatives of DMABN

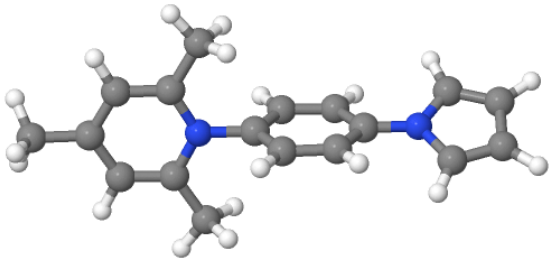

(a) Structure C1

Figure A17.1: Charged set of DMABN derivatives

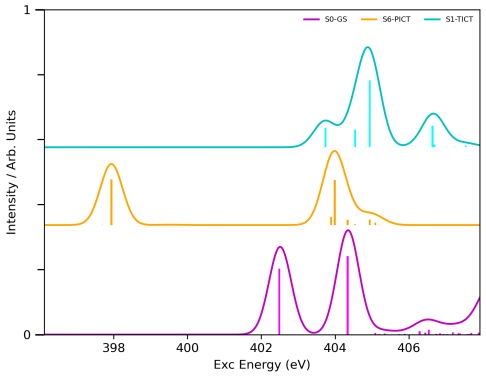

(a) Structure C1, Nitrogen K-Edge, XAS

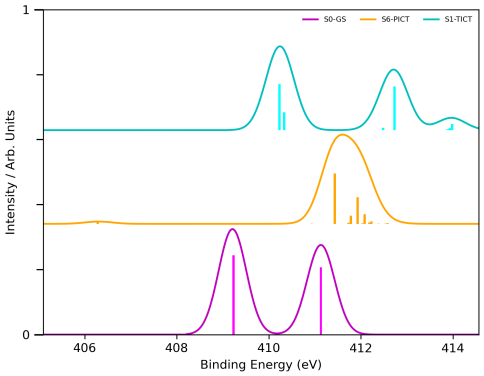

(b) Structure C1, Nitrogen K-Edge, XPS

Figure A17.2: Various X-ray Absorption/Photoelectron Spectrum of Charged Derivatives of DMABN

Here begins the first of two sections that seek to evaluate particularly unique derivatives of DMABN. Wherein the previous sections identified general trends in DMABN-type derivatives that enhance the rate of CT formation or enhance the resolution of the CT signal, the next few sections are concerned with specific derivatives of DMABN that are potentially of interest to those seeking to study the charge transfer process due to their uniqueness. In Figure A17.1 we display the sole charged derivative featured in this section, dubbed as C1. The TICT state of C1 has never been directly evaluated by experimental studies. However, it is inspired by a large set of ionic derivatives of DMABN that have been examined in the past, which all use the positively charged heteroatoms as extreme electron acceptors to

instigate charge transfer in the molecule of choice.[13,209–213] Typically these types of derivatives were investigated for their applicability as fluorescence probes,[214,215] and the nuclear character of the $S_1(\mathbf{R}_{TICT})$ structure for compounds of this design has not been evaluated for some time.[212,213] C1 takes advantage of the noted charge transfer of probes designed in this format, while also using the familiar pyrrole electron donor to further increase the availability of the $S_1(\mathbf{R}_{TICT})$ structure. This has extreme effects on the electronic character of the molecule, and its associated excited state dynamics. For example, C1 lacks a low lying $S_1(\mathbf{R}_{LE})$ structure, absorbs primarily at a $S_6(R_{PICT})$ structure, and at the ground state minimum structure, the character of the S1 state resembles a TICT state. When performing optimizations to find the $S_1(\mathbf{R}_{LE})$ and $S_1(\mathbf{R}_{TICT})$ minima at various twisting angles, the state at S1, as dictated by CASSCF, CASPT2, and DFT/MRCI(2), always resembled the TICT state and not the $S_1(\mathbf{R}_{LE})$ structure, so its likely the $S_1(\mathbf{R}_{LE})$ minimum does not exist. Therefore, the two state model does not apply, the internal conversion from the PICT state in particular to the TICT state is expected to be more complex, and it is only with a time resolved study can it be determined whether the charge transfer process occurs. Furthermore, XAS and XPS signals comparing the $S_1(\mathbf{R}_{TICT})$ structure and other significant signals (Fig A17.2e and f), are not uniquely well resolved, and better resolution has been found in previous sections (although the Nitrogen K-Edge XPS spectra observes the $S_1(\mathbf{R}_{TICT})$ signal as distinct by around 1 eV from all other important signals). This design was more effective as a stepping stone for the next set of derivatives, that takes advantage of an entirely separate excited state process to increase the resolution of the $S_1(\mathbf{R}_{TICT})$ structure. See the next Appendix section for an indepth review as to the applicability of taking advantage of an entirely separate process, the ESIPT process, to encourage the TICT charge transfer process in analogues similar to C1, while also producing a set of excited state dynamics that involves a sequential ESIPT and TICT set of processes.

A18: ESIPT Derivatives, Main Analysis

The focus of this section is on a final class of derivatives that take advantage of an entirely separate excited state process that has been evaluated in a litany of experimental and theoretical works, the Excited State Intramolecular Proton Transfer (ESIPT) process.[3,216–223] An in depth review of its usefulness in crafting fluorescence probes can be found elsewhere,[220] however it is necessary to illustrate the basics of the process to understand future simulated spectrum. Molecules that undergo the ESIPT process are characterized by the presence of two electronegative heteroatoms, one bonded to a hydrogen atom, and some other adjacent heteroatom which is not. After excitation, if the two heteroatoms are close enough together, the change in electronic structure induced by the photoexcitation encourages proton transfer between the two atoms. This process has been demonstrated to be extremely fast, hundreds of femtoseconds,[224,225] and sometimes even less than 50 fs,[226–229] with a small or non existent reaction barrier between the two forms, before and after proton transfer on the S1 excited state. In some, but not all cases,[228,230,231] a twist is induced after the proton transfer, along the double bond between the two heteroatoms, in a way similar to the $S_1(\mathbf{R}_{TICT})$ state in DMABN (a 90 degree twist, and a bend out of plane).[227,228,230,232–237] The character of the ESIPT process/states involved often deviates from this simple picture, owing to the presence of conical intersections,[234,237] or due to solvent dependence,.[231,238–240] It is also debatable that the use of explicit solvent is important in describing the excited state dynamics of these molecules correctly (especially for protic solvents).[241,242]

The ESIPT process is in theory, a simple process; when the molecule is excited, a proton is transferred, and the resulting minimum of the excited state post electron transfer fluoresces at as separate band then the pre-proton transfer form (Going forward, the ESIPT state pre-proton transfer is defined as the $S_1(R_{ESIPT-E})$ state, and the ESIPT post-proton transfer state is defined as the $S_1(R_{ESIPT-K})$ state, to distinguish them from the entirely different $S_1(\mathbf{R}_{TICT})$ and $S_1(\mathbf{R}_{LE})$ states typical of DMABN derivatives). However, utiliz-

ing the ESIPT process when designing DMABN derivatives is difficult; the ESIPT-K state is often the most favourable, low lying state, such that the twisting of the electron donor group post or pre proton transfer is unfavourable. In short, the ESIPT process tends to be stronger than the TICT process. However, in some cases, with proper choice of nuclear structure, this process can be reversed, such that DMABN-type derivatives can have either competing ESIPT and TICT processes (ESIPT-E $\rightarrow$ ESIPT-K $\rightarrow$ TICT), or sequential ESIPT-TICT processes (ESIPT-E $\rightarrow$ ESIPT-K $\rightarrow$ TICT). With regards to the latter process, in the case of the twisting of the electron donor after proton transfer, the state is defined as the $S_1(R_{ESIPT-K-TICT})$ state, separate from the $S_1(\mathbf{R}_{TICT})$ which defines a twisting of the electron donor group, but no proton transfer. Derivatives in this manner with the correct design act similarly to C1, such that the $S_1(\mathbf{R}_{LE})$ state does not exist since the $S_1(\mathbf{R}_{TICT})$ state must be strong enough to compete with the ESIPT process. However unlike C1, the compounds included in the next section have lower lying PICT states, and the initial absorption to the $S_1(R_{ESIPT-E})$ state which is typically on S2 or S3, allows for the decay to the $S_1(\mathbf{R}_{TICT})$ and potentially $S_1(R_{ESIPT-KTICT})$ states to be much more favourable. Furthermore, molecules with competing TICT and ESIPT processes at femtosecond timescales are of interest for those seeking to design molecules with double, or even triple fluorescence. In order to evaluate derivatives of this type, the electronic structure method of choice must be able to describe the ESIPT process consistent with previous literature. Elsewhere in the Appendix, (A.19), DFT/MRCI(2) is able to recreate the absorbance and fluorescence energies for two molecules that undergo the ESIPT process, 2-(2' -hydroxyphenyl)benzothiazole and 10-hydroxybenzo[h]quinoline, as well as the the X Ray Absorption Spectrum of the latter molecule with DFT/MRCI(2) with qualitative accuracy.[227,243]

In the previous section, it was observed that by using charged DMABN derivatives, the strength of the electron acceptor portion could be heavily increased. When applied correctly, this can also be used to serve a dual purpose. As shown by other studies on ESIPT derivatives,[244,245] the strength of the ESIPT process can be strengthened or neutered with

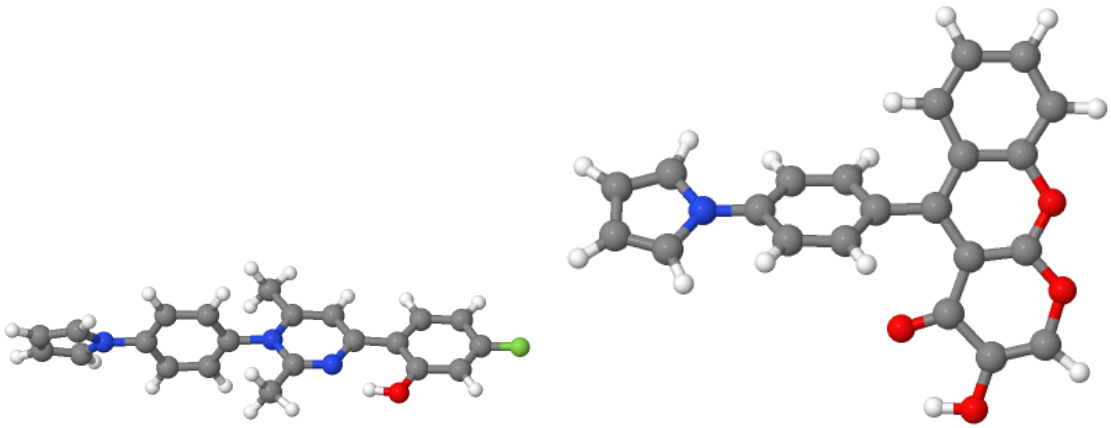

(a) Structure D1

(b) Structure D2

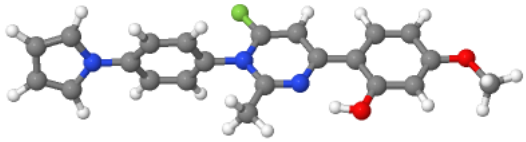

(c) Structure D3

Figure A18.1: DMABN derivatives that take advantage of the ESIPT process

the appropriate placement of electron withdrawing and electron accepting groups. The positively charged nitrogen in molecules such as C1 can act as a fantastic electron withdrawer not just for the dimethylamino-like portion of the molecule, but also for the heteroatoms involved in the ESIPT process, weakening its strength. Applying this principle led to the three derivatives shown in Figure A18.1. In D1 and D3, note the use of a fluorine atom to act as an additional withdrawing group when needed, designated in green. All structures in Figure A18.1 were optimized with CASSCF, however due to the massive amount of excited state structures involved, it is necessary to record the results of these optimizations and evaluate their implications. This is done elsewhere (Appendix, A.19), here the focus is on whether the charge transfer states of these compounds are well resolved using XAS and XPS. Figure A18.2 displays the most significant XAS spectra for the compounds in Figure A18.1. Here, the $S_1(\mathbf{R}_{TICT})$ state typical of DMABN derivatives is considered, as well as the $S_1(R_{ESIPT-E})$ (pre-proton transfer), $S_1(R_{ESIPT-K})$ (post proton transfer), and $S_1(R_{ESIPT-K-TICT})$ (post proton transfer and twist of electron donor group) excited state

minimums optimized for these compounds, when applicable.

The XAS spectra are poorly resolved; the sheer excess of heteroatoms involved on each molecule creates very similar absorptions for the TICT, ESIPT, and ESIPT-K-TICT states, most overlaping with absorptions from the ground state. For D1, the enol/keto ESIPT states are well resolved (Figure A18.2b) as is consistent with previous literature on the XAS of ESIPT molecules, however reproducing this was not the main goal of this study. With regards to D2, the ESIPT-E and ESIPT-K states were very weak and did not optimize properly, so the only significant structures involved were the ground state and the TICT minimum, which do see a small amount of resolution at the Nitrogen K-Edge (Figure A18.2c). With regards to D3, the $S_1(R_{ESIPT-K-TICT})$ state is well resolved compared to the $S_1(\mathbf{R}_{TICT})$ and $S_1(R_{ESIPT-E})$ states at the Oyxgen K-Edge (Fig A18.2f). The extent of the resolution is small, about 1 eV, however the potential to detect a sequential ESIPT-TICT process as a result of the individual resolution of the $S_1(R_{ESIPT-E})$, $S_1(R_{ESIPT-K})$, and $S_1(R_{ESIPT-K-TICT})$ states is evident. Proving that this process exists would be an interesting premise for a time resolved study.

In summary, in this section a wide variety of DMABN derivatives were examined to study under what conditions the TICT state is favourable, and under what conditions the TICT state is spectroscopically distinguishable. First, DMABN, DIABN, and ABN were examined. It was found that the nitrogen XAS and XPS spectrum would be effective in proving the existence of the two state model, both spectrum possessed unique spectroscopic signals attributed to the $\pi\sigma*$ state, and the latter possessed unique spectroscopic signals attributed to the TICT state. Combining the two methods in a time resolved study would allow for tracking of the excited state populations of the $S_1(\mathbf{R}_{LE})$, $S_1(\mathbf{R}_{\pi\sigma*})$, and $S_1(\mathbf{R}_{TICT})$ states. Next, a series of derivatives of DMABN were analyzed, to encourage future spectroscopies that could be performed to better resolve the TICT state, and to increase the rate at which the charge transfer process occurs. With respect to these results, each compound evaluated had its advantages and disadvantages; but overall simulated XAS and XPS was useful in

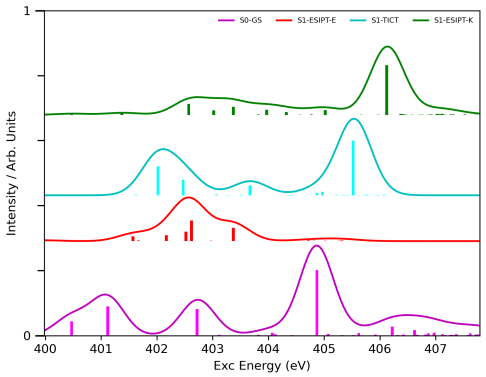

(a) Structure D1, Nitrogen K-Edge, XAS

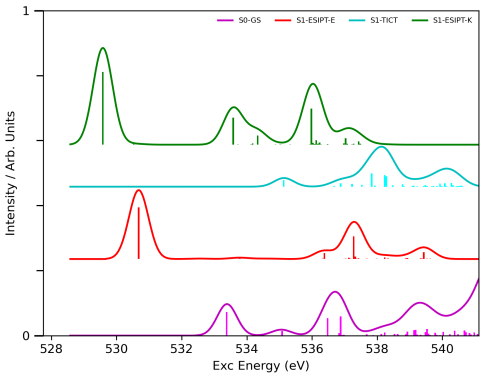

(b) Structure D1, Oxygen K-Edge, XAS

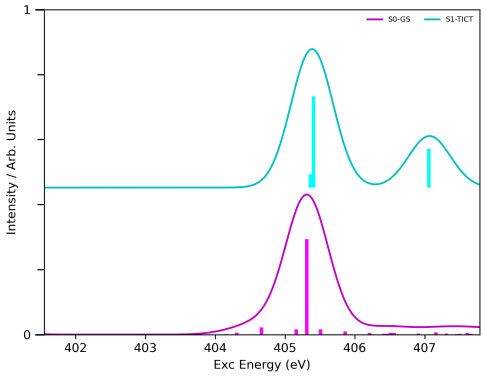

(c) Structure D2, Nitrogen K-Edge, XAS

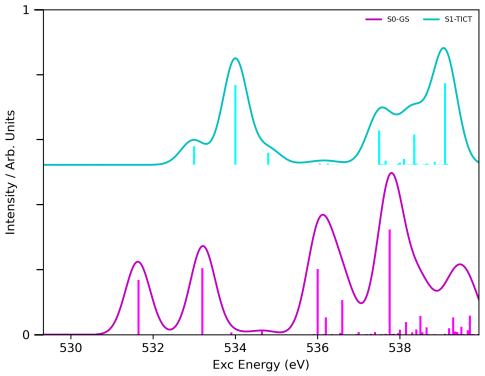

(d) Structure D2, Oxygen K-Edge, XAS

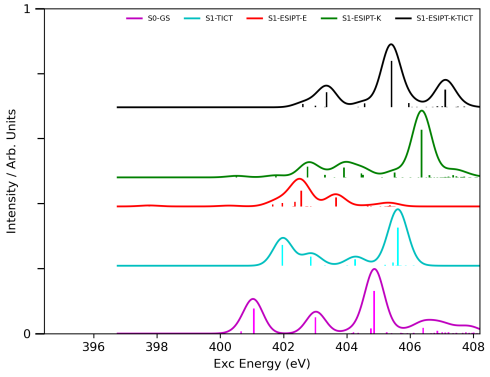

(e) Structure D3, Nitrogen K-Edge, XAS

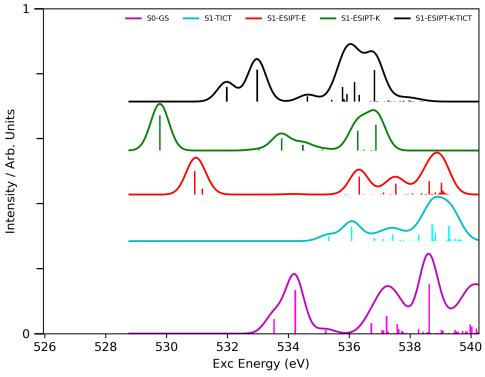

(f) Structure D3, Oxygen K-Edge, XAS

Figure A18.2: Various X Ray Absorption Spectrum of DMABN derivatives that take advantage of the ESIPT process

establishing the consistent resolution of the TICT state for all of these analogues in varying degrees.

A19: ESIPT Derivatives, Supplementary Results

Here we show that DFT/MRCI(2) is able to calculate absorbance/fluorescence energies of the first derivative shown in Figure A19.1 with relative accuracy in Table A19.1. Then, we demonstrate that we can recreate the qualitative nature of the most prominent ESIPT XAS study available with TDDFT using DFT/MRCI(2) in Figure A19.2, as well as compute further spectrum in Figure A19.3. Note that S1-ESIPT-E designates the enol form of the molecule being studied, and S1-ESIPT-K designates the keto form, as discussed in the main text.

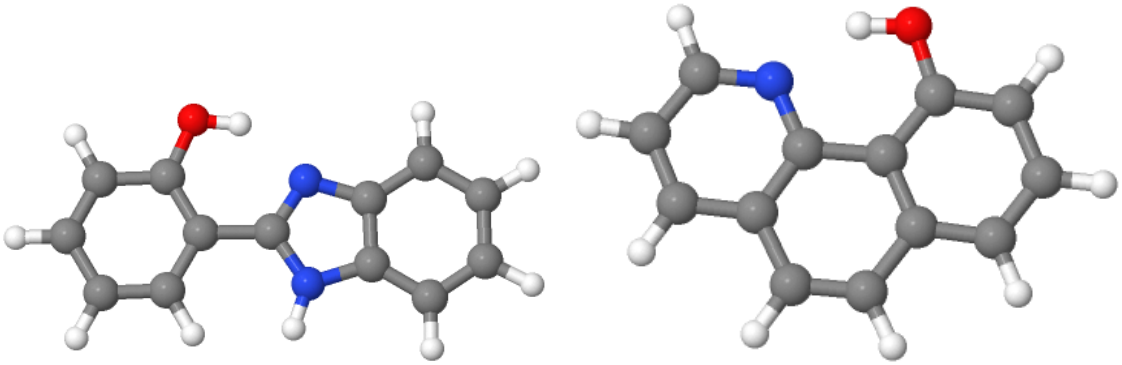

(a) 2-(2,-hydroxyphenyl)benzothiazole (b) 10-hydroxybenzo[h]quinoline

Figure A19.1: ESIPT molecules used as a benchmark for DFT/MRCI(2)

Table A19.1: Absorbance/Fluorescence based on optimized excited state structures (CASSCF, 10/9), with energies eval. with DFT/MRCI(2), compared with other methodologies

Molecule	Method	Transition	Energy (eV)
2-(2,-hydroxyphenyl) benzothiazole	DFT/MRCI(2)	Abs, S0-GS to S1	4.39
	DFT/MRCI(2)	Flu, S1-ESIPT-E to S0	3.85
	DFT/MRCI(2)	Flu, S1-ESIPT-K to S0	2.55
	DFT/MRCI(2)	Absolute energy, S1/S0 CI relative to ground state	3.80
	CASSCF[227]	Abs, S0-GS to S1	5.46
	CASSCF	Flu, S1-ESIPT-K to S0	2.83
	CASSCF	Absolute energy, S1/S0 CI relative to ground state	3.61
	TDDFT[227]	Abs, S0-GS to S1	3.86
	TDDFT	Flu, S1-ESIPT-K to S0	2.55
	TDDFT	Absolute energy, S1/S0 CI relative to ground state	2.6
	Exp.[227]	Abs, S0-GS to S1	3.68

We note a few things about Table A19.1. Firstly, the energies returned by TDDFT were not taken at optimized structures on S1,[246] and so are not directly comparable to the CASSCF optimized S1 structures, that were then evaluated with DFT/MRCI(2) to return the energies. Overall, we find that DFT/MRCI(2) represents a middle ground between the CASSCF and TDDFT methods, with the inaccuracies involved in optimizing the structures with CASSCF instead of DFT/MRCI(2) likely compounding on the energies being on the high end.

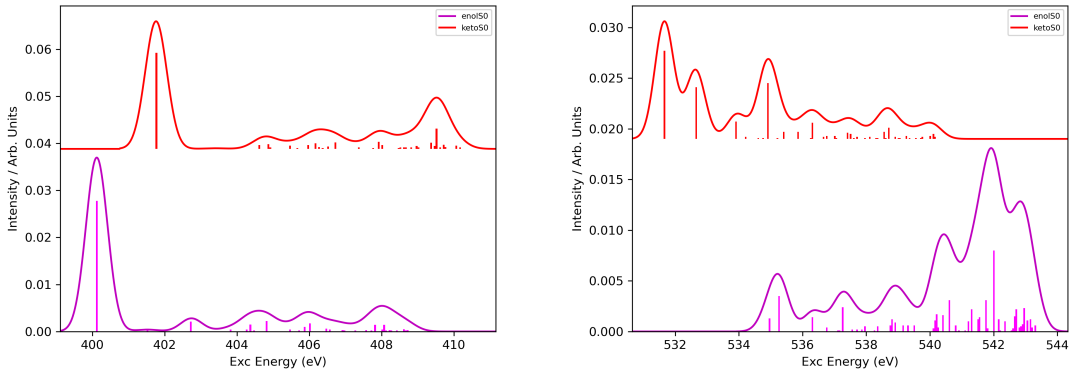

(a) N Edge (b) O Edge

Figure A19.2: Simulated ground state XAS Spectra for E2 with DFT/MRCI(2) with structures optimized with CASSCF(10,9) at the Nitrogen and Oxygen Edges, evaluated in the gas phase

Excited State ESIPT X Ray Absorption or X Ray Photoelectron Spectra do not exist currently. The closest thing is a study conducted on 10-hydroxy benzo[h]quinoline which evaluated the XAS spectra of the ground state enol and ground state keto orientations of the molecule. Figure A19.2 shows a direct comparison of the analogous spectra to the ones evaluated with TDDFT,[243] evaluated with DFT/MRCI(2) based on structures optimized with CASSCF(10,9). Figure A19.3 shows additional spectra not present in the aforementioned paper, taken using the structures optimized at the respective S1 excited states of the two conformers as well (aka, core excitations from the S1-ESIPT-E and S1-ESIPT-K states as opposed to the S0-enol and S0-keto states in Figure A19.1). We find that although there represents a significant absolute shift compared to TDDFT, we recreate the distance betweeen the major excitations of the enol and keto core absorptions fairly well. This early finding

provided a further impetus to study TICT compounds while taking advantage of the ESIPT process, considering we have now established that DFT/MRCI(2) has the ability to recreate the qualitative accuracy of EOM-CCSD for peaks associated with the TICT process,,[194] and here the qualitative accuracy of TDDFT for peaks associated with a very simple ESIPT process.[243]

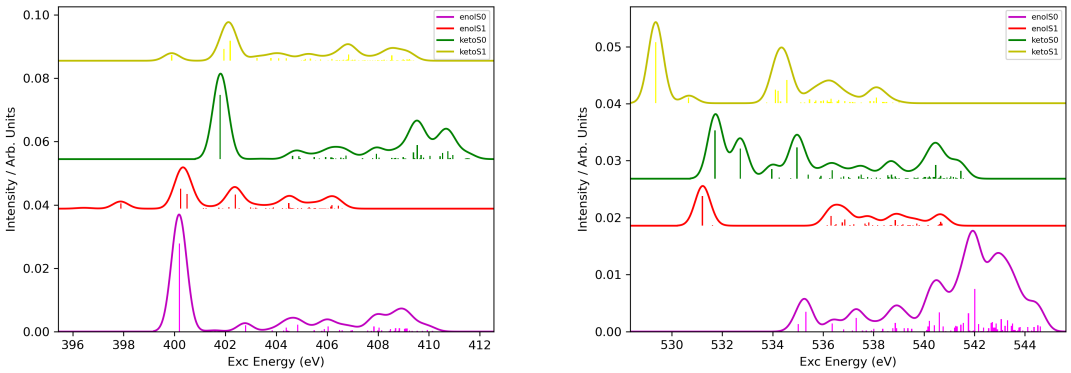

(a) N Edge (b) O Edge

Figure A19.3: Simulated ground state and excited state XAS Spectra for D2 with DFT/MRCI(2) with structures optimized with CASSCF(10,9) at the Nitrogen and Oxygen Edges, evaluated in the gas phase

After verifying the qualitative ability of DFT/MRCI(2) to recreate absorbance/fluorescence energies of the excited states involved in the ESIPT process, as well as the shape of the XAS spectrum, the derivatives in the main text D1, D2, and D3 were evaluated using XAS and XPS as well. However, in order to evaluate these compounds properly, a host of excited state structures needed to be optimized to describe the complex dynamics at play. A summary of these results for each compound is found in Table A.19.2.

Structure D1 was an example of a molecule that has directly competing TICT and ESIPT processes, with the S1-TICT excited state being the absolute minimum found on S1, according to the absolute energies returned by DFT/MRCI(2). Structure D2 also had a low lying S1-TICT excited state; however it seems the proton transfer between two adjacent oxygen atoms was weaker, as the molecule only directly absorbed with significant oscillator strength to the S2-PICT state, and therefore the ESIPT process is unlikely for this molecule. In

Table A.19.2: Summary of the relevant excited states of structures evaluated in the ESIPT Derivatives section of the main text. Structures were optimized using CASSCF(10,9), and energies were evaluated using DFT/MRCI(2).

Molecule	Excited State Minimum Geometry	Electronic State	Osc. Strength	Absolute Energy (eV)
D1	Ground State Minimum	S0	N/A	0.0
	Ground State Minimum	S2-ESIPT-E	0.3633	3.36
	Ground State Minimum	S4	0.6385	4.08
	TICT Minimum	S1-TICT	0.0001	2.75
	ESIPT-E Minimum	S1-ESIPT-E	0.1107	3.13
	ESIPT-K Minimum	S1-ESIPT-K	0.0024	3.10
D2	Ground State Minimum	S0	N/A	0.0
	Ground State Minimum	S1-TICT	0.0512	1.99
	Ground State Minimum	S2-PICT	0.4623	2.02
	TICT Minimum	S1-TICT	0.0002	1.35

the design of Structure D3, it was hoped that by placing the electron withdrawing fluorine closer to the cationic nitrogen, that the ESIPT state would be weaker, and a hypothetical ESIPT-K-TICT state could be possible. Essentially, after the proton transfer happens, converting the excited state population in this case from ESIPT-E to ESIPT-K, perhaps the pyrrole ring could twist afterwards, leading to the population of an S1-ESIPT-K-TICT state. CASSCF predicted an excited state minimum that fit this hypothetical state (see Appendix, A.19), lying at an absolute energy distant to the ground state absorption to the S2-ESIPT-E state, and 0.2 eV below the ground state absorption to the S4-PICT state according to DFT/MRCI(2). However, out of all the excited state minimum structures evaluated, it still lied at the highest absolute energy (compared to the S1-TICT, and S1-ESIPT-E and K states), therefore it seems extremely unlikely that this state would be populated, especially since it would have to occur after the proton transfer, and due to competition with the lower lying S1-ESIPT-K minimum. Therefore, it is most likely impossible that this chained ESIPT/TICT process would occur, however we thought it worth evaluating with XAS due to its distinct electronic character as an excited state minimum.

There are numerous advantages to designing molecules in this manner. For example, Structure D3 did prove that the location of certain withdrawing groups, like the fluorine atom, could strengthen or weaken one process over the other, as the S1-TICT minimum is more likely to be populated compared to the S1-ESIPT-K minimum in the case of D3 over D1. Furthermore, the design of these three molecules do not suffer from the same pitfalls as C1; absorptions to the initial ESIPT are not as high lying, and typically lie at S2 to S4, meaning that the excited state population could potentially reach the S1-TICT state slightly faster after occupation of either the PICT or ESIPT-E states above it. For example, when comparing C1 and D1, D1 is more likely to populate the charge transfer state owing to the strong absorption to S2 from the GS to the ESIPT-E state, which may couple easier to the S1-TICT state then the S6-PICT state that C1 absorbs to. Unfortunately, it is still unlikely D1, D2, or D3 could be studied in an experimental study, owing to the inherent difficulties in evaluating

the excited state dynamics of a reactive ionic compound. Solvents that possess the capability for hydrogen bonding especially are infeasible to use when studying these compounds. These compounds instead work best as a theoretical base from which to design compounds that may be able to possess competing excited state pathways; the cationic form of D1-D3 was necessary to lower the energy of the charge transfer states present on the potential energy surfaces evaluated by CASSCF, but perhaps a different electronic method may be able to predict low lying charge transfer states for compounds of this form without the use of such a strong electron acceptor. Also, even if specific states are too high lying to be occupied over the course of a time resolved study for some of these compounds, evaluating their excited state spectroscopies is still useful, as we have elected to do with the S1-ESIPT-K-TICT state. Even if, for the derivatives studied in this paper, the ESIPT-K-TICT state is unlikely to be occupied, evaluating its electronic character via X Ray studies may still be a useful metric when derivatives with lower lying states are designed in the future. However so far, the search for a neutral compound that maintains competing TICT and ESIPT processes has proven to be a difficult needle to thread.

Finally, we show the nuclear structures mentioned in Table A.19.2, all optimized as minima on S1 using CASSCF (10,9) in the gas phase.

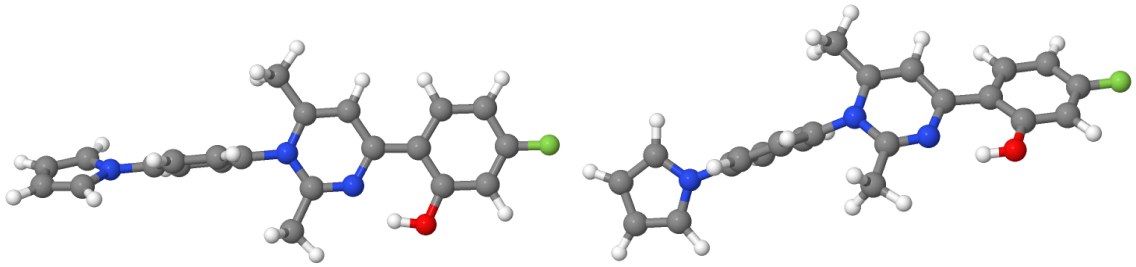

(a) Ground State Minimum

(b) TICT minimum

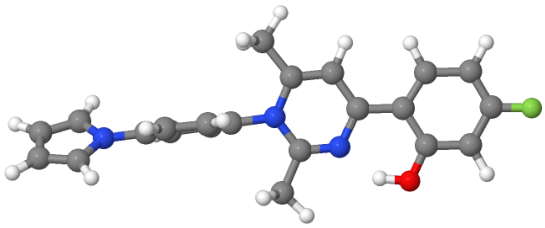

(c) ESIPT-E minimum

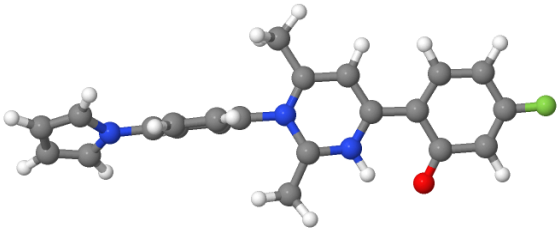

(d) ESIPT-K minimum

Figure A19.4: Nuclear structures of excited state minima on S1 of ESIPT derivatives, D1

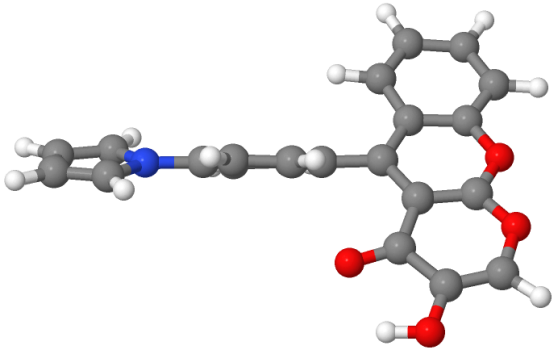

(a) Ground State Minimum

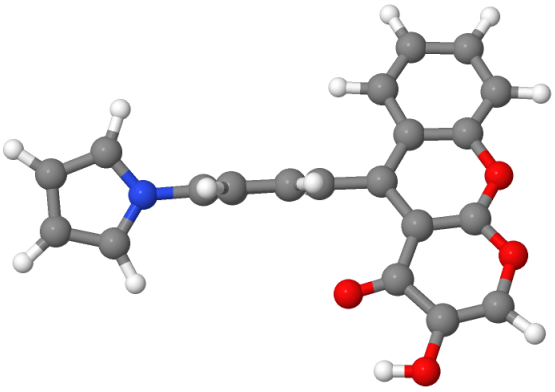

(b) TICT minimum

Figure A19.5: Nuclear structures of excited state minima on S1 of ESIPT derivatives, D2

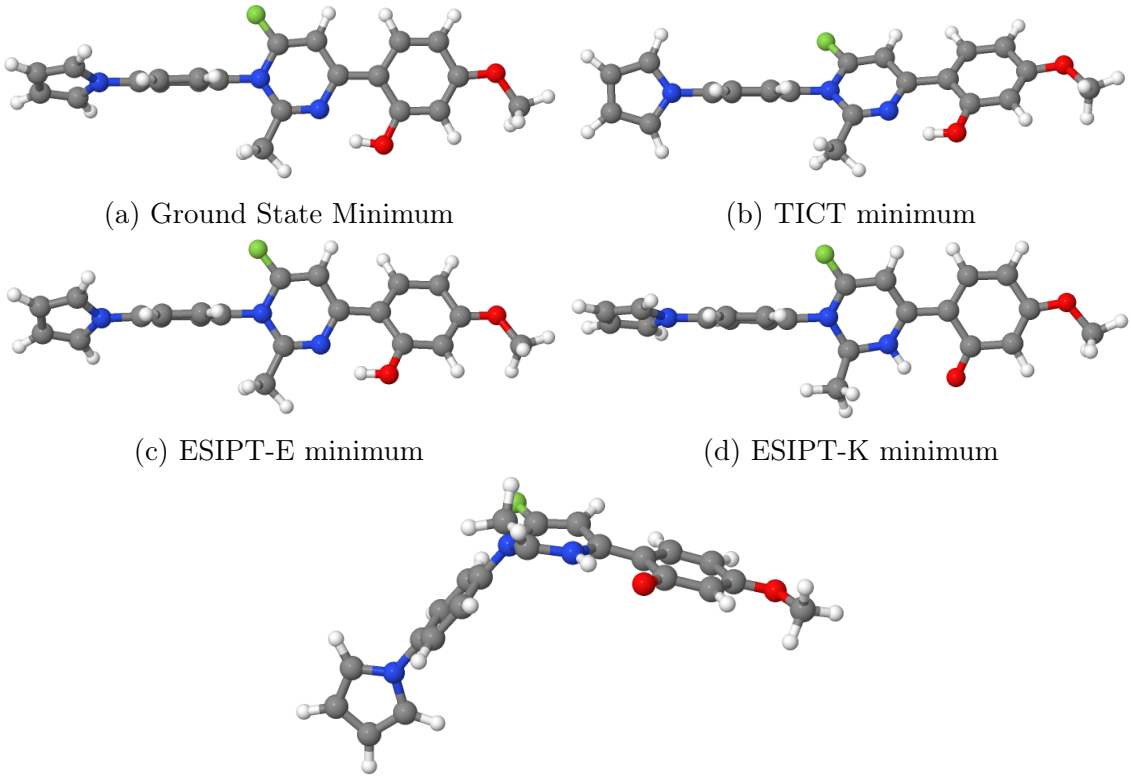

(a) Ground State Minimum

(b) TICT minimum

(c) ESIPT-E minimum

(d) ESIPT-K minimum

(e) ESIPT-K-TICT minimum

Figure A19.6: Nuclear structures of excited state minima on S1 of ESIPT derivatives, D3

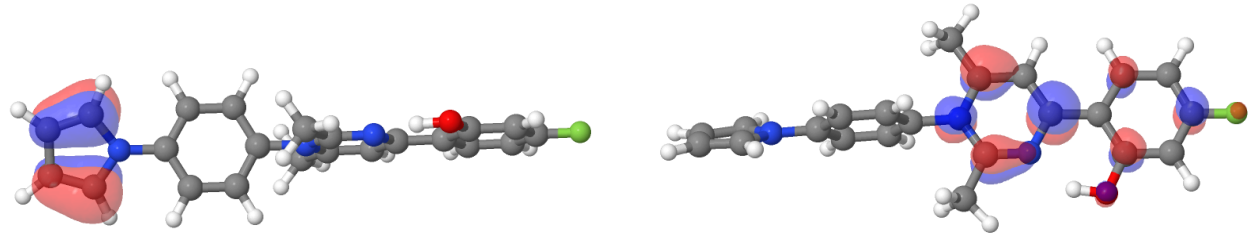

(a) S1-TICT, D1-GS minimum

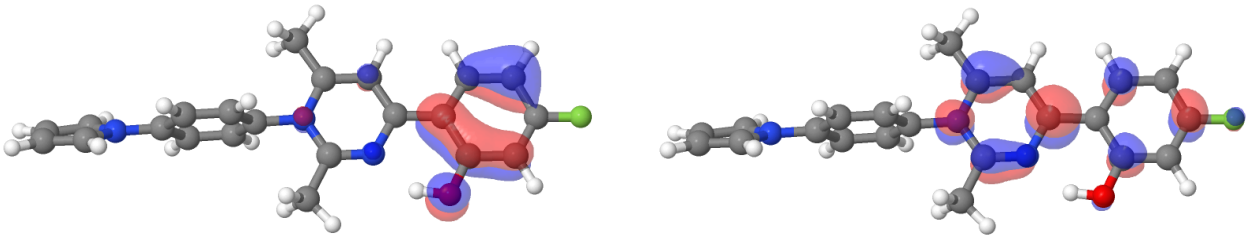

(b) S2-ESIPT-E, D1-GS minimum

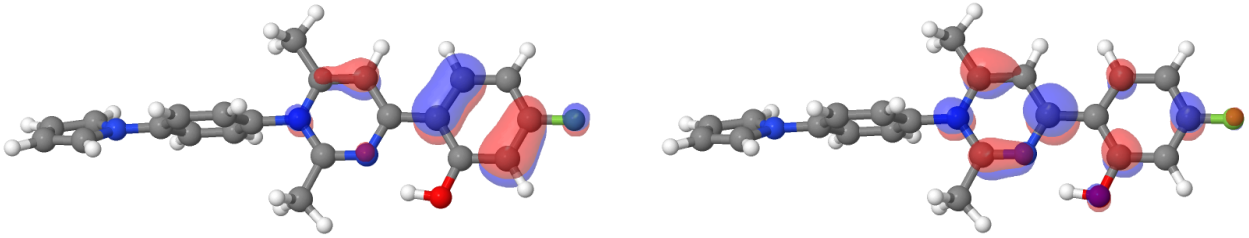

(c) S4, D1-GS minimum

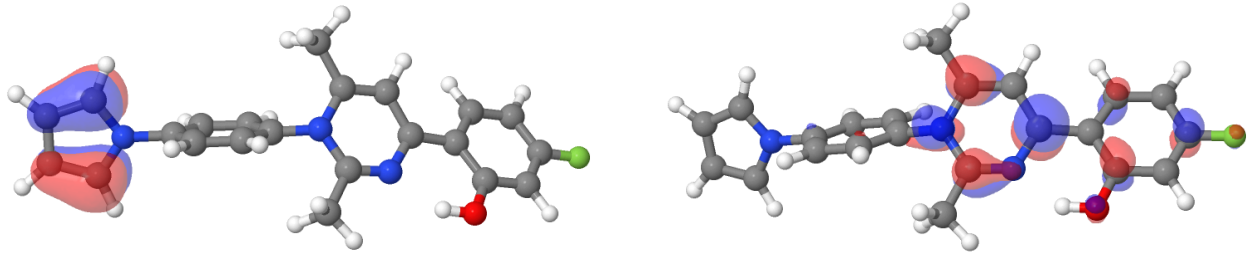

(d) S1-TICT, D1-TICT minimum

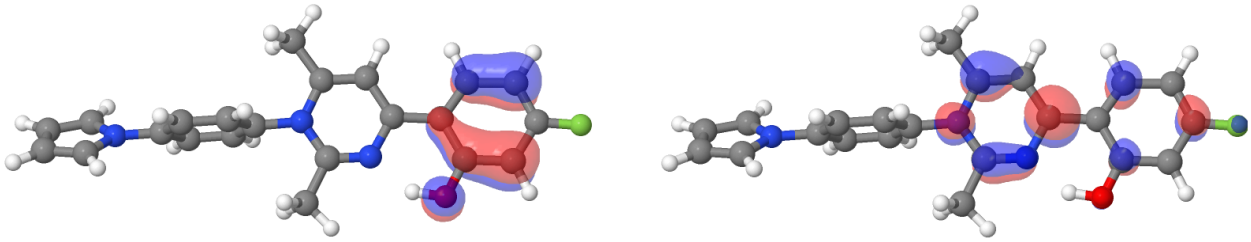

(e) S1-ESIPT-E, D1-ESIPT-E minimum

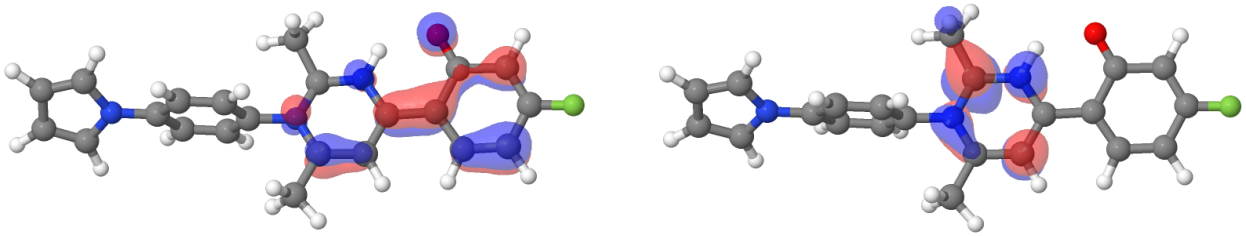

(f) S1-ESIPT-K, D1-ESIPT-K minimum

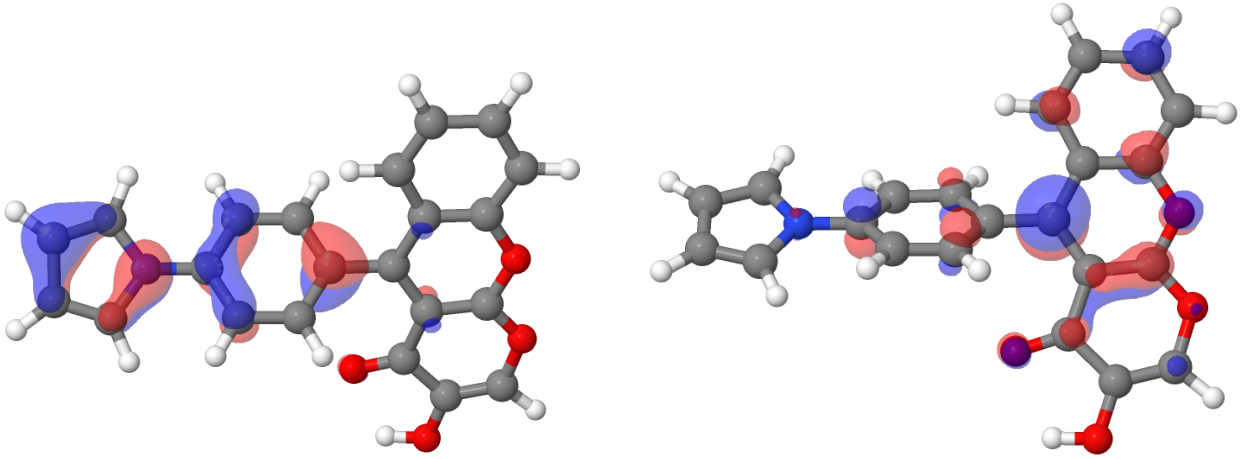

(g) S2-PICT, D2-GS minimum

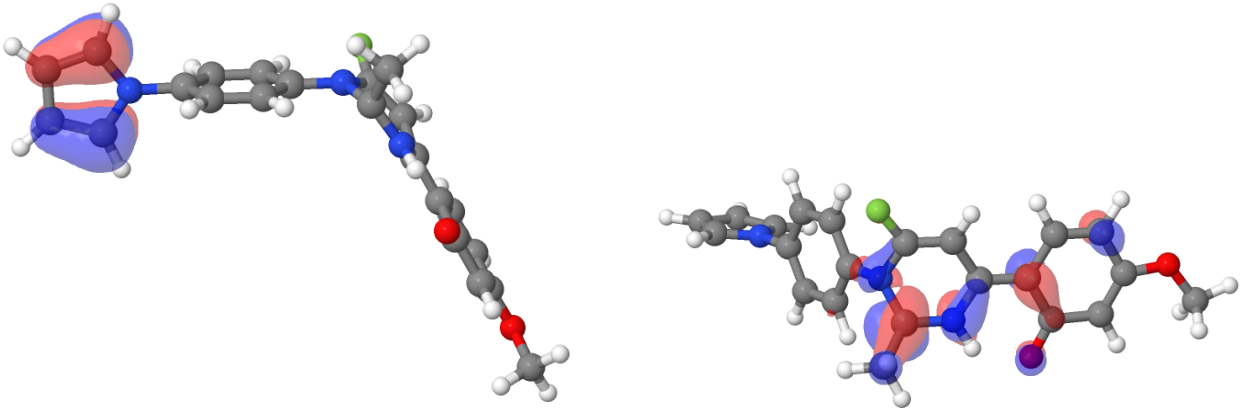

(h) S1-TICT, D3-ESIPT-K-TICT minimum

Figure A19.7: Dominant NTO pairs, some excited state descriptions of states evaluated in Table A.19.2 (truncated).

A20: Cartesian Coordinates of Excited State structures of DMABN and its analogues

DMABN

S0-GS

21

C 3.007849 -1.253795 -0.116671

N 2.276400 0.000425 -0.089128

C 3.005972 1.255608 -0.121462

H 2.796249 1.879389 0.766597

H 4.082555 1.046083 -0.137153

H 2.764098 1.855399 -1.018394

C 0.899532 -0.000337 -0.055648

C 0.161627 1.212870 -0.039748

C -1.225720 1.207035 -0.003811

C -1.946690 -0.001673 0.017404

C -1.224477 -1.209708 0.000649

C 0.162879 -1.214253 -0.035268

H 0.679589 -2.172119 -0.047611

H -1.765073 -2.157664 0.015754

C -3.378055 -0.002340 0.054674

N -4.543337 -0.002883 0.085015

H -1.767288 2.154486 0.007799

H 0.677380 2.171211 -0.055613

H 2.799080 -1.874483 0.773771

H 2.766873 -1.857380 -1.011297

H 4.084122 -1.042730 -0.133170

S1-LE

21

C 3.03531357 -1.20966423 0.10885379

N 2.26818120 0.00212364 -0.09362588

C 3.02554350 1.21084436 -0.34502586

H 3.22673265 1.77567108 0.57124252

H 3.98149190 0.94383978 -0.79367457

H 2.50347027 1.85686104 -1.04673801

C 0.90135611 0.00533514 -0.05527626

C 0.18011905 1.23854588 0.06212970

C -1.25710820 1.23851781 0.10029338

C -1.96931247 0.00056044 0.01645489

C -1.27081858 -1.24374502 -0.10342440

C 0.16300849 -1.25505219 -0.13631498

H 0.67460566 -2.18158038 -0.33306290

H -1.82811683 -2.16226388 -0.19553441

C -3.40302785 0.00667506 0.05171275

N -4.56665301 0.01223545 0.08026642

H -1.80063457 2.16270836 0.21440662

H 0.69930237 2.16619797 0.23335858

H 2.54571321 -1.86258305 0.82685781

H 3.19309718 -1.76420686 -0.82206434

H 4.01130235 -0.94788640 0.51585517

S1-$\pi\sigma*$

21

C 2.99932184 -1.30211974 0.00836426

N 2.25798607 -0.04825309 0.00096489

C 3.00769838 1.20090801 -0.00804116

H 2.79939697 1.79760743 0.88096019

H 4.06838245 0.97365858 -0.02009292

H 2.77949665 1.79567864 -0.89321983

C 0.91436783 -0.04311820 0.00776820

C 0.18060376 1.18321610 0.00528362

C -1.19011112 1.18456340 0.00974861

C -1.95739977 -0.05714018 0.01762811

C -1.19762933 -1.26085208 0.02196067

C 0.17210468 -1.26314158 0.01764782

H 0.69217609 -2.20641708 0.02156031

H -1.73629931 -2.19696474 0.02918246

C -3.43213515 -0.08500161 0.02160418

N -4.11676808 0.97034292 0.01763070

H -1.74780105 2.10782779 0.00754053

H 0.70537407 2.12400567 0.00030937

H 2.78582120 -1.88647898 0.90439528

H 2.76882767 -1.90641957 -0.86984310

H 4.06152224 -1.08220776 -0.00470465

S1-pTICT

21

C 3.01872881 -1.07527464 0.54633682

N 2.26778699 -0.03620537 -0.12138333

C 3.00596314 0.96918080 -0.85194708

H 2.44639509 1.89215282 -0.86705778

H 3.97965669 1.11797665 -0.40364677

H 3.12928530 0.62473786 -1.87920828

C 0.88245212 -0.00486980 -0.06291959

C 0.20851334 1.17566925 0.39091615

C -1.16503390 1.19810400 0.45598066

C -1.93927213 0.05895617 0.05616250

C -1.25366086 -1.11321271 -0.40526406

C 0.12009441 -1.15292055 -0.45614090

H 0.61702916 -2.02174698 -0.84547890

H -1.81796961 -1.97331490 -0.71022423

C -3.37254908 0.09137617 0.11664949

N -4.53514613 0.11767352 0.16571328

H -1.66225899 2.08221755 0.80573956

H 0.77517607 2.02043764 0.73536832

H 3.94350026 -1.26701281 0.01791771

H 3.24353981 -0.73870629 1.55890615

H 2.42133435 -1.97207675 0.61027352

S1-TICT

21

C 3.19523251 -1.15365120 0.87843150

N 2.29798128 -0.25310943 0.19348013

C 2.86477214 0.71201238 -0.73229613

H 3.56295620 1.36000341 -0.19811046

H 3.41232374 0.18535467 -1.51712216

H 2.06415954 1.30042406 -1.16519829

C 0.89926190 -0.38060821 0.41015537

C 0.27086568 0.76388091 1.03815103

C -1.01883841 1.14184101 0.71843796

C -1.75759691 0.48921962 -0.31577628

C -1.11975413 -0.56595833 -1.03362632

C 0.17231082 -0.96225497 -0.73747361

H 0.63741463 -1.75335550 -1.31274448

H -1.67432759 -1.09460046 -1.79730731

C -3.09258779 0.88921152 -0.62774885

N -4.18105709 1.21864476 -0.88495555

H -1.49405779 1.93218398 1.28401403

H 0.80172111 1.29780409 1.81667823

H 3.03036332 -1.05808023 1.95187346

H 2.94689205 -2.17718741 0.59305626

H 4.23192481 -0.93509666 0.63093945

S2-PICT

21

C 3.00970351 -1.24517599 -0.11569647

N 2.26052229 0.00051117 -0.09720839

C 3.00827609 1.24699164 -0.11959713

H 2.79643179 1.83710992 0.77217423

H 4.06897637 1.02528621 -0.14872941

H 2.74726681 1.83478111 -0.99977677

C 0.89778748 -0.00020970 -0.05942606

C 0.15979107 1.24492106 -0.04171217

C -1.22003871 1.24354441 -0.00509142

C -1.96176561 -0.00173174 0.01619931

C -1.21858090 -1.24621310 -0.00001577

C 0.16124971 -1.24612255 -0.03664812

H 0.68484709 -2.18784343 -0.04778347

H -1.74956793 -2.18560469 0.01691423

C -3.36418264 -0.00247953 0.05205067

N -4.51535776 -0.00309280 0.08152379

H -1.75212721 2.18237403 0.00798750

H 0.68228121 2.18720149 -0.05681772

H 2.79967214 -1.83209522 0.77863293

H 2.74827390 -1.83665980 -0.99325050

H 4.07010617 -1.02235087 -0.14703604

S2/S1 CI (22 degree twist)

21

C 3.02603078 -1.18909166 0.18717542

N 2.24562813 0.00025692 -0.09620205

C 3.00701082 1.19123746 -0.42129933

H 3.26442744 1.74606145 0.48546284

H 3.92979670 0.89089556 -0.91516581

H 2.44138347 1.83139033 -1.08879498

C 0.88024528 -0.00046400 -0.05762049

C 0.15295082 1.23619729 0.11790739

C -1.22575446 1.23328638 0.15892668

C -1.96887754 -0.00185692 0.01605923

C -1.23331777 -1.23600558 -0.16548368

C 0.14579039 -1.23797535 -0.19579003

H 0.67465898 -2.16140790 -0.37495592

H -1.77045192 -2.16530316 -0.27950708

C -3.37303653 -0.00255384 0.05297933

N -4.52356047 -0.00337492 0.08321584

H -1.75702352 2.16205320 0.30114475

H 0.68970400 2.16010839 0.26913258

H 2.49568562 -1.83396219 0.87852037

H 3.24179329 -1.73922669 -0.73319059

H 3.97038137 -0.88705313 0.63749875

S1-TS CASSCF

21

C 2.889772 -1.661921 0.760924

N 2.326793 -0.482634 0.151957

C 3.230395 0.585954 -0.216222

H 3.723239 1.004931 0.668661

H 4.005589 0.209377 -0.887698

H 2.672781 1.374421 -0.712693

C 0.936125 -0.288113 0.197565

C 0.410182 0.786715 1.022199

C -0.823621 1.364157 0.724578

C -1.577682 0.967157 -0.449505

C -1.034627 -0.048319 -1.300910

C 0.210849 -0.634393 -0.995731

H 0.628530 -1.373154 -1.665417

H -1.620561 -0.427768 -2.125054

C -2.851391 1.560067 -0.725250

N -3.865154 2.032732 -0.948960

H -1.253900 2.093408 1.396728

H 0.961302 1.110967 1.893639

H 2.883601 -1.570499 1.854211

H 2.289802 -2.531690 0.495725

H 3.916178 -1.809684 0.426256

S1-TS CASPT2

21

C 3.025192 -1.217362 -0.447600

N 2.254180 -0.037989 -0.092427

C 2.908704 1.258259 -0.093555

H 2.686317 1.772416 0.854792

H 3.992638 1.134588 -0.224678

H 2.484160 1.862181 -0.913661

C 0.882996 -0.154511 0.193008

C 0.298651 0.502055 1.277408

C -1.096134 0.683111 1.349682

C -1.865883 0.357724 0.155965

C -1.254938 -0.263410 -0.944373

C 0.073582 -0.678545 -0.938380

H 0.567331 -1.048231 -1.839819

H -1.862921 -0.438037 -1.839643

C -3.249390 0.700620 0.085064

N -4.401364 0.992834 0.037329

H -1.561475 1.170318 2.206565

H 0.937997 0.834581 2.105022

H 2.345045 -2.075276 -0.500793

H 3.541422 -1.058297 -1.408249

H 3.784010 -1.384864 0.338755

DIABN

S0-GS

33

C 1.85184360 -1.54181386 -0.04388173

N 1.23637814 -0.19951667 -0.11930397

C -0.14711328 -0.08215124 -0.19712385

C -0.76950571 1.12537588 -0.61187427

C -2.14837067 1.24186157 -0.71309189

C -2.99250492 0.15608540 -0.41466199

C -4.41508235 0.27397110 -0.52623738

N -5.57334779 0.36927205 -0.61672613

C -2.39603948 -1.04796676 -0.00126038

C -1.01637787 -1.16341221 0.11247855

H -0.61767817 -2.10779592 0.47803121

H -3.02772280 -1.90140870 0.25170784

H -2.58422339 2.18584880 -1.04491453

H -0.16000396 1.98128545 -0.88740235

C 2.12429441 0.94947049 0.18945567

C 2.50428379 1.80704945 -1.03214949

H 2.83081325 1.17550426 -1.87140551

H 3.33613714 2.48087893 -0.76762900

H 3.92107460 -1.06661660 -0.66931474

C 1.64500792 1.79782726 1.37753575

H 2.42732451 2.52588031 1.64555750

H 0.72676302 2.36130475 1.15899630

H 3.06063020 0.47829755 0.52277845

H 1.67698011 2.43846850 -1.38862243

C 2.19114220 -1.96618513 1.39395527

H 2.57070110 -3.00078359 1.41226496

H 1.45082137 1.16344278 2.25597595

H 1.30514173 -1.91378459 2.04523730

C 3.06162772 -1.68171504 -0.98094819

H 3.40034866 -2.73010831 -0.98584501

H 1.09723252 -2.23683744 -0.43513578

H 2.79448697 -1.40462024 -2.01211755

H 2.97116900 -1.32205602 1.83294470

S1-LE

33

C 2.03348835 1.26841406 -0.30012239

N 1.22781426 0.05074629 -0.09821168

C -0.16828402 0.11914525 -0.22729310

C -0.94667846 -1.06016085 -0.43961634

C -2.37839802 -0.98787419 -0.55727477

C -3.03063819 0.27642509 -0.45968432

C -4.45728073 0.34515935 -0.57215313

N -5.60344669 0.39981720 -0.66176070

C -2.28291802 1.47372712 -0.24615108

C -0.85373959 1.41335319 -0.13611856

H -0.33101256 2.30005547 0.17633774

H -2.80015360 2.41250370 -0.12752867

H -2.95621643 -1.87814584 -0.74685637

H -0.47505823 -2.00491302 -0.62910718

C 1.94204428 -1.13618499 0.41522533

C 1.36217191 -1.67168648 1.72616129

H 1.25452907 -0.86766838 2.45552780

H 2.04552923 -2.41712653 2.13952377

H 3.21655216 1.24811269 1.54401414

C 2.18252422 -2.24138778 -0.62093949

H 2.95496985 -2.91635467 -0.24474159

H 1.29836781 -2.84332920 -0.82097216

H 2.92795029 -0.75481692 0.66664753

H 0.38955672 -2.14111887 1.59555149

C 3.19232620 1.03505498 -1.27340553

H 3.67631769 1.99086450 -1.48398994

H 2.52951322 -1.82687659 -1.56691696

H 2.82791240 0.62752987 -2.21719854

C 2.50478447 1.88776014 1.01784880

H 3.00373078 2.83947423 0.82225796

H 1.37956487 1.97793948 -0.79161378

H 1.66236415 2.07546088 1.68464015

H 3.95687962 0.36426484 -0.87837072

S1-TICT

33

C 1.56376044 1.29447295 0.38570790

N 1.26575003 -0.10219223 0.02203941

C -0.11861813 -0.53071315 -0.21978582

C -0.71319662 0.02842951 -1.42009450

C -2.05029765 0.36661678 -1.46276034

C -2.87990569 0.26622595 -0.30765373

C -4.26101570 0.62442620 -0.36121800

N -5.36545053 0.91385103 -0.40314740

C -2.28867856 -0.19845916 0.90355778

C -0.95372071 -0.54171557 0.96740293

H -0.54475308 -0.89477110 1.90543907

H -2.90968156 -0.31621069 1.78160045

H -2.48845498 0.68241334 -2.40018744

H -0.11891817 0.11441787 -2.32080047

C 2.37974101 -1.11395673 -0.10752563

C 2.18267133 -2.22924049 0.91702236

H 2.16549655 -1.83932422 1.93551983

H 3.01645441 -2.92913247 0.83785226

H 3.16850952 0.92413671 1.83363453

C 2.43277534 -1.63910428 -1.54066653

H 3.26612270 -2.33867739 -1.62691198

H 1.51180845 -2.15937017 -1.79838206

H 3.30128804 -0.58060875 0.11435432

H 1.25517154 -2.76824603 0.73137693

C 2.42532275 1.97019792 -0.68288091

H 2.53337745 3.02500644 -0.42609501

H 2.59405879 -0.83277205 -2.25724096

H 1.95200786 1.91025057 -1.66268645

C 2.17870601 1.38061150 1.78403231

H 2.28332887 2.43266109 2.05325478

H 0.59258010 1.77965372 0.40461465

H 1.53447452 0.90733981 2.52473307

H 3.42551665 1.53883211 -0.74683133

S2-PICT

33

C 1.957871 1.323681 0.360798

N 1.175419 0.112793 0.063015

C -0.195355 0.160648 -0.103293

C -0.948668 -0.999784 -0.389224

C -2.315877 -0.965908 -0.557877

C -3.027637 0.224674 -0.453586

C -4.456753 0.257932 -0.630683

N -5.587087 0.284082 -0.770998

C -2.309961 1.381458 -0.172424

C -0.941136 1.357728 -0.001925

H -0.472749 2.300507 0.212920

H -2.829445 2.325551 -0.083609

H -2.839370 -1.886654 -0.775372

H -0.468570 -1.953043 -0.484298

C 1.967043 -1.127206 -0.039680

C 1.690613 -2.155284 1.066623

H 1.720731 -1.676309 2.045925

H 2.468548 -2.922235 1.042274

H 3.399163 0.499944 1.804056

C 2.012803 -1.740267 -1.446340

H 2.783649 -2.514264 -1.472962

H 1.078664 -2.199509 -1.762329

H 2.984093 -0.797657 0.145875

H 0.731895 -2.661151 0.975824

C 2.950078 1.671448 -0.753690

H 3.423686 2.631815 -0.537376

H 2.273516 -0.980008 -2.183474

H 2.435160 1.755692 -1.712232

C 2.625362 1.267038 1.738729

H 3.100122 2.226310 1.957396

H 1.267805 2.152236 0.404687

H 1.884164 1.070621 2.515325

H 3.747290 0.933286 -0.858364

S1-TS CASSCF

33

C 1.948316 1.268782 0.064512

N 1.312142 -0.053880 -0.017603

C -0.078938 -0.140541 -0.124408

C -0.688534 -0.247452 -1.448693

C -2.053733 0.057984 -1.663855

C -2.856540 0.537499 -0.571636

C -4.241654 0.837109 -0.763026

N -5.346376 1.076544 -0.919769

C -2.259386 0.690464 0.713581

C -0.906365 0.404906 0.938536

H -0.491615 0.523303 1.928162

H -2.881186 1.001066 1.541471

H -2.514470 -0.166831 -2.613859

H -0.077014 -0.547922 -2.285619

C 2.131147 -1.265320 0.076557

C 1.780950 -2.063927 1.336299

H 1.897285 -1.455600 2.234193

H 2.443143 -2.928181 1.421937

H 3.552752 0.833501 1.494873

C 2.042621 -2.141869 -1.175502

H 2.742664 -2.974548 -1.080312

H 1.043620 -2.558107 -1.304971

H 3.162846 -0.930025 0.166236

H 0.751975 -2.423216 1.296129

C 2.848586 1.534026 -1.146306

H 3.228869 2.556891 -1.104108

H 2.306202 -1.579528 -2.072483

H 2.289021 1.418029 -2.075311

C 2.689055 1.492173 1.386173

H 3.053054 2.520707 1.427490

H 1.124016 1.977581 0.024512

H 2.027183 1.334727 2.238379

H 3.708995 0.862200 -1.174649

S1-TS CASPT2

33

ABN

S0-GS

15

H 2.784729 -0.851616 -0.163993

N 2.287094 0.000011 -0.379259

H 2.783744 0.852986 -0.167070

C 0.899151 -0.000504 -0.220968

C 0.163100 1.204330 -0.152329

C -1.225699 1.204148 -0.043794

C -1.936066 -0.001715 0.013010

C -1.224281 -1.206952 -0.039130

C 0.164519 -1.205922 -0.147665

H 0.666835 -2.157979 -0.179949

H -1.754011 -2.147348 0.010294

C -3.376620 -0.002335 0.130973

N -4.510065 -0.002822 0.223577

H -1.756537 2.144104 0.001991

H 0.664300 2.156843 -0.188308

S1-LE

15

H 2.74698342 -0.82044549 -0.10062207

N 2.28147925 0.00662349 -0.41925725

H 2.75095977 0.82907269 -0.09433087

C 0.90809329 0.00879028 -0.22613146

C 0.19442000 1.24278719 -0.17333724

C -1.23667679 1.24558212 -0.04496048

C -1.94595363 -0.00359923 0.02263993

C -1.23878110 -1.25390460 -0.04027502

C 0.18849110 -1.25440287 -0.16896350

H 0.72841463 -2.18738158 -0.23059570

H -1.78848603 -2.18019131 0.00978522

C -3.37123167 -0.00155399 0.15067227

N -4.53089557 0.00066908 0.25565097

H -1.78368851 2.17357653 0.00003670

H 0.72706483 2.17960668 -0.24293152

S1-TICT

15

H 2.962025 0.036636 -0.819209

N 2.248021 0.007068 -0.108124

H 2.529257 -0.048654 0.864108

C 0.858783 0.039118 -0.504704

C 0.147958 1.241115 -0.202546

C -1.203657 1.219381 0.002873

C -1.931047 -0.003667 0.017330

C -1.202125 -1.226493 -0.157195

C 0.151553 -1.223478 -0.369600

H 0.676625 -2.160728 -0.510958

H -1.735884 -2.167070 -0.131715

C -3.339342 -0.023596 0.242295

N -4.468058 -0.044319 0.422758

H -1.736146 2.149665 0.147272

H 0.672228 2.190252 -0.195207

S2-PICT

15

H 2.805530 -0.832103 -0.018243

N 2.332360 0.028709 -0.296811

H 2.826513 0.864840 0.018246

C 0.938377 0.043078 -0.168750

C 0.223988 1.300612 -0.107805

C -1.136895 1.326514 -0.009756

C -1.897772 0.074228 0.015740

C -1.167376 -1.194549 -0.055101

C 0.193721 -1.198120 -0.152858

H 0.738122 -2.147868 -0.219647

H -1.736055 -2.128154 -0.035530

C -3.302354 0.089888 0.087049

N -4.484243 0.103102 0.147506

H -1.682713 2.272370 0.043529

H 0.791283 2.238651 -0.140838

References

(1) Ishida, T.; Rossky, P. J. Consequences of strong coupling between solvation and electronic structure in the excited state of a betaine dye. *The Journal of Physical Chemistry B* **2008**, *112*, 11353–11360.

(2) Kharlanov, V.; Rettig, W. Experimental and theoretical study of excited-state structure and relaxation processes of betaine-30 and of pyridinium model compounds. *The Journal of Physical Chemistry A* **2009**, *113*, 10693–10703.

(3) Kumpulainen, T.; Lang, B.; Rosspeintner, A.; Vauthey, E. Ultrafast elementary photochemical processes of organic molecules in liquid solution. *Chemical Reviews* **2017**, *117*, 10826–10939.

(4) Gómez, I.; Reguero, M.; Boggio-Pasqua, M.; Robb, M. A. Intramolecular charge transfer in 4-aminobenzonitriles does not necessarily need the twist. *Journal of the American Chemical Society* **2005**, *127*, 7119–7129.

(5) Gomez, I.; Castro, P. J.; Reguero, M. Insight into the mechanisms of luminescence of aminobenzonitrile and dimethylaminobenzonitrile in polar solvents. An ab initio study. *The Journal of Physical Chemistry A* **2015**, *119*, 1983–1995.

(6) Jmol development team, Jmol. `http://jmol.sourceforge.net/`.

(7) Kochman, M. A.; Durbeej, B. Simulating the Nonadiabatic Relaxation Dynamics of 4-(N, N-Dimethylamino) benzonitrile (DMABN) in Polar Solution. *The Journal of Physical Chemistry A* **2020**, *124*, 2193–2206.

(8) Georgieva, I.; Aquino, A. J.; Plasser, F.; Trendafilova, N.; Köhn, A.; Lischka, H. Intramolecular charge-transfer excited-state processes in 4-(N, N-Dimethylamino) benzonitrile: The role of twisting and the $\pi\sigma^*$ state. *The Journal of Physical Chemistry A* **2015**, *119*, 6232–6243.

(9) Druzhinin, S. I.; Ernsting, N. P.; Kovalenko, S. A.; Lustres, L. P.; Senyushkina, T. A.; Zachariasse, K. A. Dynamics of ultrafast intramolecular charge transfer with 4-(dimethylamino) benzonitrile in acetonitrile. *The Journal of Physical Chemistry A* **2006**, *110*, 2955–2969.

(10) Coto, P. B.; Serrano-Andrés, L.; Gustavsson, T.; Fujiwara, T.; Lim, E. C. Intramolecular charge transfer and dual fluorescence of 4-(dimethylamino) benzonitrile: ultrafast branching followed by a two-fold decay mechanism. *Physical Chemistry Chemical Physics* **2011**, *13*, 15182–15188.

(11) Li, Y.; Liu, T.; Liu, H.; Tian, M.-Z.; Li, Y. Self-assembly of intramolecular charge-transfer compounds into functional molecular systems. *Accounts of chemical research* **2014**, *47*, 1186–1198.

(12) Cole, J. M. Enumerating Intramolecular Charge Transfer in Conjugated Organic Compounds. *Journal of Chemical Information and Modeling* **2020**, *60*, 6095–6108.

(13) Grabowski, Z. R.; Rotkiewicz, K.; Rettig, W. Structural changes accompanying intramolecular electron transfer: focus on twisted intramolecular charge-transfer states and structures. *Chemical reviews* **2003**, *103*, 3899–4032.

(14) Chica, B.; Wu, C.-H.; Liu, Y.; Adams, M. W.; Lian, T.; Dyer, R. B. Balancing electron transfer rate and driving force for efficient photocatalytic hydrogen production in CdSe/CdS nanorod–[NiFe] hydrogenase assemblies. *Energy & Environmental Science* **2017**, *10*, 2245–2255.

(15) Upadhyayula, S.; Nunez, V.; Espinoza, E. M.; Larsen, J. M.; Bao, D.; Shi, D.; Mac, J. T.; Anvari, B.; Vullev, V. I. Photoinduced dynamics of a cyanine dye: parallel pathways of non-radiative deactivation involving multiple excited-state twisted transients. *Chemical science* **2015**, *6*, 2237–2251.

(16) Xu, J.-Y.; Tong, X.; Yu, P.; Wenya, G. E.; McGrath, T.; Fong, M. J.; Wu, J.; Wang, Z. M. Ultrafast dynamics of charge transfer and photochemical reactions in solar energy conversion. *Advanced Science* **2018**, *5*, 1800221.

(17) Bottari, G.; de la Torre, G.; Guldi, D. M.; Torres, T. Covalent and noncovalent phthalocyanine- carbon nanostructure systems: synthesis, photoinduced electron transfer, and application to molecular photovoltaics. *Chemical reviews* **2010**, *110*, 6768–6816.

(18) Gust, D.; Moore, T. A.; Moore, A. L. Solar fuels via artificial photosynthesis. *Accounts of chemical research* **2009**, *42*, 1890–1898.

(19) Wasielewski, M. R. Self-assembly strategies for integrating light harvesting and charge separation in artificial photosynthetic systems. *Accounts of chemical research* **2009**, *42*, 1910–1921.

(20) Fukuzumi, S.; Ohkubo, K.; Suenobu, T. Long-lived charge separation and applications in artificial photosynthesis. *Accounts of chemical research* **2014**, *47*, 1455–1464.

(21) Walker, G. C.; Aakesson, E.; Johnson, A. E.; Levinger, N. E.; Barbara, P. F. Interplay of solvent motion and vibrational excitation in electron-transfer kinetics: experiment and theory. *The Journal of Physical Chemistry* **1992**, *96*, 3728–3736.

(22) Alam, B.; Morrison, A. F.; Herbert, J. M. Charge separation and charge transfer in the low-lying excited states of pentacene. *The Journal of Physical Chemistry C* **2020**, *124*, 24653–24666.

(23) Wiberg, J.; Guo, L.; Pettersson, K.; Nilsson, D.; Ljungdahl, T.; Mårtensson, J.; Albinsson, B. Charge recombination versus charge separation in donor- bridge- acceptor systems. *Journal of the American Chemical Society* **2007**, *129*, 155–163.

(24) Duvanel, G.; Banerji, N.; Vauthey, E. Excited-State Dynamics of Donor- Acceptor Bridged Systems Containing a Boron- Dipyrromethene Chromophore: Interplay between Charge Separation and Reorientational Motion. *The Journal of Physical Chemistry A* **2007**, *111*, 5361–5369.

(25) Wilken, S.; Scheunemann, D.; Dahlström, S.; Nyman, M.; Parisi, J.; Österbacka, R. How to reduce charge recombination in organic solar cells: There are still lessons to learn from P3HT: PCBM. *Advanced Electronic Materials* **2021**, *7*, 2001056.

(26) Rettig, W. *Electron Transfer I*; Springer, 2005; pp 253–299.

(27) Misra, R.; Bhattacharyya, S. P. *Intramolecular charge transfer: theory and applications*; John Wiley & Sons, 2018.

(28) Zhang, D.; Heeney, M. Organic Donor–Acceptor Systems. 2020.

(29) Lippert, E.; Lüder, W.; Moll, F.; Nägele, W.; Boos, H.; Prigge, H.; Seibold-Blankenstein, I. Umwandlung von elektronenanregungsenergie. *Angewandte Chemie* **1961**, *73*, 695–706.

(30) Su, S.-G.; Simon, J. D. The importance of vibrational motion and solvent diffusional motion in excited state intramolecular electron transfer reactions. *The Journal of chemical physics* **1988**, *89*, 908–919.

(31) Kato, S.; Amatatsu, Y. A theoretical study on the mechanism of charge transfer state formation of 4-(N, N-dimethylamino) benzonitrile in an aqueous solution. *The Journal of Chemical Physics* **1990**, *92*, 7241–7257.

(32) Parusel, A. B.; Rettig, W.; Sudholt, W. A comparative theoretical study on DMABN: significance of excited state optimized geometries and direct comparison of methodologies. *The Journal of Physical Chemistry A* **2002**, *106*, 804–815.

(33) Rappoport, D.; Furche, F. Photoinduced intramolecular charge transfer in 4-(dimethyl) aminobenzonitrile- a theoretical perspective. *Journal of the American Chemical Society* **2004**, *126*, 1277–1284.

(34) Park, M.; Kim, C. H.; Joo, T. Multifaceted ultrafast intramolecular charge transfer dynamics of 4-(dimethylamino) benzonitrile (DMABN). *The Journal of Physical Chemistry A* **2013**, *117*, 370–377.

(35) Rotkiewicz, K.; Grellmann, K. H.; Grabowski, Z. R. Reinterpretation of the anomalous fluorescense of p-n,n-dimethylamino-benzonitrile. *Chem. Phys. Lett* **1973**, *19*, 315–318.

(36) Grabowski, Z.; Dobkowski, J. Twisted intramolecular charge transfer (TICT) excited states: energy and molecular structure. 1983.

(37) Rotkiewicz, K.; Grabowski, Z. R.; Jasny, J. Picosecond isomerisation kinetics of excited p-dimethylaminobenzonitriles studied by oxygen quenching of fluorescence. *Chemical Physics Letters* **1975**, *34*, 55–59.

(38) Köhler, G.; Rechthaler, K.; Rotkiewicz, K.; Rettig, W. Formation and stabilization of twisted intramolecular charge transfer states in binary mixed solvents. *Chemical physics* **1996**, *207*, 85–101.

(39) Okada, T.; Uesugi, M.; Köhler, G.; Rechthaler, K.; Rotkiewicz, K.; Rettig, W.; Grabner, G. Time-resolved spectroscopy of DMABN and its cage derivatives 6-cyanobenzquinuclidine (CBQ) and benzquinuclidine (BQ). *Chemical physics* **1999**, *241*, 327–337.

(40) Rettig, W.; Lutze, S. Mechanistic considerations for the dual fluorescence of dimethylaminobenzonitrile: a fluorescence anisotropy study. *Chemical physics letters* **2001**, *341*, 263–271.

(41) von Der Haar, T.; Hebecker, A.; Il'Ichev, Y.; Jiang, Y.-B.; Kühnle, W.; Zachariasse, K. A. Excited-state intramolecular charge transfer in donor/acceptor-substituted aromatic hydrocarbons and in biaryls. The significance of the redox potentials of the D/A subsystems. *Recueil des Travaux Chimiques des Pays-Bas* **1995**, *114*, 430–442.

(42) Zachariasse, K.; Grobys, M.; Von der Haar, T.; Hebecker, A.; Il'Ichev, Y. V.; Jiang, Y.-B.; Morawski, O.; Kühnle, W. Intramolecular charge transfer in the excited state. Kinetics and configurational changes. *Journal of Photochemistry and Photobiology A: Chemistry* **1996**, *102*, 59–70.

(43) Zachariasse, K.; Grobys, M.; Von der Haar, T.; Hebecker, A.; Il'Ichev, Y. V.; Morawski, O.; Rückert, I.; Kühnle, W. Photo-induced intramolecular charge transfer and internal conversion in molecules with a small energy gap between S1 and S2. Dynamics and structure. *Journal of Photochemistry and Photobiology A: Chemistry* **1997**, *105*, 373–383.

(44) Il'ichev, Y. V.; Kühnle, W.; Zachariasse, K. A. Intramolecular charge transfer in dual fluorescent 4-(dialkylamino) benzonitriles. Reaction efficiency enhancement by increasing the size of the amino and benzonitrile subunits by alkyl substituents. *The Journal of Physical Chemistry A* **1998**, *102*, 5670–5680.

(45) Zachariasse, K. A. Comment on "Pseudo-Jahn–Teller and TICT-models: a photophysical comparison of meta-and para-DMABN derivatives"[Chem. Phys. Lett. 305 (1999) 8]: The PICT model for dual fluorescence of aminobenzonitriles. *Chemical Physics Letters* **2000**, *320*, 8–13.

(46) Yoshihara, T.; Druzhinin, S. I.; Zachariasse, K. A. Fast intramolecular charge transfer with a planar rigidized electron donor/acceptor molecule. *Journal of the American Chemical Society* **2004**, *126*, 8535–8539.

(47) Zachariasse, K. A.; Druzhinin, S. I.; Bosch, W.; Machinek, R. Intramolecular charge

transfer with the planarized 4-aminobenzonitrile 1-tert-butyl-6-cyano-1, 2, 3, 4-tetrahydroquinoline (NTC6). *Journal of the American Chemical Society* **2004**, *126*, 1705–1715.

(48) Ma, C.; Kwok, W. M.; Matousek, P.; Parker, A.; Phillips, D.; Toner, W.; Towrie, M. Excited states of 4-aminobenzonitrile (ABN) and 4-dimethylaminobenzonitrile (DMABN): Time-resolved resonance Raman, transient absorption, fluorescence, and ab initio calculations. *The Journal of Physical Chemistry A* **2002**, *106*, 3294–3305.

(49) Hättig, C.; Hellweg, A.; Köhn, A. Intramolecular charge-transfer mechanism in quinolidines: The role of the amino twist angle. *Journal of the American Chemical Society* **2006**, *128*, 15672–15682.

(50) Dreyer, J.; Kummrow, A. Shedding light on excited-state structures by theoretical analysis of femtosecond transient infrared spectra: intramolecular charge transfer in 4-(dimethylamino) benzonitrile. *Journal of the American Chemical Society* **2000**, *122*, 2577–2585.

(51) Kwok, W. M.; Ma, C.; Matousek, P.; Parker, A.; Phillips, D.; Toner, W.; Towrie, M.; Umapathy, S. A determination of the structure of the intramolecular charge transfer state of 4-dimethylaminobenzonitrile (DMABN) by time-resolved resonance Raman spectroscopy. *The Journal of Physical Chemistry A* **2001**, *105*, 984–990.

(52) Sobolewski, A. L.; Domcke, W. Charge transfer in aminobenzonitriles: do they twist? *Chemical physics letters* **1996**, *250*, 428–436.

(53) Sobolewski, A. L.; Domcke, W. Promotion of intramolecular charge transfer in dimethylamino derivatives: Twisting versus acceptor-group rehybridization. *Chemical physics letters* **1996**, *259*, 119–127.

(54) Sobolewski, A.; Sudholt, W.; Domcke, W. Ab initio investigation of reaction path-

ways for intramolecular charge transfer in dimethylanilino derivatives. *The Journal of Physical Chemistry A* **1998**, *102*, 2716–2722.

(55) Zgierski, M. Z.; Lim, E. C. The role of $\pi\sigma^*$ state in intramolecular electron-transfer dynamics of 4-dimethylaminobenzonitrile and related molecules. *The Journal of chemical physics* **2004**, *121*, 2462–2465.

(56) Zgierski, M. Z.; Lim, E. C. Electronic and vibrational spectra of the low-lying π σ^* state of 4-dimethylaminobenzonitrile: Comparison of theoretical predictions with experiment. *The Journal of chemical physics* **2005**, *122*, 111103.

(57) Lee, J.-K.; Fujiwara, T.; Kofron, W. G.; Zgierski, M. Z.; Lim, E. C. The low-lying π σ^* state and its role in the intramolecular charge transfer of aminobenzonitriles and aminobenzethyne. *The Journal of chemical physics* **2008**, *128*, 164512.

(58) Gustavsson, T.; Coto, P. B.; Serrano-Andrés, L.; Fujiwara, T.; Lim, E. C. Do fluorescence and transient absorption probe the same intramolecular charge transfer state of 4-(dimethylamino) benzonitrile? *The Journal of chemical physics* **2009**, *131*, 031101.

(59) Soujanya, T.; Saroja, G.; Samanta, A. AM1 study of the twisted intramolecular charge transfer phenomenon in p-(N, N-dimethylamino) benzonitrile. *Chemical physics letters* **1995**, *236*, 503–509.

(60) Parusel, A. B.; Köhler, G.; Nooijen, M. A coupled-cluster analysis of the electronic excited states in aminobenzonitriles. *The Journal of Physical Chemistry A* **1999**, *103*, 4056–4064.

(61) Parusel, A. B. A DFT/MRCI study on the excited state charge transfer states of N-pyrrolobenzene, N-pyrrolobenzonitrile and 4-N, N-dimethylaminobenzonitrile. *Physical Chemistry Chemical Physics* **2000**, *2*, 5545–5552.

(62) Gómez, I.; Mercier, Y.; Reguero, M. Theoretical investigation of luminescence behavior as a function of alkyl chain size in 4-aminobenzonitrile alicyclic derivatives. *The Journal of Physical Chemistry A* **2006**, *110*, 11455–11461.

(63) Perveaux, A.; Castro, P. J.; Lauvergnat, D.; Reguero, M.; Lasorne, B. Intramolecular charge transfer in 4-aminobenzonitrile does not need the twist and may not need the bend. *The Journal of Physical Chemistry Letters* **2015**, *6*, 1316–1320.

(64) Cogan, S.; Zilberg, S.; Haas, Y. The electronic origin of the dual fluorescence in donor-acceptor substituted benzene derivatives. *Journal of the American Chemical Society* **2006**, *128*, 3335–3345.

(65) Jamorski Jödicke, C.; Lüthi, H. P. Time-dependent density functional theory (TDDFT) study of the excited charge-transfer state formation of a series of aromatic donor- acceptor systems. *Journal of the American Chemical Society* **2003**, *125*, 252–264.

(66) Scalmani, G.; Frisch, M. J.; Mennucci, B.; Tomasi, J.; Cammi, R.; Barone, V. Geometries and properties of excited states in the gas phase and in solution: Theory and application of a time-dependent density functional theory polarizable continuum model. *The Journal of chemical physics* **2006**, *124*, 094107.

(67) Zgierski, M. Z.; Fujiwara, T.; Lim, E. C. Role of the $\pi\sigma^*$ State in Molecular Photophysics. *Accounts of chemical research* **2010**, *43*, 506–517.

(68) Carlotto, S.; Polimeno, A.; Ferrante, C.; Benzi, C.; Barone, V. Integrated approach for modeling the emission fluorescence of 4-(N, N-dimethylamino) benzonitrile in polar environments. *The Journal of Physical Chemistry B* **2008**, *112*, 8106–8113.

(69) Köhn, A.; Hättig, C. On the nature of the low-lying singlet states of 4-(dimethylamino) benzonitrile. *Journal of the American Chemical Society* **2004**, *126*, 7399–7410.

(70) Lommatzsch, U.; Brutschy, B. Ab initio calculations and supersonic jet studies on the geometry of 4-dimethylaminobenzonitrile (DMABN) and related compounds in the ground and excited state. *Chemical physics* **1998**, *234*, 35–57.

(71) Modesto-Costa, L.; Borges Jr, I. Discrete and continuum modeling of solvent effects in a twisted intramolecular charge transfer system: The 4-N, N-dimethylaminobenzonitrile (DMABN) molecule. *Spectrochimica Acta Part A: Molecular and Biomolecular Spectroscopy* **2018**, *201*, 73–81.

(72) Curchod, B. F.; Sisto, A.; Martínez, T. J. Ab initio multiple spawning photochemical dynamics of DMABN using GPUs. *The Journal of Physical Chemistry A* **2017**, *121*, 265–276.

(73) Kochman, M. A.; Durbeej, B.; Kubas, A. Simulation and Analysis of the Transient Absorption Spectrum of 4-(N, N-Dimethylamino) benzonitrile (DMABN) in Acetonitrile. *The Journal of Physical Chemistry A* **2021**, *125*, 8635–8648.

(74) Kochman, M. A.; Tajti, A.; Morrison, C. A.; Miller, R. D. Early events in the nonadiabatic relaxation dynamics of 4-(N, N-dimethylamino) benzonitrile. *Journal of chemical theory and computation* **2015**, *11*, 1118–1128.

(75) Rhinehart, J. M.; Challa, J. R.; McCamant, D. W. Multimode charge-transfer dynamics of 4-(dimethylamino) benzonitrile probed with ultraviolet femtosecond stimulated Raman spectroscopy. *The Journal of Physical Chemistry B* **2012**, *116*, 10522–10534.

(76) Segarra-Martí, J.; Coto, P. B. A theoretical study of the intramolecular charge transfer in 4-(dimethylamino) benzethyne. *Physical Chemistry Chemical Physics* **2014**, *16*, 25642–25648.

(77) Zachariasse, K. A.; Druzhinin, S. I.; Kovalenko, S. A.; Senyushkina, T. Intramolecular charge transfer of 4-(dimethylamino) benzonitrile probed by time-resolved fluorescence

and transient absorption: No evidence for two ICT states and a π σ $*$ reaction intermediate. *The Journal of chemical physics* **2009**, *131*, 224313.

(78) Galván, I. F.; Martín, M. E.; Aguilar, M. A. On the absorption properties of the excited states of DMABN. *Chemical Physics Letters* **2010**, *499*, 100–102.

(79) Galván, I. F.; Martín, M. E.; Aguilar, M. A. Theoretical study of the dual fluorescence of 4-(N, N-dimethylamino) benzonitrile in solution. *Journal of Chemical Theory and Computation* **2010**, *6*, 2445–2454.

(80) Lee, J.-k. Intramolecular Charge Transfer in Dimethylaminobenzonitrile and Related Aromatic Nitriles. Ph.D. thesis, University of Akron, 2009.

(81) Du, L.; Lan, Z. An on-the-fly surface-hopping program jade for nonadiabatic molecular dynamics of polyatomic systems: implementation and applications. *Journal of chemical theory and computation* **2015**, *11*, 1360–1374.

(82) Medders, G. R.; Alguire, E. C.; Jain, A.; Subotnik, J. E. Ultrafast electronic relaxation through a conical intersection: Nonadiabatic dynamics disentangled through an oscillator strength-based diabatization framework. *The Journal of Physical Chemistry A* **2017**, *121*, 1425–1434.

(83) Gómez, S.; Soysal, E. N.; Worth, G. A. Micro-Solvated DMABN: Excited State Quantum Dynamics and Dual Fluorescence Spectra. *Molecules* **2021**, *26*, 7247.

(84) Rhinehart, J. M.; Mehlenbacher, R. D.; McCamant, D. Probing the charge transfer reaction coordinate of 4-(dimethylamino) benzonitrile with femtosecond stimulated Raman spectroscopy. *The Journal of Physical Chemistry B* **2010**, *114*, 14646–14656.

(85) Druzhinin, S. I.; Mayer, P.; Stalke, D.; von Buülow, R.; Noltemeyer, M.; Zachariasse, K. A. Intramolecular charge transfer with 1-tert-butyl-6-cyano-1, 2, 3, 4-tetrahydroquinoline (ntc6) and other aminobenzonitriles. a comparison of experimen-

tal vapor phase spectra and crystal structures with calculations. *Journal of the American Chemical Society* **2010**, *132*, 7730–7744.

(86) Stolow, A. Time-resolved photoelectron spectroscopy: Non-adiabatic dynamics in polyatomic molecules. *International Reviews in Physical Chemistry* **2003**, *22*, 377–405.

(87) Wu, G.; Neville, S. P.; Schalk, O.; Sekikawa, T.; Ashfold, M. N.; Worth, G. A.; Stolow, A. Excited state non-adiabatic dynamics of N-methylpyrrole: A time-resolved photoelectron spectroscopy and quantum dynamics study. *The Journal of Chemical Physics* **2016**, *144*, 014309.

(88) Boguslavskiy, A. E.; Schalk, O.; Gador, N.; Glover, W. J.; Mori, T.; Schultz, T.; Schuurman, M. S.; Martínez, T. J.; Stolow, A. Excited state non-adiabatic dynamics of the smallest polyene, trans 1, 3-butadiene. I. Time-resolved photoelectron-photoion coincidence spectroscopy. *The Journal of chemical physics* **2018**, *148*, 164302.

(89) Coates, M. R.; Larsen, M. A.; Forbes, R.; Neville, S. P.; Boguslavskiy, A. E.; Wilkinson, I.; Sølling, T. I.; Lausten, R.; Stolow, A.; Schuurman, M. S. Vacuum ultraviolet excited state dynamics of the smallest ring, cyclopropane. II. Time-resolved photoelectron spectroscopy and ab initio dynamics. *The Journal of chemical physics* **2018**, *149*, 144311.

(90) Röder, A.; Petersen, J.; Issler, K.; Fischer, I.; Mitric, R.; Poisson, L. Exploring the excited-state dynamics of hydrocarbon radicals, biradicals, and carbenes using time-resolved photoelectron spectroscopy and field-induced surface hopping simulations. *The Journal of Physical Chemistry A* **2019**, *123*, 10643–10662.

(91) Glover, W. J.; Mori, T.; Schuurman, M. S.; Boguslavskiy, A. E.; Schalk, O.; Stolow, A.; Martínez, T. J. Excited state non-adiabatic dynamics of the smallest polyene, trans

1, 3-butadiene. II. Ab initio multiple spawning simulations. *The Journal of chemical physics* **2018**, *148*, 164303.

(92) Schuurman, M. S.; Blanchet, V. Time-resolved photoelectron spectroscopy: the continuing evolution of a mature technique. *Physical Chemistry Chemical Physics* **2022**, *24*, 20012–20024.

(93) Ullrich, S.; Schultz, T.; Zgierski, M. Z.; Stolow, A. Electronic relaxation dynamics in DNA and RNA bases studied by time-resolved photoelectron spectroscopy. *Physical Chemistry Chemical Physics* **2004**, *6*, 2796–2801.

(94) Milne, C.; Penfold, T.; Chergui, M. Recent experimental and theoretical developments in time-resolved X-ray spectroscopies. *Coordination Chemistry Reviews* **2014**, *277*, 44–68.

(95) Norman, P.; Dreuw, A. Simulating X-ray spectroscopies and calculating core-excited states of molecules. *Chemical reviews* **2018**, *118*, 7208–7248.

(96) McNeil, B. W.; Thompson, N. R. X-ray free-electron lasers. *Nature photonics* **2010**, *4*, 814–821.

(97) Huang, Z.; Kim, K.-J. Review of x-ray free-electron laser theory. *Physical Review Special Topics-Accelerators and Beams* **2007**, *10*, 034801.

(98) Chergui, M. Emerging photon technologies for chemical dynamics. *Faraday Discussions* **2014**, *171*, 11–40.

(99) Attar, A. R.; Bhattacherjee, A.; Pemmaraju, C.; Schnorr, K.; Closser, K. D.; Prendergast, D.; Leone, S. R. Femtosecond x-ray spectroscopy of an electrocyclic ring-opening reaction. *Science* **2017**, *356*, 54–59.

(100) Pertot, Y.; Schmidt, C.; Matthews, M.; Chauvet, A.; Huppert, M.; Svoboda, V.; Von Conta, A.; Tehlar, A.; Baykusheva, D.; Wolf, J.-P., et al. Time-resolved x-ray

absorption spectroscopy with a water window high-harmonic source. *Science* **2017**, *355*, 264–267.

(101) Zalogina, A.; Carletti, L.; Rudenko, A.; Moloney, J. V.; Tripathi, A.; Lee, H.-C.; Shadrivov, I.; Park, H.-G.; Kivshar, Y.; Kruk, S. S. High-harmonic generation from a subwavelength dielectric resonator. *Science Advances* **2023**, *9*, eadg2655.

(102) Chen, L. X. Probing transient molecular structures in photochemical processes using laser-initiated time-resolved X-ray absorption spectroscopy. *Annu. Rev. Phys. Chem.* **2005**, *56*, 221–254.

(103) Gessner, O.; Gühr, M. Monitoring ultrafast chemical dynamics by time-domain x-ray photo-and Auger-electron spectroscopy. *Accounts of chemical research* **2016**, *49*, 138–145.

(104) Cooper, B.; Kolorenč, P.; Frasinski, L. J.; Averbukh, V.; Marangos, J. P. Analysis of a measurement scheme for ultrafast hole dynamics by few femtosecond resolution X-ray pump–probe Auger spectroscopy. *Faraday discussions* **2014**, *171*, 93–111.

(105) Stöhr, J. *NEXAFS spectroscopy*; Springer Science & Business Media, 2013; Vol. 25.

(106) Van Bokhoven, J. A.; Lamberti, C. *X-ray absorption and X-ray emission spectroscopy: theory and applications*; John Wiley & Sons, 2016; Vol. 1.

(107) Liekhus-Schmaltz, C. E.; Tenney, I.; Osipov, T.; Sanchez-Gonzalez, A.; Berrah, N.; Boll, R.; Bomme, C.; Bostedt, C.; Bozek, J. D.; Carron, S., et al. Ultrafast isomerization initiated by X-ray core ionization. *Nature communications* **2015**, *6*, 8199.

(108) Rimmerman, D.; Leshchev, D.; Hsu, D. J.; Hong, J.; Kosheleva, I.; Chen, L. X. Direct observation of insulin association dynamics with time-resolved X-ray scattering. *The journal of physical chemistry letters* **2017**, *8*, 4413–4418.

(109) Bokarev, S. I.; Kühn, O. Theoretical X-ray spectroscopy of transition metal compounds. *Wiley Interdisciplinary Reviews: Computational Molecular Science* **2020**, *10*, e1433.

(110) Kubin, M.; Guo, M.; Kroll, T.; Löchel, H.; Källman, E.; Baker, M. L.; Mitzner, R.; Gul, S.; Kern, J.; Föhlisch, A., et al. Probing the oxidation state of transition metal complexes: a case study on how charge and spin densities determine Mn L-edge X-ray absorption energies. *Chemical science* **2018**, *9*, 6813–6829.

(111) Chatterjee, R.; Weninger, C.; Loukianov, A.; Gul, S.; Fuller, F. D.; Cheah, M. H.; Fransson, T.; Pham, C. C.; Nelson, S.; Song, S., et al. XANES and EXAFS of dilute solutions of transition metals at XFELs. *Journal of synchrotron radiation* **2019**, *26*, 1716–1724.

(112) Seidu, I.; Neville, S. P.; MacDonell, R. J.; Schuurman, M. S. Resolving competing conical intersection pathways: time-resolved X-ray absorption spectroscopy of trans-1, 3-butadiene. *Physical Chemistry Chemical Physics* **2022**, *24*, 1345–1354.

(113) Besley, N. A.; Asmuruf, F. A. Time-dependent density functional theory calculations of the spectroscopy of core electrons. *Physical Chemistry Chemical Physics* **2010**, *12*, 12024–12039.

(114) Coriani, S.; Christiansen, O.; Fransson, T.; Norman, P. Coupled-cluster response theory for near-edge x-ray-absorption fine structure of atoms and molecules. *Physical Review A* **2012**, *85*, 022507.

(115) Lopata, K.; Van Kuiken, B. E.; Khalil, M.; Govind, N. Linear-response and real-time time-dependent density functional theory studies of core-level near-edge x-ray absorption. *Journal of chemical theory and computation* **2012**, *8*, 3284–3292.

(116) Roemelt, M.; Maganas, D.; DeBeer, S.; Neese, F. A combined DFT and restricted open-shell configuration interaction method including spin-orbit coupling: Application

to transition metal L-edge X-ray absorption spectroscopy. *The Journal of chemical physics* **2013**, *138*, 204101.

(117) Dutta, A. K.; Gupta, J.; Vaval, N.; Pal, S. Intermediate Hamiltonian Fock space multireference coupled cluster approach to core excitation spectra. *Journal of Chemical Theory and Computation* **2014**, *10*, 3656–3668.

(118) Wenzel, J.; Wormit, M.; Dreuw, A. Calculating core-level excitations and X-ray absorption spectra of medium-sized closed-shell molecules with the algebraic-diagrammatic construction scheme for the polarization propagator. *Journal of Computational Chemistry* **2014**, *35*, 1900–1915.

(119) Wenzel, J.; Wormit, M.; Dreuw, A. Calculating X-ray absorption spectra of open-shell molecules with the unrestricted algebraic-diagrammatic construction scheme for the polarization propagator. *Journal of chemical theory and computation* **2014**, *10*, 4583–4598.

(120) Wenzel, J.; Holzer, A.; Wormit, M.; Dreuw, A. Analysis and comparison of CVS-ADC approaches up to third order for the calculation of core-excited states. *The Journal of Chemical Physics* **2015**, *142*, 214104.

(121) Neville, S. P.; Averbukh, V.; Ruberti, M.; Yun, R.; Patchkovskii, S.; Chergui, M.; Stolow, A.; Schuurman, M. S. Excited state x-ray absorption spectroscopy: Probing both electronic and structural dynamics. *The Journal of Chemical Physics* **2016**, *145*, 144307.

(122) Nascimento, D. R.; DePrince III, A. E. Simulation of near-edge X-ray absorption fine structure with time-dependent equation-of-motion coupled-cluster theory. *The journal of physical chemistry letters* **2017**, *8*, 2951–2957.

(123) Jin, Y.; Bartlett, R. J. Accurate computation of X-ray absorption spectra with ion-

ization potential optimized global hybrid functional. *The Journal of Chemical Physics* **2018**, *149*, 064111.

(124) Seidu, I.; Neville, S. P.; Kleinschmidt, M.; Heil, A.; Marian, C. M.; Schuurman, M. S. The simulation of X-ray absorption spectra from ground and excited electronic states using core-valence separated DFT/MRCI. *The Journal of Chemical Physics* **2019**, *151*, 144104.

(125) Tenorio, B. N. C.; Moitra, T.; Nascimento, M. A. C.; Rocha, A. B.; Coriani, S. Molecular inner-shell photoabsorption/photoionization cross sections at core-valence-separated coupled cluster level: Theory and examples. *The Journal of Chemical Physics* **2019**, *150*, 224104.

(126) Vidal, M. L.; Feng, X.; Epifanovsky, E.; Krylov, A. I.; Coriani, S. New and efficient equation-of-motion coupled-cluster framework for core-excited and core-ionized states. *Journal of Chemical Theory and Computation* **2019**, *15*, 3117–3133.

(127) Fransson, T.; Brumboiu, I. E.; Vidal, M. L.; Norman, P.; Coriani, S.; Dreuw, A. XABOOM: An X-ray absorption benchmark of organic molecules based on carbon, nitrogen, and oxygen 1s$\rightarrow \pi^*$ transitions. *Journal of Chemical Theory and Computation* **2021**, *17*, 1618–1637.

(128) Rankine, C. D.; Penfold, T. J. Progress in the theory of x-ray spectroscopy: From quantum chemistry to machine learning and ultrafast dynamics. *The Journal of Physical Chemistry A* **2021**, *125*, 4276–4293.

(129) Nascimento, D. R.; Govind, N. Computational approaches for XANES, VtC-XES, and RIXS using linear-response time-dependent density functional theory based methods. *Physical Chemistry Chemical Physics* **2022**, *24*, 14680–14691.

(130) Wadey, J. D.; Besley, N. A. Quantum chemical calculations of X-ray emission spectroscopy. *Journal of Chemical Theory and Computation* **2014**, *10*, 4557–4564.

(131) Fransson, T.; Dreuw, A. Simulating X-ray emission spectroscopy with algebraic diagrammatic construction schemes for the polarization propagator. *Journal of chemical theory and computation* **2018**, *15*, 546–556.

(132) Vidal, M. L.; Krylov, A. I.; Coriani, S. Dyson orbitals within the fc-CVS-EOM-CCSD framework: theory and application to X-ray photoelectron spectroscopy of ground and excited states. *Physical Chemistry Chemical Physics* **2020**, *22*, 2693–2703.

(133) de Moura, C. E.; Sokolov, A. Y. Simulating X-ray photoelectron spectra with strong electron correlation using multireference algebraic diagrammatic construction theory. *Physical Chemistry Chemical Physics* **2022**, *24*, 4769–4784.

(134) Neville, S. P.; Chergui, M.; Stolow, A.; Schuurman, M. S. Ultrafast x-ray spectroscopy of conical intersections. *Physical review letters* **2018**, *120*, 243001.

(135) Tsuru, S.; Vidal, M. L.; Pápai, M.; Krylov, A. I.; Møller, K. B.; Coriani, S. Time-resolved near-edge X-ray absorption fine structure of pyrazine from electronic structure and nuclear wave packet dynamics simulations. *The Journal of Chemical Physics* **2019**, *151*, 124114.

(136) List, N. H.; Dempwolff, A. L.; Dreuw, A.; Norman, P.; Martínez, T. J. Probing competing relaxation pathways in malonaldehyde with transient X-ray absorption spectroscopy. *Chemical Science* **2020**, *11*, 4180–4193.

(137) Szabo, A.; Ostlund, N. S. *Modern quantum chemistry: introduction to advanced electronic structure theory*; Courier Corporation, 2012.

(138) Domcke, W.; Yarkony, D.; Köppel, H. *Conical intersections: electronic structure, dynamics & spectroscopy*; World Scientific, 2004; Vol. 15.

(139) Benavides-Riveros, C. L.; Lathiotakis, N. N.; Marques, M. A. Towards a formal def-

inition of static and dynamic electronic correlations. *Physical Chemistry Chemical Physics* **2017**, *19*, 12655–12664.

(140) Martin, J. M. Electron Correlation: Nature's Weird and Wonderful Chemical Glue. *Israel journal of chemistry* **2022**, *62*, e202100111.

(141) Marian, C. M.; Heil, A.; Kleinschmidt, M. The Dft/Mrci Method. *Wiley Interdisciplinary Reviews: Computational Molecular Science* **2019**, *9*, e1394.

(142) Roos, B. O.; Taylor, P. R.; Sigbahn, P. E. A complete active space SCF method (CASSCF) using a density matrix formulated super-CI approach. *Chemical Physics* **1980**, *48*, 157–173.

(143) Roos, B. O. The complete active space self-consistent field method and its applications in electronic structure calculations. *Advances in Chemical Physics: Ab Initio Methods in Quantum Chemistry Part 2* **1987**, *69*, 399–445.

(144) Andersson, K.; Malmqvist, P. A.; Roos, B. O.; Sadlej, A. J.; Wolinski, K. Second-order perturbation theory with a CASSCF reference function. *Journal of Physical Chemistry* **1990**, *94*, 5483–5488.

(145) Stein, C. J.; von Burg, V.; Reiher, M. The delicate balance of static and dynamic electron correlation. *Journal of chemical theory and computation* **2016**, *12*, 3764–3773.

(146) Andersson, K.; Malmqvist, P.-Å.; Roos, B. O. Second-order perturbation theory with a complete active space self-consistent field reference function. *The Journal of chemical physics* **1992**, *96*, 1218–1226.

(147) Plasser, F.; Lischka, H. Multi-Reference Configuration Interaction. *Quantum Chemistry and Dynamics of Excited States: Methods and Applications* **2020**, 277–297.

(148) Park, J. W.; Al-Saadon, R.; MacLeod, M. K.; Shiozaki, T.; Vlaisavljevich, B. Multireference electron correlation methods: Journeys along potential energy surfaces. *Chemical Reviews* **2020**, *120*, 5878–5909.

(149) Heil, A.; Marian, C. M. DFT/MRCI Hamiltonian for odd and even numbers of electrons. *The Journal of Chemical Physics* **2017**, *147*, 194104.

(150) Neville, S. P.; Schuurman, M. S. Removing the deadwood from DFT/MRCI wave functions: The p-DFT/MRCI method. *Journal of Chemical Theory and Computation* **2021**, *17*, 7657–7665.

(151) Neville, S. P.; Schuurman, M. S. A perturbative approximation to DFT/MRCI: DFT/MRCI (2). *The Journal of Chemical Physics* **2022**, *157*, 164103.

(152) Saunders, V.; Van Lenthe, J. The direct CI method: A detailed analysis. *Molecular Physics* **1983**, *48*, 923–954.

(153) Shavitt, I. *Methods of electronic structure theory*; Springer, 1977; pp 189–275.

(154) Neville, S.; Schuurman, M. GRaCI: General Reference Configuration Interaction. 2021; `https://github.com/schuurman-group/graci.git`.

(155) Grimme, S.; Waletzke, M. A combination of Kohn–Sham density functional theory and multi-reference configuration interaction methods. *The Journal of chemical physics* **1999**, *111*, 5645–5655.

(156) Neville, S. P.; Seidu, I.; Schuurman, M. S. Propagative block diagonalization diabatization of DFT/MRCI electronic states. *The Journal of Chemical Physics* **2020**, *152*, 114110.

(157) Neville, S. P.; Mirmiran, A.; Worth, G. A.; Schuurman, M. S. Electron transfer in photoexcited pyrrole dimers. *The Journal of Chemical Physics* **2019**, *151*.

(158) Plasser, F.; Wormit, M.; Dreuw, A. New tools for the systematic analysis and visualization of electronic excitations. I. Formalism. *The Journal of chemical physics* **2014**, *141*, 024106.

(159) Rice, O. K.; Ramsperger, H. C. Theories of unimolecular gas reactions at low pressures. *Journal of the American Chemical Society* **1927**, *49*, 1617–1629.

(160) Kassel, L. S. Studies in homogeneous gas reactions. I. *The Journal of Physical Chemistry* **1928**, *32*, 225–242.

(161) Marcus, R. A. Unimolecular dissociations and free radical recombination reactions. *The Journal of Chemical Physics* **1952**, *20*, 359–364.

(162) Wang, H.; Frenklach, M. Calculations of rate coefficients for the chemically activated reactions of acetylene with vinylic and aromatic radicals. *The Journal of Physical Chemistry* **1994**, *98*, 11465–11489.

(163) Davis, S. G.; Law, C. K.; Wang, H. Propyne pyrolysis in a flow reactor: An experimental, RRKM, and detailed kinetic modeling study. *The Journal of Physical Chemistry A* **1999**, *103*, 5889–5899.

(164) Miller, J. A.; Klippenstein, S. J. The recombination of propargyl radicals: Solving the master equation. *The Journal of Physical Chemistry A* **2001**, *105*, 7254–7266.

(165) Song, D.; Su, H.; Kong, F.-a.; Lin, S.-H. Anharmonic Rice-Ramsperger-Kassel-Marcus (RRKM) and product branching ratio calculations for the partially deuterated protonated water dimers: Dissociation and isomerization. *The Journal of Chemical Physics* **2013**, *138*.

(166) Shiroudi, A.; Zahedi, E.; Oliaey, A. R.; Deleuze, M. S. Reaction mechanisms and kinetics of the elimination processes of 2-chloroethylsilane and derivatives: A DFT study using CTST, RRKM, and BET theories. *Chemical Physics* **2017**, *485*, 140–148.

(167) Beyer, T.; Swinehart, D. Algorithm 448: number of multiply-restricted partitions. *Communications of the ACM* **1973**, *16*, 379.

(168) Sun, Q.; Berkelbach, T. C.; Blunt, N. S.; Booth, G. H.; Guo, S.; Li, Z.; Liu, J.; McClain, J. D.; Sayfutyarova, E. R.; Sharma, S., et al. PySCF: the Python-based simulations of chemistry framework. *Wiley Interdisciplinary Reviews: Computational Molecular Science* **2018**, *8*, e1340.

(169) Sun, Q.; Zhang, X.; Banerjee, S.; Bao, P.; Barbry, M.; Blunt, N. S.; Bogdanov, N. A.; Booth, G. H.; Chen, J.; Cui, Z.-H., et al. Recent developments in the PySCF program package. *The Journal of chemical physics* **2020**, *153*, 024109.

(170) Whitten, J. L. Coulombic potential energy integrals and approximations. *The Journal of Chemical Physics* **1973**, *58*, 4496–4501.

(171) Feyereisen, M.; Fitzgerald, G.; Komornicki, A. Use of approximate integrals in ab initio theory. An application in MP2 energy calculations. *Chemical physics letters* **1993**, *208*, 359–363.

(172) Vahtras, O.; Almlöf, J.; Feyereisen, M. Integral approximations for LCAO-SCF calculations. *Chemical Physics Letters* **1993**, *213*, 514–518.

(173) Dunning Jr, T. H. Gaussian basis sets for use in correlated molecular calculations. I. The atoms boron through neon and hydrogen. *The Journal of chemical physics* **1989**, *90*, 1007–1023.

(174) Lipparini, F.; Lagardère, L.; Scalmani, G.; Stamm, B.; Cancès, E.; Maday, Y.; Piquemal, J.-P.; Frisch, M. J.; Mennucci, B. Quantum calculations in solution for large to very large molecules: A new linear scaling QM/continuum approach. *The journal of physical chemistry letters* **2014**, *5*, 953–958.

(175) Roos, B. O. The complete active space SCF method in a fock-matrix-based super-CI formulation. *International Journal of Quantum Chemistry* **1980**, *18*, 175–189.

(176) Malmqvist, P. Å.; Rendell, A.; Roos, B. O. The restricted active space self-consistent-field method, implemented with a split graph unitary group approach. *Journal of Physical Chemistry* **1990**, *94*, 5477–5482.

(177) Fdez. Galván, I.; Vacher, M.; Alavi, A.; Angeli, C.; Aquilante, F.; Autschbach, J.; Bao, J. J.; Bokarev, S. I.; Bogdanov, N. A.; Carlson, R. K., et al. OpenMolcas: From source code to insight. *Journal of chemical theory and computation* **2019**, *15*, 5925–5964.

(178) Barone, V.; Cossi, M. Quantum calculation of molecular energies and energy gradients in solution by a conductor solvent model. *The Journal of Physical Chemistry A* **1998**, *102*, 1995–2001.

(179) Cossi, M.; Rega, N.; Scalmani, G.; Barone, V. Energies, structures, and electronic properties of molecules in solution with the C-PCM solvation model. *Journal of computational chemistry* **2003**, *24*, 669–681.

(180) Tomasi, J.; Mennucci, B.; Cammi, R. Quantum mechanical continuum solvation models. *Chemical reviews* **2005**, *105*, 2999–3094.

(181) Lipparini, F.; Stamm, B.; Cances, E.; Maday, Y.; Mennucci, B. Fast domain decomposition algorithm for continuum solvation models: Energy and first derivatives. *Journal of chemical theory and computation* **2013**, *9*, 3637–3648.

(182) Klamt, A. The COSMO and COSMO-RS solvation models. *Wiley Interdisciplinary Reviews: Computational Molecular Science* **2011**, *1*, 699–709.

(183) Klamt, A.; Schüürmann, G. COSMO: a new approach to dielectric screening in solvents

with explicit expressions for the screening energy and its gradient. *Journal of the Chemical Society, Perkin Transactions 2* **1993**, 799–805.

(184) Truong, T. N.; Stefanovich, E. V. A new method for incorporating solvent effect into the classical, ab initio molecular orbital and density functional theory frameworks for arbitrary shape cavity. *Chemical Physics Letters* **1995**, *240*, 253–260.

(185) Weser, O. An efficient and general library for the definition and use of internal coordinates in large molecular systems. Ph.D. thesis, Georg August Universität Göttingen, 2017.

(186) Cossi, M.; Barone, V. Solvent effect on vertical electronic transitions by the polarizable continuum model. *The Journal of Chemical Physics* **2000**, *112*, 2427–2435.

(187) Fujiwara, T.; Lee, J.-K.; Zgierski, M. Z.; Lim, E. C. Intramolecular charge transfer in the excited state of 4-dimethylaminobenzaldehyde and 4-dimethylaminoacetophenone. *Chemical Physics Letters* **2009**, *481*, 78–82.

(188) Schuddeboom, W.; Jonker, S. A.; Warman, J. M.; Leinhos, U.; Kuehnle, W.; Zachariasse, K. A. Excited-state dipole moments of dual fluorescent 4-(dialkylamino) benzonitriles: influence of alkyl chain length and effective solvent polarity. *The Journal of Physical Chemistry* **1992**, *96*, 10809–10819.

(189) Druzhinin, S. I.; Demeter, A.; Zachariasse, K. A. Dual fluorescence and intramolecular charge transfer with crystalline 4-(diisopropylamino) benzonitrile. *Chemical physics letters* **2001**, *347*, 421–428.

(190) Berera, R.; van Grondelle, R.; Kennis, J. T. Ultrafast transient absorption spectroscopy: principles and application to photosynthetic systems. *Photosynthesis research* **2009**, *101*, 105–118.

(191) Ruckebusch, C.; Sliwa, M.; Pernot, P. d.; De Juan, A.; Tauler, R. Comprehensive data analysis of femtosecond transient absorption spectra: A review. *Journal of Photochemistry and Photobiology C: Photochemistry Reviews* **2012**, *13*, 1–27.

(192) Schuurman, M.; Costain, T.; Neville, S. Paramterization of DFT/MRCI(2) with QTP17 (Unpublished Work). **2023**,

(193) Pomogaev, V.; Lee, S.; Shaik, S.; Filatov, M.; Choi, C. H. Exploring Dyson's orbitals and their electron binding energies for conceptualizing excited states from response methodology. *The Journal of Physical Chemistry Letters* **2021**, *12*, 9963–9972.

(194) Datar, A.; Gudivada, S.; Matthews, D. A. Ab Initio Investigation of Intramolecular Charge Transfer States in DMABN by Calculation of Excited State X-ray Absorption Spectra. *The Journal of Physical Chemistry A* **2023**,

(195) Geneaux, R.; Marroux, H. J.; Guggenmos, A.; Neumark, D. M.; Leone, S. R. Transient absorption spectroscopy using high harmonic generation: a review of ultrafast X-ray dynamics in molecules and solids. *Philosophical Transactions of the Royal Society A* **2019**, *377*, 20170463.

(196) Liu, H.; Klein, I. M.; Michelsen, J. M.; Cushing, S. K. Element-specific electronic and structural dynamics using transient XUV and soft X-ray spectroscopy. *Chem* **2021**, *7*, 2569–2584.

(197) Milne, C. J.; Pham, V.-T.; Gawelda, W.; Van Der Veen, R. M.; El Nahhas, A.; Johnson, S. L.; Beaud, P.; Ingold, G.; Lima, F.; Vithanage, D. A., et al. Time-resolved x-ray absorption spectroscopy: Watching atoms dance. Journal of Physics: Conference Series. 2009; p 012052.

(198) Stolow, A.; Schultz, T.; Boguslavskiy, A. TRPES of DMABN and DIABN performed at the University of Ottawa. **2003**,

(199) Myhre, R. H.; Wolf, T. J.; Cheng, L.; Nandi, S.; Coriani, S.; Gühr, M.; Koch, H. A theoretical and experimental benchmark study of core-excited states in nitrogen. *The Journal of Chemical Physics* **2018**, *148*.

(200) Frati, F.; De Groot, F.; Cerezo, J.; Santoro, F.; Cheng, L.; Faber, R.; Coriani, S. Coupled cluster study of the x-ray absorption spectra of formaldehyde derivatives at the oxygen, carbon, and fluorine K-edges. *The Journal of Chemical Physics* **2019**, *151*.

(201) Vidal, M. L.; Pokhilko, P.; Krylov, A. I.; Coriani, S. Equation-of-motion coupled-cluster theory to model L-edge x-ray absorption and photoelectron spectra. *The journal of physical chemistry letters* **2020**, *11*, 8314–8321.

(202) Kirkor-Kamińska, E.; Rotkiewicz, K.; Grabowska, A. Picosecond reversible reaction kinetics of excited p-dimethylaminoacetophenone and m-methyl-p-cyanodimethylaniline studied by oxygen quenching technique. *Chemical Physics Letters* **1978**, *58*, 379–384.

(203) Dähne, S.; Freyer, W.; Teuchner, K.; Dobkowski, J.; Grabowski, Z. Dual and multiple fluorescence mechanisms of p-dimethylaminobenzaldehyde and its trimethylene-bridged double molecule. *Journal of Luminescence* **1980**, *22*, 37–49.

(204) Rettig, W.; Zietz, B. Do twisting and pyramidalization contribute to the reaction coordinate of charge-transfer formation in DMABN and derivatives? *Chemical Physics Letters* **2000**, *317*, 187–196.

(205) Rettig, W.; Wermuth, G.; Lippert, E. Photophysical Primary Processes in Solutions of p-Substituted Dialkylanilines. *Berichte der Bunsengesellschaft für physikalische Chemie* **1979**, *83*, 692–697.

(206) Weisenborn, P. C.; Huizer, A. H.; Varma, C. A. Excited-state dynamics of ethyl 4-(N, N-dimethylamino) benzoate and ethyl 4-(N, N-diethylamino) benzoate in apolar and

polar solvents. *Journal of the Chemical Society, Faraday Transactions 2: Molecular and Chemical Physics* **1989**, *85*, 1895–1912.

(207) Nowak, W.; Rettig, W. Theoretical study of singlet excited states of donor-acceptor naphthalene derivatives. *Journal of Molecular Structure: THEOCHEM* **1993**, *283*, 1–12.

(208) Lunkenheimer, B.; Köhn, A. Solvent effects on electronically excited states using the conductor-like screening model and the second-order correlated method ADC (2). *Journal of chemical theory and computation* **2013**, *9*, 977–994.

(209) Ephardt, H.; Fromherz, P. Fluorescence and photoisomerization of an amphiphilic aminostilbazolium dye as controlled by the sensitivity of radiationless deactivation to polarity and viscosity. *The Journal of Physical Chemistry* **1989**, *93*, 7717–7725.

(210) Ephardt, H.; Fromherz, P. Anilinopyridinium: solvent-dependent fluorescence by intramolecular charge transfer. *The Journal of Physical Chemistry* **1991**, *95*, 6792–6797.

(211) Ephardt, H.; Fromherz, P. Fluorescence of amphiphilic hemicyanine dyes without free double bonds. *The Journal of Physical Chemistry* **1993**, *97*, 4540–4547.

(212) Strehmel, B.; Seifert, H.; Rettig, W. Photophysical properties of fluorescence probes. 2. A model of multiple fluorescence for stilbazolium dyes studied by global analysis and quantum chemical calculations. *The Journal of Physical Chemistry B* **1997**, *101*, 2232–2243.

(213) Vogel, M.; Rettig, W. Efficient Intramolecular Fluorescence Quenching in Triphenylmethane-Dyes Involving Excited States with Charge Separation and Twisted Conformations. *Berichte der Bunsengesellschaft für physikalische Chemie* **1985**, *89*, 962–968.

(214) Fromherz, P.; Dambacher, K.; Ephardt, H.; Lambacher, A.; Müller, C.; Neigl, R.; Schaden, H.; Schenk, O.; Vetter, T. Fluorescent Dyes as Probes of Voltage Transients in Neuron Membranes Progress Report. *Berichte der Bunsengesellschaft für physikalische Chemie* **1991**, *95*, 1333–1345.

(215) Fromherz, P.; Schaden, H.; Vetter, T. Guided outgrowth of leech neurons in culture. *Neuroscience letters* **1991**, *129*, 77–80.

(216) Joshi, H. C.; Antonov, L. Excited-state intramolecular proton transfer: A short introductory review. *Molecules* **2021**, *26*, 1475.

(217) Kwon, J. E.; Park, S. Y. Advanced organic optoelectronic materials: Harnessing excited-state intramolecular proton transfer (ESIPT) process. *Advanced Materials* **2011**, *23*, 3615–3642.

(218) Sedgwick, A. C.; Wu, L.; Han, H.-H.; Bull, S. D.; He, X.-P.; James, T. D.; Sessler, J. L.; Tang, B. Z.; Tian, H.; Yoon, J. Excited-state intramolecular proton-transfer (ESIPT) based fluorescence sensors and imaging agents. *Chemical Society Reviews* **2018**, *47*, 8842–8880.

(219) Padalkar, V. S.; Seki, S. Excited-state intramolecular proton-transfer (ESIPT)-inspired solid state emitters. *Chemical Society Reviews* **2016**, *45*, 169–202.

(220) Li, Y.; Dahal, D.; Abeywickrama, C. S.; Pang, Y. Progress in tuning emission of the excited-state intramolecular proton transfer (ESIPT)-based fluorescent probes. *ACS omega* **2021**, *6*, 6547–6553.

(221) Wörner, H. J.; Arrell, C. A.; Banerji, N.; Cannizzo, A.; Chergui, M.; Das, A. K.; Hamm, P.; Keller, U.; Kraus, P. M.; Liberatore, E., et al. Charge migration and charge transfer in molecular systems. *Structural dynamics* **2017**, *4*, 061508.

(222) Hsieh, C.-C.; Jiang, C.-M.; Chou, P.-T. Recent experimental advances on excited-state intramolecular proton coupled electron transfer reaction. *Accounts of chemical research* **2010**, *43*, 1364–1374.

(223) Yang, W.-Y.; Yan, C.-C.; Wang, X.-D.; Liao, L.-S. Recent progress on the excited-state multiple proton transfer process in organic molecules. *Science China Chemistry* **2022**, *65*, 1843–1853.

(224) Verma, P.; Rosspeintner, A.; Dereka, B.; Vauthey, E.; Kumpulainen, T. Broadband fluorescence reveals mechanistic differences in excited-state proton transfer to protic and aprotic solvents. *Chemical science* **2020**, *11*, 7963–7971.

(225) Ling, F.; Liu, D.; Li, S.; Li, W.; Zhang, B.; Wang, P. Femtosecond real-time probing of the excited-state intramolecular proton transfer reaction in methyl salicylate. *The Journal of Chemical Physics* **2019**, *151*, 094302.

(226) Hsieh, C.-C.; Cheng, Y.-M.; Hsu, C.-J.; Chen, K.-Y.; Chou, P.-T. Spectroscopy and femtosecond dynamics of excited-state proton transfer induced charge transfer reaction. *The Journal of Physical Chemistry A* **2008**, *112*, 8323–8332.

(227) Barbatti, M.; Aquino, A. J.; Lischka, H.; Schriever, C.; Lochbrunner, S.; Riedle, E. Ultrafast internal conversion pathway and mechanism in 2-(2'-hydroxyphenyl) benzothiazole: a case study for excited-state intramolecular proton transfer systems. *Physical Chemistry Chemical Physics* **2009**, *11*, 1406–1415.

(228) Liu, Y.-H.; Yu, S.-B.; Peng, Y.-J.; Wang, C.-W.; Zhu, C.; Lin, S.-H. Excited-state intramolecular proton transfer with and without the assistance of vibronic-transition-induced skeletal deformation in phenol–quinoline. *RSC advances* **2021**, *11*, 37299–37306.

(229) Hsieh, C.-C.; Chou, P.-T.; Shih, C.-W.; Chuang, W.-T.; Chung, M.-W.; Lee, J.; Joo, T. Comprehensive studies on an overall proton transfer cycle of the ortho-green fluo-

rescent protein chromophore. *Journal of the American Chemical Society* **2011**, *133*, 2932–2943.

(230) Lee, J.; Kim, C. H.; Joo, T. Active role of proton in excited state intramolecular proton transfer reaction. *The Journal of Physical Chemistry A* **2013**, *117*, 1400–1405.

(231) Mu, H.; Li, H.; Sun, C.; Gao, J.; Yang, M.; Xin, C.; Jin, G. Different competition mechanism between ESPT and TICT process regulated by protic and aprotic solvent in DHP. *Journal of Molecular Liquids* **2023**, 121278.

(232) Laner, J. N.; Junior, H. d. C. S.; Rodembusch, F. S.; Moreira, E. C. New insights on the ESIPT process based on solid-state data and state-of-the-art computational methods. *Physical Chemistry Chemical Physics* **2021**, *23*, 1146–1155.

(233) Schriever, C.; Barbatti, M.; Stock, K.; Aquino, A. J.; Tunega, D.; Lochbrunner, S.; Riedle, E.; de Vivie-Riedle, R.; Lischka, H. The interplay of skeletal deformations and ultrafast excited-state intramolecular proton transfer: Experimental and theoretical investigation of 10-hydroxybenzo [h] quinoline. *Chemical Physics* **2008**, *347*, 446–461.

(234) Pijeau, S.; Foster, D.; Hohenstein, E. G. Excited-state dynamics of a benzotriazole photostabilizer: 2-(2'-hydroxy-5'-methylphenyl) benzotriazole. *The Journal of Physical Chemistry A* **2017**, *121*, 6377–6387.

(235) Tasheh, N. S.; Nkungli, N. K.; Ghogomu, J. N. A DFT and TD-DFT study of ESIPT-mediated NLO switching and UV absorption by 2-(2'-hydroxy-5'-methylphenyl) benzotriazole. *Theoretical Chemistry Accounts* **2019**, *138*, 1–17.

(236) Pijeau, S.; Foster, D.; Hohenstein, E. G. Effect of nonplanarity on excited-state proton transfer and internal conversion in salicylideneaniline. *The Journal of Physical Chemistry A* **2018**, *122*, 5555–5562.

(237) Paterson, M. J.; Robb, M. A.; Blancafort, L.; DeBellis, A. D. Theoretical study of benzotriazole UV photostability: ultrafast deactivation through coupled proton and electron transfer triggered by a charge-transfer state. *Journal of the American Chemical Society* **2004**, *126*, 2912–2922.

(238) Dong, H.; Liu, X.; Yang, H.; Zhao, J.; Zheng, Y. Harnessing Excited-State Proton Transfer Reaction for 2-(6'-Hydroxy-2'-pyridyl) benzimidazole via Solvents. *ACS Applied Bio Materials* **2021**, *4*, 1950–1957.

(239) Khodia, S.; Jarupula, R.; Baweja, S.; Shabeeb, M.; Kalal, B.; Maity, S. Excited-state deactivation via solvent-to-chromophore proton transfer in an isolated 1: 1 molecular complex: experimental validation by measuring the energy barrier and kinetic isotope effect. *Physical Chemistry Chemical Physics* **2023**, *25*, 13498–13507.

(240) Kungwan, N.; Plasser, F.; Aquino, A. J.; Barbatti, M.; Wolschann, P.; Lischka, H. The effect of hydrogen bonding on the excited-state proton transfer in 2-(2'-hydroxyphenyl) benzothiazole: a TDDFT molecular dynamics study. *Physical Chemistry Chemical Physics* **2012**, *14*, 9016–9025.

(241) Norell, J.; Ljungdahl, A.; Odelius, M. Interdependent electronic structure, protonation, and solvatization of aqueous 2-thiopyridone. *The Journal of Physical Chemistry B* **2019**, *123*, 5555–5567.

(242) Norell, J.; Eckert, S.; Van Kuiken, B. E.; Föhlisch, A.; Odelius, M. Ab initio simulations of complementary K-edges and solvatization effects for detection of proton transfer in aqueous 2-thiopyridone. *The Journal of Chemical Physics* **2019**, *151*, 114117.

(243) Loe, C. M.; Liekhus-Schmaltz, C.; Govind, N.; Khalil, M. Spectral signatures of ultrafast excited-state intramolecular proton transfer from computational multi-edge transient x-ray absorption spectroscopy. *The Journal of Physical Chemistry Letters* **2021**, *12*, 9840–9847.

(244) Tao, M.; Li, Y.; Huang, Q.; Zhao, H.; Lan, J.; Wan, Y.; Kuang, Z.; Xia, A. Correlation between Excited-State Intramolecular Proton Transfer and Electron Population on Proton Donor/Acceptor in 2-(2'-Hydroxyphenyl) oxazole Derivatives. *The Journal of Physical Chemistry Letters* **2022**, *13*, 4486–4494.

(245) Liu, K.; Zhang, J.; Shi, Q.; Ding, L.; Liu, T.; Fang, Y. Precise Manipulation of Excited-State Intramolecular Proton Transfer via Incorporating Charge Transfer toward High-Performance Film-Based Fluorescence Sensing. *Journal of the American Chemical Society* **2023**, *145*, 7408–7415.

(246) Zhao, X.; Chen, M. A TDDFT study on the singlet and triplet excited-state hydrogen bonding and proton transfer of 10-hydroxybenzo [h] quinoline (HBQ) and 7, 9-diiodo-10-hydroxybenzo [h] quinoline (DIHBQ). *Chemical Physics Letters* **2011**, *512*, 35–39.